

# NDT SPECTRA

PP 17420/07/2012(030208)

ISSUE NO. 7

NOVEMBER 2013



ISSN 2231-9891

The Official Journal of Malaysian Society  
for Non-Destructive Testing  
<http://www.msnt.org.my>





GE  
Measurement & Control

*Portable, Wireless and Robust.*



Inspection Technologies:  
**DXR250C-W Digital Detector**

Enabling the inspection of field installations to be more flexible and efficient.

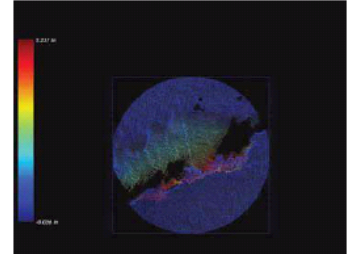
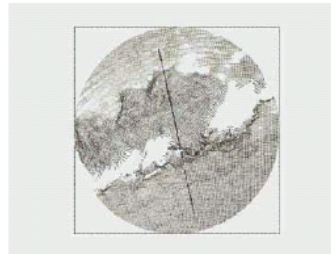
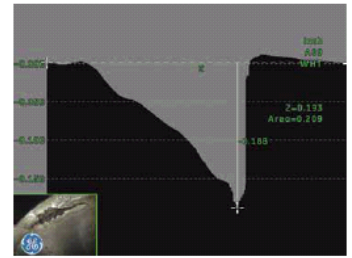


GE imagination at work



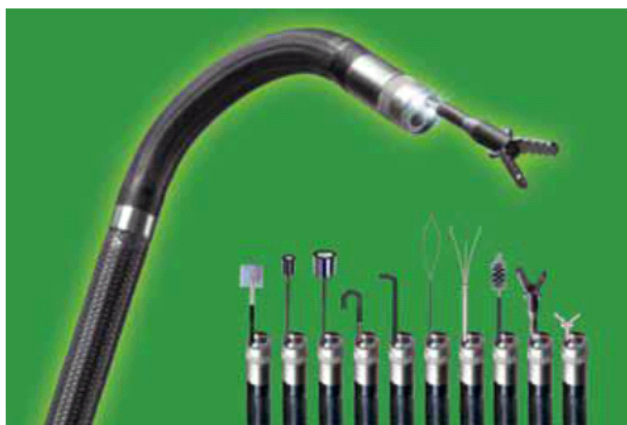
# XLG3™ VideoProbe® system with 3D Phase Measurement Technology

- today's most revolutionary remote visual inspection (RVI) tool
- provides significantly improved inspection capabilities to boost productivity in your operations
- With a host of advanced features, such as QuickChange™ probes that quickly reconfigure probe diameter and length
- 3D Phase Measurement for on-demand measurement and real-time communications for collaboration during live inspections
- delivers the versatility you need for fast, efficient and accurate decision making



# XLGo+™ VideoProbe® system with XpertSuite™ and Working Channel

The 6.2 mm diameter XL Go VideoProbe system features an internal working channel and a full suite of working tools making it the most complete FOD retrieval system in the industry.



## XpertSuite™ Improves Probability of Detection



GE imagination at work

*Authorised distributor for GE Inspection Technologies:*

**Advantech Alliance Sdn Bhd**

28, Jalan USJ 1/13, Taman Perindustrian USJ 1,  
47600 Subang Jaya, Selangor Darul Ehsan, Malaysia

T: +603 8023 7017 F: +603 8023 7016

<http://www.advantech.my> Email: [ndt@advantech.my](mailto:ndt@advantech.my)



# MS ISO /IEC 17024 ACHIEVEMENT

On 3<sup>rd</sup> October 2012, Department of Skills Development (DSD) was complied with MS ISO /IEC 17024 and was accredited as Personnel Certification Body (Scope: Non-Destructive Testing (NDT)) granted by Standards Malaysia (Accreditation Number: PERSONNEL 03102012 CB02) for period of three (3) years until 2<sup>nd</sup> October 2015.

MS ISO /IEC 17024 is a Malaysian Standard of General Requirement for Bodies Operating Certification of Persons which is worldwide accepted and recognised. This accreditation brings DSD to the top list as the first Personnel Certification Body among Malaysian government agency and the 4<sup>th</sup> rank in Asia Pacific Committee in Non Destructive Testing (APCINDT) together with Australia, New Zealand and Republic of China.



The history started in 1986, where the NDT Certification system was first set up. Since then, various documents and procedures had been developed with reference to ISO 9712 Non-Destructive Testing – Qualification and Certification of NDT Personnel and IAF Guidance on the Application of ISO/IEC 17024 (IAF GD 24:2004). Starting in 2010, DSD was closely audited by Standards Malaysia. The auditing process include monitoring on implementation of MS ISO 9001 on NDT certification management system, requirement for persons employed and as well as the certification process itself. A lot of concerns were raised along the process of accreditation in order to improve the certification system up to the international standard.



With this prestige achievement, means our NDT certification system complied with the global benchmark for personnel certification by ensuring they operate in a consistent, comparable and reliable manner worldwide. This recognition also showed that DSD, as the national certification body of skilled personnel, commit in ensuring the integrity in the NDT certification system and the quality of SKM holders in providing NDT skilled workforce development in various industries.



**DEPARTMENT OF SKILLS DEVELOPMENT**  
Ministry of Human Resources  
Level 7 - 8, Block D4, Complex D, Federal Government Administrative Centre, 62530 Putrajaya, Malaysia.  
| Phone: 03-8886 5000 | Fax: 03-8889 2430 |  
| E-mail: jpk@mohr.gov.my | Website: www.dsd.gov.my |



## Table of contents

No	Title Authors	Page
1	Analysis of composite materials, soil and automotive with high resolution computed tomography T. Paul, Holger Roth, GERMANY	1
2	Radioscopy-based digital radiography system for industry Gede B. Suparta, Wayan Sutrisna, Gede Arya Wiguna and Andreas C. Louk, INDONESIA	3
3	Single photon emission computed tomography (SPECT) as a potential NDE tool in the future: a Monte Carlo simulation study Mohd Amirul Syafiq Mohd Yunos, Jaafar Abdullah, Nuclear Malaysia, MALAYSIA	9
4	Low dose customs inspection system for freight transport control Klimenov V.A., Kasyanov S.V., Rychkov M.M., Stein M.M., Kasyanov V.A., Chakhlov S.V., Osipov S.P., Stein A.M., Sun Xiaoming, RUSSIA	17
5	Artificial intelligence in recognition of welding flaws R. Sikora, T. Chady, P. Baniukiewicz, B. Grzywacz, L. Misztal, POLAND	20
6	CR-System Performance Evaluation for Periodic System Check Denis Kiesel, GERMANY	32
7	Phased Array Ultrasonic Inspection of Electro-fusion and Butt Welded Joints in Plastic Pipes Fredrik HAGGLUND, Malcolm SPICER, Mike TROUGHTON and Tat Hean GAN, UK	40
8	Development of Full Matrix Capture Ultrasonic techniques for industrial application Miles Weston, Channa Nageswaran, Michael Tan and Tat-Hean Gan, UK	51
9	Advanced Ultrasonic Phased Array Technology Used in Industrial Applications Stanislav ŠTARMAN and Václav MATZ, CZECH REPUBLIC	59
10	Tropical woods quality assessment by using non-destructive ultrasonic technique Sidek Hj Ab Aziz, Abdul Halim Shaari, Nor Hafzan Sarah Almuin, Mohd Noorul Ikhsan Ahmad, Abd Nassir Ibrahim & Ilham Mukriz Zainal Abidin, UPM, MALAYSIA	66
11	Rail inspection technique employing advanced non-destructive testing and structural health monitoring (SHM) approaches-a review Firouz Fadaeifard, Faizal Mustapha, Khmirul Amin B. Matori, Amir Abbas Nourbakhsh, Meysam Toozandehjani, UPM, MALAYSIA	74



12	Acoustic Wave Finite Element Analysis Study for Ultrasonic Tomography M. J. Pusppanathan, N. M. N. Ayob, F. R. Yunus, R.A. Rahim, F. A. Phang, UTM, MALAYSIA	92
13	Continuous Wavelet Transform and Modal Analysis for Accurate Acoustic Emission Source Location in Steel Pipe Shukri Mohd, Karen Holford and Rhys Pullin, UK	100
14	Development of high intensity laser NDT system for critical mapping of stress distribution in CFRP component Mohd Yusnisyam Yusof, Wan Saffiey Wan Abdullah, Khairiah Yazid and Ilham Mukriz Zainal Abidin, Nuclear Malaysia, MALAYSIA	110
15	Detection Of Local Stress Concentration Zones In Engineering Products – The Lacking Link In The Non-Destructive Testing System A.A. Dubov, RUSSIA	118
16	Combined methods for determination strength of the concrete with fiber polypropylene (the Schmidt hammer and the ultrasonic pulse velocity) Belaribi Hassiba et Mellas Mekki, ALGERIA	
17	What can we obtain from nondestructive testing of wire ropes? Alexander Mironenko, RUSSIA	134
18	Sizing of Cracks of Mild Steel Material using Alternating Current Field Measurement (ACFM) Technique Jeffry, SIRIM, MALAYSIA	141
19	Modelling and Analysis of the Rust in Oil Conduits Sougrati BELATTAR, Naouar LAAIDI, MOROCCO	148
20	Distribution Of Radiation Around Labyrinth Type Exposure Room Mohamad Pauzi Ismail, Mohd Yusnisyam Yusuf, Shaharudin Sayuti, Noor Azreen Masenwat, Siti Madiha Muhammad Amir and Azhar Azmi	154
21	See the Invisible – Innovative Technology as Tool for Safety and Quality Isaac Einav, Royce Wong, CANADA	162
22	Accreditation of the Malaysian Certification Body for NDT in Accordance to ISO 17024 Salbiah Hussein, Abd. Nassir Ibrahim, JPK, MALAYSIA	173
23	TECDOC 628 (IAEA), new revision 2013 Patrick BRISSET, Isaac Einav, IAEA	181
24	Verification/Calibration and Assessment of Non-Destructive Testing(NDT) Equipment/Instrument Ang Chee Keong, SIRIM, MALAYSIA	184
25	Early experience on the implementation of ISO 17020 at NDT group, Malaysian Nuclear Agency Siti Madiha Muhammad Amir, Abd Nassir Ibrahim, Azhar Azmi, Mohamad Pauzi Ismail, Noriah Mod Ali and Sapizah Rahim, Nuclear Malaysia, MALAYSIA	199



26	Determination of optimal exposure for computed radiography systems using exposure chart Sapizah Rahim, Ilham Mukriz Zainal Abidin and Arshad Yassin, MALAYSIA	204
27	A low cost gamma-ray fluoroscopic system for Se-75 and Ir-192 industrial radiography sources N. Chankow and K. Iamsamang, THAILAND	209
28	Damage Classification in CFRP Laminates Using the NDT/E Approach M.T.H. Sultan, A.S.M. Rafie, N. Yidris, F. Mustapha and D.L. Majid, UPM, MALAYSIA	217
29	Improved Direct Assessment Technique for External Corrosion on Pipelines using a 3D Laser System Pierre-Hugues ALLARD, Jean-Simon FRASER, Carl MERCIER, Patrice PARENT, CANADA	225
30	Application of a 3D Laser Inspection Method for Surface Corrosion on a Spherical Pressure Vessel Pierre-Hugues ALLARD, Jean-Simon FRASER, Carl MERCIER, Patrice PARENT, CANADA	234
31	Video Endoscopic Metrology for Pipeline Welding Alfred Ng, HONG KONG	240
32	Determining the authenticity of gold jewelries by ultrasonic testing Amry Amin Abas, Mohamad Pauzi Ismail, Mohd Harun and Suhairy Sani, MALAYSIA	246
33	Determination of Welded Joints Metal's Mechanical Properties by Strength Parameters in Stress Concentration Zones Detected by The Metal Magnetic Memory Method S.M. Kolokolnikov, Al.A. Dubov, A.Yu. Marchenkov, RUSSIA	251
34	Detection of location of pipeline intelligent gauge jammed in pipeline by neutron device Md Fakarudin Ab Rahman, Ismail Mustapha, Nor Pa'iza Mohd Hasan and Pairu Ibrahim	262
35	Eddy current thermography: NDT technique fusion for future industrial application Ilham Mukriz Zainal Abidin, Masrol Nizam Salleh, Mohd Zaki Umar, Maslina Mohd Ibrahim, Mohd Yusnisyam Yusof and Mohd Noorul Ikhsan Ahmad, Nuclear Malaysia, MALAYSIA	268



# ANALYSIS OF COMPOSITE MATERIALS, SOIL AND AUTOMOTIVE WITH HIGH RESOLUTION COMPUTED TOMOGRAPHY

T. Paul<sup>1</sup>

<sup>1</sup> GE Measurement & Control Solutions, phoenix|x-ray, Wunstorf, Germany,

\* Corresponding author (Thomas.paul2@ge.com)

**Keywords:** *nanoCT,  $\mu$ CT, high resolution Computed Tomography, 3D micro-analysis*

## 1 Abstract

During the last decade, Computed Tomography (CT) has progressed to higher resolution and faster reconstruction of the 3D-volume. Most recently it even allows a three-dimensional look into the inside of materials with submicron resolution. High-resolution X-ray CT allows the 3D visualization and failure analysis of the internal microstructure of textile and composite materials – even where 2D X-ray microscopy would give only the integral information of the overlaying bundles of fibers. By means of nanofocus tube technology, nanoCT<sup>®</sup>-systems are pushing forward into application fields that were exclusive to expensive synchrotron techniques. But their potential, convenience and economy of these lab systems is often underestimated.

## 2 Method

Especially for modern composite materials which are used in very expensive or safety relevant applications, CT is ideal to accompany the product from development to final quality control. The tube based CT measurements for the study were performed with a granite-based phoenix|x-ray nanotom<sup>®</sup> s and m CT systems (GE Measurement & Control Solutions, Wunstorf, Germany) equipped with a 180 kV / 15 W high-power nanofocus tube with Tungsten or Molybdenum-Targets. The tube offers a wide range of applications from scanning low absorbing samples in nanofocus mode with min. voxel sizes <300 nm and high absorbing objects in high power mode with focal spot and voxel sizes of a few microns. The nanotom is the first 180 kV nanofocus computed tomography system which is tailored specifically to high resolution applications in the field of material science and micro electronics. Therefore it is particularly suitable for nanoCT-

examinations e.g. of synthetic and composite materials, metals and metal foams, ceramics etc.

The CT volume data set can be displayed in various ways; it can be sectioned and sliced in all directions, rotated and viewed from any desired angle. Highly applicable to a variety of fields, nanoCT can be a viable substitute for destructive mechanical slicing and cutting. Any internal difference in material, density or porosity within a sample can be visualized and data such as distances can be measured. Some of the many applications of nanoCT include the analysis of fiber textures, air inclusions or cracks in composite materials with voxel resolutions down to less than one micrometer. Since the contrast can be as low as 0.2 % it allows even a segmentation of e.g. C-fibers in a C-based matrix (Fig.1).

The paper will outline the hard- and software requirements for high resolution tube based CT and compare CT results of sophisticated conventional tube-based with synchrotron radiation based scans. It will showcase several quality control applications of different composite materials that were inspected with high resolution nanofocus and microfocus CT.

## 3 Results

The CT results obtained with the nanotom allow analyzing the spatial microstructure of the sample with submicrometer resolution: Any internal detail that corresponds to a contrast in material, density or porosity can be visualized and quantities like distances can be measured. Components of a sample may be visualized individually by suppressing the contrast of all but the material of interest.

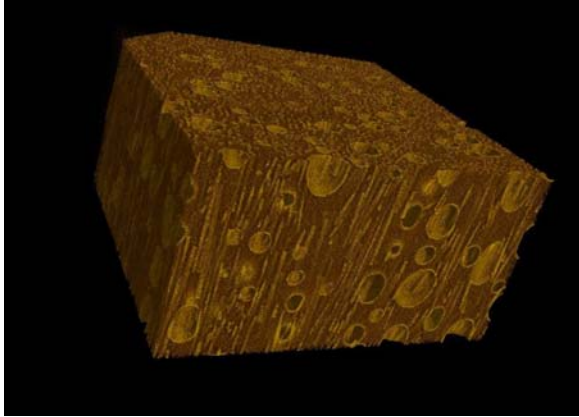


Fig. 1: nanoCT of carbon fibres and pores in polymer matrix scanned with a phoenix nanotom with molybdenum target with 0.5  $\mu\text{m}$  voxelsize. Diameter of single fibres is ca. 1-5  $\mu\text{m}$ . The texture of the fibres is clearly visible.

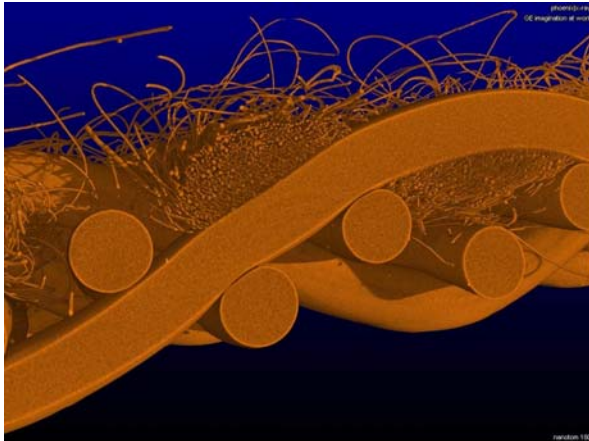


Fig. 2: Sieve scanned with 4  $\mu\text{m}$  voxelsize. Diameter of the small fibers is 0.012 mm, of the large fibers 0.5 mm. Courtesy by RWTH Aachen, Institut für Textiltechnik, Germany

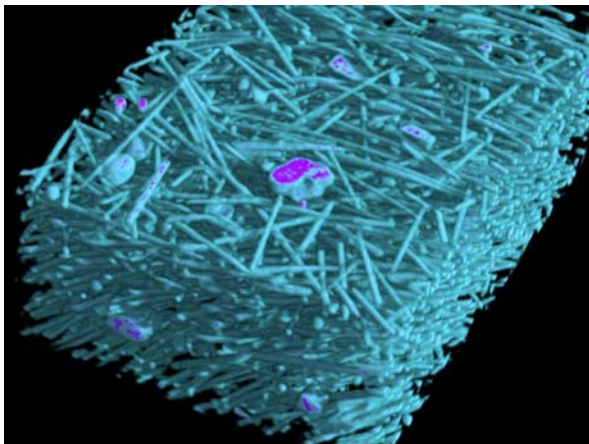


Fig. 3: nanoCT of a glass fiber reinforced plastic. Clearly visible is the orientation and distribution of the 10  $\mu\text{m}$  thin fibers as well as accumulations of the mineral filling material. The plastic is blinded out.

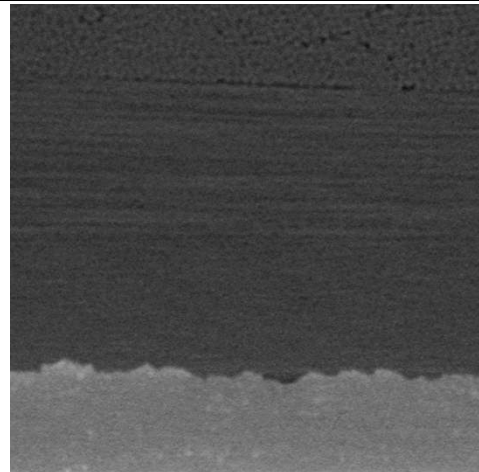
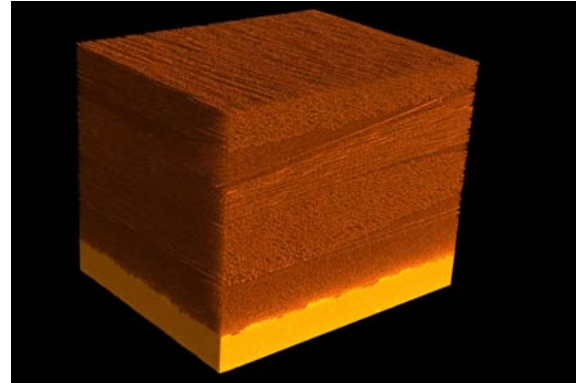


Fig. 4 a+b: nanoCT of an induction welded joint of an aluminum plate (corundum blasted) with carbon fibers in polyamide matrix. The voxel size of the scan is 0.7  $\mu\text{m}$ . Clearly visible is the orientation of the fibers (7  $\mu\text{m}$  thick), delaminations between the fiber bundles (1) as well as air entrapments (2) in the welding zone uncovering not optimized manufacturing parameters. Bright points in the aluminum plate indicate small particle inclusions with higher X-ray absorption. The length of the edge of the 3D visualisation (left image) is about 1 mm.



## Radioscopy-Based Digital Radiography System for Industry

Gede B. Suparta<sup>1</sup>, Wayan Sutrisna<sup>1</sup>, Gede Arya Wiguna<sup>1</sup> dan Andreas C. Louk<sup>2</sup>

1. Dept. of Physics, Gadjah Mada University, Sekip Utara Yogyakarta, Indonesia.

Corresponding email: [gbsuparta@ugm.ac.id](mailto:gbsuparta@ugm.ac.id)

2. Dept. of Physics, Nusa Cendana University, Kupang, East Nusa Tenggara, Indonesia.

### Abstract

A hand-made radioscopy-based digital radiography system has been made for earthenware and ceramic quality inspection at the Kasongan Handycraft Centre of Bantul, Special Region of Yogyakarta, Indonesia. It consists of an x-ray generator of 75 kV, 20 mA that can be operated using 220 VAC, a digital image converter of x-ray radioscopy, an object conveyer for sample loading and unloading, a digital image capture apparatus, and a computer system along with some software developed in our research group. The first software is software for digital image capturing and controlling conveyer. The second software is for image manipulation, processing and analysis. Some object has been tested to explore its capabilities. This paper reports the performance of the system based on some IQI standards and real object.

Key-words: *digital radiography, earthenware, radioscopy, non-destructive inspection*

### I. Background

X-ray radioscopy system [1-2] is one of old fashion system for real time analog inspection process. It consists of an x-ray generator and a radioscopy unit based on fluorescence screen [3-5]. The fluorescence material may be found on a conventional film cassette. The x-ray is exposed to the object with continuous x-ray burst [6]. This process is called fluoroscopy mode, which is in contrast with radiography mode that used impulsive x-ray burst. The fluoroscopy mode is usually used for real time online inspection, while the radiography mode is commonly used in conjunction with film radiography. Therefore, a radioscopy system is mostly used for quick and direct inspection without a need for image documentation. Once an image document is necessary, film radiography is applied, and so a radiography mode is applied [8].

An industrial radioscopy system [9-10] uses lower anode-cathode voltage (HV voltage in kV), low filament current (in mA), but longer exposure time in comparison to the radiography system that using film radiography. For online inspection, it may take 3-15 seconds exposure depend on the purpose. Exposure time may increase depend on operator experience. On the other hand, a radiography system is normally taken in less than 1 sec, but it needs higher HV voltage and higher filament current to ensure a good quality of x-ray shadow to the radiography film is achieved [8].

Since digital radiography becomes a technology trend [11-13], any analog system may be converted to be digital system or replaced by a new system with supposed to provide equivalent quality. A computed radiography (CR) system has been introduced, but it is too expensive and it is still indirect process. No significant benefits are gained when it used for industrial inspection since it fails to perform online direct inspection. On the other hand, a direct digital radiography (DDR) system is introduced. Although this system can perform direct process to obtain digital images, it is certainly unable to be used for online direct inspection [14-16]. The electronic sensor devices on the system are considered very fragile for long time exposure or intensive x-ray burst. However, for those two systems, all needs digitization process, which is technically very fast.

A radioscopy system is essentially a visual presentation. Thus, a radioscopy image can be converted into digital image directly based on video or photograph digitization [8]. The quality of digital image is increased when the digitization process is performed in total dark environment. The digital image resulted can be transferred online to a digital display, e.g. computer monitor display.

Once a digital radioscopy system can be developed [8], an online digital inspection can be performed. However, such online digital radioscopy system is still hazardous since it takes long exposure, more than 3 seconds. Therefore, an attempt to reduce radiation exposure has to be explored. This paper reports an attempt on developing a digital radioscopy system. The system is specifically used for industrial inspection, especially for quality inspection of earthenware or ceramic products.

## II. Method

A digital radioscopy system has been developed at the Department of Physics, Gadjah Mada University Yogyakarta Indonesia [3]. It has been installed at the Kasongan Handycraft Centre of Bantul, Special Region of Yogyakarta, Indonesia for earthenware and ceramic quality inspection. It consisted of an x-ray unit that is powered by a 220 VAC. It provides HV voltage up to 75 kV and filament current up to 25 mA. Exposure time for radioscopy mode can last for 3 minutes, while exposure time for radiography mode may start from 0.1 sec. The system was look like an x-ray baggage scanner, normally found at an airport as is shown in Figure 1.



Figure 1. A radioscopy-based digital radioscopy system at the Gadjah Mada University. (a) Object on conveyor, (b) Display monitor and control panel.

A target object was put on the object plate which was become unity with the conveyer belt. Then, when an inspection was carried out, the object plate was moved by operating the rotating motor so that the conveyer moved. Once the object plate reached a right position below the x-ray unit, a sensing unit triggered an automatic x-ray exposure. Therefore exposure time could be set at a radiography mode for very short expose, e.g. 0.25 – 0.50 secs. The extra benefit obtained since the x-ray power can be set at radioscopy mode for 75 kV and 25 mA. Thus, the system has used the best combination of x-ray power and time exposure. High power was used to ensure a good penetration to the object was obtained, while a low radiation dose was achieved due to short exposure.

A digitization process was performed using a conversion of dynamic visual shadow in the dark box, called converter unit. Using a CCD camera, the visual shadow was converted into



video signal. Then, the video signal was converted into digital image. The system was set to convert a time lapsed video capturing to yield 20 digital images per second. However, since the exposure time was set for 0.25 sec the number of good images obtained was about 3-5 images per exposure. All images could be displayed directly on the monitor display as digital images. Thus, the system definitely could be used for online direct real time inspection.

In order to obtain better quality image, all good images were processed to yield single good image. Firstly, a normalization using background images was carried out. After that, an image summation followed by images averaging process for all good images was performed. This was expected to reduce quantum noise. A further noise reduction was performed to remove high or low frequency signal to provide a good visual and acceptable image.

Objects being scanned are shown in Figure 2. A standard ASTM wire tester (Figure 2 (a)) was used to examine the system performance. An earthenware product e.g. ash tray (Figure 2 (b)) and a flower vast (Figure 2 (c)) as an example of ceramic product were examined.

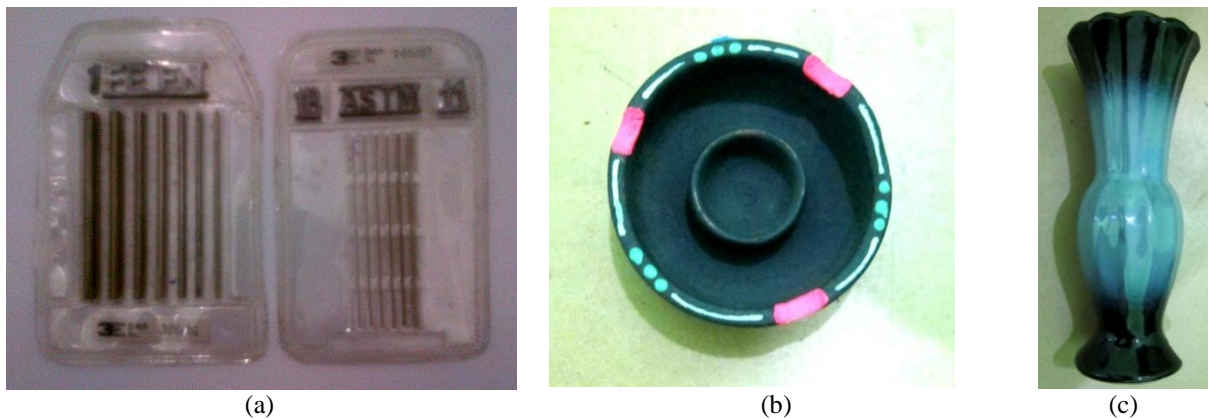


Figure 2. Real objects to test radiography-based digital radiography system. (a) wire test, (b) ash tray, and (c) vas.

### III. Results and Discussion

Performance testing to the system has been carried out using a set of wire tester. The original radiography image resulted is shown in Figure 3(a). Then, after a summation process for all obtained good images, a less noisy image was obtained as shown in Figure 3(b). The image quality was still unsatisfying although its grey-level histogram was look well distributed. Therefore, a further window leveling was carried out so that a better contrast and brightness was achieved as shown in Figure 3(c). It was more natural since a radiograph of wire test should have no degradation grey level. A further noise removal was carried out so that the image looks have good contrast and good brightness, while its grey-level histogram has good shape in Figure 3(d). The thinnest wire can be identified well.

Further testing has been carried out using a real earthenware object, a small ash tray. The original radiography image resulted is shown in Figure 4(a) and in Figure 4(b) a less noisy image yielded from a summation process for all obtained good images is shown. The image quality was unsatisfying since its grey-level histogram tends to dark. Therefore, a further window leveling was carried out to obtain better contrast and brightness, as shown in Figure 4(c). It was more acceptable since the radiograph of ash tray should have degradation grey level. To ensure good contrast and good brightness image was obtained, a further noise

removal was carried out. As a result, its grey-level histogram has good shape as shown in Figure 4(d). The defect was indicated well by non-uniformity in the centre of image.

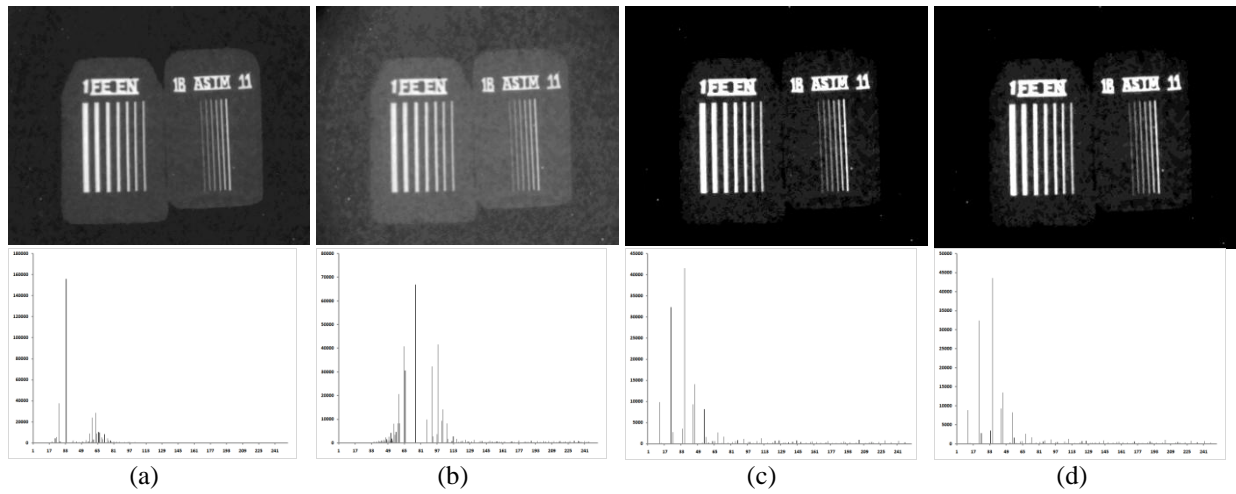


Figure 3. Radiographs of wire test along with their consecutive histogram.

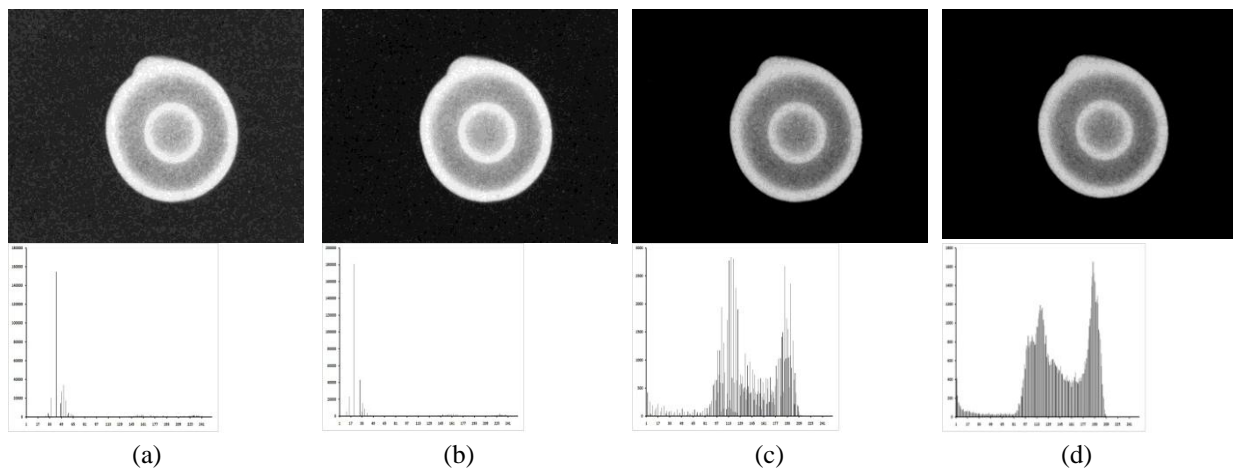


Fig. 4. Radiographs of ash tray, as an example of earthenware along with their consecutive histogram.

Another testing has also been carried out using a real ceramic object, a typical flower vas. The original radiography image resulted is shown in Figure 5(a). The image was less satisfying as it was indicated by its histogram. A less noisy image yielded from a summation process for all obtained good images is shown in Figure 5(b). The image quality was more natural since the material classification was clearly indicated. Ceramics has more fine material compared to earthenware. Therefore, the grey-level histogram tends to be well grouped. Therefore, when a further window leveling was carried out, a better contrast and brightness was obtained, as shown in Figure 5(c). To ensure good contrast and good brightness image was obtained, a further noise removal was carried out to yield image as shown in Figure 5(d). A defect on the bottom was indicated well.

From these results, good and quick digital images from radioscopy can be obtained using small x-ray power but were taken in radiography mode instead of fluoroscopy or radioscopy mode. A simple summation process to remove noise and further noise compensation may be applied. As a result, the good quality image in term of contrast and brightness can be



displayed directly on the monitor display. Some internal defects can be examined using bare eyes. Thus, a quick inspection can be performed without much treatment in image processing.

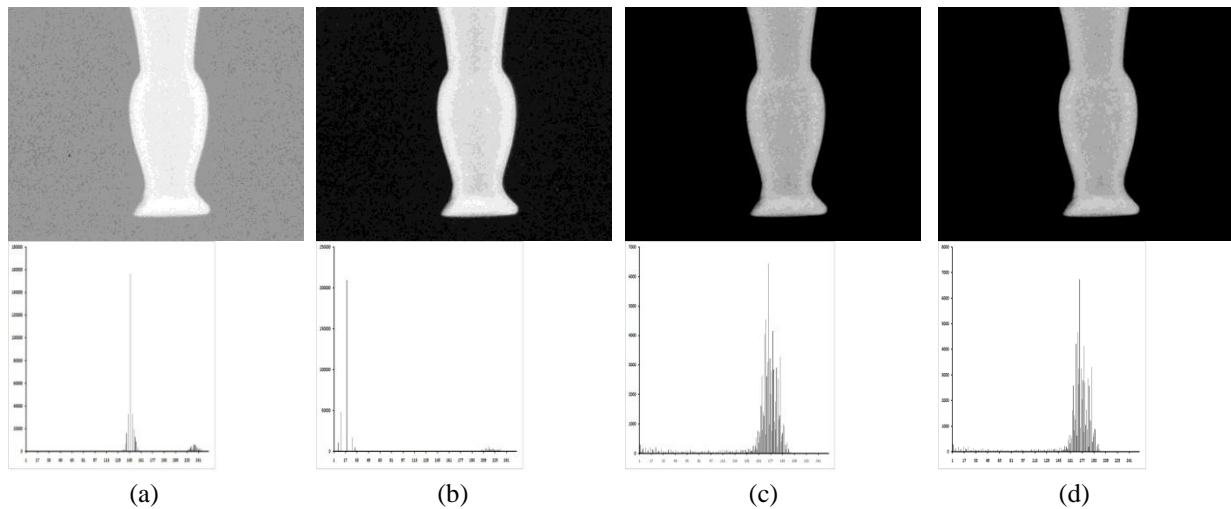


Fig. 5. Radiographs of flower vas, made from ceramics along with their consecutive histogram

#### IV. Concluding Remarks

From this project we learned the way to develop an experimental unit for earthenware or ceramics product inspection system based on x-ray digital radiography system based on radioscopy. The system has worked for medium size of product such as vas or ash tray. It was able to distinguish internal crack and material redundant within product. The system can determine any crack in a size of 1 mm. A further test on materials characterization may be performed since the materials of earthenware or ceramics may comprise various materials.

#### ACKNOWLEDGEMENT

The authors acknowledge the financial support from the MP3EI Project of Year 2012 for the research process, PT Madeena Karya Indonesia for the product realization, Bengkel Fisika FMIPA UGM for the prototyping, the Gadjah Mada University for the travel and conference support, the BIC Serpong KNRT of Indonesia for technology mediation, and the Government of Bantul Residence for the mutual collaboration.

#### REFERENCES

- [1]. H Boerner and H Strecker, "Automated X-Ray Inspection of Aluminum Castings", *IEEE Transactions On Pattern Analysis And Machine Intelligence*, **10** (1), January 1988, pp 79-91
- [2]. X Wang, B S Wong, C G Tui, K P Khoo and F Foo, "Real-time Radiographic Non-destructive Inspection for Aircraft Maintenance", 17th World Conference on Nondestructive Testing, 25-28 Oct 2008, Shanghai, China.
- [3]. S Nakajima, G Shinomiya, M Takeda, and S Chikutei, "X-ray Phosphor and X-ray Intensifying Screen using the phosphor", US Patent No. 5120619, Jan 1992
- [4]. S Pesce, P Malfatto and S Bruno, "X-ray Intensifying Screen", US Patent No. 5432351, July, 1995

- [5]. M Ercoli and C M della Rocca, “X-ray Intensifying Screen”, US Patent No.6162553, Dec, 2000
- [6]. W K van Landeghem and A R Suys, “Fluorescent X-Ray Image Intensifying Screen”, US Patent No.4205116, May, 1980.
- [7]. M Nikl, “Scintillation detectors for x-rays”, Review Article, *Meas. Sci. Technol.* **17** 2006, R37–R54
- [8]. Suparta, G.B., A.A. Moenir, dan I K Swakarma, 2005, “Sistem Radiografi Digital untuk Medis”, *Proceeding*, The Kenting Physics Forum 2005, UNS Solo, 24 September 2005.
- [9]. B Ghose and D.K. Kankane, “Estimation of location of defects in propellant grain by X-ray radiography”, *NDT&E International* **41**, 2008, pp 125 – 128.
- [10]. Peng Wan, “The Application of X-ray Detection System”, 2nd Asia International Conference on Modelling & Simulation 2008 IEEE Computer Society, pp 968-973
- [11]. H MacMahon, “Method and System for Digital Radiography”, US Patent No.6466689 B1, Oct, 2002
- [12]. Ramesh J. Patel “ Digital Applications of Radiography”, 3rd MENDT - Middle East Nondestructive Testing Conference & Exhibition, 27-30 Nov 2005 Bahrain, Manama.
- [13]. W. Harara, “Digital Radiography in Industry” 17th World Conference on Nondestructive Testing, 25-28 Oct 2008, Shanghai, China
- [14]. Suparta, G. B., M. Wahyuningsih and S. Lestari, 2009. “Image Quality of Computed Radiography and Digitized Film Radiography”, *Proc. of SPIE Vol. 7522, The 4<sup>th</sup> ICEM 2009, Singapore*, 18-20 Nov 2009, 75220P, pp 1-6.
- [15]. Lestari, S dan G. B. Suparta, 2010, “Uji Korelasi Sistem Multi-citra Radiografi XRII Digital”, *Proceeding, 7<sup>th</sup> Basic Science National Seminar*, Malang 20 Februari, paper LB07, pp II-35 – II-39, ISBN978-602-96393-0-8.
- [16]. Suparta, G.B., N. Waskito and S. Lestari, 2010, “Study on Image Quality of Computed Radiography”, *Journal of Materials Science and Engineering*, Vol. 4, No. 4, April 2010 (SN 29), pp 54-59.



# **SINGLE PHOTON EMISSION COMPUTED TOMOGRAPHY (SPECT) AS A POTENTIAL NDE TOOL IN THE FUTURE: A MONTE CARLO SIMULATION STUDY**

Mohd Amirul Syafiq Mohd Yunos, Jaafar Abdullah

Centre for Computed Tomography and Industrial Imaging,  
Malaysian Nuclear Agency, Bangi, 43000 Kajang, Malaysia

## **Abstract**

Single-photon emission computed tomography (SPECT) is a powerful non-invasive technique widely used in nuclear medicine as an imaging technique using gamma rays. It is very similar to conventional nuclear medicine planar imaging using a gamma camera. However, it is able to provide true 3D information. This information is typically presented as cross-sectional slices through the patient. SPECT has great potential to be used as an inspection tool to diagnose industrial processes non-destructively. The basic technique requires delivery of a gamma emitting radioisotope (called radionuclide) into the industrial system, normally through a special injection device into the process stream. On occasion, the radioisotope is a simple soluble dissolved ion, such as Tc-99m, I-131, Br-82, Na-24 etc, which happens to also have chemical properties to either aqueous or organic phase that allow it to be concentrated in ways of industrial interest for process abnormalities detection. This paper presents the basic principle of industrial SPECT, highlights the experimental design and gives preliminary results of a Monte Carlo simulation study on a laboratory scale process vessel. Some of the reconstructed images are presented in this paper.

## **1. Introduction**

The industrial gamma-ray tomographic scan method is a class of tomography which was derived from medical applications. X-ray CT can be divided into medical and industrial system CT according to the application area. Industrial X-ray CTs have been used for food science, electronic parts examination, material science, etc. Although the basic principle is the same as the CT imaging in medical uses, there are different problems to be solved by industrial X-ray CT. The objects for industrial X-ray CT vary widely in size and density, and therefore many different types of CT systems are needed according to those objects [1]. Imaging systems are most suitable for in situ system inspection with control purpose, diagnosis of a system or modeling for CFD validation. The field of applications of emission tomography for tracer visualization extends from chemical engineering, oil recovery, geochemistry or hydrogeology. In chemical engineering for instance, experts would like to visualize the behavior of individual phases in multiphase flow reactors, such as fluidized beds, slurry reactors, bubble columns, or any kind of system involving multiphase flow, an additional flow that conveys the tracer is added to the phase of tracer is natural in the process but in most cases, the tracer is added to flow. Classical approach, based on transfer function analysis uses spatial-temporal information. By this way, it is possible to estimate Residence Time Distribution (RTD) and thus flow rate, dead volume, loops, dispersivity, and diffusion coefficient for porous media analysis.[2]

Numerous methods based on particle tracking exist to characterize a flow, and specifically in aerodynamics for wing, car, wing mill or pump design. In case of opaque flow systems or systems involving bubbles like gas phase and vapor phase, optical methods can no longer be used. As such, ionizing radiation based methods are required. Two types of methods can be used to investigate such flows. The first one is based on the use of particle opaque to X-ray photons. In such experiments, 2 X-ray sources with the corresponding 2D detectors are assembled to 90° one of the other. The stereo vision allows the tracking of the particles. The second method makes use of radioactive sources and the techniques are called positron emission particle tracking (PEPT) and gamma ray emission radioactive particle tracking, quite frequently known as radioactive particle tracking [3].

### **Single Photon Emission Computed Tomography (SPECT)**

Single photon emission computed tomography (SPECT) uses the detection and counting of highly penetration gamma rays emitted by a single radio labeled flow follower (tracer), which is dynamically similar to the tracked phase. The detected gamma-rays are used to estimate the instantaneous coordinates of the moving tracer. The numbers of photons registered depends mainly on the distance between the tracer and the detector, but also on the attenuation of the media between the particle and the detector and the intrinsic properties of the detector. Accurate tracking requires detection of large number of photons to reduce statistical fluctuations. Since the tracking of fast moving phases has to be done at high sampling frequencies, up to 200 Hz, the tracers should generally have relatively high intensity, and the detection system requires high rate counting capability.

The specificity of single photon emission computed tomography is related to the choice of tracer, the activity to inject and the processing of waste after experiment. Tracers usually used are, as radioisotope generators, Mo/Tc-99m, Sn/In-113m, Cs/Ba-137m and as radioisotope, Br-82, I-131, La-140, or Na-24. The choice of energy of tracer is related to absorption of the different elements that constitute the system: flow, internal parts if exist, the wall of the pipe. The amount of the activity of tracer is related to the size of the vessel, the distance from detectors to the flow and the dynamic of the flow. In case of porous media analysis, low activity can be used; some experiments have been conducted with activity as low as few tenth of kBq. Conversely, in case of high velocity flow, higher amounts of activity need to be injected. Attenuation of material and dynamics of the flow are usually connected since high flow rate also means thick wall of the pipe.

### **Monte Carlo Simulation**

Monte Carlo methods are extensively used in nuclear medicine to assist in the design of new medical imaging devices, new image reconstruction algorithms, or new scatter correction techniques for emission tomography. On one hand, dedicated Monte Carlo codes have been developed for Positron Emission Tomography (PET) and for Single Photon Emission Computerized Tomography (SPECT). However, these tools suffer from a variety of drawbacks and limitations in terms of validation, accuracy, and/or support [1]. On the other hand, accurate and versatile simulation codes such as Geant3 [2], EGS4 [3], MCNP [4], and recently Geant4 [5,6] have been written for high energy physics. They all include well-validated physics models,

geometry modelling tools, and efficient visualization utilities. Nevertheless these packages are quite complex and necessitate steep learning curve.

MCNPX is a general purpose Monte Carlo radiation transport code. This code was developed and is maintained by the Los Alamos National Laboratory. MCNPX was designed to track many particle types over broad ranges of energies and to analyze the transport of neutrons, protons, gamma rays and other particles. MCNPX includes many new capabilities, particularly in the areas of transmutation and delayed particle production. In addition, many new tally sources and variance-reduction options have been developed (Pelowitz, 2008). In particular, this code can be used to simulate the irradiation of target materials with charged hadrons to optimize target design and study the activation of the materials. The INP file of MCNPX contains information on the problem of interest, including the geometry specifications, the description of materials, the selection of cross-sectional evaluations, the location and characteristics of the source, the type of answers or tallies desired, and any variance-reduction techniques used to improve efficiency. [2]

As computational power continues to increase, it becomes more practical to utilize Monte Carlo methods to perform in-situ calculations. Monte Carlo methods have gained interest due to the ability to more accurately model complex 3-dimensional geometries. Recently, there is many of the reactor parameters were analyzed by Monte Carlo model using MCNP code [5]. It can be applied for process hydrodynamics calculations, for detection characterization and radiation distributions calculations and for critically predictions. The main aim of this paper was to review performance of numerical calculation using MCNP of the phantom model and single photon emission computed tomography setup.

## 2. Principles Approach

SPECT imaging is performed by using a gamma camera to acquire multiple 2-D images (also called projections), from multiple angles. A computer is then used to apply a tomography reconstruction algorithm to the multiple projections, yielding a 3-D dataset. This dataset may then be manipulated to show thin slices along any chosen axis of the body, similar to those obtained from other tomography techniques, such as MRI, CT, and PET [3].

### Basic principle of SPECT

In SPECT tomography, the tracer distribution is estimated from projections by a reconstruction technique. The complete projection process can be set if  $A_{ij}$  represents the probability that a photon emitted from pixel  $j$  is detected in detector after considering decomposing the image reconstruct on a  $N^2$  matrix and denote the  $\lambda_j$  as the unknown intensity of pixel  $j$  and  $y_i$  as measure in the  $i_{th}$  detector. Then it can be note as:

$$y_i = \sum_{j=1}^{N^2} A_{ij} \lambda_j + \varepsilon_i \quad (1)$$

and for the set of measurements, by matrix notation:



$$y = A\lambda + \varepsilon \quad (2)$$

where  $y$  is the set of measurements,  $\lambda$  is the set of unknown intensities and  $A$  is the projection matrix of the system. The aim of computed tomography is to inverse former equation providing that matrix  $A$  is a sufficient approximation of the projection process. Matrix  $A$  includes solid angle, gamma scattering, attenuation, lead penetration and detector response. Many methods can be used to inverse the equation. Due to the lack of statistics, Expectation Maximization algorithm is generally well suited. Statistical algorithms are more intensively used in industrial imaging due to the available and stable computing power. This algorithm is a statistical approach that takes into account the statistical nature of photon detection [3].

### Expectation Maximization (EM) algorithm

Expectation Maximization algorithms are based on models that account for the stochastic nature of gamma ray photons. Algebraic algorithms described earlier and algorithms such as Fourier/convolution techniques when applied to determine the phase holdup distribution either assume the system to be azimuthally symmetric or consider the gamma ray transmission process to be deterministic hence ignoring the true stochastic nature of the data. Thus Expectation Maximization algorithms have been shown to be more suitable image reconstruction methods for determining the phase holdup distribution.

According to J. Kim (2011), the statistical image reconstruction method was used to find the pixel value to maximize the joint probability function (likelihood function). Finding the pixel value to maximize the likelihood function is equivalent in solving the following equation:

$$0 = \frac{\partial}{\partial \vec{\mu}} \sum_{i=1}^{N_y} [y_i \ln \bar{y}_i - \bar{y}_i - \ln(y_i!)] \quad (3)$$

$$\bar{y} = b_i e - \sum_{j=1}^{N_p} h_{ij} \mu_j \quad (4)$$

$$\mu_j^{(n+1)} = \frac{\sum_{i=1}^{N_y} (M_{ij}^{(n)} - N_{ij}^{(n)})}{1/2 \sum_{i=1}^{N_y} (M_{ij}^{(n)} + N_{ij}^{(n)}) h_{ij}} \quad (5)$$

The first method of solving the likelihood function was known as Expectation Maximization (EM). In transmission EM, the updating equation is denoted as Equation 5.  $M_{ij}$  is the number of photons entering the  $j_{th}$  pixel in the  $i_{th}$  measurement and  $N_{ij}$  is the number of photons coming out of the  $j_{th}$  pixel in the  $i_{th}$  measurement. Equation 5 is obtained by an approximate part of the second term of the Taylor series. This algorithm has been widely used in spite of slow convergence and computational inefficiency.[1]

### 3. MCNP Simulation Setup and Result

MCNPX is one of the most commonly used radiation transport codes. Monte Carlo simulations were performed prior to the experiment for different object models and different measurement conditions. Real measurements suffer geometrical and measurement errors while the Monte Carlo simulation doesn't take geometrical errors into account. The Monte Carlo simulation data can be regarded to contain only statistical errors. Therefore the reconstruction result from the simulation data can be compared to the original image of the simulation setup [1].

The methodology of MCNP simulation procedure was shown in Figure 1. The process start after MCNP input file has been determined. Normally, method of creating input file are simply used available Notepad to produce batch file. After completion of batch file generation, the process will continue with calculation of point source response function by using Monte Carlo code and then generate the weight matrix just after calculation is done. Next step is to further the process into image reconstruction using expectation maximization algorithm.

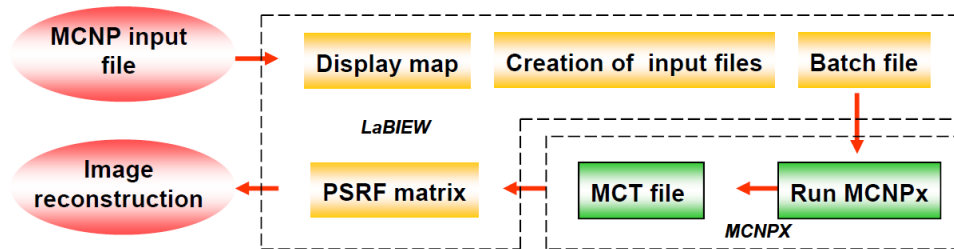


Figure 1. MCNP Simulation Procedure

To construct the batch file, detector position and details should be define before using the universe card MCNP code to make easier arrangement of detector and collimator size, materials and position. Figure 2 shows the image of MCNP code display for single detector details could be copied using array method and make it 5 units in parallel. This code will reduce much spending time to reconstruct input file.

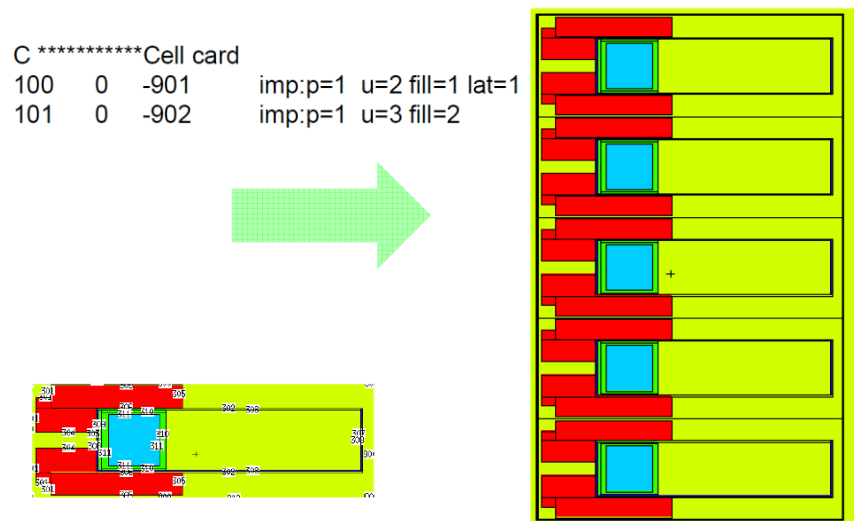


Figure 2. Cell card code for detector design and details.

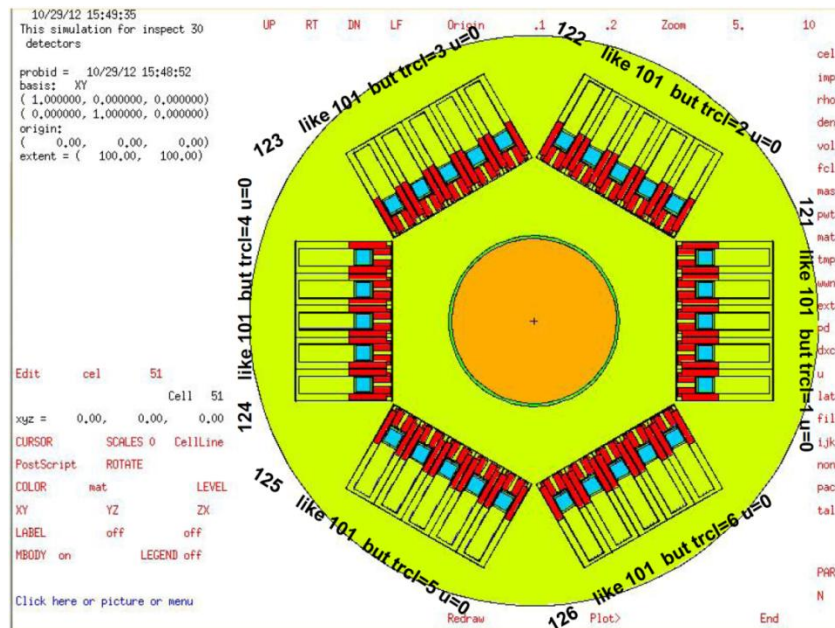


Figure 3. Full display of MCNP code batch input file of SPECT.

The simulation setup included a simple circular object with 30 detectors as shown in Figure 3. The figure shows details of the composition of the detector components also the dimensions of the source and detectors, with involvement of an iron vessel 30cm in diameter containing two estimated circular phantom 3 cm and 5 cm in diameter with different radioactivity at 10.3mCi/L and 3.5mCi/L but using same radioisotope Tc-99m which were used in the simulation setup as shown in Figure 4.

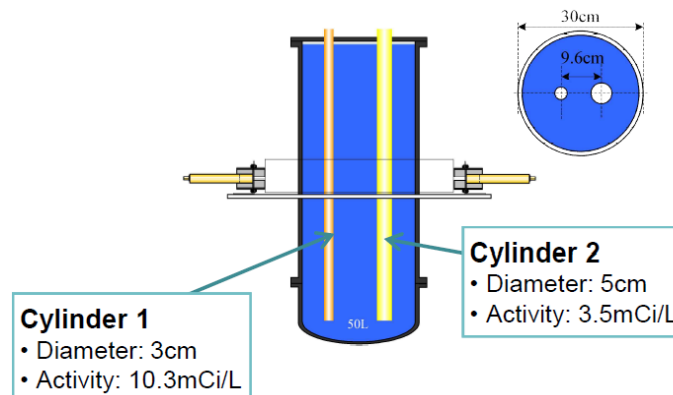


Figure 4. Estimated phantom setup to describe the vessel simulation.

The detector position Image reconstructions using the Monte Carlo simulation data have been performed. To generate the tomographic data, Monte Carlo simulations had been carried out for all source positions. The same number of MCNPX input files as that of source position was produced. Then MCNPX program was executed for all MCNPX input files. Simulation data were produced and reshaped for image reconstruction. Those tasks were done by software programmed by LABVIEW. The Figure 5 and Figure 6 show the image reconstruction result for the simulation using Monte Carlo simulations. The slice along the centerline for the



reconstructed image and true value from simulation setup are also displayed in the Figure 7 and Figure 8. This result can successfully show the outline of the vessel and phantom. Reconstructed images by MCNP and EM algorithm also their reconstruction differentiations on collimator aperture size and detector to source measurement distance are shown in Figure 5 & 6. Figure 7 shows that results from EM of Equation 5 have more reconstruction errors. This result matches the algorithm review in which statistical method was expected to be suitable in this simulation. However, the results show simulated phantom with integration of industrial single photon emission computed tomography using Monte Carlo N-Particle can be used for optimization and performance of multiphase vessel in industries.

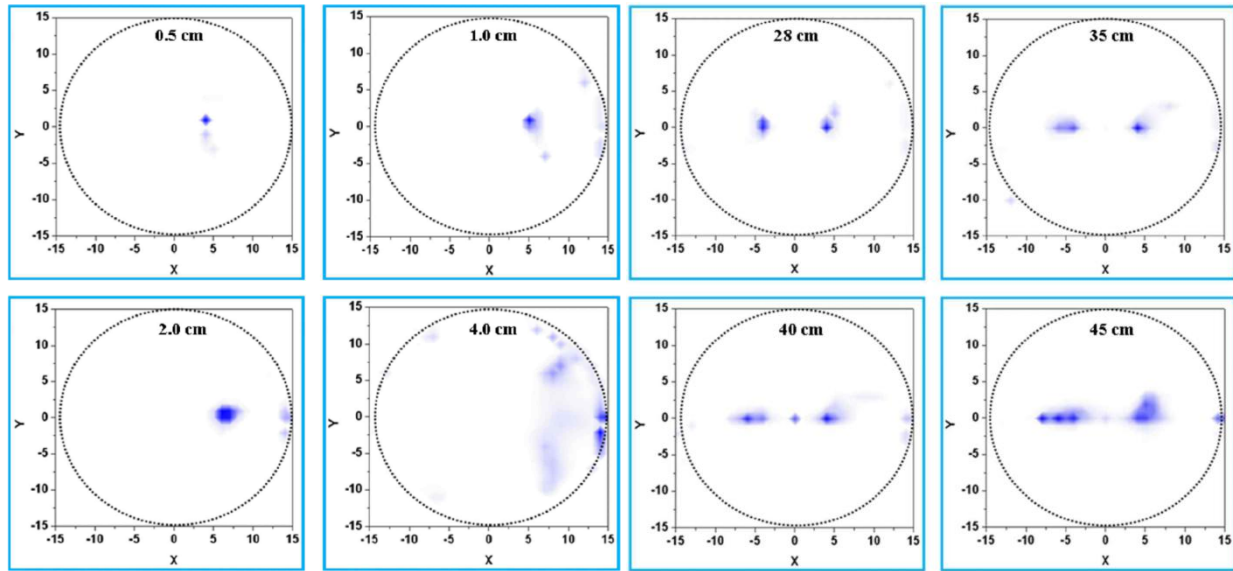


Figure 5. Reconstructed images with different collimator aperture size

Figure 6. Reconstructed images with different measurement distance

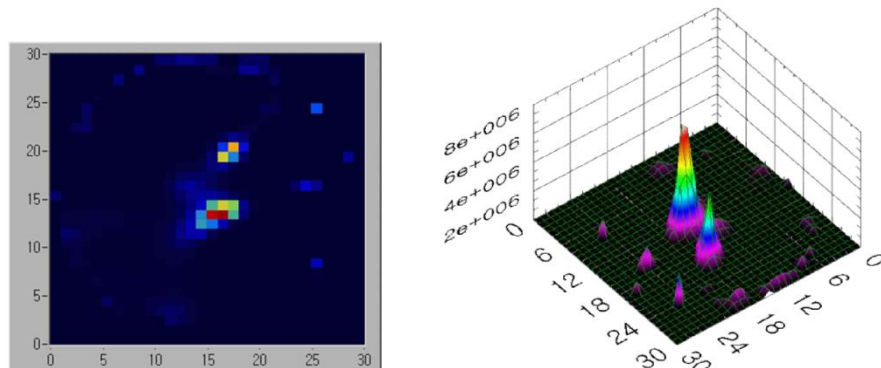


Figure 7. Images and plot of tracer distribution measurement using industrial SPECT

#### 4. Conclusion

Finally, simulation of gamma-ray tomographic scan method was successfully evaluated by Monte Carlo simulation. Statistical reconstruction methods by using Expectation Maximization algorithm showed better result in this study. Wherever applicable and affordable, SPECT might become a routine preoperative imaging solution and powerful non-destructive evaluation in the future. As technical developments in SPECT are ongoing and high-resolution

multislice CT scanners and the use of intravenous contrast will be integrated in SPECT systems, even further improved spatial resolution of CT images and a better computed tomography systems are available. Together with the use of novel portable gamma-camera systems, possibly the future will provide an integrated system that combines fused imaging with an easy operation handheld gamma-camera enabling 3D visualization. Apart from imaging development, new tracers may be integrated in the process of more accurate detection of the fluids flow behavior.

## References

1. Kim J., Jung S., Moon J., Cho G., *Industrial gamma-ray tomographic scan method for large scale industrial plants*, Nuclear Instruments and Methods in Physics Research A640 (2011) 139–150
2. Pelowitz, D.B. (Ed), 2008. *MCNPX User's Manual*, Version 2.6.0 LA-CP-07-1473.
3. Sadeghi M., Jokar N., Kakavand T., Ghafoori F.H. and Tenreiro C., 2013. *Prediction of  $^{67}\text{Ga}$  production using the Monte Carlo code MCNPX*, Applied Radiation and Isotopes 440 - 476
4. IAEA-TECDOC-1589, 2008. *Industrial Process Gamma Tomography* 38 – 42.
5. Richard B., Lawrence L., 2012. *Some Popular Monte Carlo Codes for Particle Transport* 348-367
6. Brill A.I and Robert N. Beck, 2004. *Evolution of Clinical Emission Tomography* 26 – 57
7. Bonin A., Chalmond B., Lavayssière, *Monte Carlo simulation of industrial radiography images and experimental designs*, NDT&E International 35 (2002) 503 – 510

### Low dose customs inspection system for freight transport control.

Klimenov V.A.\*, Kasyanov S.V.\*, Rychkov M.M., Stein M.M.\*, Kasyanov V.A.\*, Chakhlov S.V.\*,  
Osipov S.P.\*, Stein A.M.\*, Sun Xiaoming\*\*.

\*Tomsk Polytechnic University, Russia,

\*\*Power Scan, China

Inspection systems using X-ray units and accelerators of ionizing radiation is one of the most rapidly developing directions in digital radiography during the last decades. Accelerators with energy level up to 4 MeV having higher level of penetration ability by steel equivalent are the most popular to control oversize cargo transported by road, by railway and by river.

Betatron's usage as cyclic induction accelerator has some advantages in comparison with linear accelerators and other sources. Betatron has a small focal spot which improves the resolution of the system. Narrow-beam betatron radiation is easy to collimate so a spurious background of scattering radiation is much lower than in the systems based on other sources. The energy of accelerated betatrons could be regulated in relative units from about 0,3 to 1. Moreover, the betatron control system allows programming the radiation spectrum which could be used to determine the density of the scanned object.

Tomsk Polytechnic University has developed many types of betatrons, most of them are being produced by separate affiliated company "Foton". Technical specifications of betatrons for using in customs inspection systems are shown in Table 1.

Table 1. Technical specifications of betatrons

Parameters	MIB-2.5	MIB-5	MIB-7,5	MIB-9
Peak energy of bremsstrahlung radiation, MeV	1 - 2.5	2 - 5	2-7,5	2-9
Peak dose rate at 1m from the target, cGy/min	2	4	7,5	20
Pulse repetition rate, Hz	400	400	300	400
Power consumption, kVA	2	3	3	5
Radiator weight, kg	57	80	115	150
Total weight of units, kg	120	180	220	260
Size of focal spot, mm	0,25×2	0,25×2	0,25×2	0,25×2
Maximal controlled thickness (of steel), mm	150	200	270	330
Dimensions of the radiator, mm	Ø320×220	Ø360×230	Ø380×315	Ø450×340
Angle of beam in a vertical plane, deg	60	52	52	60

All betatrons, designed for inspection systems, have separate radiator with cylindrical – shaped form. This form minimizes radiation protective shielding. External views of radiators are shown on Fig.1 and Fig.2.



Fig.1 Betatron MIB – 5



Fig.2 Betatron MIB - 9



Customs inspection system, based on two accelerators with energy of 7,5 MeV, started to work in Bangunan Sultan Iskandor in BuHit Chaqar, November, 2012. This complex is supposed to control 180 trucks per hour or 2000 – per day.

This system has high scanning speed – up to 15 km/h, that was achieved by using ionizing radiation detectors of high-performance as well as the latest algorithms of data processing. This system also allows getting three-dimensional shadow images to increase the efficiency of freight inspection. External views of an inspection system are shown on Fig.3 and Fig.4.

Fig.3, Fig.4. Custom inspection system in Bangunan Sultan Iskandor in BuHit Chaqar, based on two betatrons with energy of 7,5 MeV



One of the most important advantages of this system is low dose rate on the object of control. It is about 50 microroentgen per one scanning. This parameter close to normal radiation background. This can be possible because of low dose rate of betatron and high sensitivity of the detector array. Comparison with different customs inspection systems can be seen in table 2.

In the future, the use of betatron with dual-energy mode will make possible to recognize materials contained in the test object. This technology could improve the information content of the entire complex and would enable to identify the explosives and drugs with higher effectiveness.

Table 2. Comparison with different customs inspection systems.

Parameters	Rapiscan Eagle	Silhouette Scan Mobile CaB 2000	HCV-Mobile	DRS CargoScan 5000M	This system
developed by	Rapiscan security Products (USA)	Smith Heimann (Germany)	Smith Heimann (Germany)	Adani, TPU (Russia, Belorussia)	TPU, Power Scan, (Russia, China)
maximum thickness of penetration in steel, mm	300	110	180 (270)	300	250
resolution, mm	3	3	3	2.5	5
sensitivity, %	2	No data	No data	3	2
scanning speed, m/s	0.3	1	0.2	0.4	3
x-ray source	6 MeV linac	3 MeV betatron	3(4) MeV linac	5 MeV betatron	7,5 MeV betatron
dose per one scanning, mR	3	0.15	1(2)	No data	Less than 0.05
type	Relocatable	Mobile	Mobile	Mobile	Relocatable

Developing and improving the accelerator's dual-energy mode to increase efficiency in identification and detection materials prohibited for transportation, is carried out on the experimental platform - the ICC, Tomsk Polytechnic University. Algorithms and operating modes tested on the platform are applied and mastered in the operating complex.

In summary, it is worth to say, that betatron is a good choice to be considered as a x-ray source in customs inspection systems, and this is an optimal decision for using in mobile and in relocatable inspection systems.

#### SOURCES

1. <http://www.eideticcorp.com/THScan/summary.htm>
2. <http://www.smith-heimann.de>
3. <http://www.rapiscansystems.com/>
4. [http://www.adani.by/prod\\_cargoscan.php](http://www.adani.by/prod_cargoscan.php)
5. <http://www.vividusa.com/products/cargoscreen.htm>

## Artificial Intelligence in Recognition of Welding Flaws

Ryszard SIKORA , Tomasz CHADY, Piotr BANIUKIEWICZ, Bogdan GRZYWACZ,  
Leszek MISZTAL

West Pomeranian University of Technology, Szczecin, Poland  
rs@zut.edu.pl

### Abstract

The paper carried a brief overview of artificial intelligence algorithms applicable to nondestructive testing. It focuses on two methods: artificial neural networks and fuzzy logic. Selected examples of applications of these methods in digital radiography and eddy current method are given.

**Keywords:** Automated Defect Recognition, Digital Radiography, Eddy currents, Neural Networks, Fuzzy Logic, Rough Sets, Attributes,

### Introduction

The reliable detection and classification of defects is one of the most important tasks in nondestructive testing (NDT). Usually, trained interpreters evaluate the achieved results of inspection. In many cases the process is laborious and time-consuming. Human interpretation is subjective, inconsistent, and often biased. The additional problems are caused by the insufficient quality of utilized signals or images. An incorrect classification may result in rejection of a part in good conditions or acceptance of a part with defects exceeding the limit defined by the relevant standards. The progresses in computer performance and development of artificial intelligence algorithms allow to make the process of evaluation automatic and more reliable.

The process of automatic evaluation can be divided into two basic phases: defect extraction and defect identification.

In the phase of defect extraction the following steps can be distinguished:

- signal acquisition: signal is taken, digitized and transferred to the computer;
- signal preprocessing: the quality of the signal is improved in order to remove noises and enhance useful information;
- signal segmentation: each signal disturbance caused by a potential defect has to be found and isolated from the rest of the signal.

In case of radiography the images are usually acquired and digitized by using digital detectors, imaging plate scanners or dedicated film scanners. Popularity of each technique depends on the application area. In case of castings inspection, the direct digital detectors becomes very popular, while in case of welding inspection the film technology is still an important source of images.

Irrespective of a source, X-ray imaging is inherently noisy because of the quantum nature of radiation. In some cases there may be only a few photons per pixel per exposure time. In addition there is a noise contribution from the digitizing procedure. The image suffers severely from both types of noise. This should be taken into account to appropriately assess usefulness of potential numerical method in designing of the automated inspection system. Therefore, various kinds of denoising techniques were proposed in the ADR systems. Majority of the methods assume that the noise is oscillatory, and that the image is smooth, or piecewise smooth. However in case of NDT radiographs, many important structures in images are as oscillatory as noise is. Thus, a separation methods based on smoothness arguments only is hazardous and may result in omission of potential defects. In example: the authors of [1, 2, 3] and many others propose to apply median filtering and contrast enhancement, in [4] a



combination of the Savitzky-Golay smoothing filter and weld profile approximation was applied, similarly in [5] the spline curve fitting algorithm was used to smooth the image, in [6] a Wavelet filter is applied, in [7] a low-pass filter, while in [8] the authors utilized adaptive wavelet thresholding and adaptive histogram equalization techniques.

The next step of the ADR procedure is an extraction of objects that are potential defects. There are several ways to implement this step, which were proposed in the past. The most popular is an indirect method, which consists in the fact that background image or a so-called golden image is subtracted from the original image. Ideally, the background image is a radiograph of the identical tested element without defects. In case of castings the golden image can be achieved from the radiograph of a defect free element. In most situations (like welding), such elements are not available and therefore, instead of the golden image, the background image based on the current radiograph is generated. Liao et al. [5] used a spline approximation to generate linear profiles of the weld. A similar approach was proposed by Kazantsev et al. [9], they obtained the background image by using a 2D median filter. Median filter is a ranking nonlinear operator where the output is the middle value of monotonically ordered input values. Median filters can suppress nearly completely the small objects in the image, whereas the large structures remain nearly not altered. Characteristic of the filter depends on size and shape of the filter mask and can be changed adaptively [10]. Instead of the median filters a low-pass filters can be utilized for background estimation [11]. Wang et al. [3] used surface fitting algorithm for estimation of the background image model. After background image estimation, it is subtracted from the original image and the resulting image is segmented by one of the thresholding algorithms [12] in order to extract potential defects. An alternative method is direct detection of defects. Gayer et al. proposed to use Fast Fourier Transform (FFT) to identify regions of images as potentially defective [13]. Next, these regions are proceeded by sequential similarity detection method using library of typical defects. Lawson et al. [10] proposed to utilize an artificial neural network (ANN) to generate binary image where each pixel is 0 when a regular structure is in the input window, or 1 when a defect is detected. A similar methodology was described by Boerner et al. [10] with the difference that he has used the classifier with linear decision function. Different method was applied by Merry and Filbert [14]. In the first step edge filter is employed to enhance abrupt changes in radiographic images. Next, the series of images is analyzed and the objects with high contrast are tracked. Results of such analysis allow to detect real defects. Next, in some cases the detected possible defects are fused by using morphological operators [10].

Finally, classification of defects into different types is carried out. The process of defect identification consists of the following operations:

- feature extraction: The potential defects are analyzed and some characteristic features are calculated;
- classification: The features of each potential defect are analyzed and assigned to one of the classes defined in relevant norms.

Various methods have been utilized for automated defect identification:

- artificial neural networks (ANN),
- statistical classifiers,
- fuzzy classifiers,
- fuzzy expert systems,

Silva et al. [2] proposed to apply standard feed-forward neural network with one hidden layer for identification of 5 categories welds' defects. Four geometrical features of the defects were used as inputs of the classifier. In order to reduce the dimensionality of the input data the technique of PCD (Principal Components of Discrimination) was utilized. A data base for training was created using over 150 images of welded joints of carbon steel provided and evaluated by TechnicControl. The error backpropagation algorithm was applied for the neural network training. The authors reported that the classifier reached the maximum performance percent (99.2%) in case of 18 neurons in the hidden layer. The achieved results are questionable because the same data were used for training as for testing. The extension of these works was presented in [15]. Authors have enlarged the training

database (over 200 radiographs) and number of features describing shape of the defects (21 geometric parameters). Nacereddine et al. [16] and Rajagopalan [17] have also utilized the conventional multilayer neural network. Selected geometric invariant moments which are insensitive regarding usual geometrical transformations constitute inputs for the classifiers. The network proposed in [16] contains two neurons in the output layer (corresponding to the pattern classes: defect and no defect) and the number of neurons in the hidden layer was heuristically selected as 10. Hernández et al. [18] used a Neuro-Fuzzy method (system ANFIS) to classify objects into one of the two classes: 'defect' or 'non-defect'. The Self-Organizing Feature Map (SOM) is used for reduction of input dimensionality. The utilized data set consisted of radiographic images of welding and contained over 1400 objects from both classes. The results are compared with a statistical classifier and the performance analysis is evaluated using the area under the Receiver Operation Curve (ROC). A significantly different solution was proposed by Liao [5]. Two fuzzy clustering methods: fuzzy k-nearest neighbors (K-NN) and fuzzy c-means were used by the authors to classify linear weld profiles as defected or without flaws. After preliminary trials, 25 features are applied in identifying welding flaws. The proposed system achieved 6% missing rate and 18% false alarm rate. Wang et al. [3] also used fuzzy k-nearest neighbour classifier but in order to classify into one of the 6 categories. Twelve numeric features were calculated to represent each defect instance. Performance of the K-NN classifier was compared with multi-layer neural network classifier. The achieved classification accuracy was equal to 92%. Liao et al. [19] continued these works and using the same data have implemented fuzzy expert system. The achieved results confirm that, the fuzzy expert system performed better than the fuzzy k-nearest neighbors algorithm and the multi-layer neural networks approach. Mery and Berti [20] made an interesting comparison of various statistical classifiers. The authors used texture features based on co-occurrence matrix and Gabor functions. In order to select features which provide flaw detection information, the Sequential Forward Selection (SFS) method was applied. Finally, seven features were utilised. They used the polynomial, Mahalanobis and nearest neighbor classifiers. The best performance was obtained by the polynomial classifier, (91% of the existing flaws were detected with 8% of false alarms). Shafeek et al. [21] propose defect classification algorithm based on a predefined identification tree and selected geometrical features. Additionally the authors introduced the algorithm to make an acceptance decision for the identified defects according to international standards.

In this paper, selected applications of artificial neural networks and fuzzy classifiers in radiography will be presented. Next, neural models dedicated for eddy current NDT systems will be described. Finally, a solution suitable for difficult cases, with data fusion algorithms is proposed.

### **Automated Radiogram Preprocessing**

The real radiograms taken on a production line are far from ideal. Of course they must meet very restrictive and precise norms concerning the quality of the image, whether digital or traditional, but the location and orientation of objects in the picture can vary. For example in practice it is hard to keep the same position of welds in all radiograms or alignment of markers such as lead letters and digits (practically no one pays attention to this aspect). The human operator is able to analyse and describe the radiogram by finding some characteristic points, objects, and indicators commonly contained in it. For example, the usual method of measuring image quality in radiography is the use of Image Quality Indicators (IQIs). The process of analysis is completely intuitive for an experienced operator but for a computer it can be a very demanding task lying in the fields of image analysis, object recognition, and computer vision. The main problems are:

- Varying appearances of radiograms even when acquired during the same process.
- Presence of various objects, which can disturb detection of other objects.
- Very low contrast of some objects (e.g. wire indicators).
- Welds intersections.

This is the main reason for developing methods of radiogram segmentation. Typically, the objects under investigation are: the weld line, and IQIs. After segmentation, extracted objects are passed to other algorithms for further analysis. The weld line is analysed by defect detection algorithms and the

IQI is used for estimation of the image quality value. Assuming that only the V butt joint geometry is taken into consideration, the cross section of the weld has a Gaussian shape with small linear trend. This assumption is the basis of the weld line detection algorithm. The algorithm utilizes robust approximation to track the weld in the radiogram. The intensity function  $I(y)$  of each column  $x$  of the radiogram, which is a weld profile, is approximated separately by the sum of the Gaussian function and linear function (1),

$$I(y)_x = a \cdot e^{\left(\frac{-(y-b)^2}{c}\right)} + d \cdot y + f \quad (1)$$

where  $y$  is the row number. Up and down bounds of parameters  $a$ ,  $b$ ,  $c$ ,  $d$  and  $f$  are set to prevent unexpected changes in function parameters in approximated columns. The function parameters of the previous weld profile are used as the start parameters of the next one. Moreover, a vector of weights  $\mathbf{w}$  associated with the response data  $I(y)$  has been introduced. The weights  $w(y)$  influence the contribution of points  $y$  to fitted curve  $I(y)$ . The vector  $\mathbf{w}_x$  for column  $x$  is estimated to be an average of approximations of  $N$  previous columns, scaled to the range 0–1. The initial values of coefficients  $a$ ,  $b$ , and  $c$  for each approximation  $I(y)$  are medians of  $N$  previous values of these coefficients. The experimental results show that the median operator works much better, making the process of approximation less susceptible to local signals of high intensity such as characters and other welds. Finally, the maxima of Gaussian functions  $I(y)_x$  define the centre of the weld, whereas the edges of the weld are assumed to be 5% of the height of  $I(y)_x$ . In the last step the centre of the weld and its edges are smoothed by means of a low-pass filter to eliminate small high-frequency variations. Examples of results of weld detection are presented also in Fig. 1. This method works correctly even in the presence of high-intensity objects near the weld line.

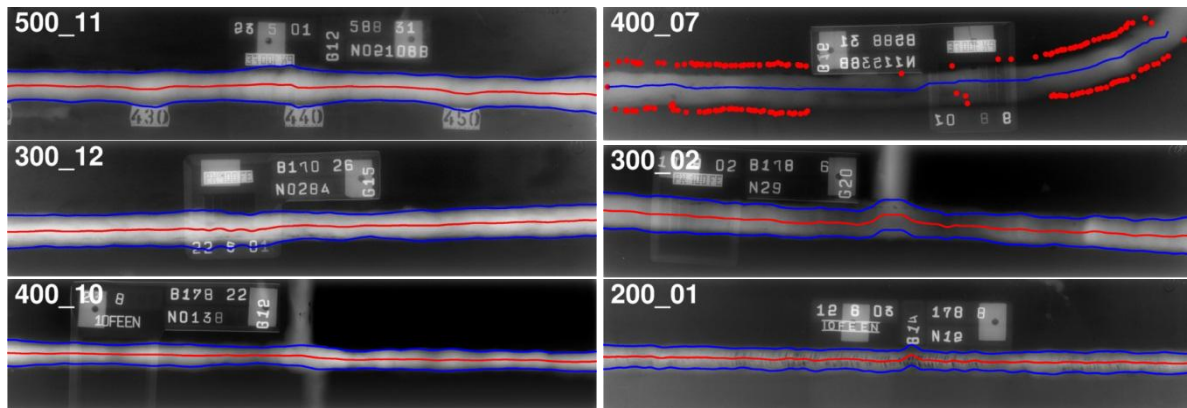


Fig. 1. Examples of results of weld detection. The second picture shows the approximated weld line from first radiogram.

## Automated Defect Recognition Algorithms in Digital Radiography

Following the analysis of radiographic system operators, an automatic system to assess the radiographs evaluation called ISAR is designed and implemented. The automatic classification of defects is based on the description of defect's shape by means of selected features. The classification is done in accordance with respective welding norms. The defects are classified into five main groups described in EN ISO 6520-1 norm [22]. All radiograms were processed in order to extract defects and make them ready for feature evaluation procedure. First, in the pre-processing step the image was normalized and rotated to set the weld line horizontally. Next, region of interest (ROI) was detected. The ROI included the weld and surrounding heat affected area, where defects are commonly located. The feature calculation procedure was based on indirect detection method [23], which, in short, uses an artificially generated background that is then subtracted from the original radiogram making defects more visible. Finally, background-free image was denoised and thresholded in order to isolate defects. After processing of the radiogram, the number of features was calculated for every extracted defect. The features describe geometrical properties of the object as well as its texture and closest

surrounding. The set of implemented features can be divided into two parts including the basis features and derivative features respectively. The derivative features are formed as nonlinear combinations of basis features. This approach extends separability of groups of defects in classification process. Table 1 shows selected basis features implemented in the ISAR system. The three first features listed in Table 1 are derived from a statistical analysis. The image of inclusion has been treated as a cloud of points in two dimensional space. Then, the principal components analysis (PCA) has been utilized in order to obtain eigenvectors that characterize distribution of data in space. The eigenvectors have been used as semi-axes of ellipse fitted to the object.

Table 1. Definition of basis features.

Feature name	Definition	Feature name	Definition	Feature name	Definition
Data lengthening	$L_D = \frac{ max_a - min_a }{ max_b - min_b }$	Texture 1	$R_{T1} = \frac{ \bar{I}_{t < t_0} - \bar{I}_{t > t_0} }{\bar{I}}$	Danielssons's coeff.	$R_D = \frac{A^3}{(\sum_i l_i)^2}$
Ellipse angle	$\alpha = \arccos\left(\frac{\vec{a} \cdot \vec{OX}}{ \vec{a} }\right)$	Mean Brightness	$R_M = \frac{1}{N} \sum_{i=1}^N I_i$	Harlick's coeff.	$R_H = \sqrt{\frac{(\sum_i d_i)^2}{P(\sum_i d_i^2) - 1}}$
Principal lengthening	$L_P = \frac{ \vec{a} }{ \vec{b} }$	Texture 2	$R_{T2} = \sqrt{\frac{\sum_i (I_i - \bar{I})^2}{N - 1}}$	Blair-Bliss coeff.	$R_B = \frac{A}{\sqrt{2\pi \sum_i r_i^2}}$
Perimeter	$P = \sum_i x e_i$	Rectangularity	$R_P = \frac{A}{L * W}$	Area	$A = \sum_i x_i$
Malinowska's coeff.	$R_{MN} = \frac{P}{2\sqrt{\pi \cdot A}} - 1$	Compactness	$R_{cp} = \frac{P^2}{4\pi A}$	Location related to the weld line	$D = \frac{2r_c}{W_w}$

The meaning of symbols from Table 1 is as follows:  $x e$  – pixel of edge of the object,  $x$  – pixel of the object,  $r$  – distances between center of object and border point,  $l$  – shortest distance between object's boundaries,  $I_i$  – intensity of  $i$ -th pixel,  $L, W$  – length and width the object evaluated along  $OX$  and  $OY$  axis,  $d$  – distance between object's border and object's center of gravity,  $a, b$  – longer and shorter principal vector respectively,  $max_a, min_a, max_b, min_b$  – minimal and maximal coordinates of object's point evaluated along principal vectors,  $r_c$  – distance between center of object and center of weld,  $W_w$  – width of weld. Both parameters,  $r_c$  and  $W_w$  are evaluated locally in closest surrounding of object.

In order to apply artificial intelligence (AI) algorithms a data base of various defects is needed. Therefore, the database consisted of over 500 defects belonged to five main groups was created. The preparation of database consisted of three main steps:

1. image acquisition,
2. pre-processing operation, defect detection,
3. feature calculation.

After analysis of the database, it is visible that some of the features are redundant due to a linear dependence among them or mutual similarity. Components that are linear combinations of other components have negative influence on performance of learning of AI systems. The common way of identifying patterns in data and expressing the data in such a way as to highlight their similarities and differences is the use of factor analysis. Factor analysis is part of the general linear model family of procedures and makes many of the same assumptions as multiple regression: linear relationships, interval or near-interval data and multivariate normality for purposes of significance testing. There are several different types of factor analysis, with the most common being principal components analysis (PCA). However, common factor analysis (FA) is preferred for purposes of causal analysis and for confirmatory factor analysis in structural equation modeling, among other settings.

Two different classifiers were used in our study for radiogram analysis: a fuzzy classification system and ANN classifier.

## Fuzzy Classification System

In this paper, the Mamdani Fuzzy Logic (FL) system has been applied to defect classification. The FL system achieves the balance between execution speed and classification accuracy. Moreover, in



comparison to neural network classifiers, the training process of the FL system is easier and more predictable. After training, the system can be tuned up manually to minimize MSE error. Fuzzy theory provides us the linguistic representation of state. It expresses degree of truth, which is represented as grade of a membership functions. Fuzzy inference systems have successfully been applied in various fields, such as automatic control, data classification, and decision-making units. Here are the four steps during fuzzy reasoning:

1. Mapping input values into 0 - 1 space by the membership functions, defined for each input.
2. Combining membership values through a specific T-norm operator to get firing strength of each rule.
3. Generating the qualified consequent of each fuzzy rule depending on its firing strength.
4. Aggregating consequents for each rule to produce crisp output.

The main goal of the FL system was to classify defects to four main groups in accordance with the norm [22]. The fifth group (undercuts) was not taken under consideration due to small number of available specimens containing that type of defects. Features of the defects processed by PCA method were used as an input data vector for the FL system. The process of tuning the Fuzzy Logic System consists of three basic steps: 1) determining membership functions (MF) parameters such as type and shape (Gauss function in most cases), 2) determining output MF and 3) building set of fuzzy rules. For simple systems, these steps can be realized manually. However, in the case of more complicated problems, as identification or approximation the correct parameters can be only obtained by automatic process. The membership functions were determined by two-sided Gaussian curves. These functions depend on two parameters that define their shape and position:  $c_1, c_2$  (coordinates of maximums),  $\sigma_1$  and  $\sigma_2$  (the bell width for left side and right side curve respectively). In this case it was assumed that  $c_1 = c_2$ . The number of MFs is determined by the user's choice. The MFs set should cover the whole range of input values for each input. Therefore, for each input, the clustering algorithm was applied to divide data into subsets. Each subset was related to one membership function. The purpose of clustering is to identify natural groups of data from a large data set. The parameter stands for the centre of cluster and it was defined as arithmetic average of maximal and minimal value in the cluster. This procedure is shown in Fig. 1 for data obtained from PCA (two inputs).

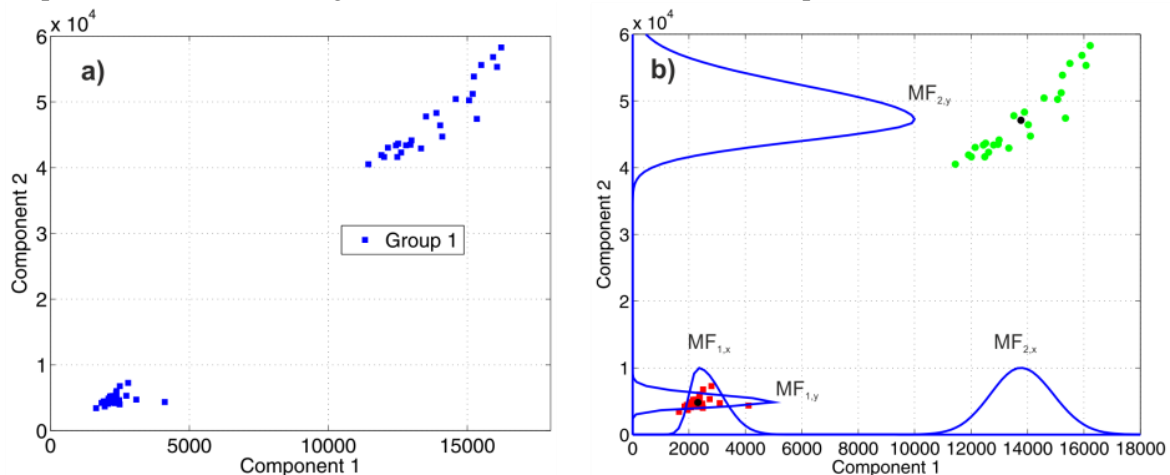


Fig. 2. Evaluation of parameters of the MF. Data representing first group of flaws (a) and membership functions fitted to each cluster for input x and y respectively (b).

In the third stage of the training process, the incomplete base of fuzzy rules was created. The rules were built utilizing basic dependences among inputs, particular membership functions and outputs. Exemplary rule defining behavior of the system for input values corresponding to first group of flaws had form:

**if input1 is MF1,x and input2 is MF1,y then output1 is high and output2 is low and output3 is low and output4 is low**

The achieved mean square errors (MSE) of defect classification using fuzzy logic system are presented in Tab. 2.

Table 2. The MSE obtained for fuzzy logic classifier.

	Group 1	Group 2	Group 3	Group 4	Group 5
MSE	0.0218	0.0444	0.0424	0.0279	NA

Small error obtained for testing data confirms that the structure of applied FL was chosen correctly. The best results were achieved for the first, group of defects (cracks), which is the most separated group in case of PCA analysis.

### The use of rough sets theory for detection of weld defects

In this part there is description of applying the rough set theory for classification of weld imperfections. For the first time the theory was presented by Pawlak [25]. The methods of data processing drawn from this theory are based on extension of sets theory. This provides ability for creation of decision table that uses collected data. In short, the rules are generated on the basis of discretization, conditional and decision attributes, estimated equivalence of classes that creates basic building blocks of indistinguishable information, lower and upper approximations that designates specific sets, reducts which indicates attributes that are meaningful for detection of classes [26]. At the end of knowledge extraction process the created rules takes the form of **IF ..THEN..** [27], which allows to interpret gained results of classification. Every induced rule additionally has got parameters that describe quality of gathered result like support, coverage, accuracy [28]. This allows to eliminate the “weaker” rules from whole rules set for the sake of classification accuracy. For estimation of accuracy of rough set classification model the parameters based on confusion matrix [29] are usually calculated. On the basis of elementary parameters FP, FN, TP, TN coefficients describing the quality, like accuracy, error rate level, positive predictive value have been estimated [30]. Additional confirmation of accuracy of gained rules was confirmed by using of cross validation technique [31]. There was conducted 10-fold validation test by dividing data into training and testing samples, generating rules and accuracy measurement for every fold. It allowed to avoid the accidental distribution of training and testing set, which could generate “one-time” good results.

In our researches data gathered in decision table for processing with use of rough sets approach describes defects of weld connections. The data is divided into conditional attributes and decision attribute. There has been used 39 parameters describing geometrical properties and textures of weld flaws and 36 parameters called moments (centered, normalized centered, invariant) as dependent attributes and class of weld defect as decision attribute. In summary there were over 1500 samples (objects) referring to weld radiographic images and each of objects has got numerical values of all attributes. There have been made four different researches with different groups of data. The reason for this was different characteristic of information saved in attributes, other approach for moments attributes as well as practical knowledge for reaching better accuracy with different sets of data. So, researches were led separately for geometrical and texture data, moments data, combined geometrical, textural and moment data and additionally for every single attribute describing moment data. Motivation for making the next classification for single moment attributes was assumption that every value of estimated moment could describe well shape of weld defect and it was perceived that every type of defect (cracks, porosity and gas cavities, entrapped slag and other inclusions, fusion and lack of joint penetration, undercuts) in real radiographic image has got different shape. Additionally there are proofs that classification with the usage of rough set on the basis of single attributes led to very accurate results on well known real data sets [32]. The effects of that approach led to achievement of classification results with very high accuracy.

For the reason of rough set usage the discretization of collected data was needed. It is also obligatory

step for many other machine learning algorithms [33]. In the researches there were used a few methods for cutting of existing data: equal-frequency binning for dividing attributes into selected number of bins with approximately the same number data based on many attempts and practical experience with different number of bins, boolean reasoning algorithm [34] and entropy algorithm [35]. In summary 50 experiments with different data discretization for every set of geometrical, moments and combined geometrical and moments data and about 200 experiments for single moments data have been carried out.

Proposed expert system based on rough set theory is compatible with many organizations and companies standards for machine learning systems – CRISP-DM [36] (cross industry standard process for data mining). The main steps of research procedure consists of:

- preparation and loading of data
- discretization of data
- estimation of attribute importance and dimension reduction
- splitting of data
- rule induction
- evaluation of results

The next section deals with more detailed presentation of procedure for induction of rules for classifying the weld defects with use of rough sets. The procedure has been realized in seven steps (see Fig. 3). These steps are listed and described below :

1. Preparing and loading data in accordance with the requirements of the RSES software [37],
2. Discretization of data – assigning of numerical values representing the conditional attributes to specific numerical ranges. Choice of discretization techniques and the number of intervals for each attribute have been done by an experimental way (many laborious attempts) with usage of equal-frequency binning or discretization methods: boolean reasoning algorithm or entropy algorithm,
3. Determination of significance of attributes and reduction of the information table in dimensions – this step was designed to determine the significance of the attributes affecting the decision-making class. The significance has been evaluated taking into account the numbers representing the cardinalities of the lower approximations and positive regions in relation to cardinality of the “universe”, or by the analysis of reducts obtained according to requirements of indiscernibility relation. The reduction in dimensions of the information table caused by removal of attributes of low importance is the last operation belonging to this step,
4. The splitting (division) of the data into training set and the testing one with keeping the division ratio of 50% to 50% . ,
5. 5 a), 5 b) Creation of two information tables: that for training and that for testing,
6. Extraction of rules from training set – application of methods based on rough sets theory to induction of set of rules identifying the specific defects in the welds,
7. Applying of the rules obtained in previous step to the testing set and calculation of so-called consistency matrix (see Table 3) containing crucial information about accuracy and coverage.

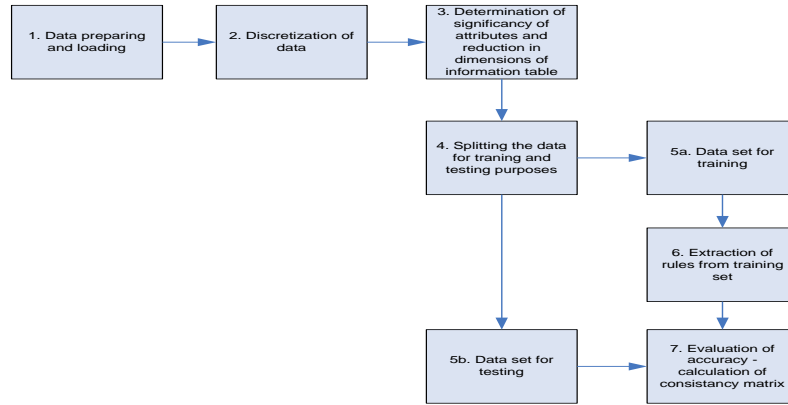


Fig. 3. Procedure for classification of defects in welds

The obtained results of classification by means the above procedure are collected in Table 3. Rows in this matrix correspond to actual decision classes (all possible 5 values of decision) while columns represent decision values as returned by classifier. Number of objects in data set that belong to the decision class “ $i$ ” corresponding to current row is denoted by  $NU_i$ . The accuracy, i.e. ratio of correctly classified objects from the class “ $i$ ” to the number of all objects assigned by classifier to the class “ $i$ ” is denoted by  $ACC_i$ . The number of correct predictions for class “ $i$ ” is denoted by  $P_{ii}$ , while  $N_{ij}$  denotes number of objects belonging to class “ $i$ ” but classified as objects belonging to class “ $j$ ” (incorrect classifications). The ACC ratio represents number of correctly classified cases (sum of values on diagonal in confusion matrix) to the number of all tested cases is labeled in Table 3 as “Total accuracy”. Finally, the percentage COV of test objects that were recognized by classifier is labeled as “Total coverage”.

Table 3: The consistency matrix containing parameters for evaluation of classification accuracy.

	1	2	3	4	5	Number of objects	Accuracy
1	P11 20 118 <u>121</u> <b>236</b>	N12 1 13 <u>9</u> <b>0</b>	N13 0 8 <u>13</u> <b>0</b>	N14 3 0 <u>2</u> <b>0</b>	N15 0 4 <u>3</u> <b>0</b>	NU1 32 242 <u>246</u> <b>237</b>	ACC1 0.833 <u>0.825</u> <b>0.818</b> <b>1.0</b>
2	N21 4 14 <u>32</u> <b>0</b>	P22 168 110 <u>71</u> <b>262</b>	N23 17 10 <u>18</u> <b>0</b>	N24 14 3 <u>1</u> <b>0</b>	N25 4 0 <u>1</u> <b>0</b>	NU2 275 231 <u>246</u> <b>262</b>	ACC2 0.812 <u>0.803</u> <b>0.577</b> <b>1.0</b>
3	N31 4 27 <u>43</u> <b>0</b>	N32 24 25 <u>35</u> <b>0</b>	P33 65 51 <u>26</u> <b>37</b>	N34 26 4 <u>1</u> <b>0</b>	N35 8 0 <u>1</u> <b>0</b>	NU3 219 240 <u>221</u> <b>39</b>	ACC3 0.512 <u>0.477</u> <b>0.245</b> <b>1.0</b>
4	N41 1 1 <u>3</u> <b>0</b>	N42 10 6 <u>9</u> <b>0</b>	N43 9 3 <u>2</u> <b>0</b>	P44 137 12 <u>4</u> <b>217</b>	N45 3 0 <u>0</u> <b>0</b>	NU4 228 35 <u>40</u> <b>219</b>	ACC4 0.856 <u>0.545</u> <b>0.222</b> <b>1.0</b>
5	N51 0 6 <u>8</u> <b>0</b>	N52 5 1 <u>5</u> <b>0</b>	N53 2 0 <u>1</u> <b>0</b>	N54 0 0 <u>0</u> <b>0</b>	P55 17 17 <u>0</u> <b>28</b>	NU5 33 39 <u>34</u> <b>30</b>	ACC5 0.833 <u>0.708</u> <b>0.000</b> <b>1.0</b>
Total accuracy	ACC 0.751 0.711 <u>0.543</u> <b>1.000</b>		Total coverage	COV 68.9 0.55 <u>0.52</u> <b>0.991</b>			



The numerical data in Table 3 define the achieved accuracy for the obtained 4 sets of classification rules (classifiers) :

1. Numbers presented by “standard fonts” – those data have been obtained for rules extracted after processing of values representing 39 conditional attributes + 1 decision-making attribute. The so-called shape moments were not included to those conditional attributes. In this case the 16 attributes were selected as significant ones
2. Numbers presented by “*italic fonts*” – all 75 conditional attributes, including the moments of the shapes, were processed,
3. Numbers presented by “underlined fonts” - those results have been obtained after processing of 36 conditional attributes representing: moments of shapes  $m_{pq}$ , centered moments of shapes  $M_{pq}$ , moments  $N_{pq}$  (i.e. normalized moments  $M_{pq}$ ), Hu’s moment invariants  $I_k$  [39], moment invariants  $NM_k$  proposed by Tadeusiewicz. As important attributes were recognized the five among them,
4. Data presented by “**bold fonts**” - those results have been obtained for the modified procedure of rules induction (see Fig. 4) on the basis of five selected moments. The set of 5 classifiers configured conceptually in “series structure”, where each of them processes the data representing single attribute, has yielded the highest accuracy.

The modification of procedure of rules induction which finally yielded results distinguished with bold fonts in Table 3 was undertaken because of observed excellent accuracy (up to 100%) for the five moments attributes, however the overall coverage assured by set of rules based on one member of that set of attributes was ranged from a several to about 40% (i.e. most of the objects – weld defects- could not be classified). Further studies have shown that intersections of attribute ranges which assigned objects to given class were almost empty. Taking the above into account the combining system shown in Fig. 4 has been proposed. With this solution the substantial increase of accuracy has been achieved. The system composed according to Fig. 4 yielded classifier composed of 22 rules. The exemplary rule for identification of the weld defect of type “5” on the basis of attribute 43 can be presented in the form:

“**X43**=(614.763,Inf> or (5.50568,5.51845> or (13.6795,13.693> or (57.3754,57.8979>or(396.398,421.598>or(4.36615,4.37103> or (12.1445,12.1459> or (38.5014,38.613>or (217.402,226.28> or (66.4694,67.2278>or (4.52656,4.53963> or (5.95757,5.96048> or (17.201,17.2217> or (234.209,243.971> or (10.5939,10.6096> or (5.5908,5.62997> or (6.4355,6.43788> or (49.0226,49.2385> or (437.402,475.1>or (76.4302,77.5492>or (6.68788,6.69557>or (251.269,319.432>or (6.60009,6.60896>or (85.5294,85.9961>or (5.86877,5.88656> or (105.803,109.526> or (67.9432,68.1373> or (18.9012,18.9039> or (4.58431,4.58875)”) => **5**”

The very good results of classification obtained by means of procedure represented in Fig. 4 were verified using so-called “cross-validation” method [31]. According to requirements of mentioned method, the procedure of induction of classifying set of rules was repeated 10 times, but before every repetition the objects for training set and testing set were selected randomly. That strategy ought to eliminate unfortunate choice of testing and training sets which incidentally yields big “overshoot” in evaluation of classification accuracy. The obtained results have been very similar for each of 10 choices: classification accuracy up to 100%, total coverage from 97% to 100%.

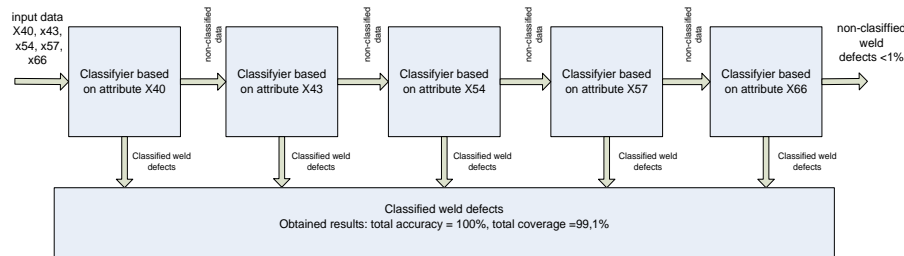


Fig. 4 Model of procedure for the classification of weld defects based on values of five moments.

The results of classification of weld defects can be summarized by the following conclusions:

- Depending on the choice of conditional attributes and procedures for rule induction the achieved overall accuracy of the classification and total coverage levels were, respectively,

(75.1%, 68.9%) (71.1%, 55%), (54.3%, 52%) (100%, 99.1%). It means, that conditional attributes those without a moments of shapes (case 1 – “standard fonts”) or, rather, those representing the selected 5 moments and moment invariants (case 4 – “**bold**”) should be chosen for weld defect classifiers.

- The results collected in Table 1 show that induction of classification rules with use of elements of rough sets theory can be done successfully, because leads to very good results of classification (case 4) or at least acceptable from technical point of view (case 1).

## Conclusions

Three different applications of FL, ANN and rough sets were presented. The achieved results prove that they are already efficient tools. However, the described algorithms and systems will be still enlarged and developed. It is very important to make sure that application of artificial intelligence will be good substitute or help of the NDT operators' work.

## Literature

- [1] Nacereddine N., M. Zemat, S. S. Belad'fa, M. Tridi: Weld defect detection in industrial radiography based digital image processing, 2004
- [2] Silva R. R., Luiz P. Calôba, Marcio H. S. Siqueira, and João M. A. Rebello: Patterns nonlinear classifiers of weld defects in industrial radiographies, 2003
- [3] Wang G., Liao T.W.: Automatic identification of different types of welding defects in radiographic images, 2002
- [4] Padua G. X., R. R. Silva, M. H. S. Siqueira, J. M. A. Rebello, L. P. Caloba, Classification of welding defects in radiographs using traversal profiles to the weld seam,
- [5] Liao T.W., Li D.-M., Li Y.-M.: Detection of welding flaws from radiographic images with fuzzy clustering methods, 1999
- [6] Wirdelius H. Hammar L.: Modelling of a high resolution digital radiographic system and development of a filtering technique based on wavelet transforms, 2004
- [7] Shaun W., Lawson, Parker G.A.: Intelligent segmentation of industrial radiographic images using neural networks, 1994
- [8] Wang X., Brian Stephen Wong: Radiographic image segmentation for weld inspection using a robust algorithm, 2005
- [9] Kazantsev I.G., Lemahieu I., Salov G.I., Denys R.: Statistical detection of defects in radiographic images in nondestructive testing, 2002
- [10] Mery D., Jaeger T., Filbert D.: A Review of Methods for Automated Recognition of Casting Defects,
- [11] Eckelt B., Mayendorf N., Morgner W., Richter U.: Use of automatic image processing for monitoring of welding process and weld inspection, Proc. of 12th World Conf. NDT, pp. 37-41, 1989
- [12] Nacereddine N., L. Hamami, D. Zjou: Image Thresholding for Weld Defect Extraction in Industrial Radiographic Testing, 2006
- [13] Gayer A., Saya A., Shiloh A.: Automatic recognition of welding defects in real-time radiography, 1990, NDT International, 23 (4), pp. 131-136, 1990
- [14] Mery D., Filbert D.: Automated Flaw Detection in Aluminum Castings Based on the Tracking of Potential Defects in a Radioscopic Image Sequence", 2002
- [15] Silva R. R. , M. H.S. Siqueira, M. P. Souza, J. M.A. Rebello, L. P. Calôbac: Estimated accuracy of classification of defects detected in welded joints by radiographic tests, 2005
- [16] Nacereddine N., Draï Redouane, Benchaala Amar: Weld Defect Extraction and Classification in Radiographic Testing Based Artificial Neural Networks, 2000
- [17] Rajagopalan C., B.Venkatraman, T.Jayakumar, P.Kalyanasundaram and Baldev Raj: A novel tool for automated evaluation of Radiographic weld images
- [18] Hernández S., Sáez D., Mery D., Silva R., Sequeira M.: Automated defect detection in aluminium castings and welds using neuro-fuzzy classifiers, 2003
- [19] Liao T.W.: Classification of welding flaw types with fuzzy expert systems, 2003
- [20] Mery D., M A Berti: Automatic detection of welding defects using texture features, 2003
- [21] Shafeek H.I., E.S. Gadelmawla, A.A. Abdel-Shafy, I.M. Elewa: Automatic inspection of gas pipeline welding defects using an expert vision system, 2004
- [22] European Norm EN ISO 6520-1:1998.
- [23] R. Sikora, P. Baniukiewicz, T. Chady, W. Ruciński, K. Świadek, M. Caryk, P. Lopato, „Comparison of selected weld defects extraction methods”, QNDE, Review of Progress in Quantitative NDE, 2007.
- [24] N. Nafa, R. Draï and A. Benchalla, Weld Defect Extraction and Classification in Radiographic Testing Based Artificial Neural Networks, WCNDT 2000
- [25] Pawlak Z., Rough Sets – Theoretical Aspects of Reasoning about Data, Kluwer Academic Publishers, 1991.
- [26] Pawlak Z., Some issues on rough sets, Springer Science, 2005
- [27] Inugushi M, Generalizations of Rough Sets and Rule Extraction, Springer, 2005.
- [28] Stepaniuk J., Rough – Granual Computing in Knowledge Discovery and Data Mining, Berlin, Springer, 2008, ISBN 978-3-540-70800-1
- [29] Olson D.L., Delen D.: Advanced Data Mining Techniques, Berlin Heidelberg, Springer, 2008, ISBN: 978-3-540-76916-3
- [30] Han J., Kamber M.: Data mining concepts and techniques, Morgan Kaufman, 2006, ISBN 13:978-1-55860-901-3
- [31] Michie D., Spiegelhalter D.J., Taylor C.C.: Machine Learning, Neural and Statistical Classification, Ellis Horwood, New York, 1994
- [32] Holte R.C., Very simple classification rules perform well on most commonly used datasets, Machine Learning vol.11, 1993
- [33] Evangelos Trantaphyllou, Giovanni Felici, Data Mining and Knowledge Discovery approaches based on rule induction techniques

- [34] Nguyen H.S. and A. Skowron A., Quantization of real-valued attributes. In Proc. Second International Joint Conference on Information Sciences, pages 34–37, Wrightsville Beach, NC, Sept. 1995
- [35] Dougherty J., Kohavi R., and Sahami M. Supervised and unsupervised discretization of continuous features. In A. Prieditis and S. Russell, editors, Proc. Twelfth International Conference on Machine Learning, pages 194–202. Morgan Kaufmann, 1995
- [36] Cross Industry Standard Process for Data Mining, <http://www.crisp-dm.org>
- [37] Site of software tool RSES: [www. logic.mimuw.edu.pl/~rses/](http://www.logic.mimuw.edu.pl/~rses/)
- [38] Flusser J., Suk T., Zitova B.: Moments and Moment Invariants in Pattern Recognition, Wiley, 2009, ISBN 978-0-470-69984-4
- [39] Hu M.K., “Visual pattern recognition by moment invariants,” IEEE trans. on Information Theory, vol. 8, pp. 179–187, 1962.

## **CR – System Performance Evaluation for periodic system check**

Kiesel, Denis

GE Sensing & Inspection Technologies GmbH Ahrensburg, Germany

### **Abstract**

More and more typical Radiographic applications get converted into digital solutions. Due to the similarities to traditional film methods in setup and handling, one of the most favored conversion technologies are Computed Radiography systems. The quality of these systems and the comparability to radiographic exposures has long been discussed, and the trade between spatial properties and contrast resolution differences has led to new specifications and standards measuring the system performance and quality.

GE Sensing & Inspection Technologies as part of GE Measurement & Control understands their NDT business as Healthcare for Industry. In this spirit we have driven the digital conversion from the start, and are as a leader in this process constantly sharing our experience, progress, recommendation and outlook. One of the essentials to a save and transparent conversion is the guidance by standards that are independent and working procedures that are industry specific. This Abstract is making the effort to promote and explain the factors influencing CR image Quality and the procedures for the industry to evaluate their systems performance.

### **1. Introduction**

Image quality in film radiography is widely known as mainly being determined by sharpness and Image density. Different film classes care for the necessary spatial resolution that is needed for varying application tasks in order to image specific discernible defect sizes.

With the shift to CR systems, where reusable, erasable IP foils are used to acquire the image and digital scanners, to extract the image from the IP in a digital format, the image quality is dependent on a set of different parameters.

Density is replaced by a measured pixel grey value and spatial resolution is a combination of the IP plate type and the scanner resolution settings. SNR is additionally influenced by electronic components and settings in the scanners, and achievable specific discernible defect detectability is a combination of new extended properties of the digital system, that allows for a much wider dynamic range and extended contrast information compared to film, however with a trade in in special resolution properties. This shift in additional image property values, demand that we use slightly different methods to qualify a system setup, the system class and the system validity during operation. Each of those 3 steps is guided by a specific standard

or industry specific procedure.

While system Setup procedures are usually industry specific, and follow a guideline such as the MAI guide for Aerospace Casting inspections, the system class verification is guided by the ASTM 2446 and/or the EN 14784-1. and is usually certified by independent 3<sup>rd</sup> party institutes such as the German BAM federal institute for material research and testing.

The third step is the verification and periodic system performance evaluation that is usually demanded within the guidelines for use such as MAI – Appendix A. Those periodic system checks are made in reference to ASTM 2445 and are the main subject in this paper, with the goal to highlight what is needed and how it is done in practice.

### **2. Periodic CR-System Evaluation**

#### **2.1. Tools and necessary checks**

In order to perform periodic system checks we need to use either a set of different Quality indicators or a test phantom including all those indicators, as described in ASTM 2445-05. A sample of a test Phantom is shown in Figure 1.



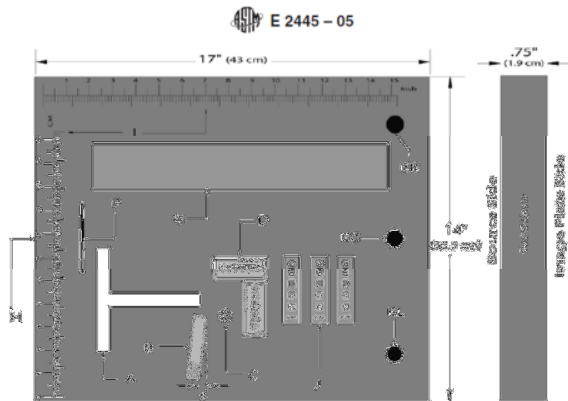


Figure 1.

The indicators include:

- A:** T-target for Laser Jitter Test Length 114 by 5 mm H (4.48 by 0.2 in.), Brass
- B:** Duplex-Wire Image Quality Indicator; in accordance with Practice E 2002
- C:** Central Beam Alignment (BAM-snail)
- D:** Converging Line Pair Quality Indicators
- E:** EL, EC, ER: Measuring Points for Shading Correction 19 mm (0.75 in.) Diameter, 0.3 mm (0.1 in.) Acrylic Removed
- F:** Cassette Positioning Locator (does not appear on radiographic image)
- G:** Homogeneous Strip: Al, 0.5 mm (0.02 in.)
- H:** Lucite Plate
- I:** Inch/cm Ruler for Linearity Check
- J:** Contrast Sensitivity Quality Indicators  
Aluminum: 12.7 mm (0.50 in.)  
Copper: 6.35 mm (0.25 in.)  
Stainless Steel: 6.35 mm (0.25 in.)

For a periodic system check not all of the indicators are necessary as some are only used after a repair or upon initial manufacturers test.

Periodic tests are recommended as per the industries specific procedure. On the example of Aerospace castings, the MAI demands checks as per table 1.

		Process Check Frequency						
Test		Initially	Quarterly	Monthly	Weekly	Daily	per shift	Repair/Replace
Computed Radiography	SRb (system spatial resolution) <sup>1,4</sup>	✓	✓					✓
	Plaque IQI block shot (visual) (contrast & spatial resolution)	✓					✓	✓
	Contrast sensitivity	✓	✓					✓
	Shading	✓	✓					✓
	Jitter	✓	✓					✓
	Afterglow (Blooming/Flare)	✓	✓					✓
	Geometric Distortion	✓	✓					✓
	EPS	✓						✓

Table 1.

For the recommended periodic tests we need a software imaging system that allows to measure and display all the relevant performance parameters. As an example we used the GE Rhythm software suite that allows for both manual and automatic measurement of the relevant parameters.

Tests that need to be performed on a quarterly basis are:

- SRb – Basic Spatial Resolution
- CNR – Contrast to Noise Ratio
- Shading & Slipping
- Jitter
- Afterglow
- Geometric Distortion

Additionally a per-shift Test would need to get performed with an IQI Block measuring CNR and SRb.

## 2.2 Definition

### 2.2.1 SRb

SRb for the long term stability is measured with a Duplex Wire indicator according to E2002. The setup process for this application is described in ASTM 2445-05 6.1.2 to 6.1.2.5.

### Example:

Positioning of the duplex wire gauges according to Figure 2.

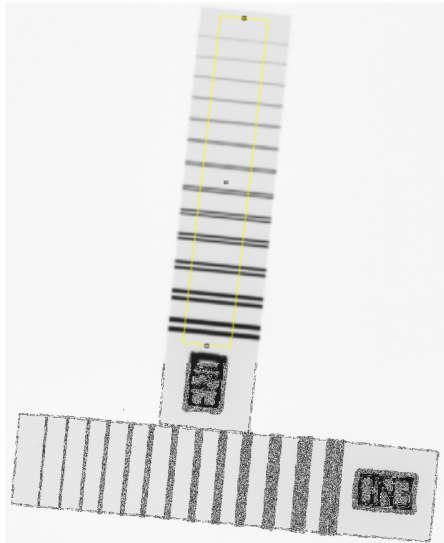


Figure 2

After exposure the software tool for Line histogram needs to get used to get the appropriate response. Figure 3 shows the line profile.

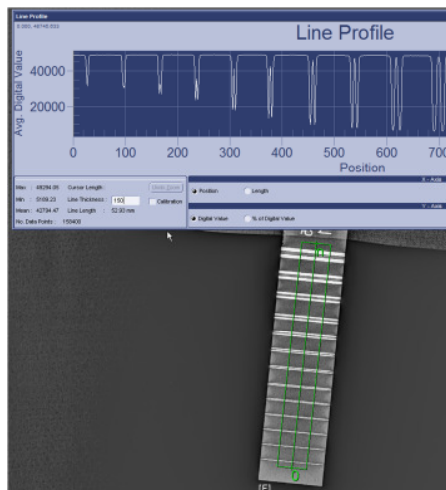


Figure 3

The standard now demands that we determine that line-pair, which is the first one that shows a dip of less than 20% of the overall amplitude. This is then the threshold SRb line pair. The value is according to table 2. Figure 4 shows a zoomed image of the last line-pair with a visible dip.

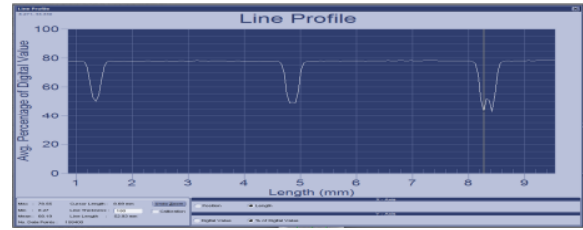


Figure 4

With the help of the Rhythm software tools we can do the math:

We need to measure the following Pixel Values (MPV):

A: MPV @ Baseline:

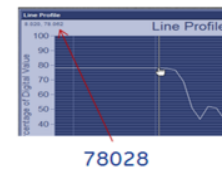


Figure 5

B: MPV @ max. Amplitude

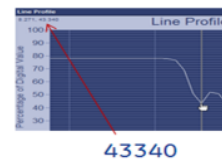


Figure 6

C: MPV @ Dip



Figure 7

$$\text{MPV } 78028 - \text{MPV } 43340 = \Delta \text{MPV } 34688 = 100\% \text{ of the signal}$$

$$\text{MPV } 78028 - \text{MPV } 52123 = \Delta \text{MPV } 25905 = 74\% \text{ of the signal} \Rightarrow \text{the dip is } 26\%$$

According ASTM 2445 the dip needs min. 20% which is given.

The wire-pair was counted as pair D11  $\Rightarrow$  Threshold SRb is then pair D12 which is 63 micrometer since this is the first unresolved one.

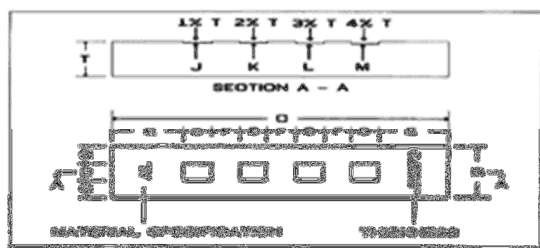
Minimum IQI value and Maximum unsharpness (ISO 19232-5) <sup>2</sup> mm	Maximum basic spatial resolution in mm (equivalent to wire thickness and spacing) <sup>2</sup>
D 13 0,10	0,05
D 12 0,125	0,063
D 11 0,16	0,08
D 10 0,20	0,10
D 9 0,26	0,13
D 8 0,32	0,16
D 7 0,40	0,20
D 6 0,50	0,25
D 5 0,64	0,32
D 4 0,80	0,4

Table 2.

### 2.2.2 CNR Contrast to Noise Ratio

CNR values are dependent on the material and the difference in material thickness. Therefore the ASTM 2445-05 refers to practice E 1647 and states that contrast measurements depend on the material. The CR Phantom recommends an IQI block of AL, CU and FE to cover different material groups. See Drawing 1.(General Layout of the Csa Gauge)

However a reference block with the exact material that is under test would be the most appropriate to use.



Drawing 1

Requirements for setup and alignment are described in the specific E1647 practice. The read-out within the software is shown in the Figures 8 and 9

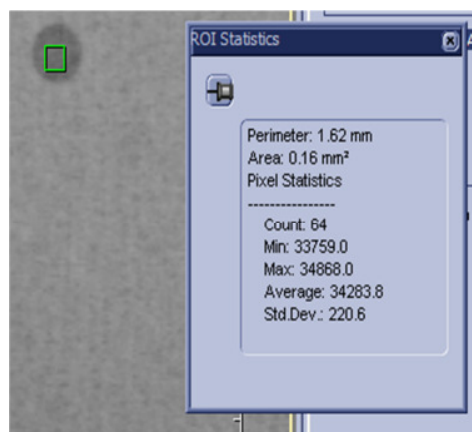


Figure 8



Figure 9

The software provides a function that allows to draw a region of interest inside a hole or groove of the indicator and on the base material of the indicator. It will give statistical data from each of the region of interest. With this data and the formula 1 below, CNR can get calculated.

$$CNR = \frac{\text{average inside Hole} - \text{average outside Hole}}{\sqrt{\frac{\sigma_{\text{inside}}^2 + \sigma_{\text{outside}}^2}{2}}}$$

Formula 1

In this particular example, the math is according to formular 2.

$$CNR = \frac{34283.8 - 32371.4}{\sqrt{\frac{220.6^2 + 209.7^2}{2}}}$$

CNR= 8,88

Formula 2

### 2.2.3 Shading & Slipping

**Shading** describes the difference in grey value across the imaging plates Laser-scan direction. If the plate has been imaged homogenously, the difference between the center of the scan line and the edges of the scanned plate, has to stay within a tolerance of max. 15% for a periodic check. Setup conditions are found in the ASTM 2445 Standard.

For shading, a line-profile needs to get drawn over a homogeneous area on the Phantom. See Figure 11

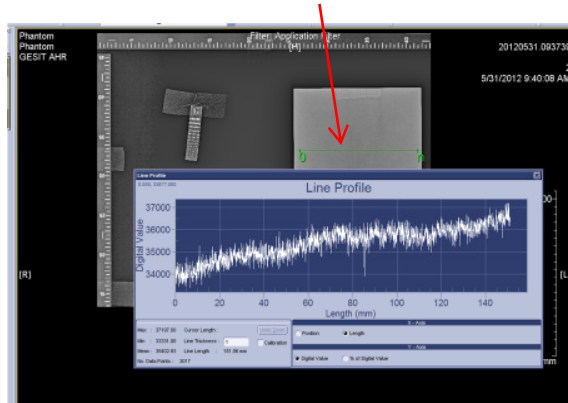


Figure 11

Ideally, but unfortunately not on the example here, the line would go over the entire 17 inch. One need to calculate how much the max. and the min. value are away from the center in%.

Example here: (the software plots the exact values at the mouse tip)

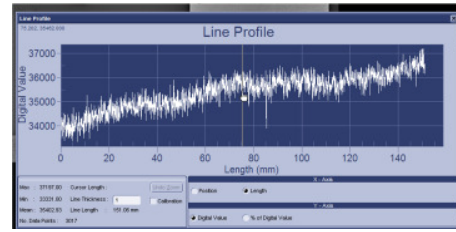


Figure 12

Grey value counts at Max. – Min. – and Center are:

Max.: 37197      Min.: 33331

Center: 35482

=>      max: 4.6%

min: 6.0%

**Slipping** refers to the transport direction of the scanner and would indicate, that a plate is not continuously transported, while the laser reads out the scan lines. In this case, slipping artifacts appear on the image. A way to evaluate slipping is to draw a line-profile on a homogenous material on the IP-Plate, such as a 1 mm AL strip. See Figure 13.

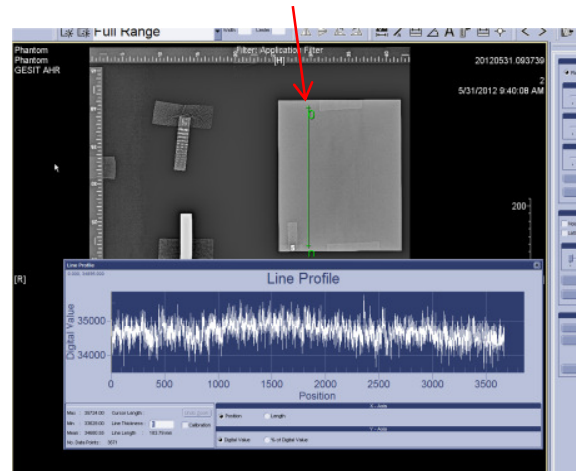


Figure 13

All values have to lie within a digital value that is not bigger than the noise of the profile. If scanner slippage appears, extreme outliers are showing digital values much lower than the noise.

### 2.2.4 Jitter

Jitter appears if the laser beam function is not working properly. As a result under- and overshoot of scan lines in transition areas



from dark to bright and vice versa, can be seen on the image. To monitor and evaluate Jitter, the T-Target on the Phantom or an equivalent high absorbing material can get used. Figure 14 shows a 10 times magnified area of the T-Target. No artifacts here along the edges, indicate a correct laser beam function.

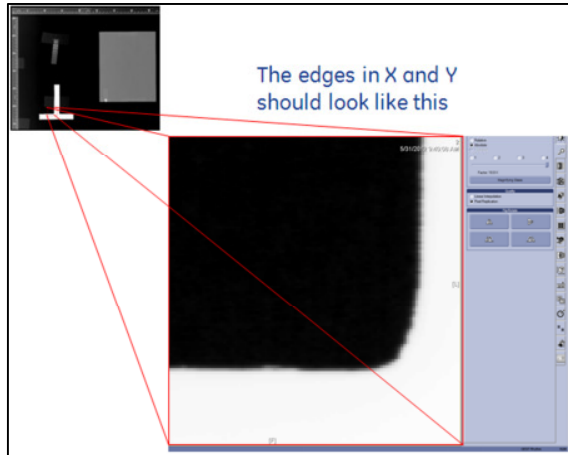


Figure 14

Figure 15 shows an artifact that would appear if Jitter is evident.

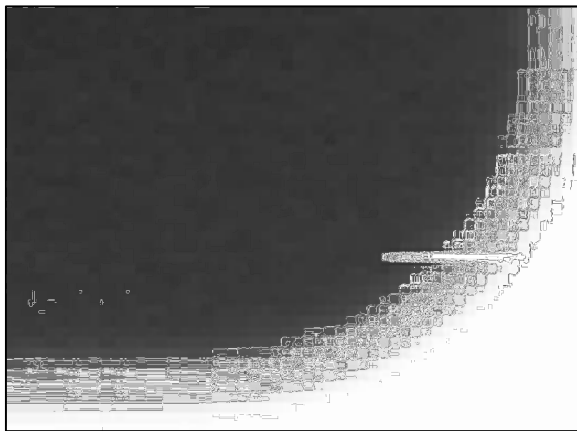


Figure 15

## 2.2.5 Afterglow

"Afterglow" can get seen as a speed limit. It corresponds to the luminescence decay time of the phosphor particles in the IP plates. If dwell time is too short, light from previous pixels is collected with current pixel  $\Rightarrow$  resolution loss and blurry images. Figure 16 shows the physical effect.

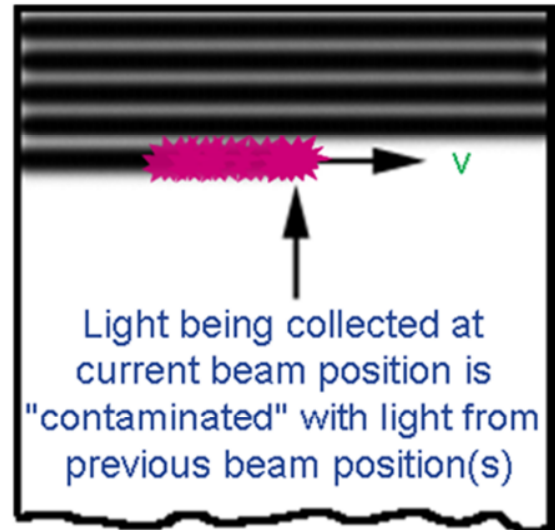


Figure 16

The T-target can get used to measure flare contribution to the image. Afterglow is a combination of fast scanning speeds with improper gain settings of the scanner. A non symmetric flare contribution can get measured with the line-profile function. Figure 17 shows the effect of Afterglow on the T-Target. The line-profile can get used to measure the contribution to flare in %. However the Standard does not give a limit to the flare contribution.

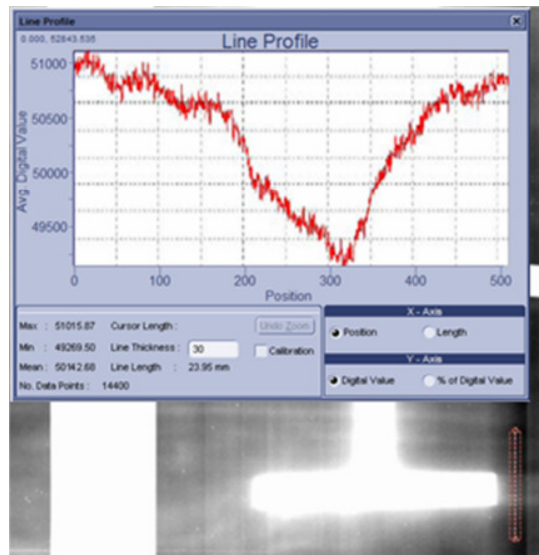


Figure 17

There is a difference of 1746.37 grey values between Max and Min count. in this sample. This is a 3.48% contribution to Flare .This test needs to get done with 2 exposures.

- Low gain – high exposure intensity
- High Gain – low exposure intensity.

### 2.2.6 Geometric distortion

The spatial linearity of the system has to be checked with high-absorbing rulers on the edge of the IP plate.

The evaluation software allows to calibrate a measurement. The measurement function is then used to validate the measurements in fast-scan and slow-scan direction. This test can also give an indication on the scanner-slippage.

Figure 18 shows the calibration and Figure 19 and 20 the verification of the result.

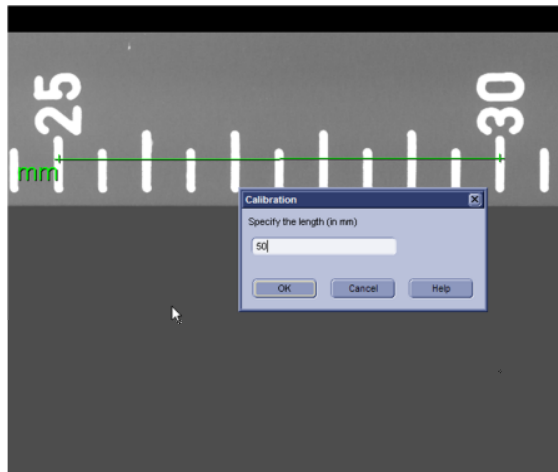


Figure 18

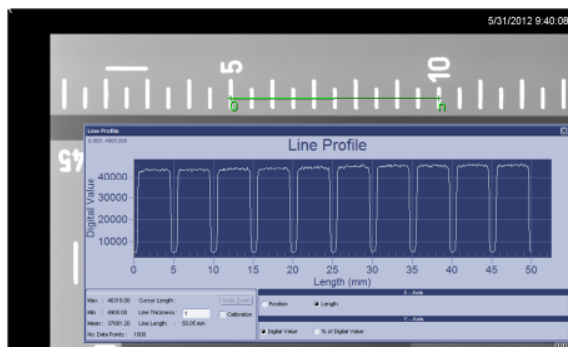


Figure 19



Figure 20

The line profile tool is used to verify the measured length in accordance to the numbers shown on the rulers. The standard allows for a 5% tolerance.

### 3. Remarks

The procedures explained and shown in this abstract require an exposure setup in accordance to the ASTM 2445 standard. The abstract makes the effort to show how the measurements and evaluations are done practically and in principle only. For the correct execution the respective standard and practice has to be used and is the only valid reference.

The software tools used here for the evaluation are the most basic functions possible, so the steps could get followed with other software systems. However for most complicated processes such as SRb and CNR, the Rhythm software suite provides automated functions to allow a quick and convenient evaluation result that is calculated automatically. While those functions are appreciated in daily routine, they are inheriting what is shown here in a step by step process.

### 4. Conclusion

Verification of system integrity is necessary on all CR scanner systems. The checks that need to get done are explained in the relevant standards. They describe the procedures as general as possible, to avoid catering to a specific system or solution.

This Paper made the effort to run through the periodic evaluation functions step by step on a specific example to visualize the idea behind the process and give a more practical approach on how to execute on the demanded system checks.

## 5. References

- [1] ASTM Designation: 2445-05  
Standard practice for Qualification and  
Long Term Stability of Computed Radiography  
Systems
- [2] MAI PCC-1 Guidelines document task 4  
Final 10-4-10  
Guidelines for the use of Digital Detector Arrays  
and Computed Radiology for Aerospace  
Castings

## **Phased Array Ultrasonic Inspection of Electrofusion and Butt Welded Joints in Plastic Pipes**

Fredrik HAGGLUND, Malcolm SPICER, Mike TROUGHTON and Tat-Hean GAN

TWI Ltd, Granta Park, Great Abington, CB21 6AL, Cambridge, UK;

Phone: +44 (0) 1223 899000, Fax +44 (0) 1223 890952;

### **Abstract**

Polyethylene (PE) pipes have been used for gas and water pipework for decades, and have also been incorporated into some non-safety piping systems in nuclear power stations. Due to the material being immune to water corrosion and highly resistant to fouling, it is considered to replace coated carbon steel in safety-critical applications in nuclear power stations. Although there are European standards for the volumetric inspection of plastic pipe welds there is a lack of commercially available Non-Destructive Testing (NDT) systems for inspecting these welds. There is best practise for the inspection of welds in large diameter steel pipes using ultrasonic testing. However, one of the main reasons why this is not implemented in the plastic pipe industry is because plastic is a difficult material to inspect due to its acoustic properties of high attenuation and low velocity. In this paper the progress of developing the inspection techniques for two types of pipe joints and different sizes is presented. The joints require several different techniques to fully cover the weld fusion zones. Detection results from the pipe samples and initial evaluation of the capability of the inspection techniques are presented.

**Keyword:** Phased array ultrasound, plastic pipe inspection, butt fusion, electrofusion, scanner,

## 1. Introduction

Plastic pipes offer significant advantages over other materials for pipework applications. However, their use is being restricted by the lack of reliable NDT method for volumetric inspection, especially for safety-critical applications in nuclear power stations [1]. Although there are European standards for the volumetric inspection of plastic pipe welds there is a lack of commercially available systems for inspecting these welds. The current best practise for inspection of welds in large diameter steel pipes uses ultrasonic testing. One of the main reasons why this is not implemented in the plastic pipe industry is because plastic is a difficult material to inspect due to its acoustic properties of high attenuation and low velocity.

Several studies have been conducted to develop reliable NDE methods for the two main types of joint in PE pipes, electrofusion (EF) and butt fusion (BF). These two joints require different inspection methods. In recent years, phased array ultrasonic technology (PAUT) has been considered to assess the integrity of EF joints [2]. However, these studies were limited to pipes with an outer diameter (OD) of 125mm and 250mm. BF joints have been examined with several different techniques using conventional ultrasonic transducers [3, 4]; including pulse-echo, tandem, creeping waves, and time-of-flight diffraction (TOFD). In recent years, work has been extended to also inspect BF joints using PAUT [5, 6].

There are commercial ultrasonic inspection systems for plastics pipes in North America and South Korea [7, 8]. The American system is limited to BF joints and uses conventional TOFD rather than phased array and is not applicable to more complex weld configurations such as elbows, reducers and tees. The Korean system is limited to EF joints and does not record data. TestPEP is a European funded project on the development and validation of an automated NDT approach for testing welded PE pipe joints. The project will develop phased array ultrasonic NDT procedures, techniques and equipment for the volumetric examination of welded joints in PE pipes of diameters from 90mm up to 1m. Initial work involved the determination of the ultrasonic properties of PE pipe material [10]. However, several additional tasks need to be solved before reaching the final system. A flexible scanner with probe holder incorporated must be adaptable for the wide range of pipe sizes and joint configurations of interest. Furthermore, a rugged instrument will be developed, capable of performing the advanced procedures required for these materials.

In this paper the progress in developing the inspection techniques and scanner system for EF and BF joints in different pipe sizes are presented. To assess the joints several individual ultrasonic techniques need to be applied to fully cover the weld fusion zones. A comprehensive development of the techniques has been undertaken, and the techniques have been evaluated on test samples. Detection results from the pipe samples and initial evaluation of the capability of the inspection techniques are presented.

## 2. Materials and Weld Configurations

The two main joint types investigated in this study have very little in common except that both have fusion zones between two PE materials. An EF joint comprises two pipe ends attached inside a coupler sleeve called a fitting, see Figure 1(a). The fitting has wires around the bore of the sleeve close to the inner surface. When a current is applied to the fitting the wires heat the surrounding pipe and fitting material and the fusion zone



is created. The BF joint, see Figure 1(b), is created by using a heating plate to melt the ends of two pipes which are then fused together by a pressure applied for a certain time. The process then creates a weld bead of the excess pipe material on both the inner and outer surface.

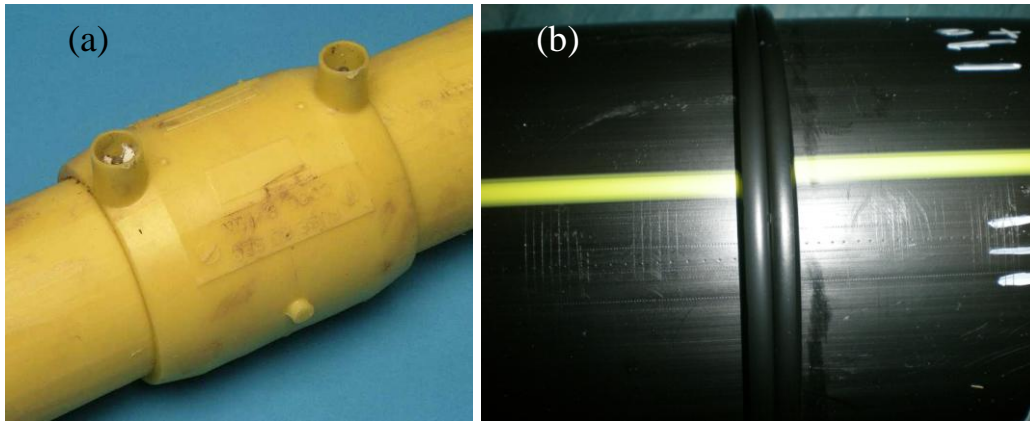


Figure 1. (a) An EF pipe joint. (b) A BF pipe joint with the outer surface weld bead.

In order to develop the PAUT technique for the EF joints initial inspection trials were carried out using unwelded fittings. It was proposed that if sufficient resolution was achieved in detecting the wires, the fusion zone located just below the wires could be inspected. When developing the inspection techniques for BF joints, test samples with artificial flaws were used, covering a range of pipe sizes between 180mm and 710mm OD. Flat bottom holes (FBHs) and slots were considered sufficient to evaluate the performance of the proposed techniques. The FBHs were used to evaluate the tandem and the sector pulse-echo techniques. The slots were used to evaluate the creeping wave and TOFD techniques. The FBHs were machined at the pipe ends and the slots were machined in the middle of the pipe. The arrangement of the FBHs and slots for 225mm OD pipes are shown in Figure 2.

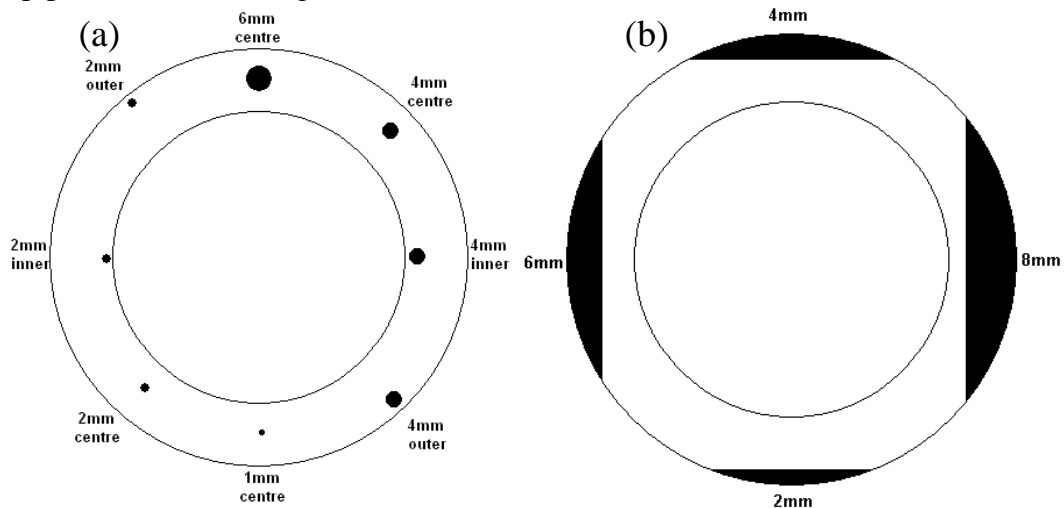


Figure 2. (a) Arrangement of FBHs in the pipe end. (b) Arrangement of slots in the pipe.

### 3. Development of Scanner System

For the evaluation of the inspection techniques 1D linear probes between 2-7MHz were evaluated. For EF joints, since no steering is required the pitch can be large without reducing the performance of the probe. In this paper 5 and 7MHz probes with 128 elements were used. For the inspections on BF joints 1D linear 4MHz probes with 32 elements were used. Angled beams are required to inspect BF joints and since the

steering capability is limited with these probes, angled wedges were used to minimize the steering by the transducer elements.

To perform the inspection on plastic pipes, novel open face water wedge prototypes have been designed and manufactured. The advantages of using a water wedge are low attenuation and a velocity ratio enabling the steering of angled beams to the fusion zone. The probes for EF joints required  $0^\circ$  wedges, and the probes for BF joints required angled wedges. The angle of the wedges was optimised to minimize the electronic steering by the transducer elements. The wedges with the probes are shown in Figure 3. The figure also shows the sealing skirt that is used to effectively keep the water in the probe wedge. The sealing material is flexible and the sealing skirt can be customised to specific shapes of the outer surface of EF fittings.

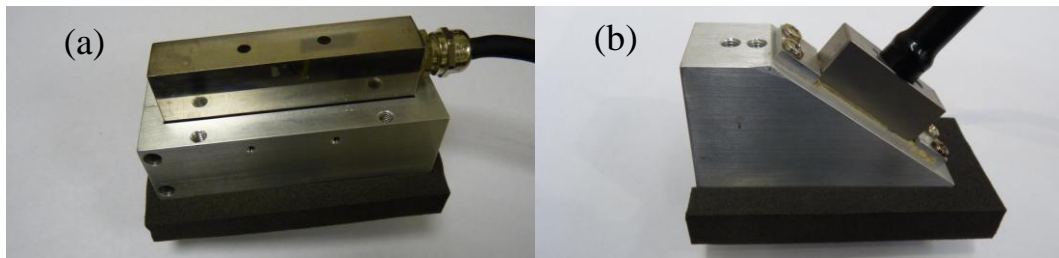


Figure 3. (a) The 0-degree water wedge. (b) The angled water wedge.

A scanner system has been designed that will be used for inspection of the welded pipes, see Figure 4. The scanner system comprises a main plate that is held in position around the pipe by several links and an adjustment mechanism. This flexible system should allow the scanner to inspect pipes with an OD from 90mm to 1m. The main plate contains the encoder and also the support for the probe holders. The two different joint configurations require different probe holders. In Figure 4(a) and 4(b) the probe holder for the EF joint and the two probe holders for the BF joint, respectively, are shown.

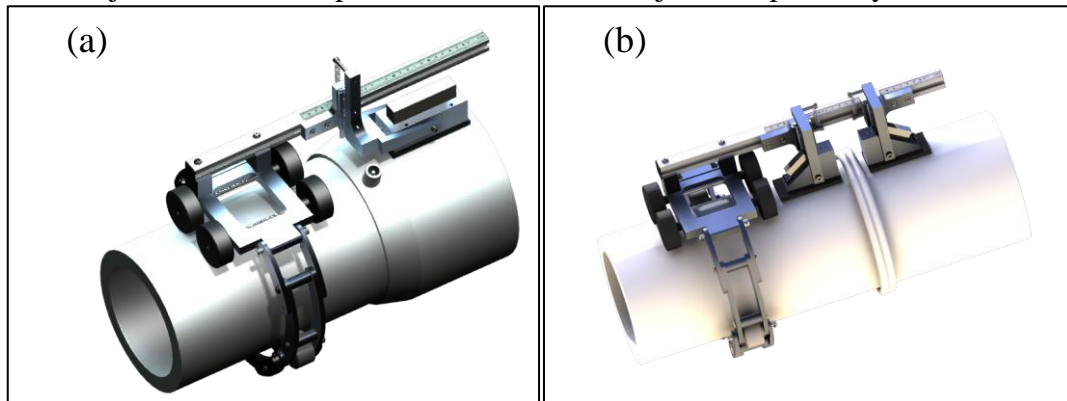


Figure 4. The flexible chain link scanner. (a) EF probe holder. (b) BF probe holder.

#### 4. Development of Inspection Techniques

The joints require different inspection techniques. The techniques used for both types of joints are shown in Figure 5 and are briefly described below.

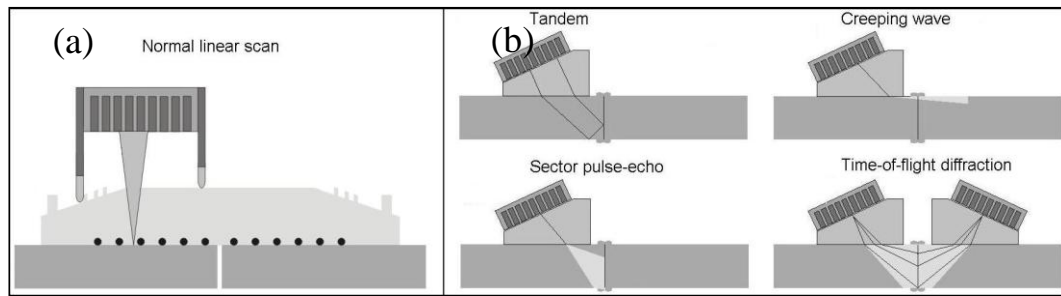


Figure 5. The developed inspection techniques. (a) EF joints. (b) BF joints.

#### 4.1 EF Joints

The inspection technique for EF joints is a normal linear scan, focusing on the fusion zone between the fitting and the pipe; see Figure 5(a). The most critical factors for the inspection of EF joints are the coverage and the resolution. The fusion zone is located below the wires and sufficient resolution for inspection between the wires is required. Generally, the resolution increases with increasing frequency. However, PE is a highly attenuating material and attenuation increases approximately with a power factor with frequency. Thus, the frequency needs to be low for larger pipes to be able to achieve sufficient propagation distance of the sound. In the larger fittings, the wire diameter and the wire spacing are also larger so the resolution is still sufficient. For smaller pipes both the wire diameter and spacing get smaller, and a probe with a higher frequency is required to be able to inspect the fusion zone.

#### 4.2 BF Joints

For the inspection of BF joints four different techniques were investigated; self-tandem; sector pulse-echo; creeping wave, and TOFD; Figure 5(b). The techniques are, in most cases, complimentary, both in terms of coverage and also types of defect to detect. The self-tandem technique uses one half of the phased array elements for transmitting and the other half for receiving. The technique is beneficial for detecting planar flaws, but the coverage area is restricted to an area closer to the inner surface.

The sector pulse-echo uses all the elements in the array to create an aperture, sweeping the beam from the lower angle to the higher angle. The technique gives an overview of the weld, and aims to cover most of the weld fusion zone, except for a few millimetres close to the outer surface.

The creeping wave technique aims to cover the region close to the outer surface, which is the part of the weld not covered by the first two techniques. The configuration for the creeping wave technique uses a high angle sector scan, producing compression waves propagating immediately under the inspection surface, to detect surface-breaking and near-surface defects.

The TOFD technique aims to cover the entire fusion zone. The technique utilises forward diffraction and is sensitive to vertical flaws. The configuration evaluated at this stage of the project is a pitch-catch technique using two sector scans. With this technique, both transducers use a large aperture to transmit beams covering the entire weld.

### 5. Results

The inspection results on the test specimens are presented. Firstly, results of the development of the technique for EF joints are shown followed by the results for the BF joints.

### 5.1 EF Results

Electronic sector scans on the EF fitting at one position around the fitting were evaluated. In the scans the top surface of the fitting is visible, along with the bottom surface with the wires located just above. Some parts of the bottom surface are masked by the wires as would be expected. Scans on a 180mm and a 710mm pipe fitting are shown in Figure 6. The electronic scans using the 7MHz probe on the 180mm fitting and the 5MHz probe on the 710mm fitting are shown. In the scans, the first replication of the top surface is shown just under the bottom surface of the fitting. In Figure 6(b), these reflections show the irregular outer surface of the 710mm fitting. This reflection can be avoided by changing the water path in the wedge.

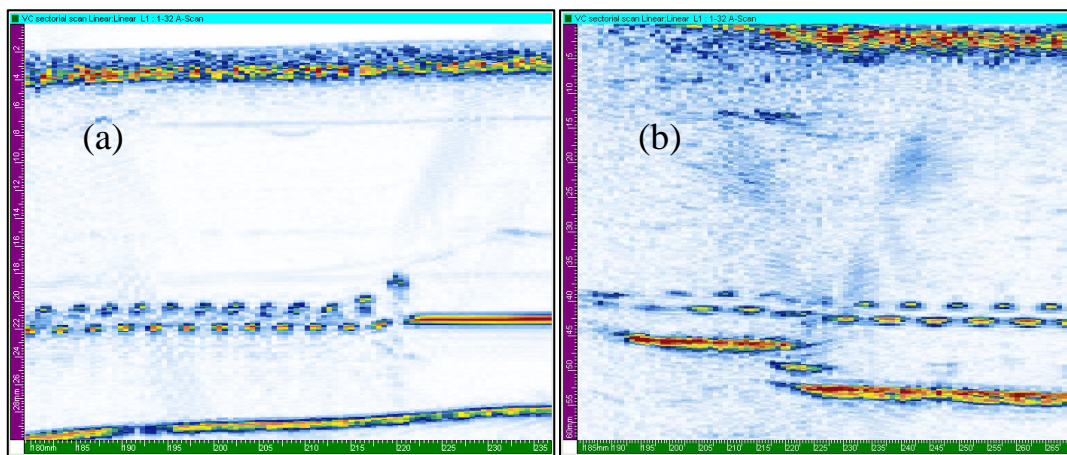


Figure 6. (a) Scanning result of a 180mm fitting. (b) Scanning result of a 710mm fitting.

Scanning results on a 180mm OD EF joint are shown in Figure 7. There are no reflections from under the wires and the fusion zone has been created. Above the wires, it is possible to see a line indicating the heat affected zone (HAZ) [2]. This can be seen clearer in Figure 7(b) where 12dB gain has been added. The position of this HAZ can be used to detect cold welds.

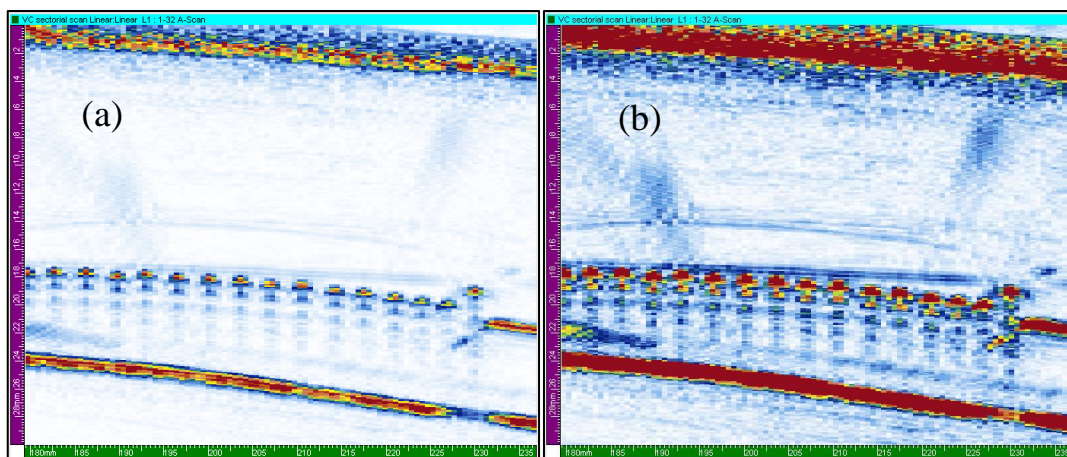


Figure 7. (a) Scanning result of a 180mm EF joint. (b) The same scan, but with +12dB gain.

### 5.2 BF Results



### 5.2.1 Single Position Inspection Results on a 225mm OD Pipe

The techniques for BF joints can be evaluated at individual positions around the pipe. In Figure 8 the sector pulse-echo and the tandem scans at the position with the 2mm FBH close to the inner surface are shown. In Figure 8(a), the sectorial scan at one position around the 225mm OD pipe using the 4MHz probe is shown, and in Figure 8(b) the tandem scan at the same position on the same pipe with the same probe is shown. Reflections from the 2mm FBH are achieved with both techniques.

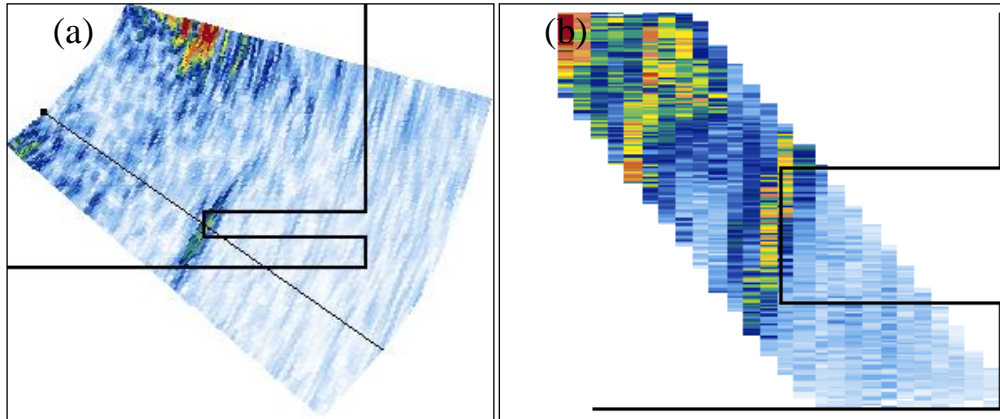


Figure 8. Results on the 225mm OD pipe. (a) Sector pulse-echo scan. (b) Tandem scan.

### 5.2.1 Circumferential Scans on a 225mm OD Pipe

To assess the inspection zone, circumferential scans were performed. Figure 9 and 10 presents data from scans on the 225mm OD pipe with FBHs and slots. In Figure 9 the results from the sector pulse-echo and the tandem techniques are presented. Figure 9(a) shows a schematic drawing of the FBHs location on the 225mm OD pipe. The bars to the left of the drawing show the theoretical coverage of the techniques (right shows sector pulse-echo and left shows tandem coverage). The lighter areas in the bars show the contributions of the beam spread.

In Figure 9(b) the B-scan side view of the sector pulse-echo scan using the 4MHz probe is shown. The axis on the left reveals at what depths the indications are found. Figure 9(c) shows the B-scan side view of the tandem scan on the same pipe using the same probe. The sector pulse-echo technique detected all the FBHs and the tandem technique detected 6/8.



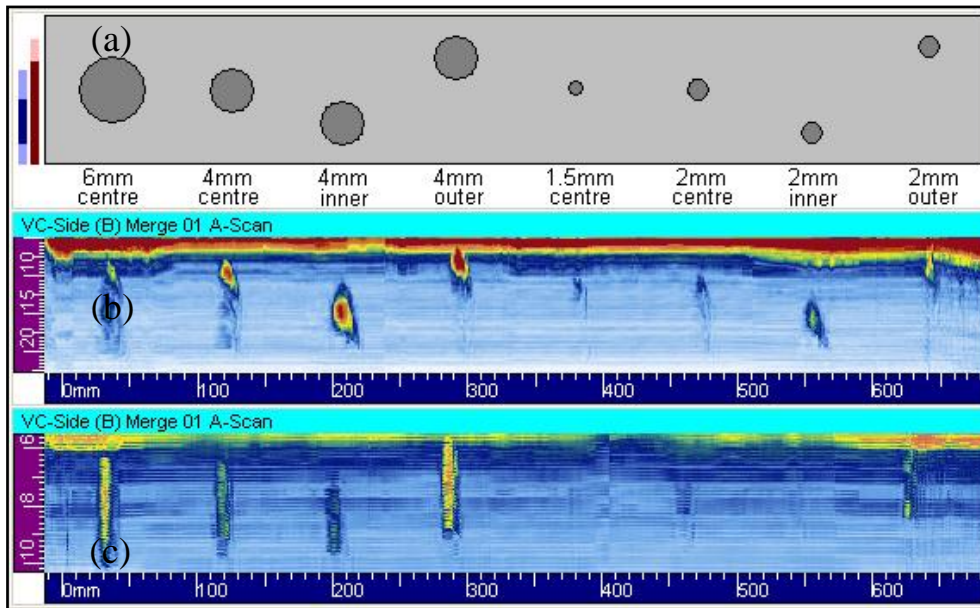


Figure 9. Inspection results on the 225mm OD pipe. (a) Location and size of the FBHs. (b) Sector pulse-echo scan. (c) Tandem scan.

In Figure 10 the results from the creeping wave and the TOFD techniques are presented. Figure 10(a) shows a schematic drawing of the slots location on the 225mm OD pipe. The bars show the theoretical coverage (right shows TOFD and left shows creeping wave). In Figure 10(b) the B-scan side view of the creeping wave scan using the 4MHz probe is shown. Figure 10(c) shows the B-scan side view of the TOFD scan on the same pipe using two identical 4MHz probes. Both techniques detected all of the slots.

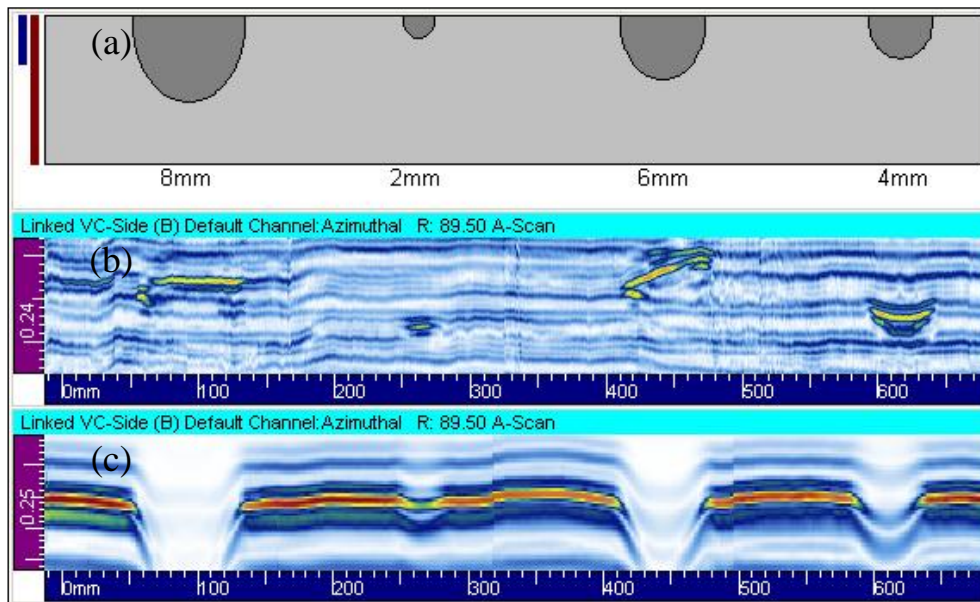


Figure 10. Inspection results on the 225mm OD pipe. (a) Location and size of the slots. (b) Creeping wave scan. (c) TOFD scan.

#### 6.2.2 Circumferential Scans on a 450mm OD Pipe

Figure 11 shows an image from a circumferential scan, using the sector pulse-echo technique with the 4MHz probe, around a 450mm OD pipe with FBHs. Figure 11(a) shows a schematic drawing of the pipe with 4 different diameters of FBHs; 8mm, 6mm, 4mm, and 2mm. The FBHs are also positioned at different depths in the pipe; three different depths for the two larger holes, and five different depths for the smaller holes.

The bar to the left of the drawing shows the theoretical coverage of the technique. In Figure 11(b), B-scan side view from the sector pulse-echo scan is shown with indications from most of the FBHs. When looking at the entire 1.4m scan, some FBHs are difficult to resolve, and closer views are required.

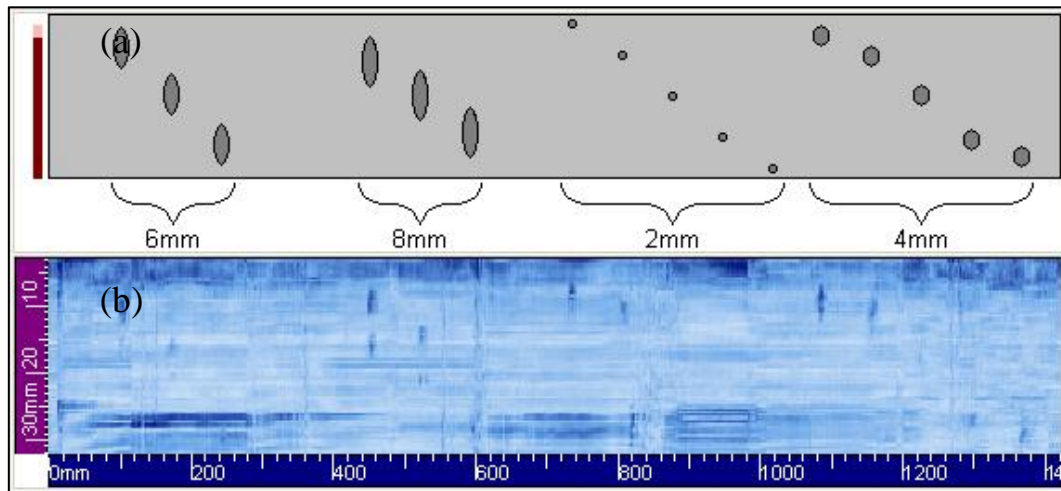


Figure 11. Inspection results on the 450mmOD pipe. (a) FBHs. (b) Sector pulse-echo scan.

Figure 12 show four closer views of the FBHs from the same scan. In Figure 12(a-c), the arrows show where all 8mm, 6mm and 4mm diameter FBHs are detected. Figure 12(d) shows that only two of the five 2mm FBHs are detected. The responses from some of the FBHs are weaker, mainly due to poor scanning results as can be seen in the image.

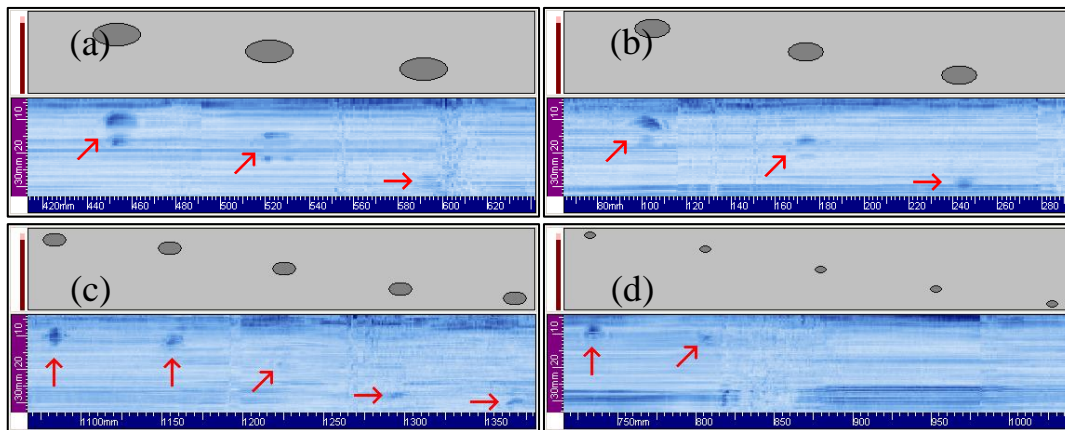


Figure 12. Drawings with the FBHs and inspection results on the 450mmOD pipe. (a) 8mm (b) 6mm (c) 4mm (d) 2mm

In the scans in Figure 11 and 12 it is possible to detect and also size the FBHs in the scan direction. In addition to this, the individual sectorial scans at each position for the FBHs can be used for an initial attempt to size and locate the FBHs in the depth direction. In Figure 13, the sectorial scans at the FBH closest to the outer surface of each size are shown. In all images, it can be seen that signals from the top and the bottom edge makes it possible to size the FBHs. The location and size for all detected FBHs are given in Table 1. In the images, the depth location is biased by 4mm from an error in the wedge delay. This bias has been removed in the table.

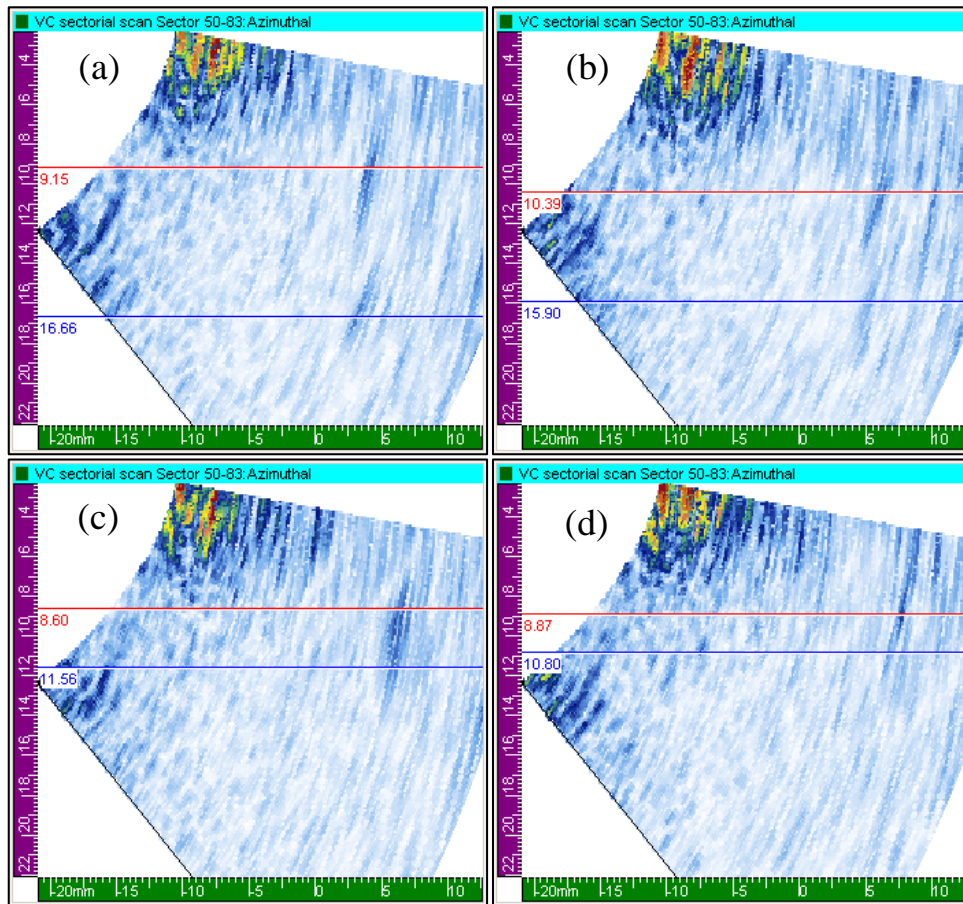


Figure 13. Sector scans at the circumferential positions of the FBHs close to the outer surface on the 450mm OD pipe. (a) 8mm (b) 6mm (c) 4mm (d) 2mm

**Table 1. The ultrasonically measured size and location of the FBHs in the 450mm OD pipe, using the sector pulse-echo technique**

Properties		Measured properties from scan		
Diameter of FBH [mm]	Depth location [mm]	Size		Location Depth [mm]
		Length [mm]	Depth [mm]	
8	8	9.28	7.51	8.91
8	14	8.25	7.10	14.07
8	20	6.19	8.95	21.20
6	6	8.25	5.51	9.15
6	14	5.16	5.24	14.79
6	22	5.15	2.96	24.61
4	4	6.19	2.96	6.08
4	7	4.12	3.45	8.39
4	14	2.06	2.41	13.32
4	21	5.16	3.03	20.70
4	24	3.12	2.20	25.88
2	2	5.15	1.93	5.84
2	7	2.06	2.00	7.18
2	14	Not detected		
2	21	Not detected		
2	26	Not detected		

## 6. Discussion

The developed PAUT techniques are part of a project aiming to be incorporated in a scanning system for on-site inspections, covering a range of PE grades and pipe sizes. Hence, performance on individual material and sizes could be optimised. Another part is to design and manufacture probes and wedges for specific joint configurations and pipe sizes. For the development work of optimising the inspection techniques, currently available probes have been used. In many cases these probes are not optimal for the specific inspection.

## 7. Conclusions

Techniques for inspection of both EF and BF joints have been developed. Initial evaluations of detection and sizing capabilities have been conducted. On the smaller BF size, all defects were detected except two FBHs with the tandem technique. However, all defects can be detected by at least one technique. On the larger BF size, the sector pulse-echo technique was evaluated. All defects except for the three 2mm FBHs closest to the inner surface were detected. These FBHs have a good chance to be detected by the tandem technique. It is also believed that when using the final optimised probes, the detection capabilities will improve.

## Acknowledgements

The research leading to these results has received funding from the European Union's Seventh Framework Programme managed by REA-Research Executive Agency [FP7/2007-2013] under grant agreement no [243791-2]. The information in this document is provided as is and no guarantee or warranty is given that the information is fit for any particular purpose. The user thereof uses the information as its sole risk and liability.

## References

1. ASME Boiler and Pressure Vessel Code Case N-755, "Use of Polyethylene (PE) Plastic Pipe. Section III, Division I, and Section XI".
2. D S Caravaca, C Bird and D Kleiner, "Ultrasonic Phased Array Inspection of Electrofusion Joints in Polyethylene Pipes", *Insight*, vol 49, no 2, February 2007.
3. M J Troughton, "Welding with integrated non-destructive examination of polyethylene pipes", *Plastics Pipes XI Conference*, Germany, September 2001.
4. I J Munns and G A Georgiou, "Ultrasonic and radiographic NDT of butt fusion welded polyethylene pipes", *Insight*, vol. 41, no. 5, May 1999.
5. C Frederick, D Zimmerman and A Porter, "High-density polyethylene piping butt-fusion joint examination using ultrasonic phased array", *PVP*, Czech Republic, July 2009.
6. S L Crawford, S E Cumblidge, S R Doctor, T E Hall and M T Anderson, "Preliminary assessment of NDE methods on inspection of HDPE butt fusion piping joints for lack of fusion", *PNNL*, May 2008.
7. B Messer, M Yarmuch and P den Boer, "Novel High Resolution Defect Detection for Thermoplastic Butt -Welds", *Pipeline and Gas Journal*, March 2003.
8. H J Shin, Y H Jang, J R Kwon and E J Lee, "Nondestructive Testing of Fusion Joints of Polyethylene Piping by Real Time Ultrasonic Imaging". *Plastics Pipes XII Conference*, Italy, April 2004.
9. L Mazeika, R Sliteris and A Vladisauskas, "Measurement of Velocity and Attenuation for Ultrasonic Longitudinal Waves in the Polyethylene Samples". *Ultragarsas*, vol. 65, No. 4, 2010.

## **Development of Full Matrix Capture Ultrasonic techniques for industrial application**

**Miles Weston, Channa Nageswaran, Michael Tan and Tat-Hean Gan**  
**TWI Ltd, Granta Park, Great Abington CB21 6AL, UK**

### **1. Introduction**

Calibration refers to setting an instrument's precision and/or accuracy against a known set of values. For ultrasonic inspections, calibration is used to accurately establish the quantitative measurements of the system within the media in which the sound propagates and achieves the required sensitivity to discontinuities in the inspection volume. The propagation of ultrasound from the transducer into the medium ahead (firstly within the wedge and then into the component through refraction) generates regions of differing acoustic pressure and sound field characteristics [1]. In order to accurately characterise flaws and achieve sizing, variations in the sound field characteristics must be compensated for by the inspection system before presenting the data for interpretation, i.e. the inspection must be calibrated to enable accurate measurements.

While calibration methods have been established in standards and codes for conventional ultrasonic inspections (i.e. using single-element transducers) [2,3] and for phased array inspections [4], techniques using full matrix capture (FMC) data have not yet been specifically supported by the main industry standards. The FMC data acquisition process is based on a sequential transmission, whereby only energy from a single element is present in the test structure at any moment in time. The technique was first introduced to NDT by Holmes et al [5], the reception pattern being all elements spanning the array, or a selection of elements in the case of half matrix or sparse array configurations.

A method to achieve uniform sensitivity to reflectors (i.e. flaws) of the same size and type within an inspection volume is essential for the inspection to be viable [6,7]. This paper describes a calibration method for use with a FMC data capture and imaging system to achieve uniform image sensitivity. Calibration was performed on FMC-imaged data generated using the sequential phased array (SPA) algorithm [8], which creates fully-focused images of the inspection volume in a test structure using a delay and sum beam forming approach. The output of this algorithm is a normalised image of the volume (presently 2D cross-sectional area) of interest in the component. The technique is based on identical imaging principles to that of the total focusing method (TFM) [5] and sampling phased array [9,10]. Algorithms and procedures to account for variations in sensitivity are presented and discussed, with calibration methods being verified experimentally on test-blocks containing artificial flaws, followed by the inspection of a double-V butt weld (common to many industrial structures and components) containing a range of representative flaws. In each case, SPA-imaged data were combined with the calibration map (generated as part of the calibration process) to produce a corrected image accounting for beam direction and distance into the material.

### **2. Calibration methods for FMC inspections**

Calibration methods applicable to data acquired through FMC were developed to utilise the established standard calibration blocks V1 and A5 [11]. To aid in this investigation, an experimental data acquisition and post-processing system was assembled, consisting of:

- i) a data acquisition system controlled by the Peak NDT MicroPulse 5PA 128/128 array controller. The system contained separate transmit and receive lines per channel and facilitated the use of parallel and sequential transmission techniques;
- ii) an Olympus 5L64-A2 transducer, containing a 64-element linear array with a pitch of 0.6 mm and a central frequency of 5 MHz. Data were sampled at a rate of 50 MHz with an 8-bit dynamic range;
- iii) a 36° Rexolite wedge optimally designed to generate shear waves in ferritic steel; and
- iv) a Windows desktop-based PC containing two Quadcore 3 GHz CPUs.



It should be observed that the calibration methods discussed refer to the calibration of the inspection to account for ultrasonic effects; there is an associated aspect of calibrating the electronics of the array controller that is normally undertaken by the manufacturer at fixed intervals, details of which are not discussed in this paper.

## 2.1 Theoretical background

When sound is emitted from a radiator of a given size, the acoustic pressure at differing points in the medium into which the sound is propagated will vary subject to several physical effects. The first of these is the ***divergence of the beam***, i.e. the extent to which the propagating wavefront area increases. Beam divergence is a function of the wavelength of the sound and the size (or aperture) of the transducer (the radiator) [1]. In general, the smaller the size of the radiator, the greater the angle of beam divergence; hence very small radiators (such as the elements of a linear array transducer) act as line sources, where the acoustic pressure decreases rapidly as the wavefront propagates away at high divergence angles. This effect implies that the energy in each of the waves that emanate from a single element of an array is small, but also that the energy is distributed over a much larger volume (due to the high divergence) and the pressure loss is predictably more uniform (i.e. the sound field is in the far-field of a transducer).

A second physical effect of sound propagating in a medium is the attenuation it experiences due to the losses induced by the medium. In general, the losses in the medium are attributed to two effects: ***scattering and absorption*** [1]. The scattering effect is due to the relative sizes of the propagating wavelength and the size of regions with differing elastic characteristics (i.e. grains). Scattering losses can lead to significant reductions in the received acoustic amplitude [12]. In low-carbon ferritic steel, scatter is predominantly caused by interactions with grain boundaries. However, by ensuring that the wavelength is much larger than the grain size, scattering losses can be reduced. The absorption effect is due to the conversion of the sound energy to heat through the resistance of the vibrating atoms of the material to the propagating wave.

A third physical effect to be considered is the ***reflection and transmission*** of the sound wave at the interface between two different media, i.e. as the sound propagates from the wedge into the component. This is not only affected by coupling variations, but also by surface roughness and the pressure at which the probe is held in contact with the medium. These factors must remain constant between the calibration piece and the test specimen to allow for repeatability and accuracy of results. When sound is incident at an interface at an oblique angle, a proportion of the energy is reflected (at the same incident angle), a proportion of the energy is transmitted (following Snell's Law) and, in addition, the wave may undergo mode conversion [1]. These effects are governed by the angle of incidence and the relative acoustic impedance's of the two media.

## 2.2 Attenuation and beam divergence in the wedge

For angled beam inspection, the path length travelled in the wedge will vary, depending on the position of the element in the array and the point of incidence at the interface. Since material attenuation and beam divergence are both dependent on path length, as discussed in Section 2.1, path length variations will impact on sensitivity. This can be accounted for by adjusting the gain for the signal from each element prior to the inspection to ensure a uniform signal response. The 100 mm radius on the V1 block was used to calculate the gain compensation for each element, as shown in **Figure 1**. Transmitting and receiving on the first element in the array only, the transducer was moved back and forth until the maximum signal response was found. The signal amplitude was then recorded and the procedure repeated for other elements in the array. For a given element in the array, the point of maximum amplitude will correspond to a sound path length in the test material of 100 mm and any variations in the maximum amplitude between elements is attributable to path length differences in the wedge. Comparing the time of flight in the wedge with signal amplitude, sensitivity variations resulting from wedge attenuation and beam divergence were compensated for using the gain.

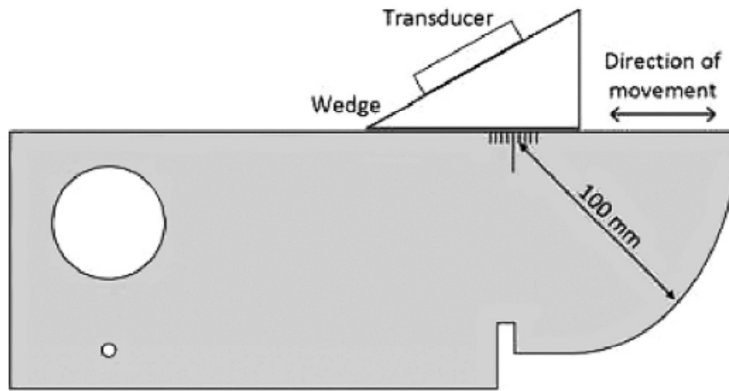


**Figure 1.** Transducer and Rexolite wedge set-up on V1 calibration block

**Figure 2** compares the signal response of four elements spaced throughout the array and illustrates the effects of attenuation and beam divergence in the Rexolite wedge. The results show that there was in fact very little difference in response from the four elements caused by changes in path length. This is likely to be due to the relatively small difference in path length (approximately 15 mm). Had a wedge with a larger wedge angle been used, where the path length difference between the bottom and top element's in the array would have been greater, the loss in sensitivity could have been more prominent. It can also be seen from **Figure 2** that some of the signals have two peaks of similar amplitude, which was caused by geometric reflections in the V1 calibration block.

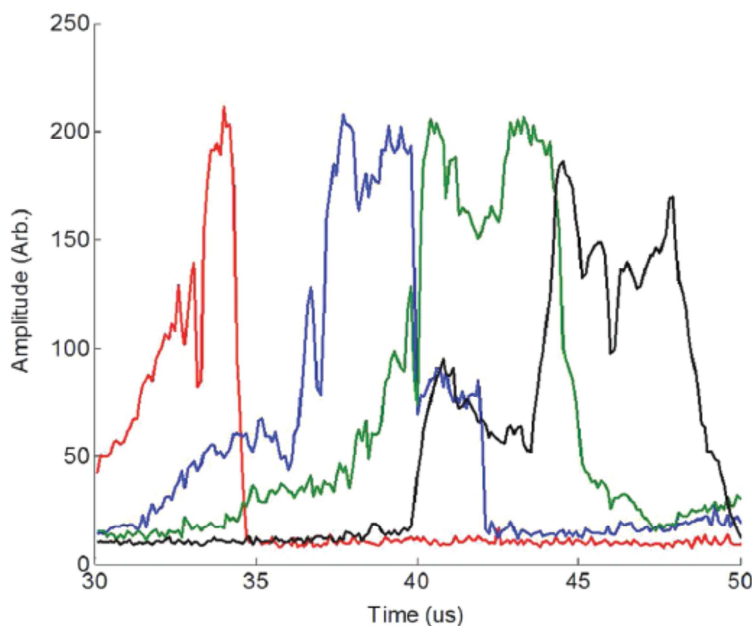


**Figure 2.** Effect of beam spread and attenuation in the Rexolite wedge for element 1 (red), element 22 (blue), element 43 (green) and element 64 (black) of the ultrasonic array. The path length in the Rexolite wedge for elements 1, 22, 43 and 64 were 8, 17, 26 and 35 mm, respectively

### 2.3 Attenuation and beam divergence in the component

To account for the effects of material attenuation and beam divergence in the component, the A5 calibration block was used, as shown in **Figure 3**. By transmitting and receiving on a single element in the array, the transducer was moved back and forth until the maximum signal response from a side-drilled hole (SDH) at a given depth was found. The procedure was then repeated for several SDHs at varying depths. Then, by comparing the path length with the signal amplitude, the total attenuation due to the material and beam divergence was established.

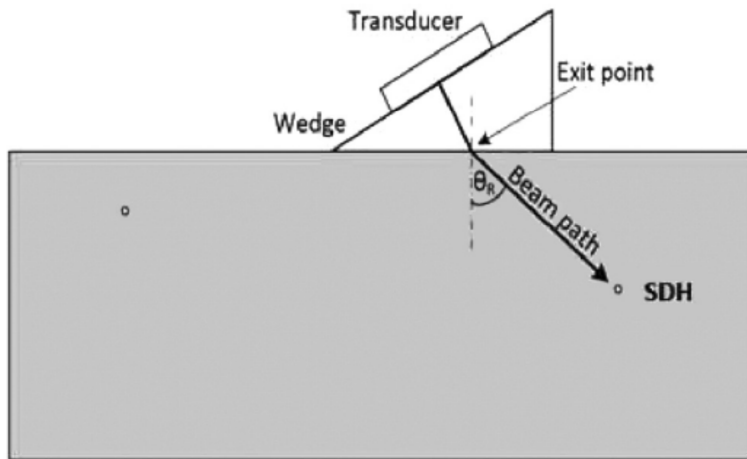


**Figure 3.** Illustration of the transducer on the A5 calibration block to evaluate beam directivity using the SDH at a depth of 25 mm, where R is the refracted beam angle

## 2.4 Transducer element beam directivity

The linear array transducer used in this paper had an element size of approximately half the wavelength of the emitted sound wave (along the active direction), leading to a widely diverging wavefront, implying that the received signal amplitude will be dependent on both the transmitted and received beam angles.

The directivity, i.e. the dependence of signal amplitude on beam angle, can be accounted for using the SDH at a depth of 25 mm in the A5 calibration block, as shown in **Figure 3**. Firstly, compensation for changes in signal amplitude due to the total attenuation in the wedge and component was applied, such that the only variable to affect signal strength was the beam divergence. Next, FMC data was continuously acquired (using all the elements on the array), processed and imaged while the transducer was moved back and forth on the A5 calibration block. Thus, the position of the SDH was tracked relative to the exit point for a given element. Concurrently, the A-scan information for the same element was used to monitor the signal amplitude from the SDH target and hence the directivity pattern of the beam emanating from the element was determined.

The relationship between the directivity and angle of refraction into the component, shown in **Figure 4**, was found experimentally. **Figure 4(a)** shows the maximum beam strength to be at an angle of refraction of approximately  $48^\circ$ . However, this plot does not consider the effects of beam divergence and attenuation, which would bias the result due to the path length differences that will occur as the transducer is moved back and forth. **Figure 4(b)** shows the maximum beam strength to be at a refraction angle of approximately  $56^\circ$  after compensating for the effects of attenuation and beam divergence. Hence, there is a difference in beam angle of  $8^\circ$  taking into account all the physical effects, illustrating the importance of compensating for attenuation and divergence.

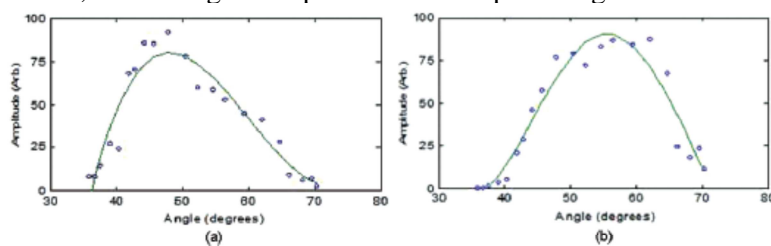


**Figure 4.** Plot of directivity (a) without compensation and (b) with compensation for attenuation and beam divergence; both plots were generated for the same element

Note that to be able to accurately calibrate data using FMC, the beam divergence of each element in the array must be determined, whereas in parallel transmission techniques, which transmit and receive using an aperture containing several elements (i.e. phased array), only a single average beam divergence for the aperture needs to be determined.

## 2.5 Implementation of calibration methods

Methods to determine variations in signal strength due to the characteristics of the ultrasonic transducer and material properties of the test structure have been discussed. Such variations in signal strength were mapped onto a 2D grid known as a correction map. This correction map contained the same number of pixels as cross-sectional images generated using the SPA reconstruction algorithm. The correction map contains the summed contribution of all transducer and material properties that affect signal strength. Multiplying the pixel values in the generated cross-sectional images by the corresponding cells in the correction map allowed variations in signal amplitude to be accounted for and a uniform image sensitivity to be achieved (as expressed in **Figure 5**).

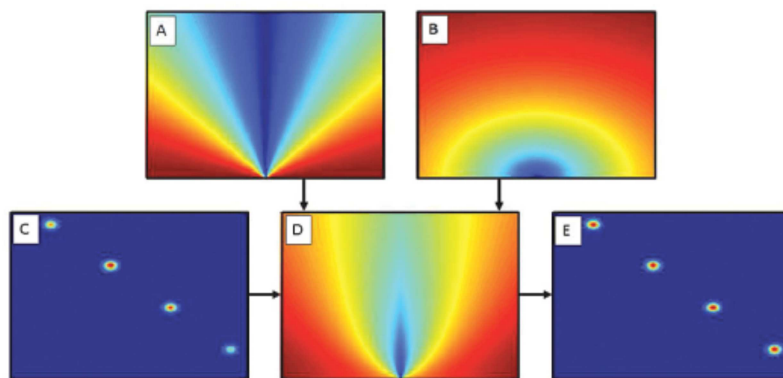


**Figure 5. Plot of calibration maps: (a) accounting for angle; (b) accounting for distance; and (d) the summation of calibration maps (a) and (b). The calibration map (d) is added to the input image (c) to produce the final corrected image (e)**

## 3. Validation of calibration techniques

The methods to calibrate the sensitivity of an FMC inspection system described in Section 2 were verified experimentally on test-blocks containing artificial flaws, followed by the inspection of a double-V butt weld (common to many industrial structures and components) containing a range of representative flaws.

A ferritic steel block containing a series of equally-spaced (10 mm), vertically-aligned 3 mm SDHs was used to evaluate the difference between using an uncalibrated and a calibrated system. The transducer and wedge described in Section 2 were used with stand-off distances set up for inspection of the double-V butt weld. The wedge angle was designed for shear wave inspections in ferritic components and so the set-up allowed the vertical SDHs to be viewed within the optimal 40-70° beam angle range.

In addition to the visual imaging of the signal amplitudes from the SDHs, quantitative analysis was performed using the relative amplitude parameter, which is the normalisation of the peak response from each SDH against the peak response over the whole image, as given in Equation (1):

$$\text{Relative Amplitude} = \frac{\text{max. amplitude SDH}}{\text{max. amplitude image}} \dots\dots\dots(1)$$

**Figure 6** shows the image of five vertically-aligned SDHs in the validation block, generated using uncalibrated and calibrated inspection systems. The imaged SDHs ranged in depth from 20 to 60 mm, corresponding to a beam angle range of 40-70° relative to the normal (see **Figure 3**). In the

uncalibrated image of Figure 6(a) the peak response in the image is from the SDH at 59°. The signal response then decays with increasing depth, with the weakest response coming from the SDH located at 40°. The analysis using the relative amplitude parameter is summarised in Table 1, which corresponds to the image shown in **Figure 6(a)**.

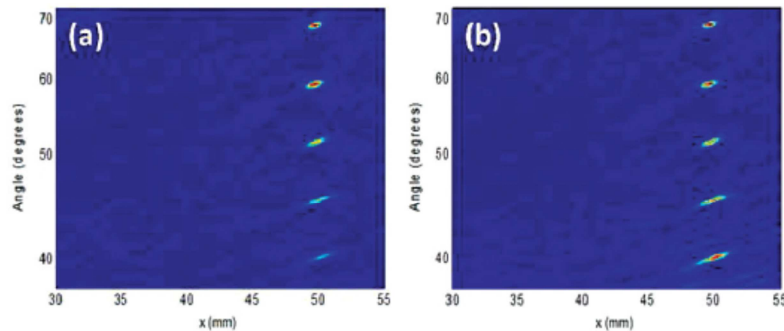


**Figure 6. Images showing five vertically-aligned SDHs using (a) uncalibrated and (b) calibrated systems**

The calibrated image in **Figure 6(b)** shows a more uniform signal response between SDHs and therefore an improved uniformity in sensitivity compared to the uncalibrated image. This is shown quantitatively using the relative amplitude parameter in Table 1, where the maximum deviation in signal amplitude was 1.5 dB.

**Table 1. Quantitative analysis of the images shown in Figure 6 using the relative amplitude parameter (Equation 1)**

Depth (mm)	Angle (°)	Uncalibrated relative amplitude (dB)	Calibrated relative amplitude (dB)
20	68.2	-0.3	0
30	59	0	-0.2
40	51.3	-2.7	-1.5
50	45	-5.5	-1.2
60	39.8	-8.4	-0.5

While a calibrated system improved the uniformity in response, this was at the cost of an increase in noise, which can be seen when comparing the plots in Figure 6. In the present case, the increase in noise did not interfere with the effective analysis of the inspection data. Incoherent noise could be reduced through the use of frequency filters, averaging over a number of A-scans or increasing the size of the array; coherent noise could be reduced by increasing the angular range with which the inspection volume is interrogated.

### 3.1 Inspection of a double-V butt-welded plate

The calibrated system was used to inspect a 25 mm-thick double-V butt weld with known flaws: lack of root penetration (LORP), porosity and toe cracking. **Figure 7** shows images of the flaws contained within the weld using both the uncalibrated and calibrated systems. In all images the reference amplitude was the response from the 3 mm SDH in the validation block at a depth of 30 mm. The amplitude range (represented in colour) used for imaging was from 6 to -25 dB, with 0 dB corresponding to the signal amplitude from the reference target.



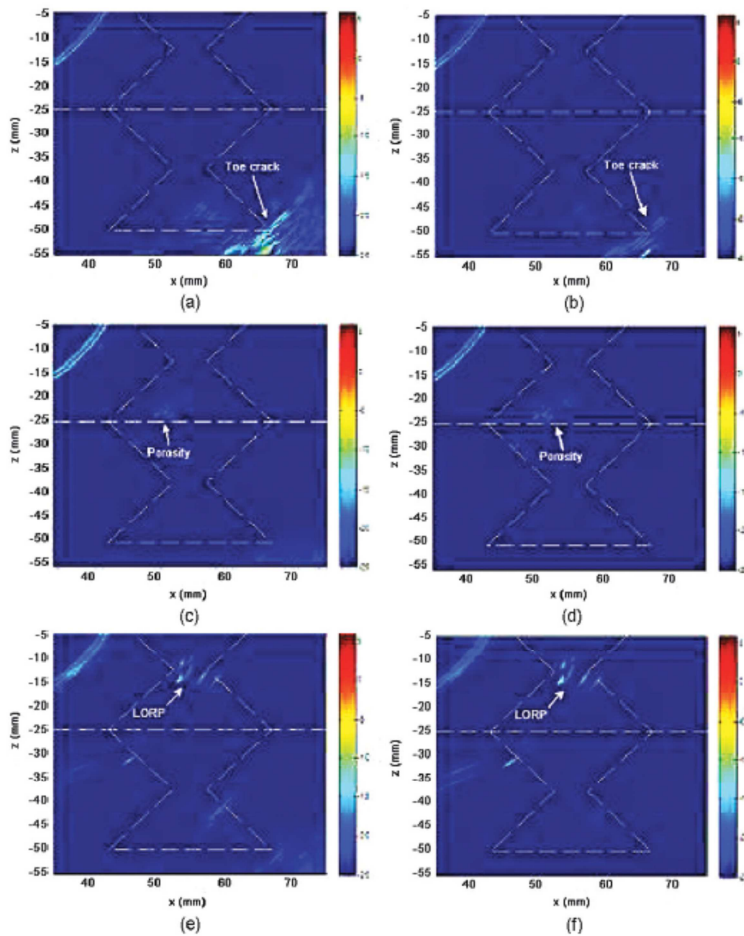


**Figure 7. Inspection data showing calibrated images of toe crack (a), porosity (b) and LORP (c); and data showing uncalibrated images of toe crack (d), porosity (e) and LORP (f)**

The inspection set-up was such that the position of this reference target was at the centre of the imaging volume, which corresponded to the weld body in direct incidence and skipped incidence, ie the beam was incident after reflecting at the backwall. A weld overlay was applied to the images shown in Figure 7, where the dashed horizontal line represents the backwall of the image and any indication above this was in direct incidence and below in skipped incidence.

**Table 2** shows an analysis of the flaw signals, uncalibrated and calibrated. The toe crack signal was  $-11.2$  dB when uncalibrated but was stronger at  $-3.2$  dB when calibrated. The significance of this difference is that it impacts on how operators would classify such flaws during site inspections: the degree of change in the imaged amplitude could make the difference between the flaw being deemed a defect requiring a repair or allowed to exist under monitoring.

**Table 2. Summary of the image amplitudes shown in Figure 7 for the flaws in the butt weld**

Flaw type	Uncalibrated relative amplitude (dB)	Calibrated relative amplitude (dB)
Toe crack	$-3.2$	$-11.2$
Porosity	$-12.8$	$-12.5$
LORP	$-6.6$	$-7.2$

The changes in imaging amplitudes for the porosity and LORP between uncalibrated and calibrated inspections were within 1 dB. This is because they are both in the inspection volume close to the point where the reference amplitude was set, hence the correction was not significant. During inspection the imaged amplitude range should be tailored according to the acceptance criteria for the component being inspected, along with thresholds generated using sufficient qualification evidence.

#### 4. Conclusions

The following conclusions are drawn from the work presented in this paper:

- i) Inspections using full matrix capture (FMC) data can be effectively calibrated for industrial applications.
- ii) The factors that affect the sensitivity of FMC are related to material and transducer properties, including attenuation, beam divergence and element directivity.
- iii) The inspection of SDHs in Section 3 showed that the calibration method described in this paper significantly improved the achievable uniformity in image sensitivity. Quantitative analysis showed that a maximum deviation of 1.5 dB was achieved using the calibration method for this inspection scenario.
- iv) Inspection of a typical butt weld of a plate showed that differences in sensitivity between calibrated and uncalibrated inspections for a critical flaw type could be greater than 6 dB.

#### Acknowledgements

The authors wish to acknowledge TWI Ltd, the University of Manchester and the University of Birmingham for their facilities and technical support, and the Engineering and Physical Sciences Research Council (EPSRC) for funding the studentship at TWI Ltd, the University of Manchester and the University of Birmingham.

#### References

1. J Krautkramer and H Krautkramer, *Ultrasonic Testing of Materials*, New York, Springer-Verlag, 1990. ISBN: 0 387 51231 4.
2. BS EN 12668-3: Non-destructive testing. Characterization and verification of ultrasonic examination equipment. Combined equipment.
3. BS EN 583-2: Non-destructive testing. Ultrasonic examination. Sensitivity and range setting.
4. ASME E2491: Standard guide for evaluating performance characteristics of phased array ultrasonic examination instruments and systems.
5. C Holmes, B W Drinkwater and P D Wilcox, 'Post-processing of the full matrix of ultrasonic transmit-receive array data for non-destructive evaluation', *NDT&E International*, Vol 38, No 8, pp 701-711, December 2005.
6. J Zhang, B W Drinkwater and P D Wilcox, 'Effects of array transducer inconsistencies on total focusing method imaging performance', *NDT&E International*, Vol 44, No 4, pp 361-388, July 2011.
7. D Duxbury, J Russell and M Lowe, 'Designing a calibrated full matrix capture-based inspection', *Proc AIP Conf*, Vol 1335, pp 851-858, June 2011.
8. M Weston, P Mudge, C Davis and A Peyton, 'Time-efficient auto-focusing algorithms for ultrasonic inspection of dual-layered media using full matrix capture', *NDT&E International*, Vol 47, pp 43-50, April 2012.
9. N Portzgen, D Gisolf and G Blacquiere, 'Inverse wave field extrapolation: a different NDI approach to imaging defects', *IEEE Transactions on Ultrasonics, Ferroelectrics, and Frequency Control*, Vol 54, No 1, pp 118-127, January 2007.
10. J Verkooijen and A Boulavinov, 'Sampling phased array: a new technique for ultrasonic signal processing and imaging', *Insight – Non-Destructive Testing and Condition Monitoring*, Vol 50, No 3, pp 153-157, March 2008.
11. BS 2704: 1978 – Specification for calibration blocks for use in ultrasonic flaw detection. (Superseded).
12. E P Papadakis, 'Revised grain-scattering formulas and tables', *J Acoust Soc Am*, Vol 37, pp 703-710, 1965.

# **Advanced Ultrasonic Phased Array Technology Used in Industrial Applications**

Stanislav STARMAN and Vaclav MATZ

STARMANS electronics s.r.o.  
V Zahradach 24/836, Prague 8, 180 00  
Tel: +420 283 842 063, Fax: +420 283 841 067  
E-mail: nano@starmans.net, Www: www.starmans.net  
Czech Republic, European Union

## **Abstract**

Over the past few years, all improvements in the field of ultrasonic non-destructive testing have led to significant advances in ultrasonic signal processing and image construction techniques. The main focus in non-destructive testing area is to improve the resolution of defect detection and make the detection process as fast and accurate as possible. Many techniques have been proposed and implemented to improve the flaw and crack detection processes. In general, these techniques can be divided into two main parts. As first, many proposals consider the construction of ultrasonic transducers and systems. The second part is mainly focused on proposal of efficient signal processing algorithms that improve sensitivity (noise reduction) during ultrasonic signal acquisition. This paper presents our fully developed ultrasonic portable system with implemented phased array technology. All acquired ultrasonic signals are consequently processed using our proposed filtering algorithms.

**Keywords:** Ultrasonic testing, phased array, signal processing

## **1. Introduction**

Ultrasonic non-destructive testing (UT) is commonly used for flaw detection in materials. Ultrasound uses the transmission of high-frequency sound waves in a material to detect a discontinuity or to locate changes in material properties (1). Ultrasonic wave propagation in tested materials is essentially influenced by the tested material structure. In general, due to material structure the acquired ultrasonic signal can be corrupted with relatively high noise level, commonly called backscattering noise (2). In present, the most desired task is to detect the fault echo in ultrasonic signal; it means to locate the subsurface cracks or defects in materials. The noise level mainly influences the flaw detection efficiency and on this account the efficient signal processing techniques used for noise reduction have to be proposed. As all acquired signals are processed with our implemented signal processing methods than all signals are reconstructed to create flaw visualization using phased array technology.

## **2. Ultrasonic portable system with implemented phased array technology**

During the last three years, we have been developing a completely new ultrasonic non-destructive testing portable instrument. The main goal was to develop the highly robustness ultrasonic portable instrument including conventional ultrasonic testing (1), EMAT testing (3) and testing based on phased array ultrasonic technology (4). All these non-destructive methods were successfully implemented into one device called "DEFECTOBOOK DIO1000". Except implemented ultrasonic non-destructive testing methods we were also focused on proposal of efficient signal processing algorithms that contribute for flaw detection and efficiently suppress noise. Conventional ultrasonic testing and EMAT testing have been already implemented in DIO2000 system four years ago. The main objective of our development was to have the best phased array instrument with on-line measurement and visualization of material bulk. Our phased array technology is based on transmitting of ultrasonic waves from all elements simultaneously and consequently receiving of all reflected

signals back to phased array transducer. For our experiments we use commercial phased array transducer including 16 up to 64 elements.

All mentioned non-destructive testing methods were implemented based on previous research. First of all, we have implemented conventional ultrasonic method and EMAT testing method. As all acquired ultrasonic signals are corrupted with relatively higher noise level, methods used for effective noise reduction were searched. During the research we have tested many algorithms used for noise reduction but the main goal was to find efficient noise reduction and simple methods that could be easily implemented as algorithm processing the signals in real time. This goal was successfully achieved and averaging, digital filters and correlation methods were implemented into DIO1000 signal processor.

### 3. Signal processing algorithms – Averaging and Digital filters

#### 3.1 Averaging

Averaging (2) the ultrasonic signal is a common method of enhancing the signal-to-noise (S/N) ratio. This method slows down data acquisition, because the pulse repetition rate of ultrasonic instruments is orders of magnitudes slower than the processing time needed to perform averaging. In general, many (e.g. 64) signals are acquired and these are averaged over all signals. The main advantage of averaging is that this method is relatively easier to implement. On the other hand, the main disadvantage is that number of acquired signals and consequent averaging of these signals essentially makes the processing time much higher. But, of course with used digital signal processor it can be used for real time application. On the following Figure 1, there can be seen the example of using averaging by 64 acquired signals. The acquired signal (see Figure 1a) is corrupted with relatively higher effective noise level amplitude. By using averaging (see Figure 1b) of 64 signals, both flaw echo and back-wall echo are easily visible.

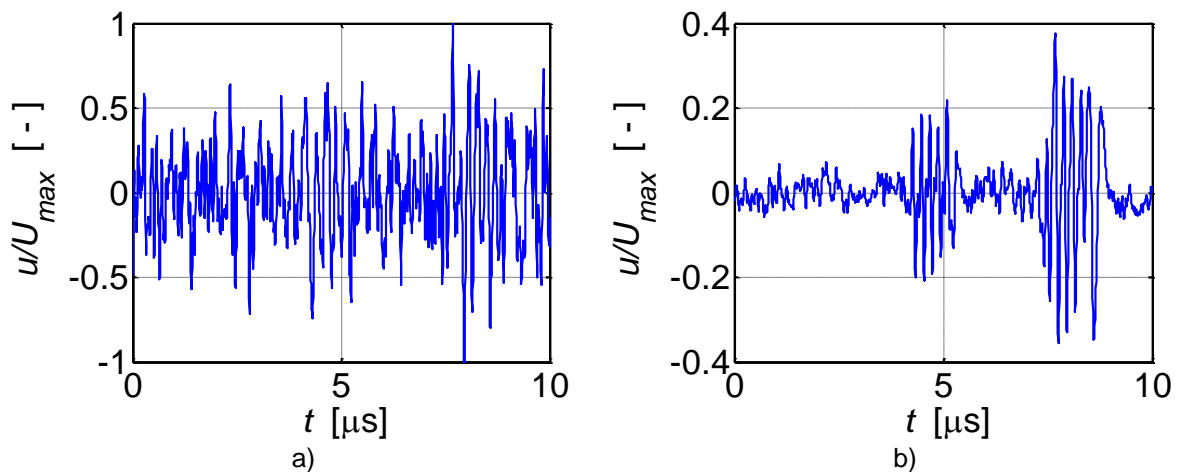


Figure 1. Example of averaging: a) acquired ultrasonic signal – flaw 2 mm, b) averaged signal by 64× signals

#### 3.2 Digital filter – Finite Impulse Response (FIR) filter

Zero-phase digital filtering (2) can be realized using non-casual filtering method. This method is based on processing the input data in both the forward and reverse directions. After filtering in the forward direction, the filtered sequence is reversed and fed back through the filter. The resulting sequence has precisely zero-phase distortion and double the original filter order.

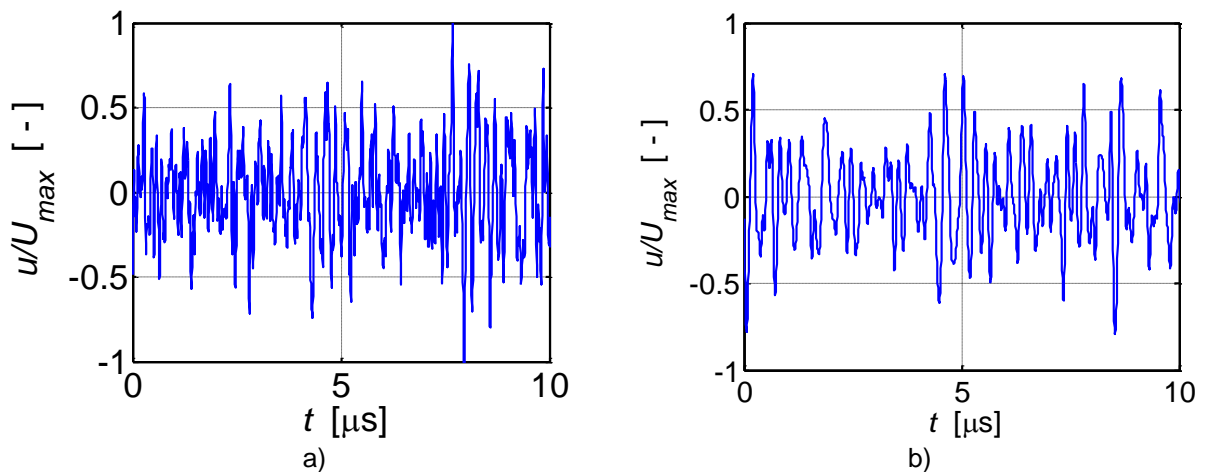


Figure 2. Application of FIR: a) acquired ultrasonic signal – flaw 2 mm, b) filtered signal

As can be seen in previous Figure 2, noise was successfully suppressed. The main objective is to detect the flaw. This as well as a frequency band of proposed filter depends used ultrasonic transducer. In the previous Figure2 we used the ultrasonic transducer with central frequency 4 MHz. The proposed and implemented anti-causal filter has bandwidth 4MHz.

#### 4. Phased Array technology

Next step was to implement the advanced ultrasonic phased array technique (5) and visualize the internal bulk of material in detail. Phased array holds the promise of being able to efficiently detect all significant flaws by combining many angles and focus depths into one probe and image the resulting reflections in an understandable way. Flaw acceptance still requires the comparison of flaw reflections represented as an A-scan with the A-scan of a known artificial reflector such as a side-drilled or flat-bottomed hole. The use of special signal processing and image reconstruction algorithms allows generating A-scans of several angles and/or sector-scans, which can be implemented in real time. With parallel computing structures, this principle is used for automatic testing systems at very high inspection speed.

Over the past few years, many companies have introduced systems making use of phased array technology. Phased array training courses for operators usually address general principles and only few examples of real applications. One of the major difficulties often omitted during training and in practice is the actual coverage of phased arrays. It is easy to say that a sector scan will detect all defects in a material as it passes through a large range of probe angles. Although a high probability of detection can be achieved – certainly a lot higher than manual UT – it is by no means guaranteed that all defects will be detected. The resolution in terms of the step width between angles and the focus depth range are of major importance to detect defects and discriminate between adjacent flaws. The angle at which an ultrasonic reflector is detected is not only dependent upon the angle of incidence of the transducer array, but is also dependent upon the position of the transducer relative to the weld axis. When these parameters are not adequately addressed, these factors can seriously affect the degree of success of phased array inspection.

As we mentioned before, the first implemented phased array technology is based in synchronous transmitting of signals from all elements followed by receiving of reflected signals, we are working on improvements. These improvements are based on transmitting of each element independently with some delay based on focused point. Other elements transmit ultrasonic signals with derived delay. The following drawing represents our calculation of



time delay of each element. We suppose, the transducer is located on the tested material and each element is transmitting signal with derived delay. The following Figure 3 shows the curve of time delay based on each element location deviated from central position of phased array transducer (see central axis in Figure 3).

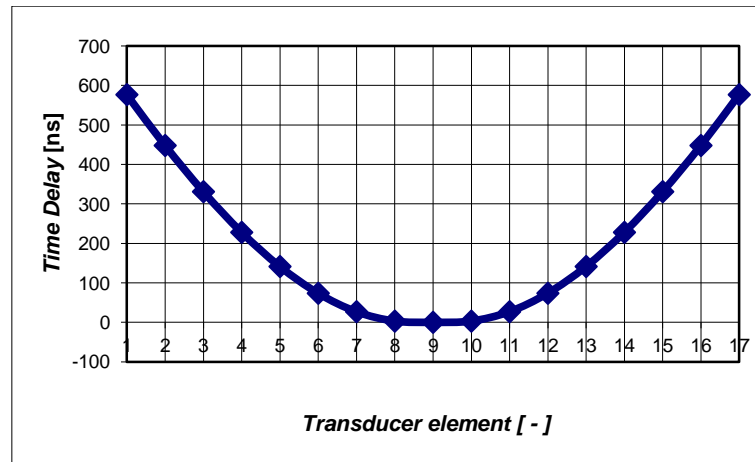


Figure 3. Time delay of transmitted signals

As can be seen in Figure 3, the transmitting of all elements has semicircle curve shape. By calculated time delay we are able to receive signals with unique information about flaw location during manual testing. Our analysis supposes there is circled flaw in the center of the material under the phased array transducer.

The mentioned idea was implemented into our designed ultrasonic system, called DEFECTOBOOK DIO1000. The following picture represents our full-developed ultrasonic system with implemented phased array technology.



Figure 4. Constructed system DIO1000, phased array – calibration gauge

As can be seen in Figure 4., we have successfully constructed ultrasonic phased array instrument with implemented advanced signal processing algorithms. Using this system and phased array technique, we are able to easily detect flaws within the range of scanned angles. To verify the proposed system and properly configure all parameters we also constructed calibration gauge with defined flaws (see Figure 4.). When we passed all tests and initial experiments we were able to see the flaws on calibration gauge. Using the predefined settings we use our system for industrial application, see below.

During the last few years we have been working on improvements in resolution. Based on special settings and configuration we have reached the resolution to recognize two flaws located 1 mm between each other. The main improvements were made in signal processing; the noise has been successfully suppressed and signal representing flaws and cracks are simply displays.

## 5. Applications

### 5.1 Testing of railway rails

The following Figure 5., presents one sector scan where we can see all side drilled holes.



Figure 5. Testing of railway Rais

Using of phased array probe without adapter with ultrasonic signal deflection on both angle sides can be seen in Figure 6. Our system visualizes all three side drilled holes (see Figure 6b.).

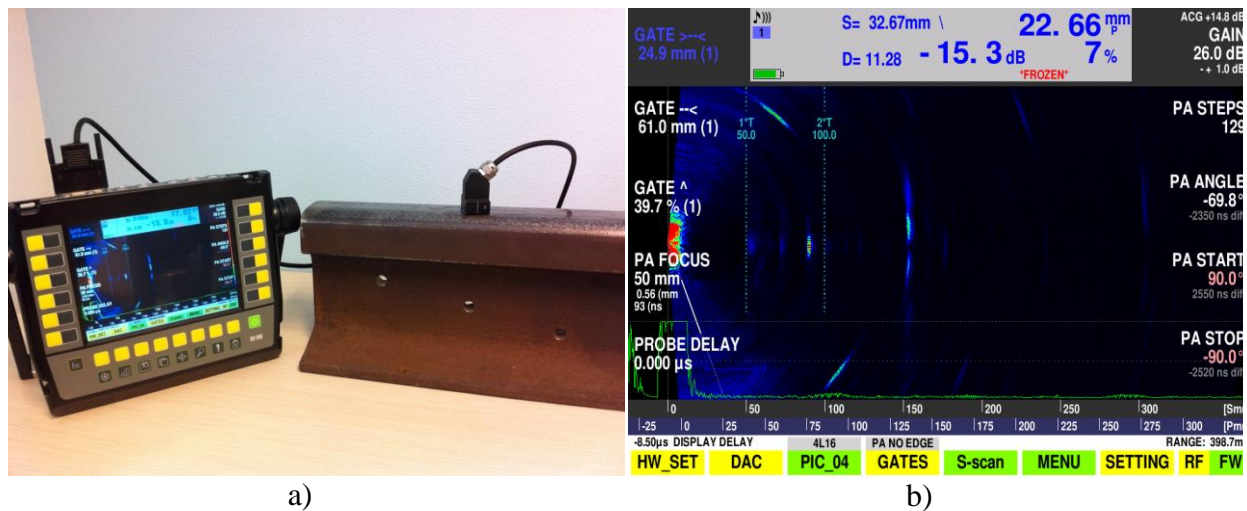
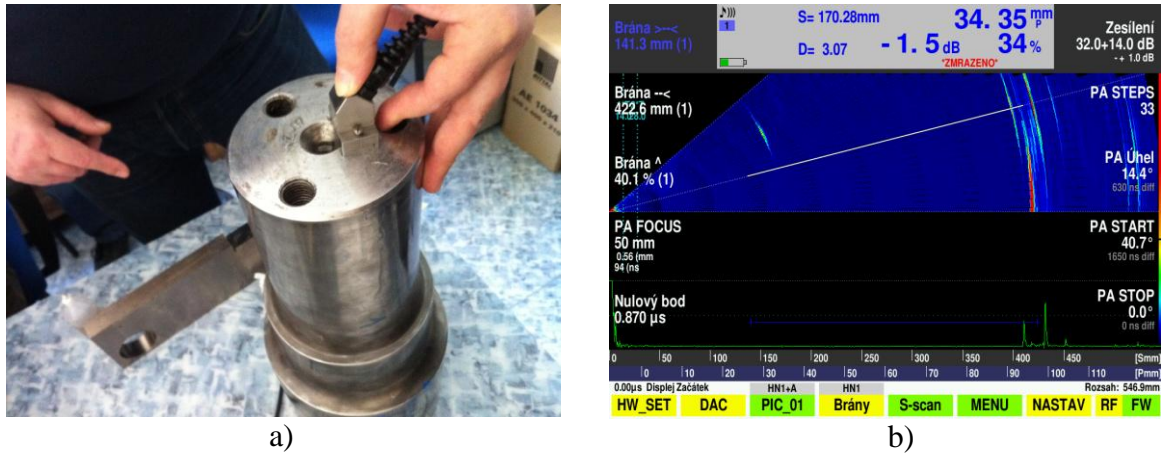


Figure 6. Testing of railway rails, a) probe without adapter, b) detected flaws

### Testing of railway axles

Testing of railway axles from side – axis of the axle. It is possible to see the orientation of the cut of axle from one probe location.



**Figure 7.** Testing of railway axles, a) placed probe on the side of axle, b) detected flaws

### Testing of welds

The testing of welds is a standard option in our proposed system, The following Figure 8. shows the result of weld testing.

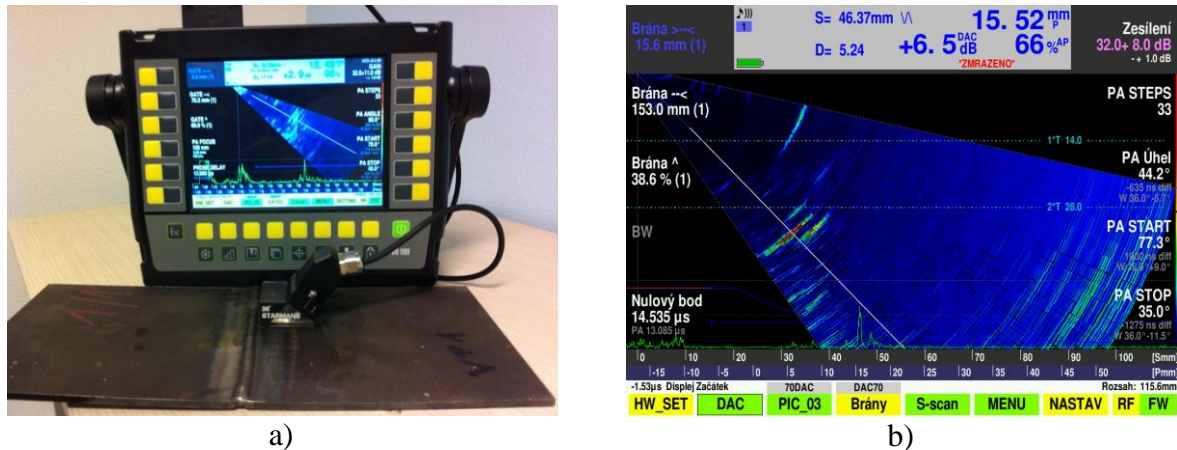


**Figure 8.** Testing of welds, a) tested material with weld, b) detected cracks

During the weld testing, it is possible to set the deflection angle within 35-90°. Based on the advanced settings and automatic amplitude correction, it is possible to successfully detect cracks hidden in welds.

## 6. Conclusion

This paper presented our developed ultrasonic portable system with phased array technique and possible applications. The developed system contains implemented conventional ultrasonic testing, EMAT testing and phased array testing. As all signals are corrupted with relatively higher amplitude noise level, our system contains signal-processing methods based on averaging and digital filters. The presented system is equipped with phased array technology. As we are at the beginning of our experiments we are able to scan flaws using transmitting and receiving signal s at the same time. The presented paper describes phased array technique using transmitting the signals with derived time delay based on distance from focused point.

### Acknowledgement

This research work has received support from research program No. 2A—1TP1/092 “[Research of piezoelectric laminated nanoforms for high-temperature ultrasonic transducers](#)” of the Ministry of Industry and Trade.

### References

1. Krautkramer J., Krautkramer H.: *Ultrasonic Testing of Materials*. Springer-Verlag, 4th fully revised edition, 1990, 670 p., ISBN 3-540-51231-4.
2. Matz, V., Šmíd, R., Štarman, S., Kreidl, M.: Signal-to-noise ratio enhancement based on wavelet filtering in ultrasonic testing. *Ultrasonics*, Elsevier: In press, 2009.
3. Masahiko Hirao, Hirotugu Ogi: *Emats for science and industry, Noncontacting ultrasonic measurements*. Massachusetts, USA: Kluwer Academic Publishers, 2003.
4. Robert E. Green, Jr.: *Non-contact ultrasonic techniques*, Ultrasonics, Volume 42, Issues 1-9, April 2004, Pages 9-16.
5. Noël Dubé: *Advances in Phased Array ultrasonic technology applications*. Waltham, MA: Olympus NDT, 2007.
6. A Bulavinov *et al*, ‘Sampling phased array a new technique for signal processing and ultrasonic imaging’, Berlin, ECNDT, 2006.

## ELASTIC STUDIES OF TROPICAL WOODS BY USING NON-DESTRUCTIVE ULTRASONIC TECHNIQUE

Sidek Hj Ab Aziz<sup>1</sup>, Abdul Halim Shaari<sup>1</sup>, Nor Hafzan Sarah Almuin<sup>1,2</sup>,  
Mohd Noorul Ikhsan Ahmad<sup>2</sup>, Abd Nassir Ibrahim<sup>2</sup> & Ilham Mukriz Zainal Abidin<sup>2</sup>

<sup>1</sup> Glass and Ultrasonic Studies Centre (GUSC), Department of Physics  
Faculty of Science, Universiti Putra Malaysia  
43400 UPM Serdang, Selangor, MALAYSIA

<sup>2</sup> NDT Group, Industrial Technology Division, Malaysian Nuclear Agency  
Ministry of Science, Technology and Innovation  
43000 Bangi, Kajang, Selangor, Malaysia

\*Email: [sidek@science.upm.edu.my](mailto:sidek@science.upm.edu.my)

### Abstract

Destructive testing is always being employed to acquire the quality of woods particularly from their strength. However, the non-destructive ultrasonic testing shows some potential in accessing the physical characteristics of woods and hence to determine their qualities. This method has not been widely used in Malaysia although it was largely carried out elsewhere. This paper describes the measurement of longitudinal wave velocities propagated in our tropical woods as measured at room temperature in order to obtain detailed information of their physical properties. The elastic constants of local wood samples, having orthotropic symmetry, can be assessed if the ultrasonic wave velocity and density of samples are known. More than 50 species of our tropical hardwoods, medium hardwoods and softwoods were successfully evaluated by employing the portable ultrasonic tester Steinkamp BPV (Germany). Their variations of the wave velocities and elastic constants as function of density are reported. We found that the wave velocity – density and elastic constant – density relations might be used to classify and predict the quality of wood samples.

### INTRODUCTION

The non-destructive ultrasonic methods of wood testing are vital to be used for quality control especially during the production stage, where they can detect cracks in boards, their size densities perpendicular to the board plane and also their surface irregularities. Furthermore those methods show some potential in accessing the physical characteristics of woods and hence to determine their qualities. This method has not been widely used in Malaysia although it was largely carried out elsewhere. So far the destructive testing is always being employed to acquire the quality of woods particularly from their strength (Mazzanti & Uzielli, 2010). Table 1 shows some methods of non-destructive wood testing.

Dinh et al. (2010) has developed the experimental devices that are able to measure the mechanical properties of wood on well-identified minute samples (a few millimetres) in longitudinal and transverse (radial or tangential) directions. The device is conceived and built to perform a rigorous 4-point bending test on microsamples where the wood sample, can be considered as a beam, is placed on two fixed cylinders, free to rotate, and this wood sample defines the measurement length (L). The force is evenly applied on two moving cylinders of



same diameter separated by the length (l). The force is applied stepwise to the sample. For each load level, the beam curvature is measured without contact using a laser micrometer in order to measure the Young's modulus of wood sample.

Table 1: Summary of methods of non-destructive wood testing (Niemz, 2010)

Property	Basic physical principles	Measurable properties
Mechanical properties	Drilling resistance, hardness, intrusion behaviour	Detection of fungal decay, density
Electrical properties	Electrical resistance	
	Correlation between electrical resistance and moisture content	Moisture content
	Correlation between electrical resistance and fungal decay	Detection of fungal decay
	Dielectrical properties	Moisture content
Acoustical properties	Sound velocity; sound reflection; sound attenuation	Elastic constants (E,G) Defect detection
	Acoustic emission	Micro cracks, eating noise of insects
	Eigenfrequency	Elastic constants (E,G) Delamination in glued wood joints
Thermal properties	Heat radiation (thermography)	Defects on near-surface areas (error adhesion of inlay, opened fugues)
Particles	Neutron radiation	Allocation of humidity
Electromagnetic waves	Visible light (ageing)	Colour measuring (CI-Lab), aging, colour differences Video Image Correlation (cross correlation, strain distribution)
	IR/NIR radiation	humidity, chemical analysis (impurities), partly mechanical attributes
	X-ray (absorption/diffusion)	density, local density allocation, annual grow ring profiles, angle in S2 (Sylviscan)
	Synchrotron radiation	micro structure analysis

This paper describes the measurement of longitudinal wave velocities propagated in our tropical woods as measured at room temperature in order to obtain detailed information of their elastic properties.

## EXPERIMENTAL TECHNIQUES

Wood is an anisotropic material where its physical and mechanical properties depend dramatically on the material direction and on its structural features (Simpson & TenWolde, 1999) (anatomy, cell wall macromolecular arrangement). Wood may be described as an orthotropic material; that is, it has unique and independent mechanical properties in the directions of three mutually perpendicular axes: longitudinal, radial, and tangential. The longitudinal axis  $L$  is parallel to the fiber (grain); the radial axis  $R$  is normal to the growth rings (perpendicular to the grain in the radial direction); and the tangential axis  $T$  is perpendicular to the grain but tangent to the growth rings. These axes are shown in Figure 1.

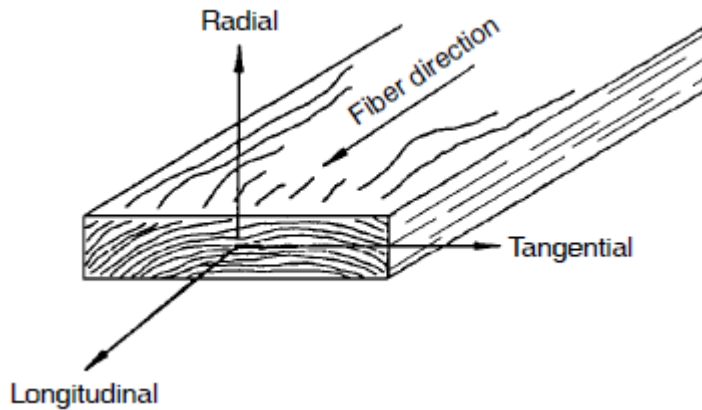


Figure 1. Three principal axes of wood with respect to grain direction and growth rings.

Twelve constants (nine are independent) are needed to describe the elastic behaviour of wood: three moduli of elasticity  $E$ , three moduli of rigidity  $G$ , and six Poisson's ratios  $\mu$ . The moduli of elasticity and Poisson's ratios are related by expressions of the form

$$\frac{\mu_{ij}}{E_i} = \frac{\mu_{ji}}{E_j}, \quad i \neq j \quad i, j = L, R, T$$

Elasticity implies that deformations produced by low stress are completely recoverable after loads are removed. When loaded to higher stress levels, plastic deformation or failure occurs. The three moduli of elasticity, which are denoted by  $E_L$ ,  $E_R$ , and  $E_T$ , respectively, are the elastic moduli along the longitudinal, radial, and tangential axes of wood.

The measurements presented in this paper were performed on samples cut from local tropical trees. Generally the Malaysian tropical woods are divided into four categories: Heavy hardwood, Medium Hardwood, Light Hardwood and Softwood. In this study, all the tropical hardwood, medium hardwood and softwood samples are obtained from the Forest Research Institute Malaysia (FRIM), Kepong, Selangor. Detailed wood samples preparation are available elsewhere (FRIM) (Anon, 1988; Sidek et al., 1995). All specific types of wood samples are prepared at room temperature enable accurate mechanical measurement on and along the three material directions. Each of wood samples are clean, with straight grain, or as much as possible, and cut in preferable sizes of 11cm (length) x 7 cm (width) x 1cm (thick) for ultrasonic wave measurement. After cutting, the specimens are put in the box in order to be equilibrated at similar moisture contents (Engku, 1980).

A through transmission method is more suitable for the acoustic measurement of coarse grained and porous materials like wood compared with pulse-echo method. In the present study, an ultrasonic tester (model BP5) complete with two 45 kHz probes with conical stainless steel contact points was used. These probes are especially suitable for samples with rough surfaces and can operate without the need of couplants (Steinkamp, 1995).

## RESULT AND DISCUSSION

The dynamic modulus of elasticity  $E (= \rho V^2)$  of wood can be accessed through the measurement of ultrasonic wave velocity ( $V$ ) and density ( $\rho$ ) of a sample. All the wood samples are assumed to be infinite homogeneous isotropic medium (Steinkamp, 1995). Table 2-4 show the average density, elastic constants and ultrasonic wave velocities of different types of tropical hardwood, medium hardwood and softwood samples. These moduli are presented in term of  $E_L$ ,  $E_R$  and  $E_T$  which are usually obtained from compression tests. It is observed that the elastic constants themselves vary within and between species and with moisture content and specific gravity.

Table 2. The average density, elastic constants and ultrasonic wave velocities of different types of tropical hardwood samples.

Sample	Local Name	Scientific Name	Average Density (kgm <sup>-3</sup> )	Elastic Constant (GPa)				Wave Velocity (ms <sup>-1</sup> )		
				$E_L$	$E_T$	$E_R$	$E_L^*$	$V_L$	$V_T$	$V_R$
A1	Tembusu	<i>Fagraea fragrans</i>	800	14.70	2.00	2.30	14.00	4287	1581	1696
A2	Merbau	<i>Intsia palembanica</i>	800	15.70	1.90	2.00	15.40	4430	1541	1581
A3	Giam	<i>Hopea spp.</i>	975	16.70	2.10	2.40	16.50	4139	1468	1569
A4	Balau Merah	<i>Shorea spp.</i>	880	17.40	1.90	2.30	17.00	4447	1469	1617
A5	Resak	<i>Vatica spp.</i>	945	18.80	1.80	2.40	18.10	4460	1380	1594
A6	Kekatong	<i>Cynometra spp.</i>	975	18.70	2.20	2.40	18.40	4379	1502	1569
A7	Chengal	<i>Neobalanocarpus heimii</i>	945	19.60	2.30	2.40	19.60	4554	1560	1594
A8	Keranki	<i>Dialium spp.</i>	960	15.60	2.20	2.30	20.10	4031	1514	1548
A9	Balau	<i>Shorea spp.</i>	975	17.30	2.10	2.30	20.10	4212	1468	1536
A10	Bitis	<i>Madhuca utilis</i>	1105	21.90	2.40	2.60	23.80	4452	1474	1534
A11	Bakau	<i>Rhizophora spp.</i>	1040	19.90	2.30	2.50	20.70	4374	1487	1550

Table 3. The average density, elastic constants and ultrasonic wave velocities of different types of tropical medium hardwood samples.

Sample	Local Name	Scientific Name	Average Density (kgm <sup>-3</sup> )	Elastic Constant (GPa)				Wave Velocity (ms <sup>-1</sup> )		
				$E_L$	$E_T$	$E_R$	$E_L^*$	$V_L$	$V_T$	$V_R$
B1	Meransi	<i>Crallia spp.</i>	800	14.10	1.70	2.20	13.40	4198	1458	1658
B2	Simpoh	<i>Dillenia spp.</i>	735	14.90	1.60	1.90	14.30	4502	1475	1608
B3	Rengas	<i>Gluta spp.</i>	835	15.20	2.00	2.30	14.90	4267	1548	1660
B4	Kulim	<i>Scorodocarpus</i>	835	15.10	1.90	2.20	14.90	4253	1508	1623
B5	Punah	<i>Tetramesrista glabra</i>	720	15.40	1.70	1.90	15.40	4625	1537	1624
B6	Merawan	<i>Hopea spp.</i>	690	16.20	1.90	2.30	15.50	4845	1659	1826
B7	Keledang	<i>Artocarpus spp.</i>	800	15.70	1.60	2.10	15.50	4430	1414	1620

B8	Mengkulang	<i>Heritiera spp.</i>	755	16.50	1.80	2.00	16.00	4675	1544	1628
B9	Mata Ulat	<i>Kokoona littoralis</i>	880	17.60	1.90	2.40	16.30	4472	1469	1651
B10	Kasai	<i>Pometia spp</i>	800	18.40	1.50	2.30	17.00	4796	1369	1696
B11	Kelat	<i>Eugenia spp.</i>	800	17.70	1.70	2.30	17.60	4704	1458	1696
B12	Tualang	<i>Koompassia excelsa</i>	835	18.10	1.70	2.00	17.80	4656	1427	1548
B13	Merpauh	<i>Swietonia spp</i>	755	18.70	1.50	1.90	18.10	4977	1410	1586
B14	Kempas	<i>Koompassia</i>	880	19.00	1.90	2.40	18.60	4647	1469	1651
B15	Kapur	<i>Dryobalanops spp</i>	755	19.80	1.80	2.10	18.00	5121	1544	1668
B16	Keruing	<i>Dipterocarpus</i>	880	20.10	1.90	2.30	22.30	4779	1469	1617

Table 4. The average density, elastic constants and ultrasonic wave velocities of different types of tropical softwood samples.

Sample	Local Name	Scientific Name	Average Density (kgm <sup>-3</sup> )	Elastic Constant (GPa)				Wave Velocity (ms <sup>-1</sup> )		
				E <sub>L</sub>	E <sub>T</sub>	E <sub>R</sub>	E <sub>L</sub> *	V <sub>L</sub>	V <sub>T</sub>	V <sub>R</sub>
C1	Terentang	<i>Camposprema spp.</i>	435	10.9	1.7	1.8	7	5006	1977	2034
C2	Jelutong	<i>Dyera costulata</i>	465	11.9	1.3	1.8	8	5059	1672	1967
C3	Pulai	<i>Alstonia spp</i>	465	13.9	1.4	2	7.1	5467	1735	2074
C4	Sesendok	<i>Endospermum malaccensis</i>	530	14	1.6	1.9	8.5	5140	1737	1893
C5	Melantai	<i>Hopea macroptera</i>	530	12.1	1.7	2.1	7.9	4778	1791	1991
C6	Geronggang	<i>Cratoxylon</i>	545	12.5	2	2.2	8	4789	1916	2009
C7	Meranti merah muda	<i>Shorea spp</i>	545	14	2.1	2.4	19.4	5068	1963	2098
C8	Petai	<i>Parkia spp</i>	545	11.3	1.2	2.3	10.7	4553	1484	2054
C9	Perupok	<i>Lophopetalum spp</i>	560	13.8	2	2.2	12.6	4964	1890	1982
C10	Machang	<i>Mangifera spp</i>	560	14.5	1.8	2.1	14.3	5089	1793	1936
C11	Kedondong	<i>Burseraceae</i>	575	14.5	1.3	2.4	12.9	5022	1504	2043
C12	Terap	<i>Paratocarpus spp</i>	575	13.4	1.6	2.2	12	4827	1668	1956
C13	Panarahan	<i>Myristicaceae</i>	595	14.5	1.6	1.8	9.4	4937	1640	1739
C14	Medang	<i>Lauraceae</i>	610	15.3	1.6	2.2	12.6	5008	1620	1899
C15	Ramin	<i>Gonystylus bancanus</i>	625	14.6	1.7	2.3	16.4	4833	1649	1918
C16	Kayu Getah	<i>Hevea brasiliensis</i>	640	13.2	1.7	2	9.2	4541	1630	1768
C17	Mersawa	<i>Anisoptera spp</i>	655	13.7	1.8	2.1	12.6	4573	1658	1791
C18	Melunak	<i>Pentace spp</i>	655	13.6	1.8	2	12	4557	1658	1747
C19	Meranti kuning	<i>Shorea spp</i>	675	13.8	2	2.2	12.1	4522	1721	1805
C20	Meranti puteh	<i>Shorea spp</i>	675	14.6	1.7	2.2	19.4	4651	1587	1805
C21	Kungkur	<i>Pithecellobium spp</i>	675	12.6	1.7	2.2	10.7	4320	1587	1805
C22	Meranti bakau	<i>Shorea uliginosa</i>	675	15	1.6	1.8	14.7	4714	1540	1633
C23	Sepetir	<i>Sindora spp</i>	675	14.9	1.6	2	13.6	4698	1540	1721

C24	Merawan	<i>Hopea spp</i>	690	15.9	1.1	1.9	15.5	4800	1263	1659
C25	Gerutu	<i>Parashorea lucida</i>	690	20.6	1.7	2	20.6	5464	1570	1703
C26	Bintangor	<i>Calophyllum spp</i>	690	18.4	1.9	2.2	14.3	5164	1659	1786
C27	Durian	<i>Durio spp</i>	705	16.2	1.8	2.1	15.8	4794	1598	1726
C28	Kembang semangkok	<i>Scaphium spp</i>	705	16.4	2	2.2	17	4823	1684	1767
C29	Meranti	<i>Shorea spp</i>	705	15.4	2.1	2.4	13.9	4674	1726	1845

Figure 2 shows the various elastic constants calculated from the velocities and densities of each wood samples. Also shown is regression lines representing the effect of density on these elastic constants at three major directions; longitudinal (L), radial (R) and tangential (T).

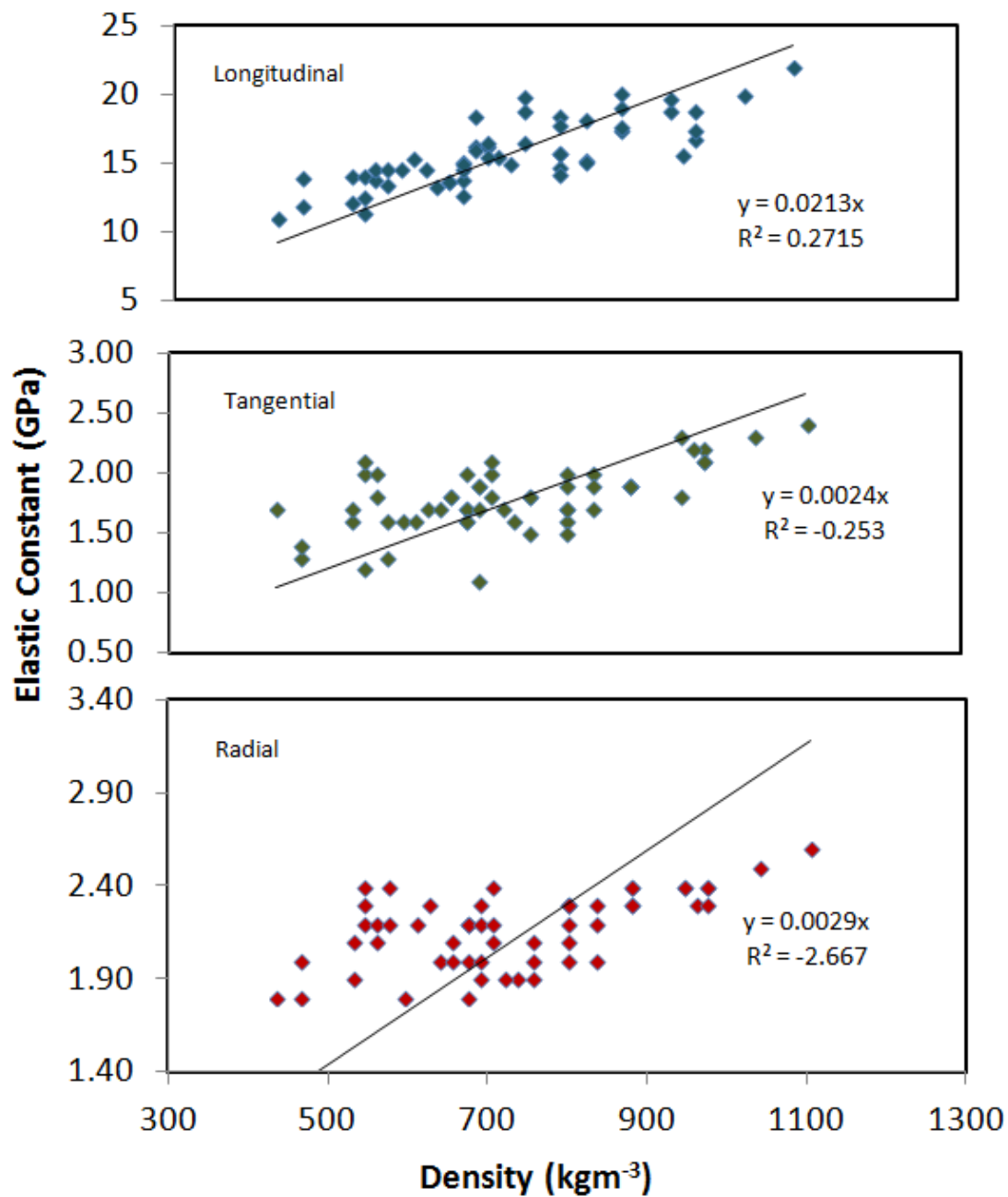




Figure 2: The elastic constant of tropical wood sample versus density at longitudinal (L), radial (R) and tangential (T) directions.

The modulus of elasticity (MOE) measures a wood's stiffness, and is a good overall indicator of its strength. Technically it's a measurement of the ratio of stress placed upon the wood compared to the strain (deformation) that the wood exhibits along its length. MOE is expressed in gigapascals (GPa). This number is given for wood that has been dried to a 12% moisture content, unless otherwise noted.

The definition of tropical softwood and hardwood has significant relation to the wood's materials properties: for example the softwood *Terentang* is less stiff than the medium hardwood *Meransi* and hardwood *Tembusu* as shown in Table 2-4. This is mainly due to the ultra low density, as the stiffness (and also strength) of wood correlates with density. Figure 2 show the elastic constant of tropical wood sample versus density at longitudinal (L), radial (R) and tangential (T) directions. The values of elastic modulus ( $E_L$ ,  $E_T$  and  $E_R$ ) show that wood is reasonably stiff. Wood is a composite material, and so to stretch the wood samples the cellulose microfibrils in the wood have to be stretched. The Young's modulus of cellulose fibrils is 100 GPa, and that of lignin and hemicellulose averages to 6 GPa. Almost all the tropical wood samples follow the usual trend where the longitudinal modulus is greater than radial modulus and tangential modulus (i.e.  $E_L > E_R > E_T$ ).

Figure 3 shows the comparison of elastic constant measured using ultrasonic and static methods along the longitudinal wood direction. At higher density as well as elastic constant, there is almost good relationship between static and ultrasonic (dynamic) method of wood testing. As expected the values given by ultrasonic is relatively higher than the static method by less than 10%.

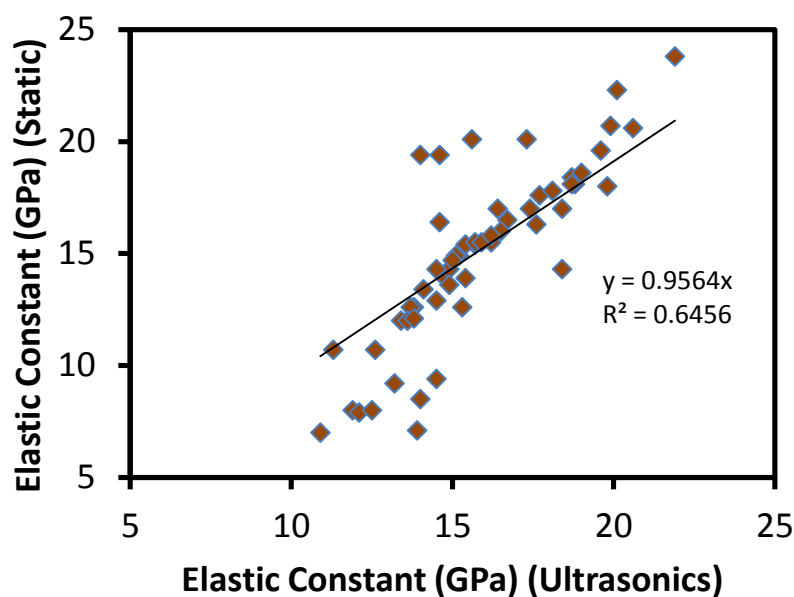


Figure 3. Comparison of elastic constant measured using ultrasonic and static methods.

## CONCLUSION

An ultrasonic nondestructive testing method has been used to determine the elastic properties of various types of tropical wood samples. The approach is based on the wave velocity measurements in each wood samples and their bulk density. The relation of the wave velocities and elastic constants with the density of tropical woods is found to be nonlinear. However the values of wave velocity, elastic constant can be used to classify and predict the quality of tropical wood samples. At higher density as well as elastic constant, a good relationship between static and ultrasonic (dynamic) method of wood testing is observed where the elastic constant measured by ultrasonic is relatively higher than the static method by less than 10%.

## BIBLIOGRAPHY

- A. T. Dinh, G. Pilate, C. Assor, P. Perré (2010) Measurement of the Elastic Properties of Minute Samples of Wood Along the Three Material Directions, in *Wood Science for Conservation of Cultural Heritage –Braga 2008*, Joseph Gril. (ed) – Firenze :Firenze University Press, pp. 30-35.
- Anon. (1988) Annual Book of ASTM Standards. Section 4. Volume 4.09 Wood. American Society for Testing and Materials. Philadelphia, U.S.A.
- C., Coutand, Jeronimidis G., Chanson B., Loup C. 2004. Comparison of mechanical properties of tension and opposite wood in Populus. *Wood Science and Technology* 38, 11-28
- Engku, A.R C (1980) Basic Grade Stresses for Some MalaysianTimbers. Malaysian Forest Service. Trade Leaflet NO. 37. Malaysian Timber Industry Board, Kuala Lumpur, Malaysia.
- I.G. Steinkamp (1995), User Handbook for Ultrasonic Test Instrument Type BP5., Germany.
- L.Brancheriau, H. Bailleres, D.Guitard : Comparison between modulus of elasticity values calculated using 3 and 4 point bending tests on wooden sample. *Wood Science and Technology* 36 (2002) 367-383.
- P. Mazzanti, L. Uzielli (2010) Strength and MOE of Poplar Woo (Populus Albal.) Across the Grain: Expeimental Data, in *Wood Science for Conservation of Cultural Heritage –Braga 2008*, Joseph Gril. (ed) – Firenze : Firenze University Press, pp 62-66
- P. Niemz (2010) Methods of Non-Destructive Wood Testing, in *Wood Science for Conservation of Cultural Heritage –Braga 2008*, Joseph Gril. (ed) – Firenze : Firenze University Press, pp. 163 - 168
- Sidek H A Aziz, A Halim Shaari & S.P. Chow (1995) Elastic Constant Determination of Tropical Wood by Using Dynamic Ultrasonic Technique, *Pertanika J. Sci. And Technol.* 3(2), pp. 389-399
- W. Simpson, TenWolde, A. (1999): “Physical Properties and Moisture Relations of Wood”, *Wood Handbook: Wood as an Engineering Material*, Forest Products Laboratory, Madison: Ch 3, 3-8.

# **Rail inspection technique employing advanced nondestructive testing and Structural Health Monitoring (SHM) approaches- A review**

Firouz Fadaeifard<sup>1</sup>, Meysam Toozandehjani<sup>3</sup>, Faizal Mustapha<sup>2</sup>, Khamirul Amin B. Matori<sup>1</sup>, Mohd Khairul Anuar b. Mohd Ariffin<sup>3</sup>, Nur Ismarrubie bt. Zahari<sup>3</sup>, Amir Abbas Nourbakhsh<sup>4</sup>

1 Materials Synthesis and Characterization Laboratory, Institute of Advanced Technology, University Putra Malaysia, 43400 UPM Serdang, Selangor, Darul Ehsan, Malaysia

2 Department of Aerospace Engineering, Faculty of Engineering, Universiti Putra Malaysia, 43400 UPM Serdang, Selangor, Darul Ehsan, Malaysia

3 Department of Mechanical Engineering, Faculty of Engineering, Universiti Putra Malaysia, 43400 UPM Serdang, Selangor, Darul Ehsan, Malaysia

4 Department of Materials Sciences and Engineering, Shahreza Branch, Islamic Azad University, Isfahan, Iran

**Keywords:** Non-destructive Test (NDT), Phased Array, EMAT, Structural Health Monitoring (SHM)

## **Abstract**

In modern railway technology exploitation, rails are exposed to a constant increase of speed and loading on the vehicle axles and to constant stress increase in welded railway tracks. To meet the increased exploitation requirements, new requirements for rail steel quality in manufacturing process and inspection methods in manufacturing and service process have been pursued. In the first part of this review, probable defect in different stages such as melting, rolling, HT, drilling, cutting, installing, termite welding and exploiting are classified and their suitable non-destructive testing (NDTs) is described. In the second part of this review, the ability and sufficiency of different NDT methods for detecting a certain defect are explained. Advantages and disadvantages of Phased Array and EMAT are compared. New approaches in structural health monitoring (SHM) for rail inspecting and monitoring are investigated. In this paper a review has been conducted to bridging conventional and advanced NDT methods to new inquiries of Structural Health Monitoring (SHM) for rail monitoring including defect detection and interpretation.

## **1.Introduction**

Rails are expanding as a heart of the railway system. In modern railway, rails are subjected to a very high speed and operating loads as well as harsh environmental conditions. Thus, the maintenance issues are becoming more concerned [1].

Presence of various types of defects is a major threat to the safe operation of a railway system. Defects are initiated within the rail during the manufacturing or due to fatigue and other failure mechanisms. As the rail operation proceeds, defects can worsen if no recovery action is undertaken and finally they may develop to complete rail breakage, which is a major cause for train derailment [1,2]. Due to that applying of conventional and new NDT method is important in manufacturing and rail services. This

paper has briefly reviewed the rail defects, NDT in rail manufacturing with more attention to ultrasonic tests and related methods for in-service inspection. Due to advancement and the increasing use of Structural Health Monitoring (SHM) the role of wireless sensor in the future of rail inspection and monitoring is presented.

## 2. Rail defects

In the rail industry, the numerous types of defects can be found in a rail. Defects in rail are categorized in many different ways. In this paper, we are categorized rail defects based on their origins. These three categories of defects are: rail defects in the manufacturing process, unsuitable use or handling rail defects, and in-service defects [2-8].

Rail defects during manufacturing are generally non-metallic inclusion origin or metallurgical origin defects due to wrong local mixings of the steel components. These defects later under operative loads, generate local concentration of stresses, which cause rail failure [2]. Manufacturing process defects during manufacturing are divided into external (surface) and internal defects. Any hot marks, protrusions, scratches, rolled in scale, seams, cold marks and microstructural damage on the surface of the rails are surface defect. Internal defects are usually cracks and inclusions. The second type of defects including improper use or handling of rails are generally due to spinning of train wheels on rails or sudden train brakes. Wheel burn area typical defect of this type of damage [3].

Defects in the in-service rails which can develop in the head, web or foot of the rail track. The majority of rail defects is detected at the rail head although a significant number of defects are also found on the web as well as the foot of the rail [4]. Rail head defects can be distinguished to those having an internal origin, such as progressive transverse cracking or kidney-shaped fatigue cracks, horizontal cracking with or without transverse cracking of the rail head, horizontal cracking beneath the gauge corner, and longitudinal-vertical cracking, and those having surface origin, such as RCF damage (Fig 1) which including gauge corner cracking, head checks, squats, shelling, and corrugation), and indentures. The rail foot considers as most critical part of the rails and further analysis must be done on the foot. Because conventional NDT techniques are not sensitive to defect in this part and can not detect them. Rail web and rail foot defects include longitudinal and vertical cracking, cracking occurring at fishplate bolt holes or other holes found in the web (Fig 2) star-cracking, transverse fatigue cracking, and rail foot corrosion. Profile irregularities and low levels of conicity that develop with time due to wear of the rail head can also be considered as rail defects [5, 6, 7].

Alumino-thermic welds are employed widely for joining in railways. Despite their vast application, there is a significant problem in the rail industry, since internal defects such as shrinkage cavities, microporosities, inclusions and a coarse dendrite microstructure, (during the solidification process), can

affect the structural integrity and fatigue performance by acting as crack initiation points. As a result, the failure of alumino-thermic welds can take place very rapidly with no indication of fatigue cracking [9].

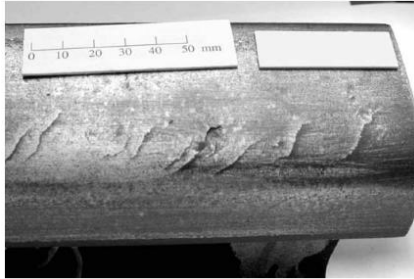


Fig 1: RCF damage[8]

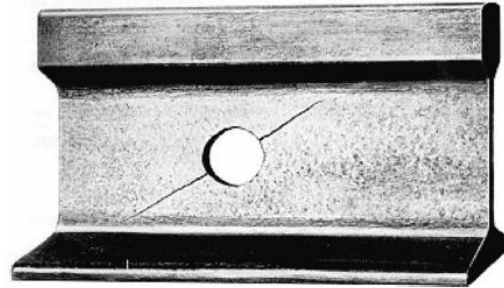


Fig 2 : Star cracking from fish bolt hole[8]

### 3. Rail defect management (RDM)

Failure is expensive then efforts must be toward control and prevent failure. This control process is sometimes known as RDM. RDM aims to prevent rail failure by detecting defects by inspection before the rail breaks. A measurement of defect management efficiency is the ratio of broken rails to detected defects. A high ratio means that many rails break before defects are found. A low ratio means that inspection methods are effective in finding defects. Two main objectives of RDM are: to detect and to eliminate rail defects before they cause rail breaks. Generally RDM strategies focus on the first objective. The goal of zero rail breaks which may not be practically possible drives reductions in breaks and the development of RDM systems and wheel–rail technology [10].

### 4. Non destructive testing ( NDT) in rails

Since any rail break and failure can cause a serious disaster in a mass transportation system such as a train, concern of inspection and monitoring of railway tracks has increased over decades. For this reason, many nondestructive testing methods (NDTs) for defect detection have employed [11].

Non destructive testings (NDTs) have been used over decades as a major means of rail inspection for detection of railway defects all over the world [12]. The first application of NDT methods for the detection of defects in rails dates back to 1877 [13], and followed by development of rail inspection cars by Dr Sperry 50 years later which used magnetic induction sensors [14].

The NDT methods are commonly used in order to inspect rail tracks. They are visual, or using eddy current testing [15,16], magnetic flux leakage testing (MFL) [12,17], magnetic particle inspection, ultrasonic testing. Novel high-speed NDE equipments are recently developed including high speed cameras [18], Alternating Current Field Measurement (ACFM) probes [19-21], Electromagnetic



Acoustic Transducers (EMATs)[22-25], Field Gradient Imaging (FGI)[26,12], ultrasonic phased arrays [27], and long range ultrasonic, laser Ultrasonics, and multi-frequency eddy current sensors[12,28], infrared thermography and acoustic emission [30]. Radiography has found limited use in weld inspection s well[31-32].

NDTs are used in order to a systematic inspection for internal and surface defects in the manufacturing process and in-service condition [17]. During the manufacturing process, first, rails are examined visually for any surface damage such as laminar defects, inclusions as well as tension cracks in the rail head, web and base then rails are inspected using automated optical cameras and eddy current sensing systems for any surface damage, while the presence of internal defects is assessed through ultrasonic inspection[12,15]. Similarly, in-service rails are systematically inspected for internal and surface defects using the same nondestructive evaluation (NDE) techniques as well. The summary of defects and related NDT can be seen in table 2.

#### **4. 1 Ultrasonic testing for rail inspection**

Ultrasonic transducers were added to the Sperry test vehicles and used for the high speed inspection of rails for the first time in 1953[14]. Until now inspection by means of ultrasonic testing (UT) is one of the most widely employed methods for rail flaw detection system [16,33,34].

Ultrasonic inspection is carried out by the means of different method and instruments ranging from hand-held (portable) devices to rail automated rail cars [14]. In most cases rail inspection is performed by special ultrasonic probes mounted on the undercarriage of the test train. Portable ultrasonic are still used in many countries but the fluid-filled ultrasonic wheel probes are the most common methods used to couple the piezoelectric transducers to the rail[12]. These methods are shown in Figure 3.

Typically, conventional ultrasonic testing uses of transducers which operating in pulse-echo configuration. Transducers are located inside a fluid-filled tire known as Roller Search Unit, or RSU that conforms to the rail head. Transducers applied at  $0^\circ$  (normal incidence) and  $70^\circ$  to the running surface of the rail on the center line. These transducers enables detection of horizontal crack, inclusions (by normal incidence ) and transverse cracks ( by  $70^\circ$  transducer). Also it is possible to detect vertical cracks running normal to the axis of the rail, particularly if they have rough surfaces[34-36].

However, Ultrasonics have shown their satisfactory capabilities in detection and sizing of defects but for many reason their application is limited[16,34]. First, they are not suitable for surface and near-surface cracking where many of the faults are located [16]. Transverse cracking (TDs), vertical cracking or any cracks inclined to the top surface not detectable by conventional methods[37]. Another

problem with either method for detection of these defect is that cracks running close and almost parallel to the running surface of the rail can block wave path[35]. However, in some cases using a tandem arrangement of a pair of transducers operating in pitch-catch mode is more suited for the detection of transverse cracks, but it is more complicated to deploy [35,12]. Second, presence of horizontal surface damage such as shelling and head checks prevent the ultrasonic beams from reaching the internal defects which result in false negative readings. In the case of alumino-thermic welds, the large material grain size of welds strongly scatters ultrasonic and rises the attenuation and reflected signals that are very difficult to interpret[35].



Figure 3: portable and hi-rail vehicle for ultrasonic testing [36]

Moreover, the inspection speed of this method is limited and there need a contact between the rail and the inspection wheel. A problem related to conventional techniques is that transducers must be acoustically coupled to the rail to be tested [37]. This coupling medium can cause transit time errors, while partial transmission and partial reflection of the ultrasonic energy in the couplant layer may cause a change in the shape of the waveform leading to errors in attenuation measurements. Then concerns are toward other techniques which are non-contact ultrasound[37].

Non-contact techniques allowed generation and detection of acoustic waves with less modification of the detected waveform or frequency spectrum, although all systems are bandwidth of system is limited more than others. Non-contact techniques can be used in hot and cold materials and in other hostile environments, in geometrically difficult to access locations and at relatively large distances from the structure to be tested [37].

Non-contact acoustical techniques are recently being available and successfully are used for rail track. Researchers in the Johns Hopkins University Center for Non-destructive Evaluation (CNDE) have developed non-contact ultrasound techniques for railroad rail and wheel inspection [38-42]. In order to the increase rail flaw detection reliability researches continue toward the development of ultrasonic

technologies. Technologies investigated to date include laser-generated ultrasound, guided ultrasonic waves, and ultrasonic phased arrays.

## 4.2 Laser ultrasonic test

Laser-based ultrasonics is a remote implementation of conventional ultrasonic inspection systems that normally use contact or non-contact transducers, squirter transducers, or immersion systems[12,17]. This system has the capability of detecting near surface defects in the rail as well as defects in the foot of the rail[43].

Laser ultrasonic testing comprises the sensitivity of ultrasonic inspection with the flexibility of optical systems in dealing with complex inspection problems. Its remote nature allows the rapid inspection of curved surfaces on fixed or moving parts. It can measure parts in hostile environments or at temperatures well above those that can be tolerated using existing techniques. Its accuracy and flexibility have made it an attractive new option in the nondestructive testing market [12].

In this method, first, ultrasound waves are generated by using a pulsed laser through a thermoplastic process or by ablation. Pulsed lasers can be used to generate all types of ultrasonic waves, including compression, surface, shear and plate waves. When the ultrasonic wave reaches the surface of the sample, the resulting surface displacement is measured with a laser ultrasonic receiver based on an adaptive interferometer[12,41,44,45].

In this case, Transportation Technology Centre Inc. (TTCI) in cooperation with Tecnogamma Spa developed a LAHUT system (laser-air hybrid ultrasonic technique) which is dedicated to rail inspection[44]. The laser-air hybrid ultrasonic technique pulsed lasers and detection using air-coupled acoustic transducers. They showed this system can be used to inspect the entire rail section from rail head to base.

## 4.3 Long range ultrasonic testing (LRUT)

The inspection of large structures using conventional ultrasonic bulk wave techniques is slow because scanning is required if the whole structure is to be tested. Ultrasonic testing by using guided waves (UGWs) have been potentially used as a solution for many years for the in-service testing of rail inspection instead of conventional methods [34,35].

In guided wave methods by a decrease in the frequency of acoustic wavelength increases and the waves become confined or guided and the scattering effect is much reduced [35,46]. The effective range of these waves over distances up to 30m from the transducer. However, various factors can significantly attenuate the signal and reduce the effective distance of wave travelling and may only be

a few meters[12]. Then, in order to exploit the potential of employing guided waves in the rail, there is a need to characterize their behavior with respect to the rail structure of interest [46]. Guided waves are sensitive to the structure's cross-sectional shape, to change in the cross-sectional area of the component, thickness and material properties (Poisson's ratio, Young's modulus and density) [45,47]. Guided waves can be used in three regimes, each of which has been extensively researched: short range ( $\ll 1\text{m}$ ), medium range (up to about 5m), and long range (up to around 100m) [35].

Long range ultrasonic testing (LRUT) is one of the preferred techniques in rail inspection which is based on the use of ultrasonic guided wave which typically are in the range of 20-300 kHz with relatively long ultrasonic wavelengths in comparison with conventional UT[47,48]. The technique utilizing a range of wave modes including Lamb, Plate, Rayleigh. Long-range ultrasonics is a technique based on transmitting ultrasound as volumetric waves into the structure such as a rail. In most cases, piezoelectric transducers are designed and placed so that ultrasonic guided waves can be excited at one location and can be transmitted into the structure and will propagate many meters[17,35].

The test is usually operated in pulse-echo mode, by transmitting the guided wave along the structure, and returning echoes indicating the presence of defects or other structural features. Reflections from fixed reference points, such as girth welds, can be detected as well as changes in cross sectional areas, such as cracks or corrosion. By analyzing reflections are recorded reflection the probability, approximate size and location of the defect can be obtained [11].

Nowadays, ultrasonic guided waves (UGWs) have benefits over conventional ultrasonic methods (wheel-type ultrasonic) for rail monitoring [49-56]. The main attraction of inspection by guided waves is that it can inspect a large area of the structure to be tested only from a single transducer position, so avoiding the time consuming scanning required by conventional ultrasonic or eddy current methods. This technique becomes even more attractive for the part of the structure which are difficult to access.

They are also potentially possess a high sensitivity to detect small flaws and can benefit from built-in transduction. They are not sensitive to surface shelling because they can run underneath this type of discontinuities. Small defects near to the surface will also not mask more severe, deeper, transverse cracks. A further advantage is that at the frequencies used, material attenuation due to grain boundary scattering is very low and hence alumino-thermic weld material can be readily penetrated and tested[34,35]. Moreover, because these waves propagate along, rather than across the rail, they are ideal for detecting the critical (vertical) transverse defects [34,35]. These guided waves can propagate with low attenuation, which allows the ultrasonic waves to propagate for long distances with full coverage of the cross section and are sensitive to changes in the geometry and acoustic characteristics

of the medium[45,47,57]. Guided waves are therefore eminently suitable for permanently installed automatic monitoring systems allowing coverage of significant lengths of infrastructure from a small number of monitoring points [57].

Many researchers have reported their finding regarding this technique for inspection of different parts of rail track [11,47,52,58-60]. Wavesin solids LLC. has developed a hi-rail system , known as prism, based on guided waves which is suitable for detecting large transverse rail head defects and[11]in certain setup condition for the inspection of the whole rail [61].

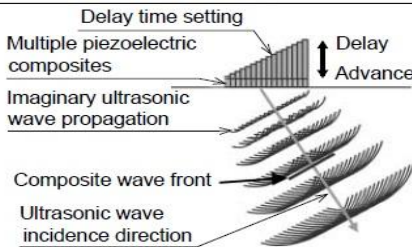
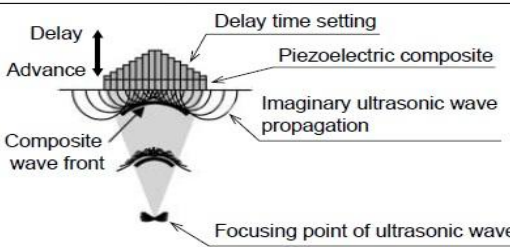
A monitoring system using permanently attached piezoelectric transducers in transmission mode was developed by IMT in South Africa [62]. Their system is used to complete detection of rail breaks and transmit and receive stations spaced approximately 1.5km apart. But the damage needs to be large enough to be detected as shown in the reference [63,64] according to a numerical analysis offixed receivers and train induced noise.

#### 4.4 Ultrasonic Phased Array (PA)

Ultrasonic Phased Array technique for non-destructive testing of structural components utilizes multiple ultrasonic piezoelectric elements and electronic time delays to create beams by constructive and destructive interference [12]. In fact, the Phased Array probe consists of a large number of transducer elements which can be arranged linearly or 2-dimensionally (2D) instead of a single transducer and beam in conventional ultrasonics which can be activated individually [65].

Phased arrays has significant technical advantages over conventional ultrasonics since the phased array ultrasonic beams can be steered, scanned, swept and focused electronically [12,17,65,66]. Unlike the conventional UT, phased-array probes have special parameters such as scanning range and focusing range of ultrasonic-wave beams and its performance depends largely on the number and size of piezoelectric elements[67]. In Table 1 principle and features of both parameters are shown.

Table 2 Principle and feature of phased-array UT[67]

Method	Electronic scanning	Electronic focusing
Control principle		
Features	Probing speed increases as a result of minimization of difficult-to-inspect areas by scanning at various angles of refraction and by electronic scanning.	Space resolution (detecting ability) is improved by ultrasonic-wave beam focusing.



Beam steering permits the optimization of beam angle, ultrasonically, by orienting them perpendicular to the predicted discontinuities, (for example lack of fusion (LOF), shrinkage, porosity, etc in alumino-thermic rail welds). Because in alumino-thermic welds beams are attenuated because of the microstructural nature of aluminumo-thermic welds (i.e. large dendritic grains) in the upper sections of the rail and causes defects in the deeper part remains undetected. Figure 4 illustrates phased array steering [33,67,68]:

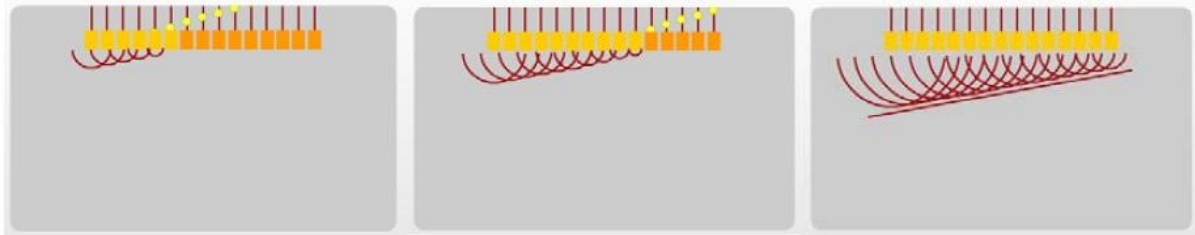


Figure 4 – Illustration of wave front formed by independent delayed firing of phased array elements (illustration courtesy of the Olympus NDT website) [33]

Ref [33] utilizes phased array beam steering principles, in order to keep the beam straight while the rail head varies. Their proposed technique (2020) is an RSU that is perfectly matched for every rail cross section. Figure 5 illustrates a comparison of the conventional ultrasound beams versus the steered phased array ultrasound beams.

Electronic focusing is another advantage of using PA technology. Focusing allows optimizing the beam shape and size at the expected discontinuity location, as well as optimizing the probability of detection (PoD).

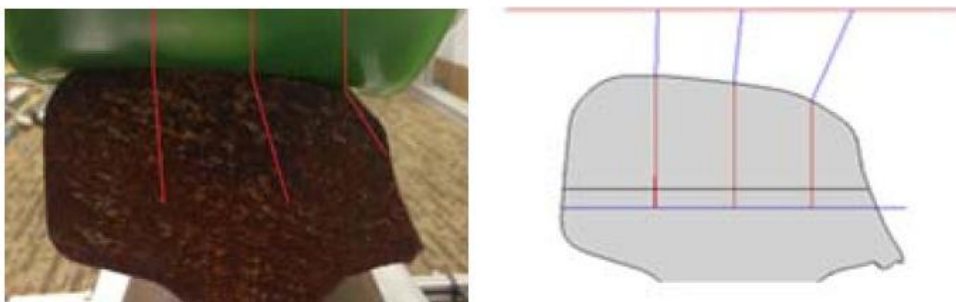


Figure 5 – Comparison of passive conventional ultrasound (left) misguided wave compared to proper wave steering possible from phased array (right) [33].

In PA technique probes are statically placed along the side of the railhead, Without moving the probes, a complete scan of the structure can be performed in a few seconds. The way this technique was applied is by setting two PA transducers along the railroad as Figure 8 shows and then recording the data [68].

The geometry changes due to wear can influence the angle at which current conventional ultrasonic approaches inspect the rail. Then by placing the transducer between the gage and field side of the railhead effect of wear geometry and surface condition on flaw sizing will be reduced [68].

Ultrasonic phased array method, by using of steering and focusing increases the energy of the beam can detect the defect in deeper parts of welds. By sweeping a focused beam all along the flaw, sizing of the transverse length of the flaw can be performed[33,68]. The Transportation Technology Center, Inc., reported feasible use of the ultrasonic phased-array (PA) technology in detection of induced transverse defects (TDs) in the web, base and of the rail. They also showed that by using a linear array approach, PA technology was capable of sizing the TD by providing a fairly accurate inspection of the flaw size across the railhead from gage to field[68].

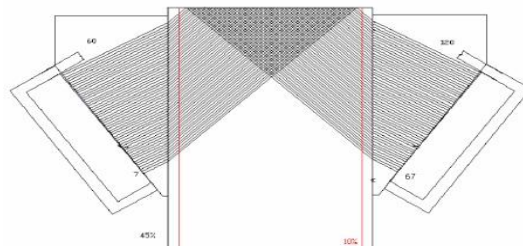


Figure 6. Electronic Scanning Configuration [12]

The first major application of the phased-array UT is inspection of complex geometry parts. When conventional UT is used, the inspecting areas must be scanned entirely with the probe. If the inspecting area includes any portion having a straight part that is too short to probe, such a difficult-to-probe portion has to be omitted from the inspection. However, such conventionally difficult portions can be inspected by using the beam scanning function of the phased-array UT instead of scanning with probe[67].

The second application is inspection of parts made of high-noise materials such as stainless steel castings and weldings. Coarse grain crystals contained in these parts deflect and scatter the ultrasonic waves and lower the propagation. By focusing an ultrasonic wave beam on these parts, the defect echoes level is made clear and the signal-to-noise ratio is improved [67,68]

The advantage of using the PA approach, for width sizing, can be found in the ease for which localizing or identifying diffracted waves from the defect can be done without moving the probe. Information on the width is clear, and the sizing is quite reliable. The PA process evaluated during this research effort uses an electronic scanning method of transmitting and receiving ultrasonic energy from various locations of the railhead. Electronic scanning is the ability to move an ultrasonic beam electronically along one axis of the array without any mechanical movement. The movement is

performed by time multiplexing the active elements. Beam movement depends on probe geometry and can be either linear scanning or circular scanning [65-69].

#### 4.4 Electromagnetic acoustic transducer (EMAT)

EMAT (Electro Magnetic Acoustic Transducer) (see Figure 7) technology is an alternative method of generating and receiving ultrasonic energy. These are transducers that are made up of coils that are placed in close proximity to the test piece. The coils produce a magnetic field that interacts with the metal, producing a deformation in the surface of the material. This deformation produces the wave of ultrasonic energy[70,71].

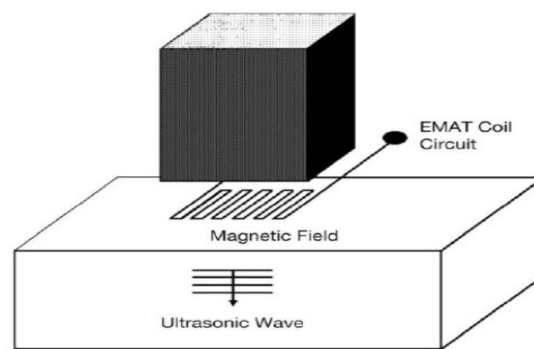


Fig 7: EMAT transducer [70]

A commercial hi-rail inspection vehicle based on an EMAT system called (RailPro) has been developed by NDT Olympus in Canada. The RailPro system uses several EMAT configurations for the generation of surface and bulk ultrasonic waves in order to inspect the whole section of rail. The system has been successfully tested on a special evaluation track containing several types of defects, including transverse fissures, horizontal and vertical head splits, split webs, bolt hole cracking, and RCF damage at inspection speeds between 5–9 km/h[70,71]. Advances in EMAT sensor technology for high-speed rail inspection and quantification of RCF damage on rail has been reported by several researchers [72]. The advantages of these units are:

- An EMAT is a non-contact transducer
- There is no need for a couplant
- They lend themselves to applications that normally have limitations, such as the examination of high-temperature components. Because this type of transducer depends on the induction of a field, the transducer has to work in close proximity to the work surface. The strength of the magnetic field is reduced as the distance between the transducer and the component surface increases.

- The gap between the transducer and the work face need not be composed of air. Examination of components that have been coated with some protective layer is possible. It is the front surface of the component material that actually generates the ultrasonic energy.
- Focusing of the beam is also possible, as is steering the beam at various angles.
- Horizontally polarized shear wave energy can be produced. The polarity is important in that horizontally polarized shear waves do not mode convert when striking surfaces that are parallel to the direction of polarization. This has certain advantages, particularly when examining austenitic welds and other materials with dendritic grain structure, e.g., certain cast stainless steels.

The disadvantages include:

- Low efficiency compared with piezoelectric transducers.
- Relatively large transducer size.
- Producing ultrasonic energy in nonconductive material is only possible if a conductive layer is applied to the surface.

According to the literature review, conventional and novel methods of NDT are briefly described. A summary of these methods and their capabilities in detecting different types of defects is presented in Table 1.

## **5. New approach in the rail monitoring**

Recent years have shown a range of different technologies and sensing techniques developed for damage detection in metallic and composite materials. This includes Acousto-Ultrasonics and guided Ultrasonic waves. Both technologies utilizes optical fiber and piezoceramic sensors for damage detection. New techniques are capable of achieving continuous monitoring, integrated and on-line damage detection systems for maintenance. Recent developments in advanced signal processing, such as neural networks or wavelets, also offer the potential for more reliable and robust damage detection and prediction. It is now clear, that sooner or later, new damage detection techniques, combined with advanced signal processing, are destined to become one of the core monitoring elements of different industry and structure. The integration of sensors, actuators, signal processors and controllers is associated with a new design philosophy leading to multifunctional and adaptable structures. The attractive potential of such technologies arise from a number of elements such as: reduced life cycle costs, reduced inspection/maintenance effort, improved performance, improved high rate operator availability, extended life of structures and improved safety.

## 5.1 Structural Health Monitoring obstacle for rails

Due to the, long structure in rails there are limitations for applying continuous health monitoring in railways. It means that, this kind of engineering structure has a very long length and due to that, the array of sensor as a receiver or transmitter shows difficulty. But new development in sensors and networks are trying to solve this problem. New generation of sensors-wireless sensor are revolving in health monitoring of huge and long structures. New investigations in rail are also expectable. In the following some new researches in wireless sensor has been explained.

Wireless sensor can monitor the structure any time and place without human intervention for a long period. This device is used to transmit and acquire sensor data in a real time mode and perform signal analysis over the tested structures [73].

Mascarenas et al [74] proposed a wireless sensor node known as Thinner that powered and operated from very low power. This device has employed ATmega128L microcontroller and few components such as AD7745 capacitance-to-digital converter and X-Bee radio. The device also implies the low cost impedance measuring chip and RF module in delivering RF energy via UAV. Park et al [75] has developed an improved wireless impedance sensor node with both functions of structural damage identifications and sensor self-diagnosis. The design focused on developing reliable and adjustable Sensor nodes for both hardware and software and introduced a temperature effect-free sensor self-diagnosis algorithm. The device used ATmega128L microcontroller and a few components such as impedance chip (AD5933), temperature sensor (ADT75) and multiplexer (ADG706) for multiple sensors integrated.

## 6. Conclusion

Up to origin of the defect in rails – manufacturing or services – type, shape and size of flaws are different and due to that, wide variety of NDT methods have been using for rail inspection. In manufacturing system online NDT including ET, RT and UT have been applied. For in service inspection because of safety and effectiveness guided wave ultrasonic and, phased array as an advanced method are used. Due to rail shape non-contact probe such as laser ultrasonic and EMAT are preferred. By new improving in wireless sensor, applying of Structural Health Monitoring which consist of sensors, signal processing and network in rails is expected as well.

## 7. Acknowledgment

The authors are grateful to UPM grant (RUGS 9348100) for their financial support.

Table 2: rail defect and suitable NDT technique [17].

Rail Defect	NDT technique	Performance
Surface defects, rail head internal defects, rail web and foot defects	Ultrasonics (UT)	Reliable manual inspection but can miss rail foot defects. At high speed can miss surface defects smaller <4mm as well as internal defects particularly at the rail foot
Surface defects and near surface internal rail head defects	Magnetic Flux Leakage (MFL)	Reliable in detecting surface defects and shallow internal rail head defects although cannot detect cracks smaller than <4mm. MFL performance deteriorates at higher speeds
Surface and near surface Internal defects	Pulsed Eddy Current including Field Gradient Imaging (PEC)	Reliable in detecting surface breaking defects. Adversely affected by grinding marks and lift-off variations
Surface breaking defects, rail head profile, corrugation, missing parts, defective ballast	Automated Visual Inspection (VT)	Reliable in detecting corrugation, rail head profile missing parts and defective ballast at high speeds. Cannot reliably detect surface breaking defects at speeds >4 km/h. Cannot assess the rail for internal defects
Welds and known defects	Radiography (RT)	Reliable in detecting internal defects in welds difficult to inspect by other means. Can miss certain transverse defects
Surface defects, rail head, web and foot internal defects	Electromagnetic Acoustic Transducer (EMAT)	Reliable for surface and internal defects. Can miss rail foot defects. Adversely affected by lift-off variations
Surface defects, rail head internal defects, rail web and foot defects	Long range ultrasonics (LRUT)	Reliable in detecting large transverse defects (>5% of the overall cross section)
Rail head, web and foot defects	Laser ultrasonics	Reliable in detecting internal defects. Can be affected by lift-off variations of the sensors, difficult to deploy at high speeds
Surface breaking defects	Alternating Current Field Measurement (ACFM)	Reliable in detecting and quantifying surface breaking defects. Cannot detect sub-surface defects. Very good tolerance to lift-off variations
Surface and near surface defects.	Multifrequency eddy current sensors	Limited experiments conducted. Has potential to reliably quantify defects detected.
Rail breaks, wheel burns, squats, wet spots, worn rail profiles	Acoustic emission (AE)	Limited experiments. Cannot detect any internal defects

## 8. References

- 1 Zumpano, G, Meo, M, "A new damage detection technique based on wave propagation for rails", International Journal of Solids and Structures 43 (2006), 1023–1046.
- 2 Toliyat, H. A., Abbaszadeh, K, Rahimian, M. M, Olson, L. E., "Rails defect diagnosis using wavelet packet decomposition", IEEE, Transactions on Industry Applications 39 (5) (2003), 1454-1461.
- 3 Cannon, D.F., Edel, K. -O., Grassie, S.L., Sawley, K., "Rail defects: an overview", Fatigue and Fracture of Engineering Materials and Structures 26 (2003), 865–887.
- 4 Network Rail Statistics, 2005–2007, from [www.networkrail.co.uk](http://www.networkrail.co.uk).



- 5 Ferreira, L. Murray, M., “*Modelling rail track deterioration and maintenance: current practices and future needs*”, Transport Reviews, 17(3), 1997, 207–221.
- 6 Grassie, S. L., “*Rolling contact fatigue on the British railway system: treatment*”, Wear 258 (2005) 1310-1318.
- 7 Epp, K. J., Mutton, P. J., “*Wheel-rail interaction: Current state of the art in the Australasian railway industry*”, Proceedings of the Railway Engineering Conference, Wollongong, November 2002.
- 8 Cannon, D. F., “*An international cross ference of rail defects*”, 2nd edition, UIC rail defect management report, June 2003.
- 9 Lonsdale, C. P., Luke S. T., “*An investigation of thermite rail weld composition and properties*”, Proceedings of the international conference of advances in welding technology, Columbus, OH, USA, 1996.
- 10 Cannon, D. F., Edel, K.-O., Grassie, S. L., Sawley, K. “*Rail defects: an overview*”, Fatigue Fracture Engineering Material Structure 26 (2003), 865–887.
- 11 Rose, J.L., Lee, C.M., Hay, T.R., Cho, Y., Park, I. K., “*Rail inspection with guided waves*”, 12<sup>th</sup> Asia-Pacific Conference on NDT (APCNDT), Auckland, New Zealand, November 2006.
- 12 Inntrack, D4.4.1, “*Rail Inspection Technologies*” Project no. TIP5-CT-2006-031415 from [www.inntrack.net](http://www.inntrack.net).
- 13 “*Devalopment of rail testing*”, from <http://www.sperryrail.com/railtesting.html>.
- 14 Bray, D. E., “*Historical review of technology development in NDE*”, Proceedings of the 15<sup>th</sup> World Conference on NDT, Roma, Italy, 2000.
- 15 Raj, M., Mallik, D., Bansal, S., Saini, R. K., Ajmeria, R. K., “*Non-Destructive Testing and Inspection of Rails at JSPL – Ensuring Safety and Reliability*”, Proceedings of 18<sup>th</sup> World Conference on Nondestructive Testing, Durban, South Africa, April 2012.
- 16 Hocking NDT Ltd, “*Rail inspection: The Eddy Current Solution*”, technical paper from [www.hocking.com](http://www.hocking.com).
- 17 Papaelias, M. PH., Roberts, C., Davis, C.L., “*A review on non-destructive evaluation of rails: state-of-the-art and future development*”, Journal of Rail and Rapid Transit 222(2008), 367-384.
- 18 Mazzeo, P. L., Nitti, M., Stella, E., Ancona, N., Distanto, A., “*An automatic inspection system for the exagonal headed bolts detection in railway maintenance*”, Proceedings of 2004 IEEE Intelligent Transportation Systems Conference Washington, D.C., USA, 2004.
- 19 Lugg, M., Topp D., “*Recent developments and applications of the ACFM inspection method and ACSM stress measurement method*”, ECNDT Conference, Berlin, September 2006.
- 20 Topp, D., Smith, M., “*Application of the ACFM Inspection Method to Rail and Rail Vehicles*”, Proceedings of ENCDT, 2005.
- 21 Howitt, M., Bombardier, “*brings ACFM into the rail industry*”, Insight 44 (6), 2002.
- 22 Edwards R.S., Dixon S., Jian X., “*Characterisation of defects in the railhead using ultrasonic surface waves*”, NDT&E International, 39 (6), 2006, 468-475.
- 23 Edwards R.S., Dixon S., Jian X., “*Depth gauging of defects using low frequency wideband Rayleigh waves*”, Ultrasonics 44, 2006, 93-98.
- 24 Edwards, R.S., Fan Y., Papaelias, M., Dixon, S., Davis, C. L. and Roberts, C., “*Ultrasonic detection of surface-breaking railhead defects*”, Proceedings of QNDE, U.S.A., 2007.
- 25 Mcaughey, K.L., Potter, D.G., Petcher P.A., Dixon, S., “*Rail track condition monitoring using electromagnetic acoustic transducers*”, proceedings of the 18<sup>th</sup> World Conference on Nondestructive Testing, Durban, South Africa, April 2012

- 26 Bentley, M. N., Lund, F. P., Withers, A., “*Field Gradient Imaging technology, applications and solutions for component and structural integrity for track and rolling stock for the rail industry*”, NEWT International Limited, NSP1001, 26/04/04.
- 27 Garcia, G., Zhang, J., “*Application of ultrasonic phased arrays for rail flaw inspection*”, Department of Transportation Report, Federal Railroad Administration, U.S., July 2006.
- 28 Davis, C. L., “*Modelling and detecting damage (wear and RCF) in rails*”, , RSSB Report, University of Birmingham, May 2003.
- 29 Greene, R. J., Yates, J. R., Patterson, E. A., “*Crack detection in rail using infrared methods*,” Optical Engineering 46(5), Article ID 051013, 2007.
- 30 Bruzelius, K., Mba, D., “*An initial investigation on the potential applicability of Acoustic Emission to rail track fault detection*”, NDT and E International, 37 (7), 2004, 507-516.
- 31 Clark, R., Singh, S., Haist, C., “*Ultrasonic characterisation of defects in rails*”, Insight, 2002, 44(6), 341-347.
- 32 Eden, K., “*Report on Rail Inspection and Maintenance*”, University of Birmingham, Trains project, April 2003.
- 33 Wigh, J., “*Development of an Improved Rail Flaw Detection System*”, Annual Conference & Exposition, Chicago, IL, September 2012.
- 34 Rizzo, P., Cammarata, M., Bartoli, I., Di Scalea F.L., Salamone, S., Coccia, S., Phillips, R., “*Ultrasonic Guided Waves-Based Monitoring of Rail Head*”, Laboratory and Field Tests, Hindawi Publishing Corporation Advances in Civil Engineering (2010), Doi:10.1155/2010/291293.
- 35 Cawley, P., “*Practical long range guided wave inspection- Application to pipes and rail*”, National Seminar of ISNT Chennai, India, 2002.
- 36 Clark, R., “*Rail flaw detection: overview and needs for future developments*”, NDT&E International 37, (2004), 11–118.
- 37 Robert E., Green Jr., “*Non-contact ultrasonic techniques*”, Ultrasonics 42, (2004), 9–16.
- 38 Scruby, C. B., Drain, L. E., “*Laser ultrasonics techniques and applications*”, (Taylor & Francis), 1990.
- 39 Lanza di Scalea, F., Kenderian, S., Green Jr., R.E., “*Non-contact ultrasonic inspection of railroad tracks*”, Proceedings of 45<sup>th</sup> International SAMPE Symposium, 2000.
- 40 Kenderian, S., Djordjevic, B.B., Green Jr., R.E., “*Point and line source laser generation of ultrasound for inspection of internal and surface flaws in rail and structural materials*”, Research in Nondestructive Evaluation 13 (2001), 189–200.
- 41 Kenderian, S., Djordjevic, B. B., Green Jr., R., “*Laser-based and air-coupled ultrasound as noncontact and remote techniques for testing of railroad tracks*”, Material Evaluation 60 (1) (2002), 65–70.
- 42 Kenderian, S., Djordjevic, B. B., Green, R.E., “*Laser/Air hybrid ultrasonic technique for railroad wheel testing*”, Material Evaluation 61 (4) (2003), 505–511.
- 43 Tournay, H.M., “*A future challenge to wheel/rail interaction analysis and design: Predicting worn shapes and resulting damage modes*”, Wear 265 (2008), 1259–1265.
- 44 Kenderian, S., “*Advanced ultrasonic techniques to determine the structural integrity of rail steel*”. PhD Thesis, The John Hopkins University, Baltimore, Maryland, USA, 2002.
- 45 Kenderian, S., Cerniglia, D., Djordjevic, B., Garcia, G., Morgan, R., Sun, J., Snell, M., “*Rail track field testing using laser/air hybrid ultrasonic technique*”, Material Evaluation 61(2003), 1129–1133.

- 46 Sanderson, R., and Smith, S., “*The use of guided waves for non destructive testing of rails: a finite element approach*”, Proceedings of the ABAQUS UK Users Group Conference, Warrington, UK, 2002.
- 47 Campos-Castellanos, C., Gharaibeh, P. Mudge, Y., Kappatos, V., “*The application of long range ultrasonic (LRUT) for the examination of hard to access areas on railway tracks*”, Brunel Innovation Centre, Brunel University, Uxbridge, Middlesex, UK.
- 48 Gharaibeh, Y., “*The application of guided waves for non-destructive examination of complex structures*”, Doctoral Dissertation, School of Engineering and Design, Brunel University, UK, 2011.
- 49 Wilcox, P., Evans, M., Pavlakovic, B., “*Guided wave testing of rail*”, *Insight* 45 (6) (2003), 413–420.
- 50 Cawley, P., Lowe, M. J. S., Alleyne, D. N., Pavlakovic, B. Wilcox, P., “*Practical long range guided wave testing: applications to pipes and rail*”, *Materials Evaluation* 61 (1) (2003), 66–74.
- 51 Hesse, D., and Cawley, P., “*Surface wavemodes in rails*”, *Journal of the Acoustical Society of America* 120(2) (2006), 733–740.
- 52 Rose, J. L., Avioli, M. J., Mudge, P. and Sanderson, R., “*Guided wave inspection potential of defects in rail*”, *NDT and E International* 37 (2) (2004), 153–161.
- 53 Bartoli, I., Lanza di Scalea, F., Fateh, M., Viola, E., “*Modeling guided wave propagation with application to the long-range defect detection in railroad tracks*”, *NDT and E International* 38 (5) (2005), 325–334.
- 54 Lanza di Scalea, F., Bartoli, I., Rizzo, P. and Fateh, M. “*High speed defect detection in rails by non-contact guided ultrasonic testing*”, *Journal of the Transportation Research Board* 1961(2006), 66–77.
- 55 Philip W. Loveday, “*Guided Wave Inspection and Monitoring of Railway Track*”, *Nondestructive Evaluation* 31 (2012), 303–309.
- 56 Edwards, R. S., Dixon, S. and Jian, X., “*Characterisation of defects in the railhead using ultrasonic surface waves*”, *NDT and E International* 39 (6) (2006), 468–475.
- 57 Cawley, P., Cegla, F., Galvagni, A., “*Guided Waves for NDT and Permanently Installed Monitoring*”, 18<sup>th</sup> World Conference on Nondestructive Testing, Durban, South Africa, April 2012,
- 58 Rose, J., Avioli, M., Song, W. “*Application and potential of guided wave rail inspection*”, *Insight* 44 (6) (2002), 353–358.
- 59 Wilcox, P., “*Long range inspection of rail using guided waves*,” in *Review of Progress in Quantitative Nondestructive Evaluation* 22 (2003), 236–243.
- 60 Fateh, M., “*On-line high speed rail defect detection*”, U.S. Department of Transportation Report, October 2005 from [www.fra.dot.gov/downloads/research/tr0507.pdf](http://www.fra.dot.gov/downloads/research/tr0507.pdf)
- 61 Cawley, P., Wilcox, P., Alleyne, D. N., Pavlakovic, B., Evans, M., Vine, K., Lowe, M. J. S., “*Long range inspection of rail using guided waves – field experience*”, Proceedings of the 16<sup>th</sup> World Conference on Non-Destructive Testing, Montreal, Canada, 2004.
- 62 Loveday, P.W. “*Development of piezoelectric transducers for a railway integrity monitoring system*”, Proceedings of SPIE, Smart Systems for Bridges, Structures and Highways 3988(2000), 330–338.
- 63 Loveday P. W., “*Guided Wave Inspection and Monitoring of Railway Track*”, Proceeding of 18<sup>th</sup> World Conference on Nondestructive Testing, Durban, South Africa, April 2012.
- 64 Ryue, J., Thompson, D.J., White, P.R., Thompson, D.R., “*Wave reflection and transmission due to defects in infinite structural wave guides at high frequencies*”, *Sound and Vibration* 330 (2011), 1737–1753.
- 65 Jörg Reinersmann, “*Phased Array technology for standard ultrasonic testing*”, Proceeding of Middle East Nondestructive Testing Conference & Exhibition, Manama, Bahrain, November 2005.

- 66 Olympus NDT, “*Advances in phased array ultrasonic technology applications*”, Hand cover, English (ISBN 0-9735933-4-2).
- 67 Kawanami, S., Kurokawa, M., Taniguchi, M., Tada, Y., “*Development of Phased-Array Ultrasonic Testing Probe*”, Mitsubishi Heavy Industries, Ltd, Technical Review 38 (3) (2001).
- 68 Federal Railroad Administration, “*Application of ultrasonic phased array for rail flow inspection*”, July 2006.
- 69 Marefat, F., Faghidi, M. R., Khodabandeh, A.R., Afshar, A.R., Amadeh, A.A., “*Risk and Reliability of Radiographic and Phased Array Ultrasonic Test on the Inspection of Boiler Connections, Based on FMEA Model*”, Proceeding of 18<sup>th</sup> World Conference on Non Destructive Testing, Durban, South Africa, 2012.
- 70 Chahbaz, A., “*Development of a mobile inspection system for rail integrity assessment*”. Tektrend International Report for the Transportation Development Centre, Montreal, Quebec, Canada, June 2000.
- 71 Chahbaz, A., Brassard, M., and Pelletier, A., “*Mobile inspection system for rail integrity assessment*”, Proceedings of the 15th World Conference of Non-Destructive Testing, Roma, Italy, 2000.
- 72 Sebko, V. P., Suchkov, G. M., and Malakhov, A. V., “Using the electromagnetic-acoustic method”, Russian Journal of Nondestructive Testing 40(7) ( 2004), 442–448.
- 73 Zainol, M. Z., Mustapha, F., Sultan, M. T. H, N.Yidris., “*Implementation of extreme low power micro-controller for a wireless structural health monitoring (SHM) system*”, Applied Mechanics and material 225 (2012), 44-49.
- 74 Mascarenas, D., Flynn, E., Todd, M., “*Wireless sensor technologies for monitoring civil structure*”, Sound and Vibration, (2008),16-20.
- 75 Park S, Shin H. H, Yun C. B., “*Wireless impedance sensor nodes for functions of structural damage identification and sensor self-diagnosis*”, Smart Materials and Structure ,18 (2009), 1-11.

# ACOUSTIC WAVE FINITE ELEMENT ANALYSIS STUDY FOR ULTRASONIC TOMOGRAPHY

<sup>1</sup>M. J. PUSPPANATHAN, <sup>1</sup>N. M. N. AYOB, <sup>1</sup>F. R. YUNUS, <sup>1</sup>R.A. RAHIM, <sup>2</sup>F. A. PHANG

<sup>1</sup>Process Tomography and Instrumentation Research Group (PROTOM-i), INFOCOMM Research Alliance, Faculty of Electrical Engineering, Universiti Teknologi Malaysia 81310 UTM Skudai, Johor, Malaysia. Phone: +607-5537801, Fax: +607-5537811

<sup>2</sup>Centre of Engineering Education (CEE), Universiti Teknologi Malaysia, 81300 UTM Skudai, Johor, Malaysia. Phone: +607-5537906, Fax: +607-553 7592

E-mail: <sup>1</sup>ruzairi@fke.utm.my, <sup>2</sup>p-fatin@utm.my

## Abstract

A study of acoustic wave transmission through obstacles and boundaries surface for ultrasonic tomography applications has been carried out. Ultrasonic tomography for water – oil two phase flow sensing will rely upon the complex ratio of sound pressure to particle velocity which is the acoustic impedance matching. According to Snell's Law, the ultrasonic transmission properties can be obtained on the basis of incidence angle, acoustic impedance and basic frequency of ultrasound, material and thickness of the pipeline. These parameters correspond to maximum transmission of an ultrasonic wave from one medium to another when the characteristic impedances are matched. To investigate the wave's transmission and diffraction on water – crude oil boundaries, several simulations using finite element method (FEM) have been carried out. The simulated result images successfully visualize the ultrasonic wave transmission and reflection characteristic in the two phase liquid flow tomography system. Thus, the wave propagation behaviors in the boundaries are also presented. The information and results obtained is useful for further development of ultrasonic tomography liquid flow measurement.

**Keywords:** ultrasonic tomography, acoustic wave, finite element analysis, liquid flow measurement

## 1. INTRODUCTION

Ultrasonic tomography is a measurement technique using ultrasonic waves to investigate the activities inside the measurement subject. This method is widely applied in oil exploitation and chemical process monitoring. This system was developed with the capability to reconstruct the gas-liquid, liquid-liquid two phase flow over the cross section of a pipe. This method is much

complex and costly due to the requirement of utilizing many transducers around the pipeline to detect the echoes scattered around the measurement subject [1].

The aim of this paper is to investigate the acoustic pressure wave propagation behavior in water-crude oil two phase liquid flow in a pipeline. The problem raised is the strong mismatch between the acoustic impedance of the phases [2, 3]. This condition creates a boundary level between two different material and phases at the water-crude oil liquid boundary. These complications will result in low efficiency and low accuracy in ultrasonic tomography flow system. Therefore, it has become necessary to get better understanding on the dynamic characteristics of acoustic wave propagation behavior in a pipeline.

## 2. THE HARDWARE CONFIGURATION AND SETUP

To investigate the ultrasonic wave transmission and reflection, the experimental ultrasonic wave propagation hardware setup is illustrated as in Figure 1.

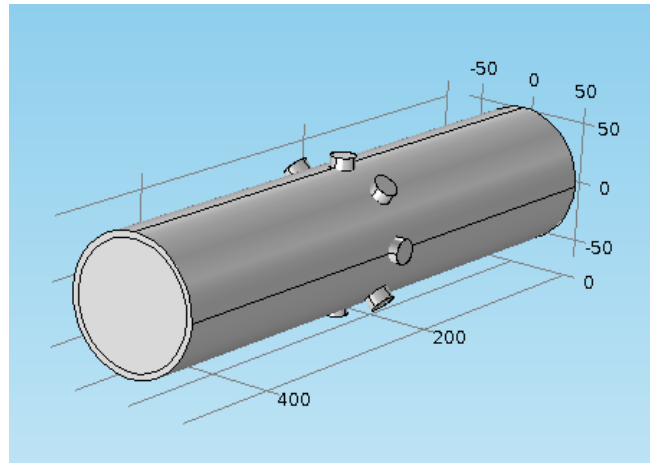


**Figure. 1.** Ultrasonic tomography system hardware setup

Ultrasonic transducers are mounted surrounding an acrylic pipeline. These sensors will produce 315 kHz pulse to measure the two phase liquid flow in an acrylic pipeline.

The ultrasonic sensor system is based upon interactions between the incident ultrasonic waves and the object to be imaged. In most non-destructive testing or medical applications, an object or field of interest is irradiated from a single viewpoint. The transmitted ultrasonic wave has a wide beam angle of  $125^{\circ}$ . Some ultrasonic process tomography utilizes a wide beam angle beam as shown in Figure 2 (a) and (b) below.



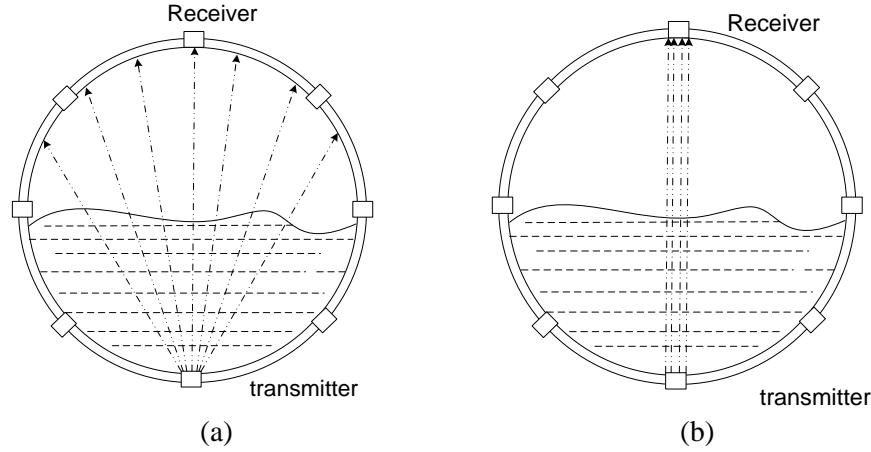


**Figure 2:** Wave beam (a) Wide beam projection (b) Narrow beam projection

Whether an ultrasonic beam is narrow or wide angel, it advances as a longitudinal wave front, in common with all sound waves.

### 3. ULTRASONIC WAVE TRANSMISSION AND REFLECTION

The ultrasonic propagation speed could be measured by using two types of configuration which is the through transmission method and pulse – echo method [4] which will only take effect if the ultrasonic wave able to transmitted through the pipe wall into the liquid medium. This system uses ultrasound to detect the changes of acoustic impedance ( $Z$ ) which is closely related to density ( $\rho$ ) of the medium. This can be a useful descriptor to identify the complex ratio of sound pressure to particle velocity which is analogous to electrical impedance. The acoustic equivalent to this relation is given by below equation [5, 6].

$$Z = \rho c \quad (1)$$

Where  $Z$  is the acoustic impedance ( $\text{kg/m}^2\text{s}$ ),  $\rho$  is the density of the medium ( $\text{kg/m}^3$ ) and  $c$  is the sound velocity in the medium ( $\text{m/s}$ ). When an ultrasonic beam reflects from the boundary, the acoustic reflection coefficient ( $R$ ) and transmission coefficient ( $D$ ) from material 1 to material 2 as in figure 2 (a) can be expressed as follows:

$$\text{Reflection coefficient, } R = \frac{p_r}{p_e} = \left[ \frac{Z_2 - Z_1}{Z_2 + Z_1} \right] \quad (2)$$

$$\text{Transmission coefficient, } D = \frac{p_d}{p_e} = \left[ \frac{2Z_2}{Z_2 + Z_1} \right] \quad (3)$$

Where  $p_e$  is the incident wave sound pressure,  $p_r$  is the reflected wave sound pressure and  $p_d$  is the transmitted wave sound pressure [7]. This incident is illustrated as below Figure 3 (a) and (b).

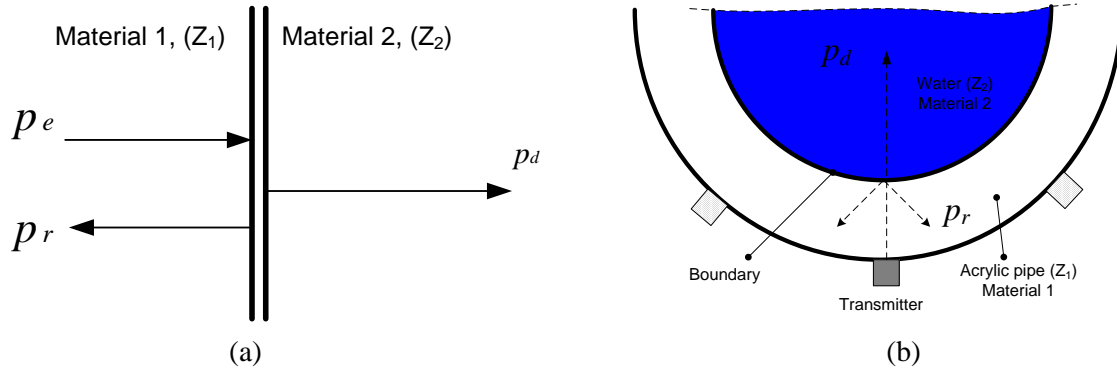


**Figure 3:** Wave propagation; (a) From material 1 to material 2. (b) From pipe section to liquid

#### 4. RESULTS AND DISCUSSION

It is mathematically proven that the 315 kHz ultrasonic wave is able to transmit through the acrylic pipe material into the water medium and further transmit through the crude oil – water boundary. Somehow, the transmitted and reflected waves will contact with one another in the pipeline. It is important to take this phenomenon into consideration before designing the tomography system. When the ultrasonic waves propagate in the acrylic cylinder pipe, it reflects off the surface wall. This leads to a distribution of ultrasonic energy in different forms that depend basically on the geometry of the pipeline and the location of sensors placing [8]. The occurrence of these overlapping waves will produce inaccurate results if the measurement system fails to differentiate between transmitted signal and overlapped signal. The direction of this sound propagation is determined by the sound speed gradients in the liquid medium.

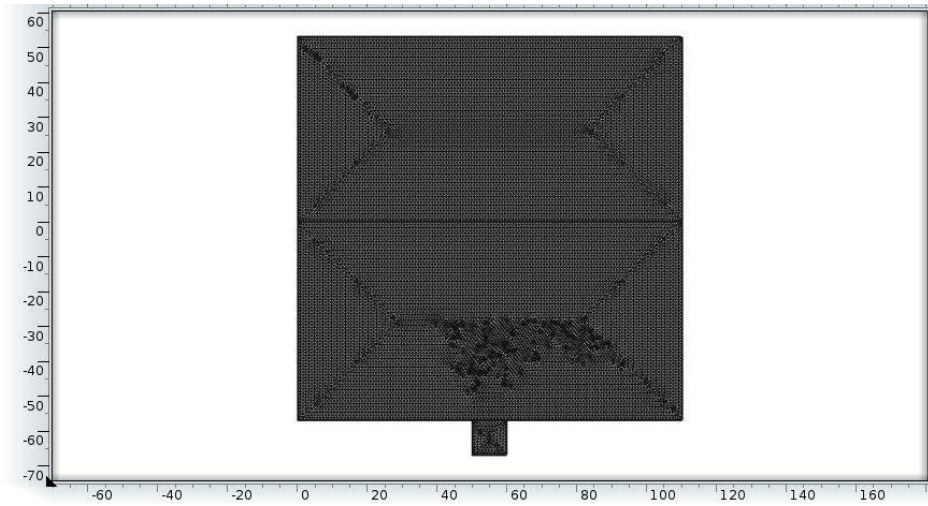
Therefore, a theoretical model of acoustic wave scattering from the liquid boundary is required to determine the acoustic pressure distribution in the mixture water/crude oil for ultrasonic tomography applications [9]. This case, a finite element method using COMSOL Multiphysics was implemented to verify the mathematical results in equation 2 and 3 and further visualize the acoustic wave propagation and the scattering effects.

The hardware model specification is as the actual measurement system setup with an acrylic pipe diameter 110 mm, 10 mm ultrasonic transmitter with 315 kHz. Below are the parameters for the material used in the two phase liquid-liquid flow measurement:

**Table 1:** Material's parameters for two phase liquid flow measurement

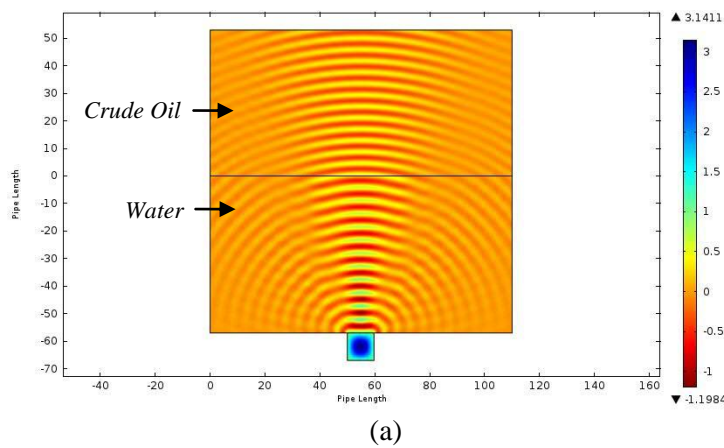
Material	Density [kg/m <sup>3</sup> ]	Speed of Sound [m/s]
Crude oil	825	1300
Water	1000	1500
Air	1.25	343

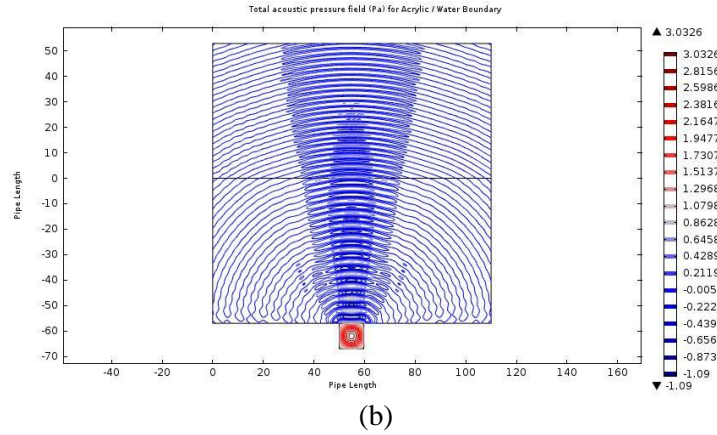
By using FEM, the cross-section region of the hardware needs to be discretized as triangular elements with mesh element size 0.009 mm to 1.0 mm. Figure 4 shows the cross-sectional meshed image.



**Figure 4:** Cross-sectional meshed image with mesh element size range 0.009 mm – 1.0 mm

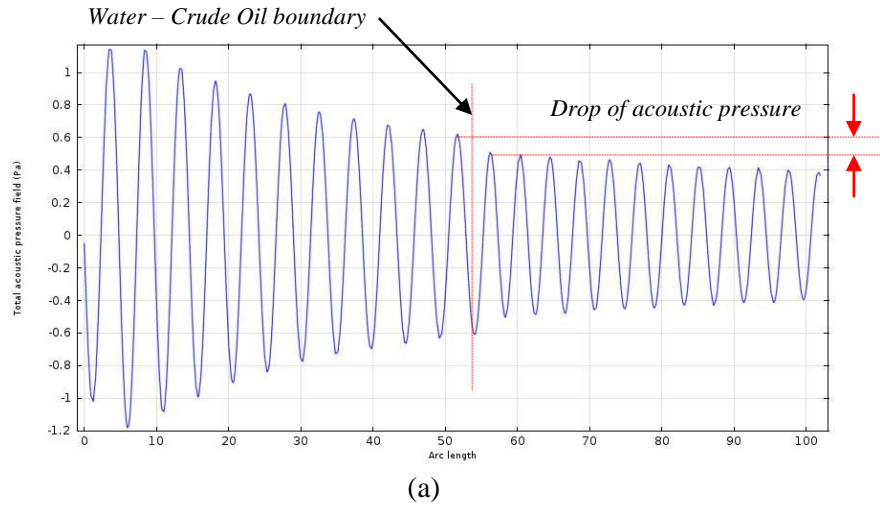
From the meshed element image, the total acoustic pressure field (Pa) for acrylic/water boundary was produced as in Figure 5 below.





**Figure 5:** Total acoustic pressure field (Pa) for water-crude oil; (a) surface view (b) contour view

The simulated result visualizes the ultrasonic wave propagating from water medium into crude oil medium and its scattering effect due to the reflection on water-crude oil boundary wall. The residual ultrasonic wave is sufficient enough to penetrate the water-crude oil boundary into the crude oil medium. Certain amount of the acoustic wave pressure will reflect back at this boundary due to the differences of impedance value between water and crude oil. The speed of sound in this two different material; water and crude oil varied from each other with the speed of 1500 m/s and 1300 m/s respectively. Below Figure 6 shows the speed of sound and the total acoustic pressure field in the measuring zone.



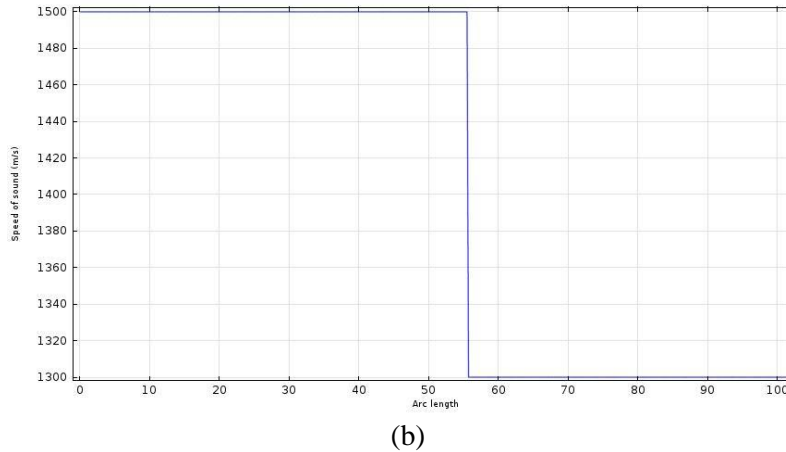


**Figure 6:** Ultrasonic wave transmission through water-crude oil boundary (Pa) distribution in a water-crude oil multiphase flow; (a) total acoustic pressure (b) speed of sound

The simulated result visualizes the ultrasonic wave behavior propagating from water into crude oil medium. Due to the high amount of acoustic wave able to penetrate through the water-crude oil boundary, the amount of reflection and scattering effect is hardly seen (Figure 6 (a)). This small amount of losses due to the interaction behavior is complex and depends not simply upon the differences in acoustic impedance, but also on the size and shape of the interface or boundary [10]. To verify and evaluate the reflected and scattered acoustic wave, the sound pressure level was computed and compared as in Figure 8.

## 6. CONCLUSION

In the present study, the acoustic wave pressure and sound pressure propagation behavior in mixing flow of water and crude oil in acrylic pipe has been simulated using COMSOL Multiphysics.

Mathematically, it is proven that the greater the difference of impedance in the materials, the higher the wave will be reflected and scattered and vice versa. This can be determined by calculating the reflection and transmission coefficients. To investigate the transmission and reflection behavior, the total acoustic wave pressure distribution, ultrasonic wave propagation, reflection and scattering effect was simulated and presented using FEM generated images.

The result obtained could aid in detection and measurement of two phase liquid flow regime particularly in the ultrasonic tomography applications.

## ACKNOWLEDGEMENTS

We greatly appreciate Universiti Teknologi Malaysia and PROTOM research group for providing the facilities which enable this project to be done. We are also grateful for the consultation and cooperation of I-Stone Sdn. Bhd during the process of this study.

## REFERENCES

- [1] S. Wada, *et al.*, "Pattern recognition and signal processing of ultrasonic echo signal on two-phase flow," *Flow Measurement and Instrumentation*, vol. 17, pp. 207-224, 2006.
- [2] R. D. M. Carvalho, *et al.*, "Application of the ultrasonic technique and high-speed filming for the study of the structure of air-water bubbly flows," *Experimental Thermal and Fluid Science*, vol. 33, pp. 1065-1086, 2009.
- [3] Y. Inoue, *et al.*, "A study of ultrasonic propagation for ultrasonic flow rate measurement," *Flow Measurement and Instrumentation*, vol. 19, pp. 223-232, 2008.
- [4] S. A. Lopez-Haro, *et al.*, "Evaluation of an ultrasonic propagation speed measurement system in the temperature range from 20 degree to 45 degree C," in *Health Care Exchange (PAHCE), 2010 Pan American*, 2010, pp. 85-89.
- [5] R. A. Williams and M. S. Beck, *Process Tomography, Principles, Techniques and Applications*. England: Butterworth Heinemann 1995.
- [6] H. Murakawa, *et al.*, "Application of ultrasonic multi-wave method for two-phase bubbly and slug flows," *Flow Measurement and Instrumentation*, vol. 19, pp. 205-213, 2008.
- [7] C. S. Wachinger, R. ; Navab, N., "Estimation of acoustic impedance from multiple ultrasound images with application to spatial compounding," in *Computer Vision and Pattern Recognition Workshops, 2008. IEEE Computer Society Conference*, 2008.
- [8] J. A. N. Bargoshadi, E., "Ultrasonic dispersion system design and optimization using multiple transducers," presented at the Waves, and Device Applications (SPAWDA) and 2009 China Symposium on Frequency Control Technology, Joint Conference of the 2009 Symposium, 2009.
- [9] O. Falou, *et al.*, "P3E-3 Finite Element Modeling of Ultrasound Scattering by Spherical Objects and Cells," in *Ultrasonics Symposium, 2006. , 2007*, pp. 2072 - 2075.
- [10] M. H. F. Rahiman, *et al.*, "Design and modelling of ultrasonic tomography for two-component high-acoustic impedance mixture," *Sensors and Actuators A: Physical*, vol. 147, pp. 409-414, 2008.



# Continuous Wavelet Transform Analysis and Modal Location Analysis Acoustic Emission Source Location in Steel Pipe

Shukri Mohd <sup>1</sup>, Karen M Holford <sup>2</sup> and Rhys Pullin <sup>2</sup>

1. Nondestructive Testing Group, Industrial Technology Division, Malaysian Nuclear Agency, 43000, Bangi, Selangor. Malaysia
2. Cardiff School of Engineering, Cardiff University, Queen's Buildings, The Parade, CARDIFF CF24 3AA  
Tel: +44(0) 29 20874070 Fax: + 44 (0)29 20874716

## Abstract

Source location is an important feature of acoustic emission (AE) damage monitoring in steel structures. The ability to accurately locate sources can assist in source characterisation and early warning of failure. This paper describe the development of a novel AE source location technique termed “ Wavelet Transform analysis and Modal Location (WTML)” based on Lamb wave theory and time-frequency analysis that can be used for global monitoring of plate like steel structures. Source location was performed on a steel pipe of 1500 mm long and 220 mm outer diameter with nominal thickness of 5 mm under a planar location test setup using H-N sources. The accuracy of the new technique was compared with other AE source location methods such as the time of arrival (TOA) technique and DeltaT location. The results of the study show that the WTML method produces more accurate location results compared with TOA and triple point filtering location methods. The accuracy of the WTML approach is comparable with the deltaT location method but requires no initial acoustic calibration of the structure.

**Keywords:** Acoustic Emission, Source Location, Wavelet Transform, Modal Theory

## 1. Introduction

In normal practice, after detection of a fatigue crack in a steel component during periodic non-destructive inspection of power plants, fracture mechanics methodologies are used to estimate the safe operational life of the steel component or structure. Furthermore, a life prediction study can be useful to determine component flaw inspection intervals along with critical flaw shape and sizes for safety acceptance criteria. Based upon this information, maintenance and replacement schedules can be drawn to ensure continued safe performance of the plant. In the recent economic environment, there is a strong and growing need for in-service inspection techniques which can reduce downtime for inspection and extend run time between inspection overhauls. Major economic advantages arise from remote monitoring or non invasive inspection techniques which provide a reliable global inspection procedure to detect and locate crack growth such as from thermal fatigue in nuclear piping systems. Remote monitoring can reduce maintenance periods and hence save costs.

Fatigue crack growth emits acoustic energy and one of the advantages of acoustic emission (AE) testing is its ability to locate this kind of defect by using an array of sensors at a distance from the source. The cost saving of deploying an AE inspection method can be achieved by minimisation of the time to perform the follow up test due to the localisation of the damage source and the downtime associated with plant shut down. Further cost saving can be achieved if defects can be sized as well as located.

This work aims to develop a new AE source location methodology using wavelet transform analysis (WT) and modal location theory, to compare the accuracy of the

new proposed method with time of arrival (TOA), triple point (TP) filtering and DeltaT methods and to seek the possibility of developing an AE crack length measurement procedure based on WTML method.

## 2. Current source location techniques; principal and limitations

Source location is an important feature of AE structural integrity monitoring and accurate source location requires the application of a series of very important processes including; accurate detection and processing of AE signals, event detection and grouping of AE signals to form an accurate event record, extraction of critical timing features and assignment of their correct propagation velocity, and application of the appropriate location algorithm. Time of arrival (TOA) source location [1] is the most widely used location method and this is the basis used in most of the commercial AE software. However, other methods such as Waveform filtering methods [1] and DeltaT method [2] can also be used.

The TOA method is based on the flight time from an AE event to detection at sensors within an array. In this method, the velocity of wave propagation in the medium is assumed to be constant and it is assumed that there is a direct path from source to sensor. By calculating the difference between two or more arrival times, the origin of the source can be identified. However, due to the noise from the environment, most of the available commercial AE systems use first threshold crossing for measuring this flight time of the AE signal instead of first hit arrival. The time delay between the actual first hit arrival and first threshold crossing can produce errors in the TOA measurement which may lead to source location inaccuracy.

DeltaT ( $\Delta T$ ) method works on the same principle as the TOA method utilising the time arrival of the signal at the sensor [2]. However, in the  $\Delta T$  method, source location is derived from a user defined “map” of the velocity profile of the structure rather than using a constant wave velocity. A map is constructed over the area of interest by analysis of the arrival time delay at pairs of sensors from particular source locations. The location of any previous, current or future AE data received from within the map area can be identified by comparing it with the  $\Delta T$  maps.

This method has been shown to be more accurate than TOA because velocity and geometry errors are minimised. Effects from boundary reflections and mode conversions are also accounted for in  $\Delta T$  location algorithm. This method is found suitable for structural health monitoring of structures with non uniform geometry such as in aircraft landing gear [2].

The main disadvantages of the  $\Delta T$  location methods are; the map should be constructed before the actual test for a specific location (i.e., the AE data from outside the map area cannot be analysed by this technique) and the analysis is only valid if the location of the sensor arrays does not change. Furthermore, since the arrival time for this location method is also determined by first threshold crossing, time of arrival error due to the delay between first hit arrival and first threshold crossing may also lead to source location inaccuracy.

### 3. Modal location theory

Conventional AE analysis techniques have mainly utilised simple signal parameters like amplitude, duration, counts and energy and the rate at which AE signals occurred. An alternative to this conventional technique exploits the dispersive nature of Lamb waves and is known as modal acoustic emission (MAE) [3, 4].

According to MAE, for a fixed plate thickness, different frequency components of Lamb waves travel at different velocities. MAE source location techniques involve determination of the arrival time of significant symmetric (extensional) and asymmetric (flexural) wave components and computing the distance of the source to sensor by measuring their temporal separation [5, 6].

Single sensor modal analysis location (SSMAL) works on the MAE theory. This method is based on the dispersive characteristic of Lamb waves that propagate in plate like structure. SSMAL utilises the time delay of the  $S_0$  and  $A_0$  mode of each waveform signal (time domain signal) and source location is determined by the velocity of these two modes and their temporal separation [5,7]. The distance of the source from sensor is determined through temporal separation between particular mode components. If the two basic components of lamb waves,  $S_0$  and  $A_0$ , travel at different velocities  $C_{S0}$  and  $C_{A0}$ , and the time lapse ( $\Delta t$ ) between their arrival is measured, then the source to sensor distance ( $D$ ) is given by [7];

$$D = \Delta t (C_{S0}C_{A0} / C_{S0} - C_{A0}) \quad (\text{Eq. 1})$$

SSMAL is expected to produce better location results compared with TOA method since the timing error due to the arrival delay between first hit arrival and first threshold crossing is minimised. However, due to dispersion characteristic of Lamb wave, superposition of the  $A_0$  mode arrival with other higher order asymmetry components will lead to source location inaccuracy due to the temporal separation measurement error.

MAE location method promises an accurate source location result if the temporal separation error due to the superposition of  $A_0$  mode from other wave components can be resolved. Temporal separation measurement error in SSMAL can be improved by deploying time-frequency analysis which can discriminate the content of AE signal instead of depending on time domain waveform analysis for temporal separation measurement.

The availability of an additional representation, in term of time frequency analysis of acoustic wave propagating in the dispersive media, by using wavelet transforms (WT) analysis [8] enables the discrimination of various frequency ranges of AE signals which, when used in conjunction with modal analysis, can improve location accuracy.

### 4. Wavelet transform analysis

WT is a mathematical tool for analysing non stationary signals, such as transient AE waves, based on time-frequency analysis. The wavelet itself is a very short, time based

signal, usually an oscillating signal with one or several cycles [9]. This wavelet is used as a basis for decomposition of the waveform into multiple component parts called coefficients, based on location and scale. WT provides two dimensional coefficients, frequency and time. The wavelet coefficient represents the correlation percentage of that particular wavelet to the waveform and its value gives a third dimension of the data, an amplitude or strength associated with them [10].

With the wavelet approach, the frequency content and the time (position) of the waveform signal can be viewed. WT can be deployed for more accurate source location and can improve SSMAI by providing more accurate temporal separation measurements and hence crack length measurement can be made.

## 5. Wavelet Transform Analysis and Modal Location (WTML) method

In this study, it is proposed that WT analysis assisted by a modified dispersion curve and modal location theory can be used to achieve a more accurate AE source location. WT assisted by a modified dispersion curve is used to distinguish the arrival  $A_0$  from the arrival of other components and noise signals and therefore improves the temporal measurement error of SSMAI method.

This novel approach is called the Wavelet Transform analysis and Modal Location (WTML) method and utilises the wavelet coefficient plot against time from a WT analysis for accurate measures of the temporal separation between  $A_0$  and  $S_0$  modes. In WTML method, temporal separation is measured from first minimum value of wavelet coefficient of those wave components rather than using peak values as used by other researcher [11, 12]. It is expected that this temporal separation measurement approach will give more accurate results since the first minimum wavelet coefficient represents the actual first arrival wave component whereas the maximum coefficient represent the peak to peak temporal separation. This temporal separation measurement is then utilised in the SSMAI calculation (Eq. 1) and it is expected that WTML approach will produce more accurate source to sensor location results compared with other location methods. Furthermore, WTML method utilises a modified dispersion curve to validate the location calculation accuracy.

The WTML method developed and used in this study involves four main steps; Waveform acquisition and processing, source to sensors distance calculation, verification of source to sensor distance measurement and location of events.

### 1. Waveform acquisition and processing

The AE waveform from an acoustic source is acquired. This waveform is then transformed into a wavelet. This transform enables the wavelet of the waveform and the plot of wavelet coefficient strength against time to be visualised

### 2. Source to sensors distance calculation.

In principle, the SSMAI equation (Eq. 1) is used to calculate the source to sensor distance. However, in WTML approach, temporal separation is determined using WT analysis instead of using the time domain waveform signal analysis.

The following are the steps for source to sensors distance calculation.

- Calculate theoretical dispersion curve (velocity against frequency) for material under investigation. The theoretical velocity of fundamental symmetry ( $cS_0$ ) and asymmetry ( $cA_0$ ) modes from this dispersion curve needs to be determined.
- Measure the temporal separation between  $S_0$  and  $A_0$  component from wavelet coefficient plot for every sensor.
- Calculate source to sensor distance using SSMAIL.

### 3. Verification of source to sensor measurement

This verification is performed by calculating a new dispersion curve, frequency against time, for material under test using the calculated source to sensor distance from the steps described above. This modified dispersion curve is then overlaid onto the transformed wavelet from step 1. The position (time) of  $S_0$  and  $A_0$  modes is then evaluated against the wavelet, wavelet coefficient plot and waveform plot.

### 4. Location of events.

The circle intersection technique has been used for determining the source location. For verified source to sensor location from the previous step, a circle is plotted around every sensor and the verified source to sensor distance is the radius of these circles. The intersection of every circle is used as the source location.

## 6. Experimental Setup and Validation Procedure

MISTRAS WD sensors (working frequency range of 100-1000 kHz) were used throughout this work. The sensors were mounted on a steel pipe and held in position with magnetic clamps. The pipe was manufactured from mild steel with dimension of 5 mm thick, 1500 mm long and 220mm diameter. A blunted notches with length of 50 mm was introduced onto the pipe specimen as shown in Figure 1 to represent the edge of a crack. Four sensors were mounted onto the pipe surface. A four channel MISTRAS AEwin DiSP data acquisition system was used for AE waveform acquisition. Detected events were pre-amplified by a 40 dB preamplifier. The acquired waveforms were stored on the computer for further analysis.

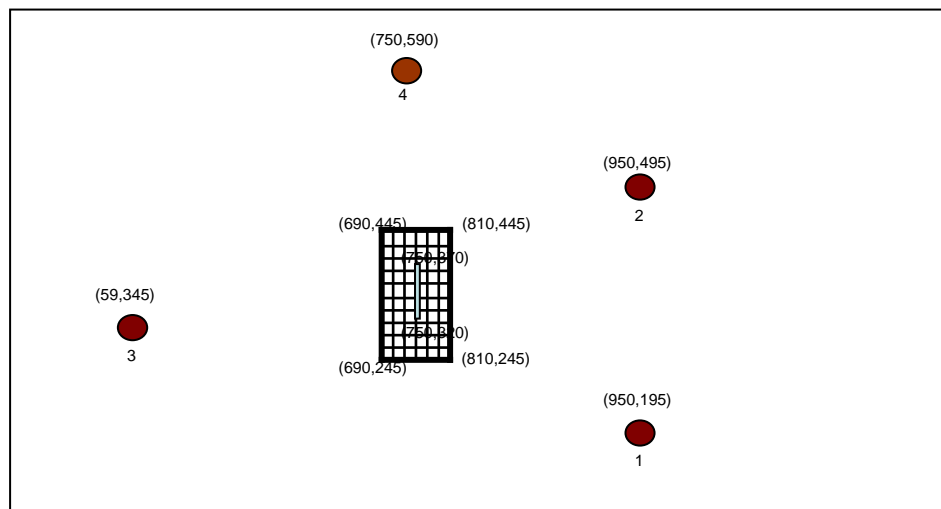


Figure 1. Sensors and grid arrangement on the unwrapped pipe surface

For DeltaT location, an area of 120mm by 200mm was selected on the pipe surface. A grid density of 20mm was constructed around the notches, creating 66 nodes. Five Hsu-Nielson (H-N) sources were conducted on each node. Figure 1 shows the location of the sensors, notch location and the grid arrangement for the DeltaT location. H-N data on every node and notch was processed using the deltaT software developed by Baxter [2] for deltaT mapping. To assess the performance of the described technique, H-N sources were conducted on each notch.

## 7. Results and Discussion

Figure 2 shows a typical result of wavelet transform of a detected waveform from H-N source at the notch tip processed by Vallen wave importer and wavelet transform software [13].

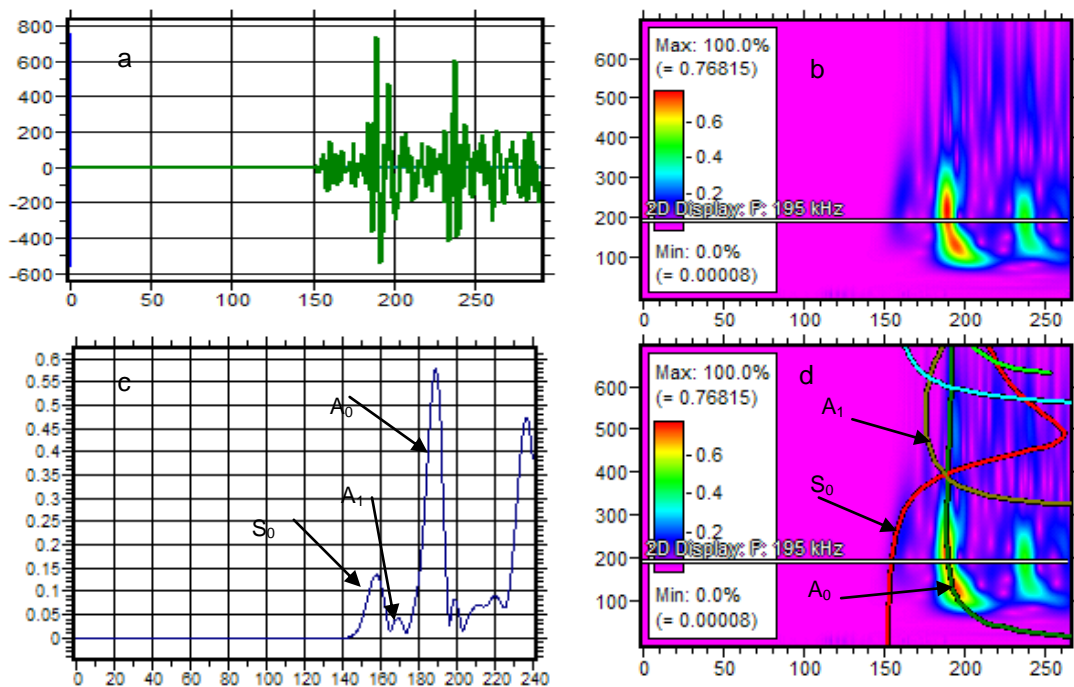


Figure 2. Typical Wavelet transforms analysis result

Figure 2a) shows a typical transient AE waveform signal produced by H-N sources. It is clearly shown in this figure that the first detected signal is the low amplitude  $S_0$  component followed by high amplitude  $A_0$  component that propagates at a slower velocity than the  $S_0$  component. The arrival of faster  $S_0$  component can be easily determined from this waveform; however the arrival of  $A_0$  component is overlapped with other low amplitude signal components which appear between the  $S_0$  and  $A_0$  modes.



Figure 2b) shows the wavelet of the waveform signal. The vertical axis shows the frequency content (in kHz) of the signal while the horizontal axis represent the time of the signal (in seconds). The colour contour represents the strength of the signal.

Figure 2c) shows a wavelet coefficient plot against time for the transformed wavelet from the above waveform. It is clearly shown in this figure that the  $A_1$  component can be easily distinguished from  $A_0$  by wavelet frequency-time analysis approach. Therefore, the accurate arrival of  $A_0$  component can be accurately determined and the temporal separation error due to superposition of  $A_0$  mode with other waveform component (which is  $A_1$  mode in this case) can be removed.

Figure 2d) shows how the modified dispersion curve, which is calculated based on the WTML, is overlaid on the wavelet signal. It is clearly shown that the modified dispersion curve of  $S_0$  and  $A_0$  modes based on this calculation is perfectly matched with wavelet transform analysis result. This result suggests that accurate location is obtained using WTML method by improving coefficient temporal separation measurement. Temporal measurement error in SSMAL is highly improved by WT location methodology.

Figure 3 shows the typical location of AE event from H-N source analysed by the WTML method showing the calculated radius of source to sensor distance based on Eq. 1

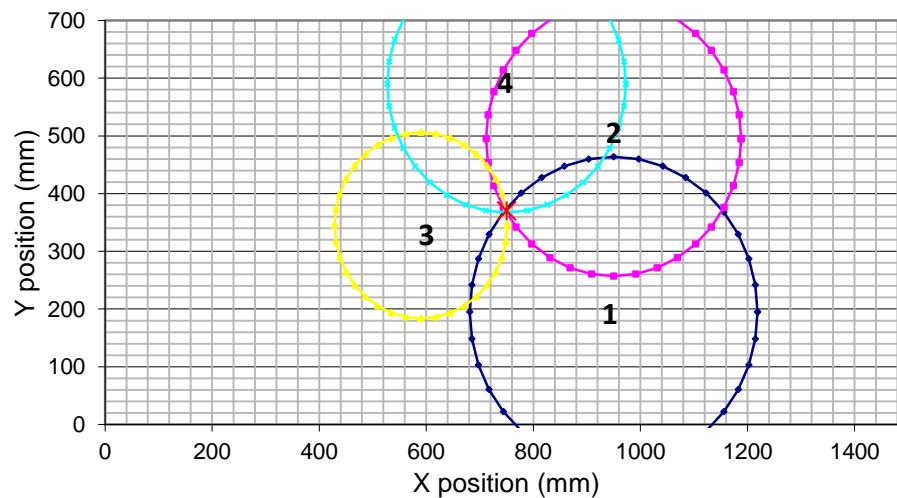


Figure 3. Typical WTML location result shown by circle intersection at upper notch tip

Four circles represent the distance of H-N source from channel 1, 2, 3 and 4 calculated by WTML methodology. The WTML source location result is achieved by using the circle intersection of these four circles. It is clearly shown that all circles intersect at almost a single point suggesting that, source to sensor distance using this new location method is very accurate.

Figure 4 shows the typical location of AE events from H-N sources analysed by TOA and triple point filtering under planar location setup, deltaT and WTML methods.

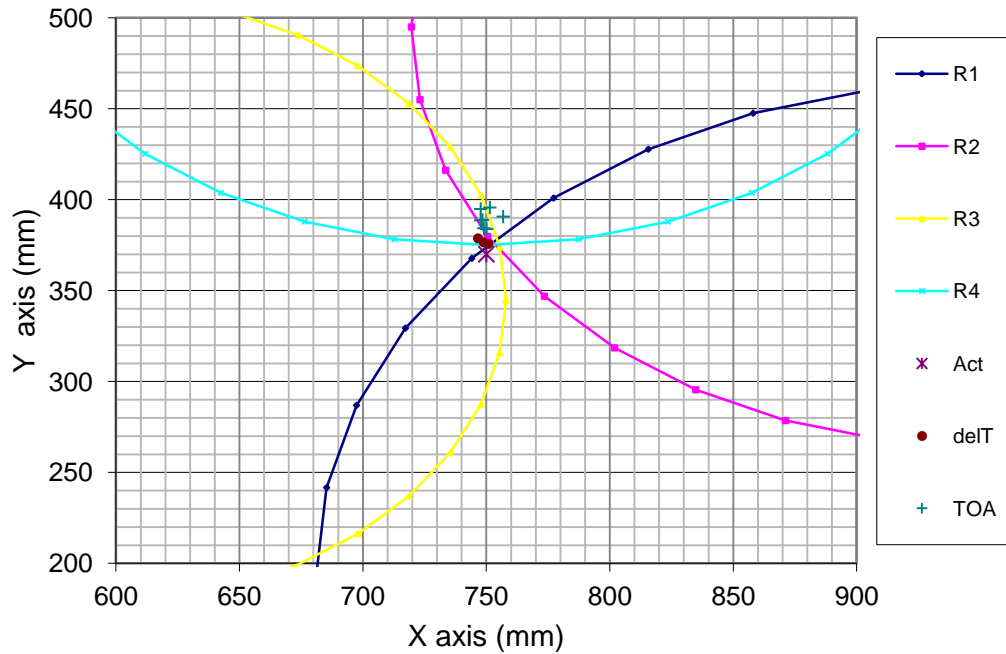


Figure 4. H-N source at notch tip located by TOA, DeltaT and WTML methods

Figure 5 presents a close up of the notch area and clearly shows that the TOA location result produces relatively the biggest location error compared with the other location methods. The possible sources of error in TOA source location are; premature triggering, inaccurate arrival time measurement or dispersion of flexural mode component as suggested by Holford [3]. The root mean square errors of location determined by different location methods and their standard deviation are shown in Table 1.

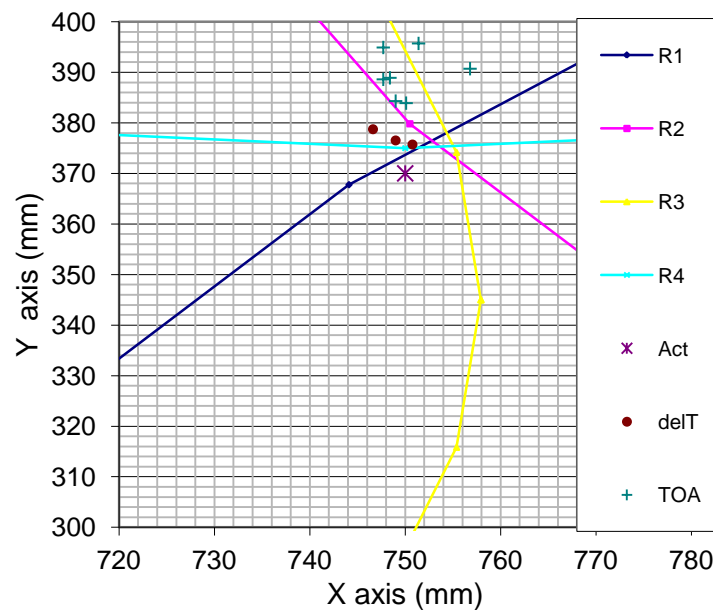


Figure 5. Close-up of H-N source location result in Figure 4

Table 1 RMS of location error calculated using TOA, DeltaT and WTML and their standard deviation

	Source to sensor distance error (mm)						
Sensor	Actual (mm)	TOA		DeltaT		WTML	
		RMS	STD	RMS	STD	RMS	STD
1	265.75	14.22	4	5.33	2.08	1.34	1.39
2	235.85	11.53	4.09	2.88	0.87	1.02	0.83
3	161.94	6.24	3.87	1.34	1.43	1.13	1.12
4	220.00	21.28	4.65	6.72	1.22	1.18	1.13

The location result as presented in Figure 5 also shows that the source to sensor distance determined by WTML method is more accurate than TOA method. The possible reason for higher accuracy achieved by WTML method is that the calculation of temporal separation does not involve the time delay from first arrival and first threshold crossing. The capabilities of WT analysis for presenting the AE signal in the time frequency domain also improved the location measurement error of SSML method by clearly discriminating the arrival of  $A_0$  from other wave components.

The accuracy of WTML location result is also comparable with DeltaT method as shown in Table 1. However, WTML can be considered as easier and more reliable method as sensors can be moved unlike DeltaT. There is also no need for a grid and H-N source for training data for initial location mapping. Further more, the standard deviation of WTML is better than delta method which suggests that this method provides a more precise result compared with other source location approaches. Furthermore, the results suggest that a single sensor WTML analysis can be used to monitor the crack growth from fatigue at known locations in nuclear piping system.

## 8. Conclusions

In this study, the novel WTML method was successfully developed for more accurate AE source location. This method is developed based on wavelet transform analysis and modal location theory.

It is found that the WTML methodology yields more accurate source location measurements than TOA method because the source location calculation does not involve a time delay from first arrival and first threshold crossing of AE triggering system. WTML method improves the location error by eliminating false threshold triggering by premature triggering and inaccurate arrival time measurement usually experienced by TOA source location.

WTML method improves the temporal separation measurement error of SSML by eliminating inaccurate arrival time measurement of  $A_0$  mode by discriminating other wavemode components by utilising time frequency analysis of wavelet transform.

The source location accuracy achieved by WTML is comparable with DeltaT location method. However, WTML could be considered as more reliable and an easier source location methodology than DeltaT since no test grid and H-N source for training data is needed. Therefore, this method could be considered as the best candidate for source location methodology to be utilised for the fatigue crack length measurement in nuclear power plant piping system. Further work aims to validate the workability of this method for detection of actual crack growth in cracked pipe.

## Acknowledgements

The authors would like to thank the Ministry of Science, Technology and Innovation of Malaysia for funding this research work. The authors also like to thank Dr. Mark Eaton and Matt Patterson for their assistant and support throughout this research work.

## References

1. Miller, R. K., McIntire, P., "Acoustic Emission Testing", in NDT Handbook Vol. 5, ASTM. 2005.
2. Baxter, M., Pullin, R., Holford, K., Evans, S. L. "Delta T sources location for acoustic emission". Mechanical system and Signal Processing. **2**: 1512-1520, 2007.
3. Holford, K.M., "Acoustic Emission – Basic Principles and Future Directions", Strain. **36** (2), 2000.
4. Gorman, M. R. "Plate Wave Acoustic Emission." J. Acoustic Society of America. **90**(1): 358-364, 1991.
5. Holford, K.M. and Carter D.C. "Acoustic Emission Sources Location", Key Engineering Materials. **167-168**, 1999.
6. Prosser W.H, Dorigi, J., Gorman M.R. "Extensional and flexural waves in a thin-walled graphite/epoxy tube." J. Compos. Mater. **26**:2016–27, 1992.
7. Pullin, R., Holford, K.M. and Baxter, M.G. "Modal Acoustic Emission Signals from Artificial and Fatigue Crack Sources in Aerospace Grade Steel, Key Engineering Materials. **293-294**:217-226, 2005.
8. Takemoto, M. and Nishino, H. "Wavelet Transform – Applications to AE signal Analysis", in T. Kishi, M. Ohtsu and S. Yuyama, Acoustic Emission – Beyond the Millennium, Elsevier, Oxford, 2000.
9. S.V Subba Rao, B. Subramanyam, "Analysis of Acoustic Emission Signal using Acoustic Emission Technique". Defence Science Journal of India, **58**(4): 559-564, 2008.
10. S. Avdakovic, A. Lukac, A. Nuhanovic, M. Music. "Wind Speed Data using Wavelet Transform". World Academy of Science, Engineering and Technology **75**: 830-834, 2011.
11. Jingpin, J., He, C., Wu, B., Fei, R., and Wang, X. "Application of Wavelet Transform on Modal Acoustic Emission Source Location in Thin Plates with One Sensor". International Journal of Pressure Vessels and Piping. **81**: 427-431, 2004.
12. Jeong, H. and Jang, Y-S. "Fracture source location in thin plates using the wavelet transform of dispersive waves," IEEE Transactions on Ultrasonic, Ferroelectrics and Frequency Control. **47**:612-619, 2000.
13. Vallen System website." <http://www.vallen.de>, Download on Tuesday, June 23, 2009, 12:01:40 PM

## **Development of high intensity laser NDT system for critical mapping of stress distribution in CFRP component**

Mohd Yusnisyam Yusof, Wan Saffiey Wan Abdullah, Khairiah Yazid and Ilham Mukriz  
Zainal Abidin

NDT Group, Industrial Technology Division, Malaysian Nuclear Agency, 43000 Bangi  
Kajang, Selangor, Malaysia

[yusnisyam@nuclearmalaysia.gov.my](mailto:yusnisyam@nuclearmalaysia.gov.my)

### **Abstract**

Digital Shearography is an optical nondestructive testing (NDT) technique that is being widely employed in production and quality control applications within aircraft, oil and gas, automotive and materials research, which is a big challenge for traditional NDT techniques. The purpose of our work is to develop a laser shearography non-destructive testing system which is capable of mapping stress distribution in Carbon Fiber Reinforced Polymer (CFRP) component. High intensity laser interferometry arrangement is utilised to map stress affected areas which leads to the assessment of the sample under investigation. The system provides a fast and real-time inspection capability in revealing defect through the mapping of high stress concentration areas. In this study, the laser system is utilized to test stress concentration area in CFRP sample of an aircraft component. The CFRP sample has the dimension of 40 mm width, 600 mm long and 200 mm height. The study shows that the system is capable to detect and observed the presence of moisture and debonding area in a CFRP sample. For comparison the Thermography technique is utilised to validate the location and shape of the same-defect in the material.

**Keywords:** laser shearography, non-destructive testing, CFRP, stress distribution mapping

### **Introduction**

There are a number of standard NDT methods that are capable of providing data on materials of composite nature that are being utilised in the aerospace industry. The increasing usage of composite materials for aerospace components is due to the benefits of reduced weight, the ease of formability and good mechanical properties offered by these materials, such as for example carbon fibre skin sandwiching Nomex core and other honeycomb structures. During manufacture and, of course, during service, the composite components should be inspected for weak areas in order to ensure proper bonding, for the obvious reasons of minimising scrap and avoiding possible catastrophic events. Composite materials are difficult to inspect for flaws such as delaminations and disbonding, however digital shearography is demonstrably well-suited in detecting such flaws with high resolution and appears for the purpose, to be positioned in the forefront of NDT technology. The technique of digital shearography detects the flaws as a result of localised variation in the gradient of the component's field of surface displacements generated in response to any stressing being applied such as mechanical, thermal, pressure or vacuum [1]. The gradient of the surface displacement emerges as a fringe pattern superimposed on the object's image, after the subtraction of two images of the object's surface, one before and the other after the stressing was imposed. The anomalies that may be observed in the fringe pattern basically display the position and approximate size of the defect, and possible to measure its depth relative to the surface. Typical laboratory shearographic NDT systems, similar to the one depicted in Figure 1, include personal

computer housing software to process the images of the object under test. The images are obtained through a CCD camera which views the object through some shearing optics and are stored in the image digitiser. A single wavelength (a laser) with expanded light source is used to illuminate the object and produce the required speckled image [2]. The inspection of aerospace sandwich structures using the technique known as *digital speckle shearography*, with vacuum stressing being applied on the surface of the objects under test, has already been demonstrated, as obviously vacuum should accentuate defects such as impact damage, debonds or delaminations. The vacuum stressing of objects being inspected for flaws using digital shearography can be classed into two categories, namely whole body and surface vacuum stressing. The whole body category implies that the object (composite material structure) is placed inside a vacuum chamber. The ambient pressure inside the chamber is reduced thus body 'expansion' is effected and any internal debonds or delaminations are accentuated causing local concentrations of the surface strain field [3]. The surface vacuum stressing category implies that vacuum is applied to an area of the surface of the object thus creating suction on the skin of the composite material structure, causing a similar effect as body 'expansion' and as a result revealing weaknesses in the bonding of the various layers. Surface suction can be accomplished through mild evacuation of the air from a small suction chamber consisting of a rigid frame with a perspex window, flexible or not airtight sides ending at a rubber surface which will accomplish the seal with the surface of the object [4]. Through the perspex window the shearography equipment's laser will be able to illuminate the surface. Through the same window the system's camera will acquire the necessary surface speckle images required to produce the surface displacement gradients field capable of indicating the presence of defects should they exist. In some instances, surface suction can be accomplished without the use of a surface suction device as described above, if one the object's surfaces can act as a vacuum chamber, for example with a cylindrical object or an object with a closed convex surface. If the two ends can be covered or sealed off, effectively the inner surface becomes a chamber that can be evacuated and therefore the outside surface of the object may be used to inspect for flaws using digital shearography [5].

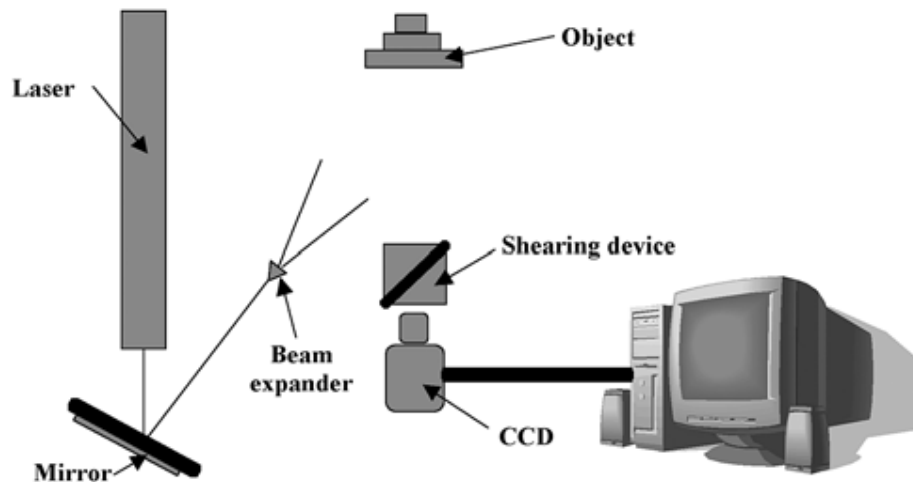
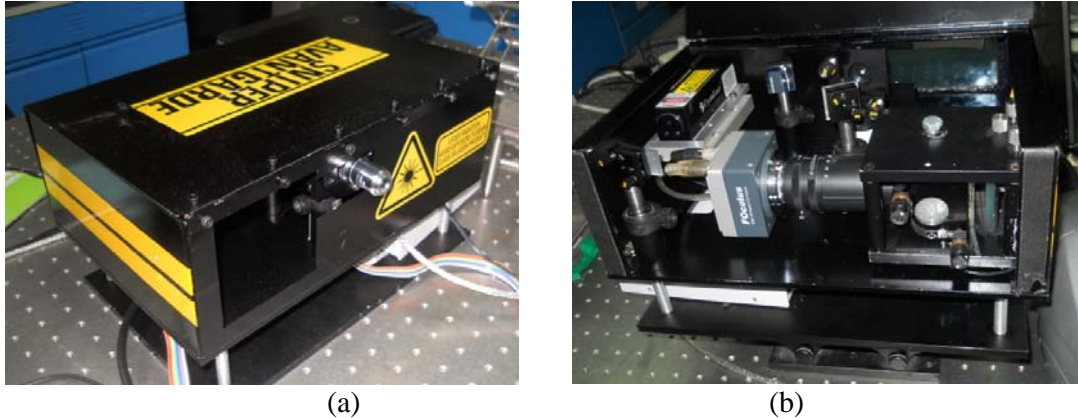


Figure 1. Typical laboratory shearographic system



## Portable Shearography System

The challenge of transferring shearographic inspection from the confines of the laboratory to the industrial environment has been met by pioneering portable shearography equipment, such as the one that was developed by the researchers at the Laser Non-Destructive Laboratory of the Malaysian Nuclear Agency. The Malaysian Nuclear Agency portable digital shearography system is depicted in Figure 2.



**Figure 2. (a) Portable Digital Shearography System (b) Optical arrangement of Portable Digital Shearography System**

The system consists of a compact shearography head, 33 cm long 22 cm wide and 9 cm height, mounted on a tripod. The shearography head is controlled by a portable industrial computer. The shearography head houses consist of a high-resolution CCD camera, a beam splitter and image shearing mirror. The focus and aperture of the camera and the tilt and pan of the image shearing mirror is accomplished mechanically from the rear of the shearography head. The illumination source, which is mounted on top of the housing, is a 532 nm, 20 mW green Nd:YAG laser module whose beam is directionally controlled by a miniature mirror mount. The head is linked to the computer for data transfer and power supply to the camera, laser and piezoelectric displacement actuator. The system is equipped with new program developed for fringe pattern processing which incorporates rapid methods for automatic fringe pattern acquisition and filtering. The algorithm for the program is written using MATLAB. Figure 3 depicted new program for fringe pattern processing.

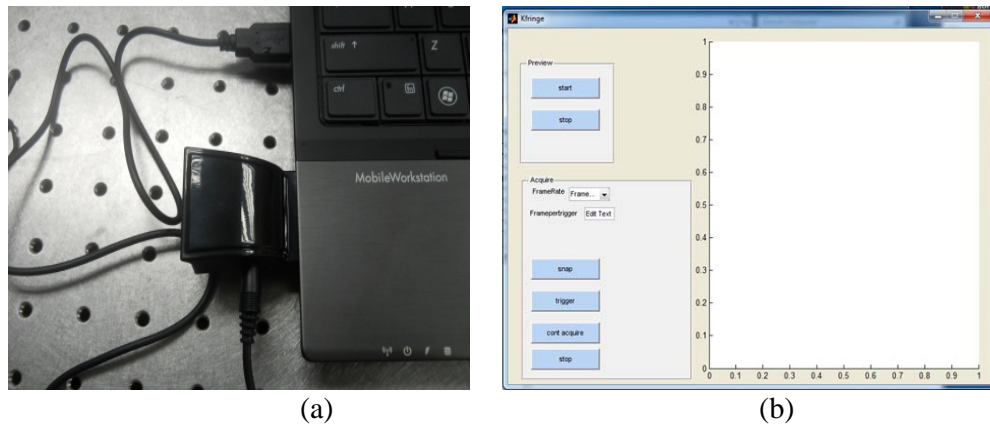


**Figure 3. (a) Firewire Cable Connection (b) Kfringe Shearography Processing Software**

## Vacuum Stressing

As mentioned in the introduction section, vacuum stressing using shearography has already been successfully demonstrated by the whole body technique, so is the surface vacuum stressing. However, the latter appears to be a turnkey solution to testing a specific object which decreases notably the versatility of the system when testing a variety of components. The challenge was to develop a hand-held chamber, which would be placed on the surface to be inspected, capable of applying vacuum. This would provide the necessary gradients of the surface displacement to be captured by the camera of the shearography head as it views directly the front of the sample surface. Through the same cover, the illumination of the surface under test will be effected with the shearography head laser [6]. In this manner, with the shearography head independent of the vacuum chamber, the versatility of the shearographic system is maintained instead of becoming a turnkey or specific purpose instrument [7].

### Laboratory surface vacuum device

The work attempted to establish the applicability of a surface vacuum chamber acting as the stress mechanism, interfacing with the surface under test. The shearography head for the system comprises of optics, camera, illumination source etc. This aspect has not been reported in the literature before and therefore constitutes a novel aspect of digital shearographic interferometry. The second phase of the study involved the attempt to detect flaws of different sizes in order to obtain the technique's sensitivity or resolution with different vacuum air suction. Both above described phases of this study were performed with a vacuum chamber specially designed for the laboratory conditions. It incorporates a perspex frame where the test composite specimens, containing various sizes of flaws, would be attached. The surface vacuum device that was manufactured consisted of a 200 x 150 x 80 mm rectangular mirror window with an 8 mm-thick edging. The window is bolted on rigid perspex sandwiching between them. A rubber seals at perspex surface and between the mirror window and perspex frame ensures airtight conditions for the space created between the mirror and sample. This space, when partially evacuated, would act as a vacuum chamber applying suction on the specimen's surface. A suitable analog vacuum gauge was provided for the chamber and also include vacuum controller between vacuum hose of vacuum chamber and vacuum motor. See Figure 4 for the various parts of the whole assembly as described above.



**Figure 4. Various Parts of Surface Body Vacuum System**

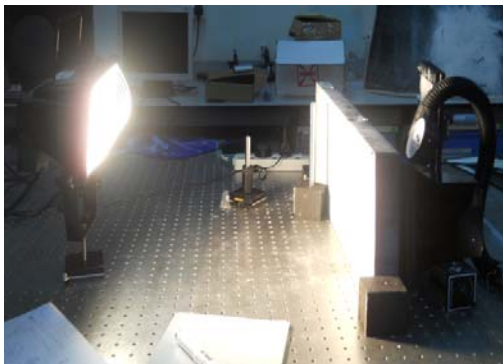
## Experimental investigation of moisture presence and debonding in Carbon Fibre Reinforced Polymer (CFRP)

In this experiment, we focus on detecting moisture presence and debonding in a CFRP sample investigation by digital shearography. The CFRP sample has the thickness of 40 mm thickness, 600 mm long and 200 mm height and divided into 3 sections of different conditions which are 1) normal, 2) with moisture presence, and 3) debonding condition, as shown in figure 5. At the area of normal condition, the sample consisted of layers of CFRP that were perfectly bonded on each side of the core without any discontinuities; intended as a reference section.



**Figure 5. CFRP sample shows three areas of test with normal, moisture and debonding**

The result from shearography technique will be compared by Thermography technique since this technique is frequently used in CFRP inspection. For shearography technique the horizontal shearing amount of 5mm was applied. The Shearography technique used the surface vacuum chamber as the stress mechanism applied at the surface of the CFRP sample. Different air suction levels are applied during experiment in unit –cm HG to realize an optimum fringe pattern while the Thermography technique uses spotlight for heating mechanism as shown in figure 6a.



(a)

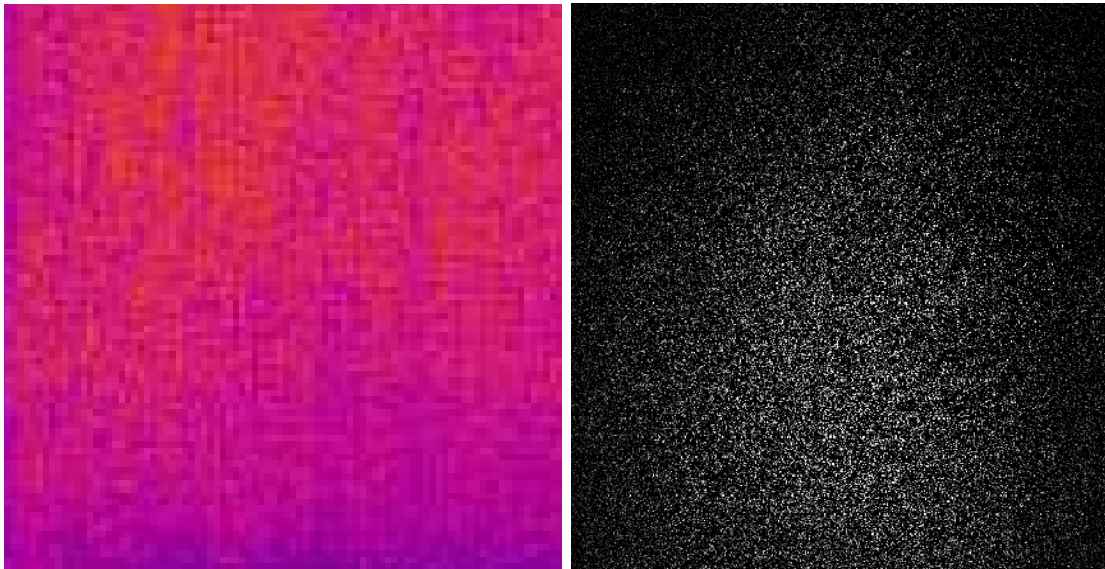


(b)

**Figure 6. (a) heating mechanism by Thermography (b) stress mechanism by Shearography**

The heat distribution result for the normal section of the CFRP sample by the Thermography technique shows that no significant temperature difference is observed at this area. While shearography result shows that no fringe pattern appears at normal condition area as shown in

figure 7. The results from these two techniques confirm that the normal condition area, which is referred to as the reference section, is perfectly bonded on each side of the core without any discontinuities.



**Thermography**

**Shearography**

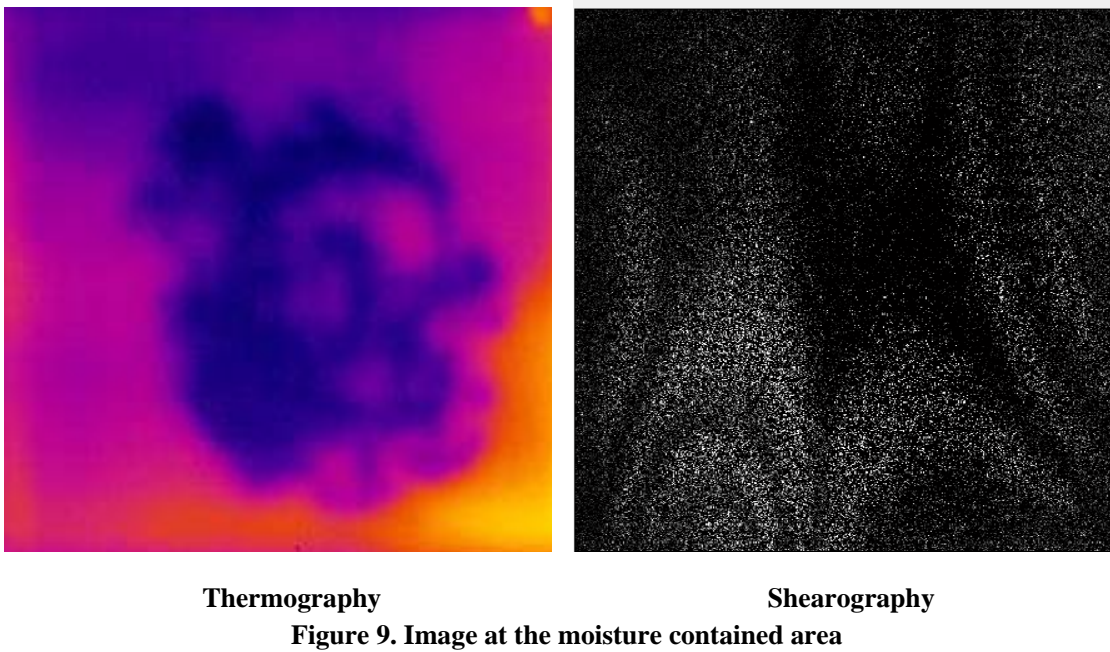
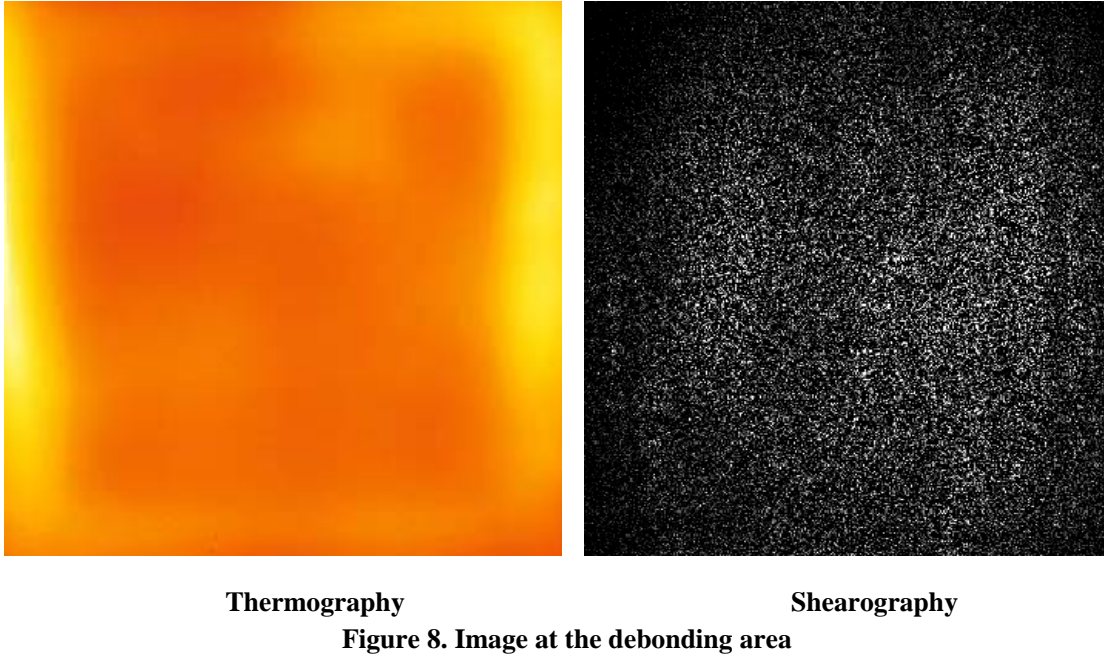
**Figure 7. Image of normal free defect area**

In the experiment for the debonding section, the sample is heated using the spotlight until it reaches the temperature of 40° celcius. From the heat distribution shown by the Thermography result, it can be seen that there is an indication of temperature difference observed at the debonding area. The debonding area can be detected from the relatively low temperature distribution which depicted as square shape boundary line inside the debonding section of the sample. For the shearography technique, the stress mechanism was from the -3.5cm HG (-0.12 bar) air suction by the surface vacuum chamber, applied at the rear side of the sample surface. The shearography fringe pattern from the subtraction of speckle pattern at two consequent events shows the stress concentration area as presented in Figure 8. The size and shape of the debonding condition be clearly observed from the left and right side of fringe pattern, which is comparable with the result obtained by the thermography technique. However, due to the height of the vacuum chamber (250mm) which did not cover the whole debonding section, poor contrasts can also be observed at the upper and lower region of the fringe pattern result.

For the section having the presence of moisture, the result for the Thermography technique indicates the moisture presence by low temperature distribution at the middle area of the section (Figure 8). Meanwhile for the Shearography technique, by using -4.5cmHG (-0.15 bar) air suction as the stress mechanism, has also managed to show the presence of moisture located at the centre of the section. Figure 9 shows the fringe pattern at the moisture area presented by the high density fringe pattern at the middle of the sample. Other bull-eye fringe pattern also appears due to global deformation of the sample. These results, presented in



Figure 8 and 9, show a good agreement between these two techniques in the detection of moisture presence in CFRP sample.



## Conclusion

It has been shown that shearography has potential application for nondestructive inspection of CFRP sample. This method provide high sensitivity, high inspection speed, integral measuring technique and suitable for different type of defect and material within the CFRP sample. The study also shows that surface vacuum chamber is suitable to be used as a stress

mechanism to be applied at the surface of the CFRP sample by controlling the vacuum air suction to -3.5cm HG (-0.12 bar) to detect debonding area and -4.5cmHG (-0.15 bar) for moisture presence of 40mm sample thickness.

## References

1. Vacuum excitation in shearographic NDT", NDT.net - [www.ndt.net](http://www.ndt.net) - Document Information: [www.ndt.net/search/docs.php3?id=4546](http://www.ndt.net/search/docs.php3?id=4546)
2. Hung Y.Y., "Shearography: a new optical method for strain measurement and nondestructive testing", Opt. Eng. 21(3), 391-395, (1982).
3. Toh S L, Chau F S, "Flaw detection and characterization using shearography", ASME ASIA '97 Congress & Exhibition, Singapore, Sept. 30 – Oct. 2, (1977).
4. Hung Y.Y., "Shearography: a new optical method for strain measurement and nondestructive testing", Opt. Eng. 21(3), 391-395, (1982).
5. Hung Y Y & Ho H P, "Shearography: An optical measurement technique and applications", Material Science and Engineering R 61-87, 49 (2005).
6. Ettemeyer A, "Laser shearography for inspection of pipelines", Nuclear Engineering and Design, 237-240, 160 (1996).
7. Kim K S, Kang K S, kang Y J & Cheong S K, "Analysis of an internal crack of pressure pipeline using ESPI and shearography", Optics & Laser Tech., 639-643, 35 (2003).



## DETECTION OF LOCAL STRESS CONCENTRATION ZONES IN ENGINEERING PRODUCTS – THE LACKING LINK IN THE NON-DESTRUCTIVE TESTING SYSTEM

*A.A. Dubov (Energodiagnostika Co. Ltd., Moscow, Russia)*

It is known that the main sources of damaging during engineering products operation are local stress concentration zones (SCZs) that form under the effect of working loads, first of all, on metallurgical and process defects.

Metallurgical and process manufacturing defects are known to cause high level of residual stresses (RS) in local zones of the product. RS control at some productions is performed on a selective basis. In this case the average (volumetric) level of RS is inspected, and local RS zones due to internal defects of the metal, as a rule, are not inspected and omitted. Besides, the location of these local zones and the method of their detection are unknown.

As a rule, RS control during the incoming inspection is not performed. For these reasons, during the very first years of products operation under the working load their “rejection” takes place. Process and metallurgical defects, causing the high level of RS in local zones of products at unfavorable combinations with stresses due to working loads, cause accelerated development of damages.

It is known that conventional NDT methods – X-ray, ultrasonic testing, the eddy-current method, magnetic powder and dye penetrant inspection – are aimed at searching and detection of pronounced defects located primarily on the products’ surface. Internal casting defects, various types of structural inhomogeneity as well as manufacturing process defects (welding, rolling, bending, heat treatment defects, etc.) remain undetected in products due to the lack of 100% quality inspection at most of the plants as well as due to imperfection of NDT methods applied. Moreover, these rejection standards of NDT methods used at products manufacturing plants are aimed at detection of defects with sizes that many times exceed those of metallurgical defects. For example, according to the norms of austenite pipes ultrasonic testing, the sizes of admissible defects do not exceed 25 mm in length and 0,3 mm in opening and depth. As practice shows, metallurgical defects of smaller sizes, when exposed to working loads, are the main sources of operational damages. In conditions of products operation practically all NDT methods are also aimed at detection of various-type discontinuity flaws with sizes significantly exceeding the size of defects that cause the development of damages.

Thus, it must be stated that the lack of RS inspection in order to detect stress concentrations on structural defects of products, both at manufacturing plants and during operation, is the lacking link in system of products NDT, which considerably reduces their safety and reliability.

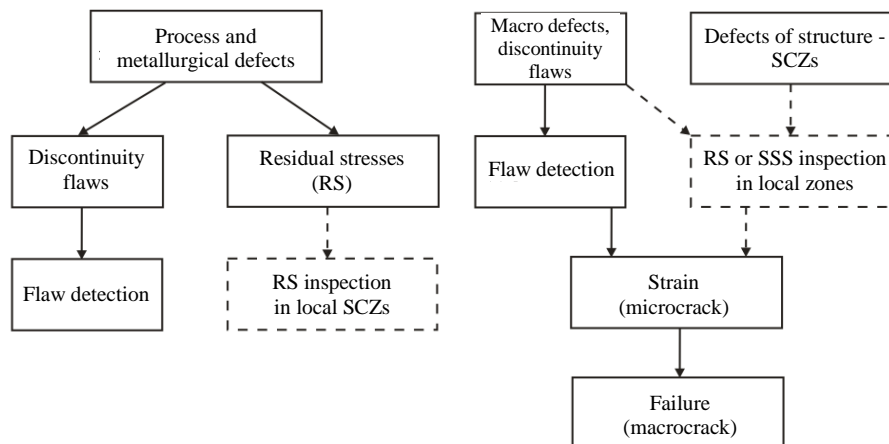


**Figure 1.** Block diagram of engineering products non-destructive testing at manufacturing plants and during operation.

Figure 1 shows the scheme of engineering products NDT arrangement that formed at present both at manufacturing plants and during operation. It can be seen in figure 1 that products inspection consists

in the usual flaw detection without any assessment of stress concentration level on apparent (discontinuity flaws) and implicit (structural) defects. The lacking link in the NDT system is marked with a dotted line in figure 1.

It should be noted that nowadays, when in most industries equipment and structures became obsolete and worn out, and the material resources are not sufficient for their mass replacement, the value of non-destructive testing and technical diagnostics gains more relevance. In these circumstances the role of quick NDT methods increases in order to ensure 100% equipment inspection and detect local SCZs, in which damages development can be expected in the course of further operation of various technical devices.

In 2008 the National Standard GOST R 53006-2008 “Lifetime Assessment of Potentially Hazardous Facilities Based on Quick Methods. General Requirements” was put into effect.

Passive NDT methods that use the internal energy of structures’ metal are referred to quick methods:

- acoustic emission (AE) method;
- metal magnetic memory (MMM) method;
- thermal control.

At present these method have become the most widespread in practice for early diagnostics of equipment and structures damaging. The fundamental difference of such an approach to the lifetime assessment is performance of the 100% IO examination with detection of all potentially hazardous stress concentration zones (SCZs) – the sources of damages occurrence during the equipment operation.

The new National Standard GOST R 53006-2008 also contains the following basic provisions:

- it is suggested to use actual energy characteristics, which can be detected by the MMM, AE and thermal methods, as basic criteria of the metal’s limiting state;
- block diagram for residual life determination with focus on modern quick methods is proposed;
- it is suggested to perform verification strength calculations with residual life assessment for SCZs remaining in operation considering the metal’s actual structural and mechanical properties determined during the inspection;
- recommendations of the National Standard GOST R 52330-2005 “Non-destructive testing. Stress-strain state control of industrial objects and transport. General requirements” were taken into account.

At implementation of the GOST R 53006-2008 standard it is possible to perform the lifetime expert estimation based on the complex examination of the equipment and to specify safe operation time in most cases without carrying out complex calibration strength calculations. It is possible to develop more specific technique for specific equipment considering the specific features and requirements of this industry.

The metal magnetic memory (MMM) method developed by Energodiagnostika Co. Ltd. (Moscow) becomes more practically implemented for solution of the problem of determination of local SCZs in new and operated products. Russian and International standards on the MMM method are published.

In accordance with GOST R ISO 24497-1-2009 “Non-destructive testing. Metal magnetic memory method. Terms and definitions” the MMM method is a non-destructive testing method based on recording and analysis of distribution of self-magnetic leakage fields (SMLF) occurring on stress concentration zones (SCZs)<sup>1</sup> and of structural inhomogeneity of products. IN this case SMLF reflect the irreversible variation of magnetization in the direction of the effect of maximal stresses due to

---

<sup>1</sup> One should distinguish the traditional concept “stress concentrator” from the material science concept “stress concentration” occurring on structural defects and in zones of stable dislocation slipbands conditioned by the effect of working loads.

working (external) loads, as well as structural and process history of products and welded joints after their fabrication and cooling in the magnetic field of the earth.

The MMM method differs fundamentally from all known magnetic NDT methods by the fact that its application does not require artificial magnetization of the product, but it uses the natural magnetization and aftereffect that appears in the form of the magnetic memory of metal related to actual strains and structural changes.

The MMM method requires no preparatory works during the inspection and differs from other NDT methods by the fact that it indicates the level of stress concentration, i.e. it indicates the degree of the detected defects' hazard.

Let us further consider the MMM method's capabilities at diagnostics of new and operated products in order to detect local SCZs – the sources of damages development.

Figure 2 shows the inspection results of a new Ø22mm (St.05X16H4Д2БТ13) rod used for fabrication of the shaft of electrical centrifugal pump (ECP) manufactured at LLC “PC Borets” production works (Lebedyan’).

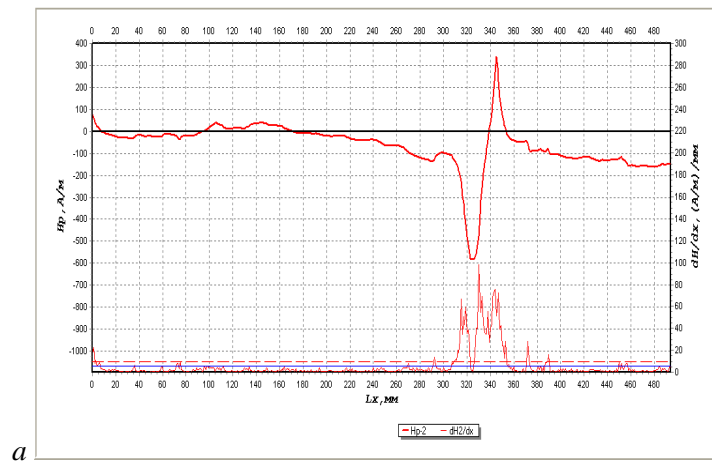
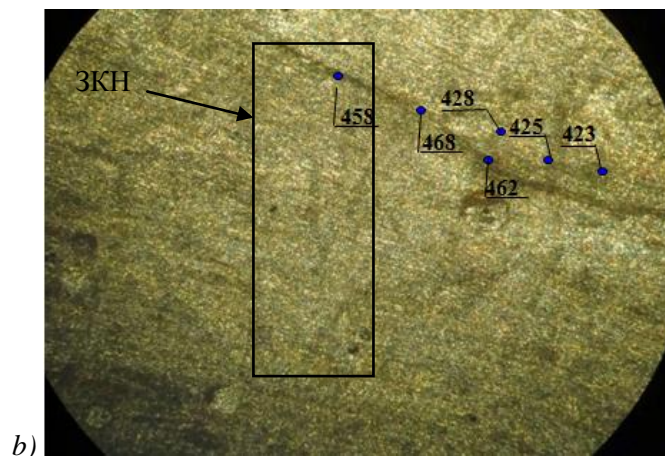


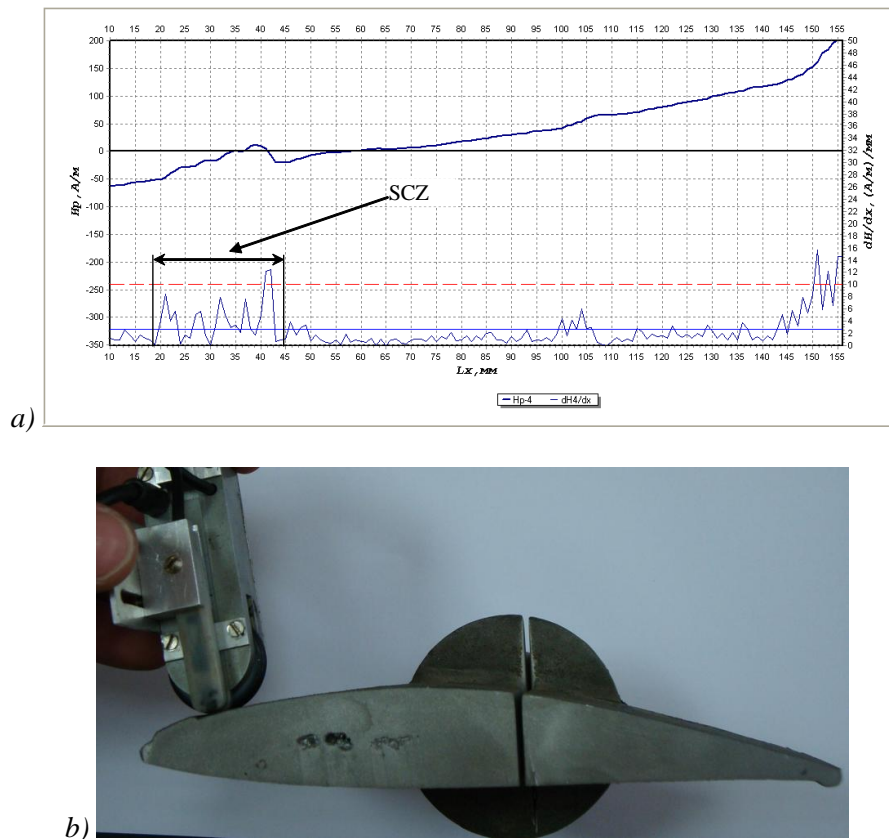
Figure 2, *a* shows the distribution magnetogram of the normal component of the self-magnetic leakage field  $H_p$  and its gradient  $dH/dx$  recorded in the stress concentration zone (SCZ) during scanning with the instrument sensor along one of the generating lines of the rod #2204. Figure 2, *b* shows the metal's structural state of the rod #2204 in the section that coincides with the SCZ. Figures indicate the micro hardness values along the line of a metallurgical defect and outside it.



**Figure 2.** Inspection results of a new Ø22mm (St.05X16H4Д2БТ13) rod used for fabrication of the shaft of electrical centrifugal pump (ECP) manufactured at LLC “PC Borets” production works

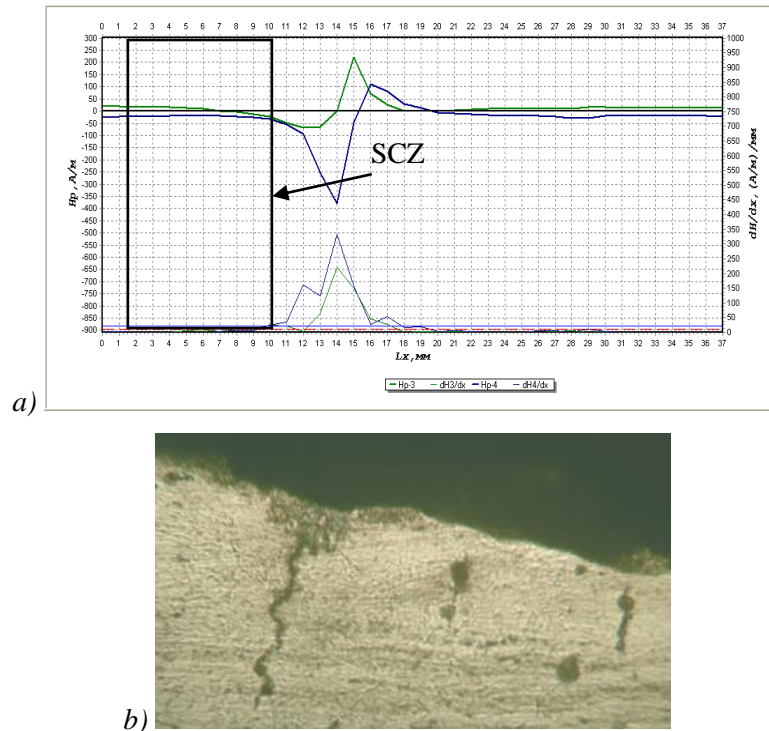
(Lebedyan'): *a* – distribution magnetogram of the normal component of the self-magnetic leakage field  $H_p$  and its gradient  $dH/dx$  recorded in the stress concentration zone (SCZ) during scanning with the instrument sensor along one of the generating lines of the rod #2204; *b* – metal's structural state of the rod #2204 in the section that coincides with the SCZ. Figures indicate the micro hardness values along the line of a metallurgical defect and outside it.

Figure 3 presents the results of inspection by the MMM method of a new hydraulic turbine blade. Figure 3, *a* shows the distribution of the magnetic field  $H_p$  and its gradient  $dH/dx$  recorded during the inspection along the external surface of the blade. SCZ characterized by local variations of the field gradient is indicated in the bottom part of the magnetogram. Figure 3, *b* shows casting defects detected in the metal depth after cutting of the blade opposite the SCZ recorded by the MMM method on the external surface.



**Figure 3.** Results of inspection by the MMM method of a new hydraulic turbine blade: *a* – distribution of the magnetic field  $H$  and its gradient  $dH/dx$  recorded during the inspection along the external surface of the blade; *b* – casting defects detected in the metal depth after cutting of the blade.

Figure 4 presents the results of inspection by the MMM method of a  $\varnothing 42 \times 7$  mm pipe of steel 10X13Г12БC2H2Д2 cut out of the new power boiler platen superheater. Figure 4, *a* shows the distribution magnetogram of the self-magnetic leakage field  $H$  and its gradient  $dH/dx$  recorded in the SCZ on one of the pipe generating lines. Despite the fact that this pipe was fabricated of stainless steel that should be practically non-magnetic in the initial (as-fabricated) state, however, a ferrite phase, recorded during the inspection by the MMM method as a magnetic anomaly, formed in the local zone due to violations of its manufacturing technology. Figure 4, *b* shows the cracks detected on the internal surface of the pipe cut out from the zone of the magnetic anomaly that corresponds to the SCZ.



**Figure 4.** Results of inspection by the MMM method of a  $\varnothing 42 \times 7$  mm pipe of steel 10X13Г12БС2Н2Д2 cut out of the new power boiler platen superheater: *a* – distribution magnetogram of the self-magnetic leakage field  $H$  and its gradient  $dH/dx$  recorded in the stress concentration zone (SCZ) on one of the pipe generating lines; *b* – cracks detected on the internal surface of the pipe sample cut out from the SCZ detected by the MMM method.

The presented in figures 2, 3 and 4 example from the practice of the MMM method application on new products of various productions clearly demonstrate general drawbacks in organization of NDT at manufacturing plants. All the above-mentioned products were tested by the NDT system currently existing at plants. However, as it was noted above, at present most of the manufacturing plants lack the inspection for detection of metal defects beyond the standardized sensitivity limits of the applied inspection methods and means. Application of the MMM method, which reveals metallurgical and technological production defects in the form of magnetic anomalies corresponding to local stress concentration zones, would allow to ensure the 100% products inspection even in mass production.

During operation of engineering products the major sources of damages development are also local SCZs, the formation sites of which are practically impossible to predict by calculation methods. Application of the MMM method offers a unique opportunity to detect the local zones with maximum stress concentration at an early stage by means of performance of the 100% inspection of various equipment units.

For classification of magnetic anomalies, characterizing SCZs by the degree of their hazard in accordance with the technique described in [1], a comparison of all magnetic anomalies detected on a specific unit by the field gradient  $dH/dx$  value is performed.

For the same-type equipment units, based on the laboratory and industrial investigations, the limiting value of the field gradient is determined, at which a microcrack is formed and the damage development starts.

In accordance with the definitions presented in paper [2], the physical sense of the magnetic parameter  $dH/dx$  is that it reflects concentration (or density) of the magnetic energy in the product's volume conditioned by the strain energy density.

Figure 5 presents the inspection results of a 120 MW steam turbine stage disk rim. Figure 5, *a* shows the magnetogram recorded on the external surface of the disk rim. The upper part of the magnetogram shows the distribution of the tangential 2 and the normal 3 components of the self-magnetic field  $H$ , and the bottom part shows the distribution of the field gradient from the above-mentioned components. The maximum value of the field gradient 55A/m/mm (or  $55 \times 10^3 \text{ A/m}^2$ ) turned out to be approximately equal to the limiting state for this turbine disk. Therefore in this case additional inspection by ultrasonic testing was performed. Mounting of the UT transducer on the disk was adjusted to the maximum field gradient value location site. During performance of the UT a discontinuity flaw was recorded in the SCZ on the internal slot surface. After cutting out of the disk segment a 2 mm deep and 20 mm long crack was detected on the internal slot surface (see figure 5, *b* and figure 5, *c*).

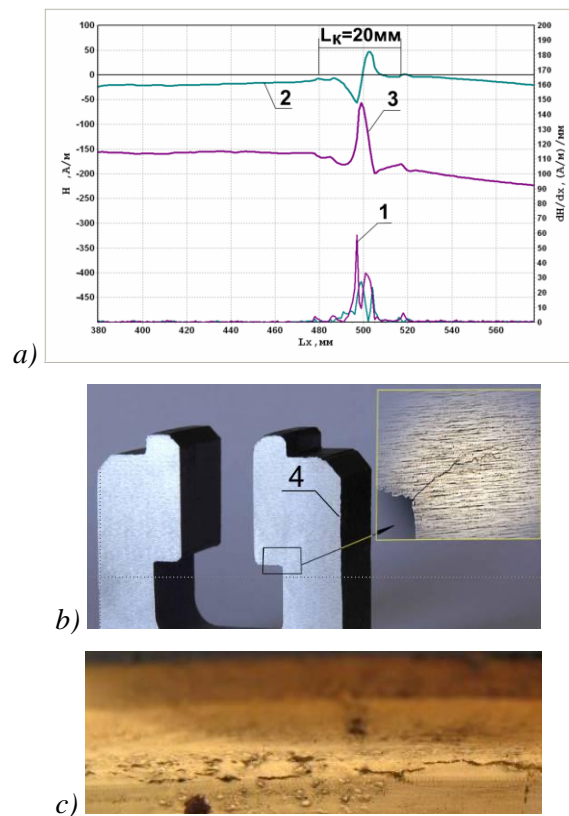


**Figure 5.** Inspection results of a 120 MW steam turbine stage disk rim: *a* – magnetogram fragment recorded on the external surface of the disk rim with upward shift approximately by 45 degree from the crack location on the internal surface of the disk; *b* – location of the detected ~2mm deep crack; *c* – location of the ~20mm long ( $l_k$ ) crack along the internal surface of the disk rim; 1 – maximum value of the gradient  $dH/dx$ ; 2 – distribution of the tangential component of the field  $H$ ; 3 – distribution of the normal component of the field  $H$ ; 4 – zone of inspection by the MMM method on the external side of the disk before the fragment cutout.

It should be noted here that at present, in accordance with the effective guideline [3], turbine disks with T-shaped blades attachment are inspected by ultrasonic testing for cracks detection in slots with the use of special specimens, but the inspection itself is a complex practical task. During the performance of the disk rim UT combined with the MMM method the technique of UT signals comparison in the SCZ, pre-detected by the MMM method, and outside this zone can be used instead of a standard specimen. IN these conditions standard specimens are not required, and the ultrasonic testing can be performed by an expert with medium qualification.

The considered example of the MMM method application for detection of the local SCZ at an early stage of the damage development clearly demonstrates the significance and efficiency of its



application in combination with other NDT methods. The experience of the MMM method application on different equipment under long-term operation in various industries shows that only 5 to 10% of the total metal volume reaches the limiting state (physical ultimate strength) and achieve the stage of damage development. Unfortunately, it is practically impossible to determine these local SCZs – the sources of damages development – by calculation methods. Such problem can be solved using the methods of early diagnostics (the MMM and AE methods).

During the analysis of products fracture mechanism determination of local zone dimensions (volume, area, length), at which the limiting state of the metal and the product itself occurs, is the most valuable. Exactly this challenge, that has so far been the subject of study on specimens in fracture mechanics, is solved using the MMM method directly on the equipment during the diagnostics of various units' condition.

### **Bibliography**

1. A.A. Dubov, Al. A. Dubov, S.M. Kolokolnikov. Metal magnetic mejmory method and inspection instruments: Training Textbook. Moscow: ZAO "Tisso", 2008. 364 p.
2. V.T. Vlasov, A.A. Dubov. Physical theory of the "strain-failure" process. Part I. Physical criteria of the metal's limiting states. Moscow: ZAO "Tisso", 2007. 517 p.
3. Guidelines for service life extension of fleet life steam turbines. Moscow: CPTI ORGRES, 2004. 170 p.

---

**COMBINED METHODS FOR DETERMINATION STRENGTH OF THE CONCRETE WITH  
FIBER POLYPROPYLENE  
(THE SCHMIDT HAMMER AND THE ULTRASONIC PULSE VELOCITY).**

---

**BELARIBI HASSIBA ET MELLAS MEKKI**

Département Génie Civil, Université de Biskra, Biskra, Algérie.

[Farsoul@yahoo.fr](mailto:Farsoul@yahoo.fr)

[mellas@yahoo.fr](mailto:mellas@yahoo.fr)

**Abstract**

The study consists of evaluation of fiber reinforced concrete (polypropylene) strength by the nondestructive methods this concrete is produced from local materials of south Algeria.

The results obtained by using the combined method using Schmidt hammer and ultrasonic pulse velocity depended mainly on the materials which constituent concrete. Then, the measurements of non-destructive tests are affected by the following parameters: the water/ Cement ratio, percentage of fibers, age of concrete and the curing conditions (eau,air).

The combined use of nondestructive methods allowed to obtain a correlation acceptable for the determination of the concrete strength determined in situ by the Schmidt hammer and the Ultrasonic Pulse Velocity. The combined nondestructive method is supposed to give reliable results.

**Key words:** Evaluation, Concrete, tests, nondestructive, strength, in situ, concrete, fibers, polypropylene.

**I - Introduction :**

Quality problems encountered in concrete structures appear at different stages of the execution of works, if for this reason that long ago an increased demand for more accurate methods and, at the same time more flexible assessment concrete quality. For that one uses the non-destructive testing (NDT) of concrete has a great scientific and practical importance. The topic has attracted increasing attention for years; particularly the need to characterize the quality of constructions made of concrete damaged by using non-destructive.

Williams (1936) introduced the first non-destructive testing, and laying it After the development of the construction sector, a range of non-destructive testing in situ, has been developed by many researchers in this field as: Jones (1962), Malhotra (1976) Bungey (1982) presented a comprehensive survey of literature for non-destructive methods normally used for testing and evaluation of concrete.

Over the years several non-destructive evaluation methods have been developed is described that the two methods used in this work: Rebound Hammer and. Ultrasonic Pulse Velocity (UPV

**I.1 Rebound Hammer (RH) ASTM C805**

A simple equipment known as Rebound Hammer or Schmidt Hammer is used for this purpose. The details of the equipment are shown in Fig. 1.



**Fig. 1: Schmidt Hammer**

It is usually used in comparing the concrete in various parts of a structure and indirectly assessing concrete strength. The hammer weighs about 1.8 kg and is suitable for use both in a laboratory and in the field. The rebound of an elastic mass depends on the hardness of the surface against which its mass strikes.

The test is described in ASTM C805 and EN12504- 2:2001. The results of rebound hammer are significantly influenced by several factors [4,6] such as: smoothness of test surface; size, shape, and rigidity of the specimens; age of the specimen; surface and internal moisture conditions of the concrete; type of coarse aggregate; type of cement; carbonation of concrete surface.

### **I-2 Ultrasonic Pulse Velocity (UPV)**

The ultrasonic pulse velocity (UPV) technique is used to evaluate the quality of concrete structure, measure of concrete uniformity and evaluate the properties of concrete. Besides that, UPV also can measure the transit time, presence of voids, path length, perpendicular crack depth and elastic modulus.

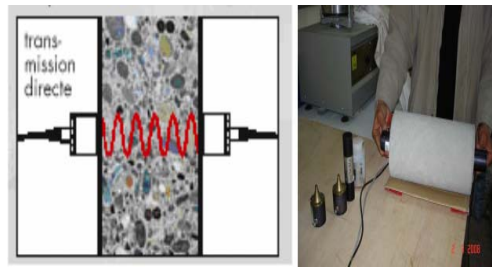


**Fig. 2: Ultrasonic**

UPV can be used not only for concrete but also for timber, ceramics, cast iron, geological specimens and other materials. UPV is classified into three categories of reading, direct test, indirect test and semi direct test. The schematic diagram of these three categories of reading is illustrated in Fig 3. UPV is used to assess of concrete quality for different structural components like roof beams, crane girders, shell beams, columns, shell roof and etc (Sahu and Jain, 1998). According to Whitehurst, 1951 concrete with density of 2400 kg/m<sup>3</sup> are considered excellent for 4500 m/s and above, good for 3500 – 4500 m/s, doubtful for 3000 – 3500 m/s, poor for 2000 – 3000 m/s and very poor for 2000 m/s and below. Besides that, the lower limit for good quality concrete is between 4100 – 4700 m/s (Jones & Gatfield, 1955). As per IS: 13311 (Part 1) – 1992, concrete quality can be classified according to Table 1. Hamidian et. al. (2011) reported the pulse velocity is a good equipment to evaluate concrete strength and quality

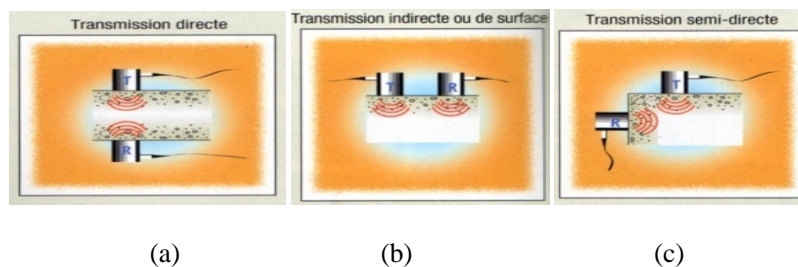


**Fig 3: UPV test for (a) semi-direct, (b) direct and (c) indirect test**

### **I.3- Combined Method**

This resistance is corrected by the values of the coefficients of influence of different constituents and their nature.

None of the tests mentioned above can provide an excellent means to establish and evaluate consistency or quality of the concrete, unless the laboratory correlations are established between the strength parameters and results of nondestructive testing in situ

The general relationship between strength and rebound number is of the form:

$$f_{cy} = A_0 + A_1 R^n \quad (1)$$

Since the  $n = 1$ , the relationship can be considered by detecting the resistance of concrete linear

$$f_{cy} = A_0 + A_1 R \quad (2)$$

The general relationship between strength and speed of its is of the form:

$$f_{cy} = A_2 V^B \quad (3)$$

$$f_{cy} = a_1 e^{bV} \dots (4)$$

Or

$f_{cy}$  = Compressive strength of cylinder

R = rebound number

V = speed of sound

$A_0, A_1, A_2, B, a, b$  = constants

Samarin and Meynink (1981) found that for the majority of concrete used commercially in Australia

The value of B can be taken as 4 and as multiple regression equation becomes...

$$f_{cy} = A_0 + A_1 R + A_2 V^4 \dots (5)$$

The second variable ( $V^4$ ) is transformed so that a linear expression may be used.

The correlation is developed using standard tests of compressive strength of specimens tested in the laboratory just before the crash; The method was developed to try to increase the reliability of nondestructive testing

There are many studies related to the UPV and rebound hammer for example Demirboga et al., 2004 studied ultrasonic velocity for high-volume mineral-admixture concrete. Yang et al 2009 evaluated the residual compressive strength of concrete subjected to evaluated temperature. Evaluation of concrete containing crumb rubber (rubbercrete) as a fine aggregate replacement using rebound hammer and ultrasonic pulse velocity (Mohammed et al., 2010). Non-destructive testing was carried out using UPV and impact rebound hammer techniques to establish a correlation with the compressive strengths of compression tests of concrete used in Algeria (Hobbs and Kebir, 2007). Solis-carcano & Moreno (2008) reported the ultrasonic pulse velocity tests are used to evaluate of concrete made with crushed limestone aggregate. Shariati et. al. (2011) used ultrasonic pulse velocity and Schmidt rebound hammer to reveals an improvement in the concrete strength estimation and produces more reliable results.

### **II-Characterization Of Materials Used:**

#### **Cement:**

The cement used was Portland cement type compound CPJ-CEM from the cement-Ain Touta (Algeria).

#### **The Gravel:**

We used crushed stone Biskra region, the gravel is of class (3/7) and class (7/15)

#### **Fibers**

The fibers used in our study are polypropylene fibers, the main features provided by the manufacturer are: • Fibre length: 12 mm Density: 0.9 kg/m<sup>3</sup>

#### Adjuvant

In our study we used before the adjuvant MEDFLUID (SF)-Comes from Granitex-Oued Smar is a liquefier. Thanks to its properties MEDFLUID (SF) can increase the mechanical strength of concrete slump and increase the fluidity and thus facilitate its implementation and to avoid the formation of honeycombs

#### Mixing water:

For making our blends, we used tap

### III-Relationship between resistance and non-destructive test results:

The tests are performed on 100 mm cubes of sides are molded with the method of Scramtaiv with water / cement ratios of 0.45, 0.55, 0.65. This choice was made so that the only variables are the water/cement ratio (W/C) and quantitative analysis of fiber. The W/C = 0, 45 has given good results why he was chosen to establish the combined expression of the speed of sound and rebound number in conserving water.

#### a)Relationship between the resistance and the speed of sound:

The figures (1), (2) show the relationship between the compressive strength and the speed of sound as a function of time and the percentage of fibers (0%, 0.5%, 1%, 1.5%), for the I / C = 0.45, and in both measurement directions (horizontal and vertical).

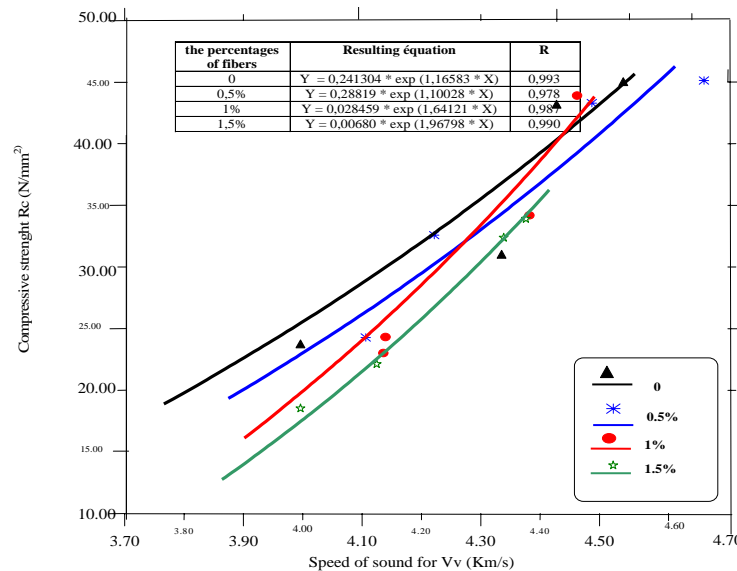


**Fig 4: Compressive strength as a function of the speed of sound for Vv W / C = 0.45, and at various percentages of fibers (in-water)**

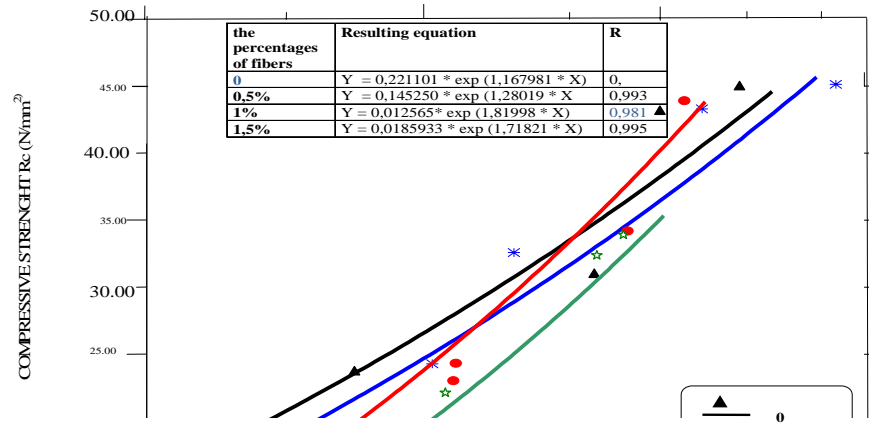


**Fig 5: Compressive strength as a function of the speed of sound for  $V_v W / C = 0.45$ , and at various percentages of fibers (in-water)**

**b) Relation between strength and rebound number**

Figures (3), (4) show the relationship between strength and rebound number versus time and the percentages of fiber (0%, 0.5%, 1%, 1.5%) for the  $E / C = 0.45$ , and in both measurement directions (horizontal and vertical)

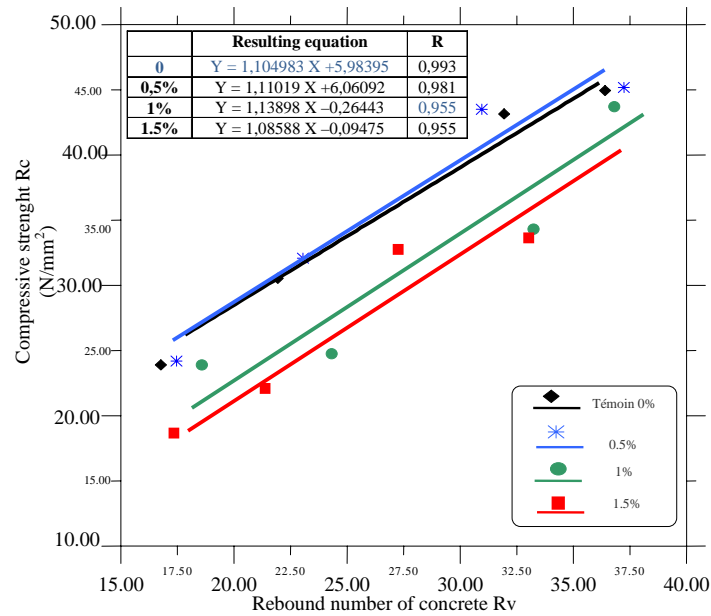


**Fig 5 : Compressive strength as a function of  $R_v$  rebound number of concrete with different fiber percentages for  $E / C = 0.45$**



The fibers used in our study are polypropylene fibers, the main features provided by the manufacturer are:• Fibre length: 12 mm Density: 0.9 kg/m<sup>3</sup>

#### Adjuvant

In our study we used before the adjuvant MEDFLUID (SF)-Comes from Granitex-Oued Smar is a liquefier. Thanks to its properties MEDFLUID (SF) can increase the mechanical strength of concrete slump and increase the fluidity and thus facilitate its implementation and to avoid the formation of honeycombs

#### Mixing water:

For making our blends, we used tap

### III-Relationship between resistance and non-destructive test results:

The tests are performed on 100 mm cubes of sides are molded with the method of Scramtaiv with water / cement ratios of 0.45, 0.55, 0.65. This choice was made so that the only variables are the water/cement ratio (W/C) and quantitative analysis of fiber. The W/C = 0, 45 has given good results why he was chosen to establish the combined expression of the speed of sound and rebound number in conserving water.

#### a)Relationship between the resistance and the speed of sound:

The figures (1), (2) show the relationship between the compressive strength and the speed of sound as a function of time and the percentage of fibers (0%, 0.5%, 1%, 1.5%), for the I / C = 0.45, and in both measurement directions (horizontal and vertical).

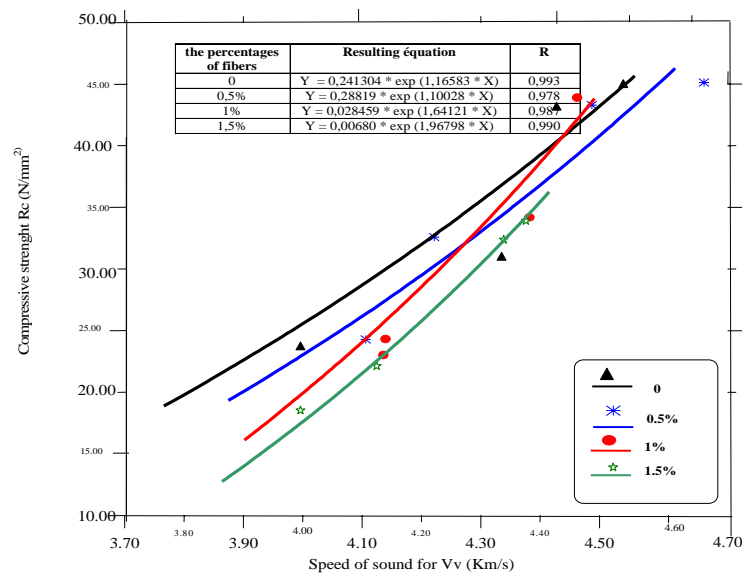


**Fig 4: Compressive strength as a function of the speed of sound for Vv W / C = 0.45, and at various percentages of fibers (in-water)**

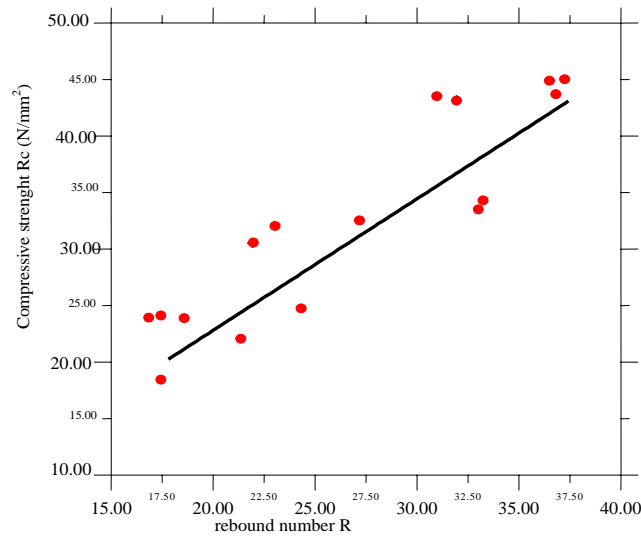


**Fig 8: Compressive strength as a function of the speed of sound V, at various percentages of the fibers**

The combined expression of the speed of sound and rebound number

$$Y = .035197 * \exp(1.48966 * X)$$

$$Y = 1.14261 2.07047 * Z$$

We obtain:

Formula to express the final values are shown as follows

$$Rc = 0,026759 \exp(1,48966 * V) + 0,57130 * R + 1,03523$$

Or: Rc: Resistance to compressions

V: velocity

A: rebound number

**d) Application and discussion of results and in situ results with the expressions:**

Now we will apply our results to the combined method of concrete test hammer method with ultrasonic pulse velocity on cores taken from a concrete slab construction or fibers made of:

→The slab contains 0.5% fiber and E/C = 0.45

→And six cubes of the same formulation of the slab which three are preserved in water and three air. Two cores were removed from the slab to 28 days with a core drill and we applied our tests (speed of sound, the hammer, and the press) on these cores and cubes for a comparison between the expressions of correlation between resistance in situ with concrete rebound number and the speed of sound. is whether they agree with those obtained in situ or not.

**Table (1) : Results in situ**

	Designation of carrot cubes		the cubes		
			Water		
	C1 <sub>0.5</sub>	C2 <sub>0.5</sub>			
Rebound number	40	38	29	32	28
The speed of sound (km/s)	4,390	4,290	3,880	4,030	3,880
strength N/mm <sup>2</sup>	42,00	41,40	25,00	31,00	26,00
the cubes					
Air					
	20	22	24		
	3,370	3,470	3,780		
	17,00	18,00	24,00		

Résultats avec l'expressions

$$R_c = 0,026759 \exp(1,48966 * V) * + 0,57130 * R + 1,03523$$

**Table (6): Results with expressions**

	Designation of carrot cubes		the cubes		
			Water		
	C1 <sub>0,5</sub>	C2 <sub>0,5</sub>			
<b>Rebound number</b>	40	38	29	32	28
<b>The speed of sound (km/s)</b>	4,390	4,290	3,880	4,030	3,880
<b>strength N/mm<sup>2</sup></b>	<b>42,40</b>	<b>38,69</b>	<b>26,26</b>	<b>30,14</b>	<b>25,69</b>
the cubes					
Air					
			20	22	24
			3,370	3,470	3,780
			<b>16,51</b>	<b>18,30</b>	<b>22,20</b>

The experimental program was conducted to obtain the resistance of fiber concrete in situ by a practical formula obtained by the method combined ultrasound-hammer. We note the results obtained in situ almost agree with those obtained by the expression. From this conclusion we can confirm that using the combined method of ultrasound-hammer, for estimating the compressive strength of fiber concrete, can be used for assessing the quality of fiber concretes with different percentages of fibers in situ.

**IV- CONCLUSION**

- ✓ The analysis of this work has shown that the parameters which influence significantly the strength of concrete fiber can influence, in the same way the results of nondestructive testing.
- ✓ The accuracy of the evaluation of compressive strength can be improved by the combined use of the Schmidt hammer and ultrasonic velocity.
- ✓ In our study the combined method has a certain accuracy of the assessment of compressive strength this is shown by the comparison between the results of expressions and destructive test results.
- ✓ The compressive strength of percentages is 0.5% larger in conservation (air and water) and whatever the E / C than the control concrete or other percentages of fibers.
- ✓ The compressive strength of the fiber concrete to retain water is higher than that of concrete kept in the air to a rebound number given.
- ✓ The compressive strength of concrete to water is kept higher than that of concrete kept in the air at a given ultrasonic velocity increases its speed when stored in water. This is attributed to the fact that the ultrasonic pulses traveling through the pores filled by water and not around the edges of pores as they do in a dry state consequently, the travel path and decreases the speed of sound increases.
- ✓ We note that introducing the fibers changes the behavior of ultrasonic pulses or low percentage of fibers increases the compactness of concrete (in our case 0.5% is the percentage of fibers positive or beneficial) and the introduction of high percentage of fibers— includes a decrease in compressive strength and difficulty of implementation.
- ✓ The fiber concrete is best when used with low values of E / C as the cement content is higher than for conventional concretes.
- ✓ The method combined the ultrasonic velocity and rebound index has proved encouraging for the estimation of concrete strength fiber.

**References :**

- Williams, J. F. (1936): A method for the estimation of compressive strength of concrete in the field. The structural engineer, Vol. 14, N°.7, July 1936, pp. 321-326.
- Jones, R. (1962): Non-destructive testing of concrete. Cambridge University Press, London, 1962, 104 pp
- Malhotra V. M. (1976): Testing hardened concrete: non-destructive methods. Monograph N°. 9. American Concrete Institute, Detroit, 1976, 188 pp
- Bungey J. H. (1989): The testing of concrete in structures. , 222 pp. (Surrey University Press)
- Sahu S.K. & Jain K.K. (1998). Assessment of concrete quality from pulse velocity tests, non destructive testing. Civil Engineering Review. pp 43-45.
- Whitehurst E.A. (1951). Soniscope tests concrete structures. J. Am. Concr. Inst. 47. pp 443 444.
- Jones R. & Gatfield E.N. (1955). Testing concrete by an ultrasonic pulse technique. DSI Road Research Tech. Paper No. 34 (London, H.M.S.O).
- IS: 13311 (Part 1) –1992. Non-destructive testing of concrete: Part 1 Ultrasonic pulse velocity.
- Hamidian, M., Shariati, M., Arabnejad, M.M.K., Sinaei, H. (2011). Assessment of High Strength and Light Weight Aggregate concrete Properties Using Ultrasonic Pulse Velocity Technique. International Journal of Physical Sciences, Volume 6, Issue 22. pp 5261-5266.
- Hamidian, M., Shariati, M., Arabnejad, M.M.K., Sinaei, H. (2011). Assessment of High Strength and Light Weight Aggregate concrete Properties Using Ultrasonic Pulse Velocity Technique. International Journal of Physical Sciences, Volume 6, Issue 22. pp 5261-5266.
- Demirboga R., Turkmen I. & Karakoc M.B. (2004). Relationship between ultrasonic velocity and compressive strength for high-volume mineral-admixtured concrete. Cement and concrete research 34. pp 2329-2336.
- Yang H., Lin Y., Hsiao C. & Liu J. (2009). Evaluating residual compressive strength of concrete at elevated temperatures using ultrasonic pulse velocity. Fire safety Journal 44. pp 121-130.
- Mohammed B.S., Azmi N.J. & Abdullah M. (2010). Evaluation of rubbercrete based on ultrasonic pulse velocity and rebound hammer tests. Construction and building material. Articles in press.

## WHAT CAN BE OBTAINED FROM NDT OF WIRE ROPES?

Alexander Mironenko

Intron Plus, Ltd., Moscow, Russia

Keywords: wire rope, inspection, strong magnetization, residual rope life.

### Abstract

Large number of ferrous steel wire ropes is in use in different industries, carrying people and freight, supporting bridges and towers, lifting pipes and vessels offshore and onshore, underground and aboveground. The bigger and the longer is the rope, the more expensive it is. Later or sooner ropes deteriorate for different reasons, their further use may be dangerous, and important question arise: whether the rope should be discarded or still may remain in operation. Premature discard and replacement with the new rope involves in unreasonable costs, while operating the rope which already reached discard criteria is dangerous. The sensible answer is discarding in time, i.e. for reason. Reasonable discard is possible based on proper inspection, otherwise technical condition of rope remains unknown. Visual inspection is obvious, but only visual examination is not sufficient due to specific rope design. Nondestructive magnetic inspection of ropes enables to gather comprehensive data for making reasoned decision. Magnetic flux leakage (MFL) equipment with strong magnetization can inspect ropes reliably, and smart software facilitates data interpretation. Reach experience with NDT of ropes spilled over into development of relevant national and international norms and standards.

### Ropes and their deterioration

Ropes are widely used for lifting operations – winders, cranes, elevators, cableways, as well as guys for bridges, antennas, chimneys, roofs, etc. Rope integrity effects reliability and safety of installation in which they are in service. Depending on the installation, ropes may have different construction, such as stranded, spiral or full locked, as well as may have rectangular cross-section (flat ropes) and rubber coating. Regardless of the construction, ropes deteriorate during their operation due to similar reasons, e.g. fatigue, corrosion, abrasion, mechanical damage, and overheating. Fatigue in wire rope is normally caused by repetitive bending on sheaves, drums, and causes wire brakes. Broken wires or fractures, allocated on very short distance, are accepted to name as localized flaws (LF). They are one of indicator of rope degradation. When the number of broken wires exceeds affordable limit, the rope must be discarded. Corrosion may occur even in very dry environment, especially on unprotected, non-galvanized wires. Abrasion is very typical for outer wires; however internal wires also may be abraded due to friction, while the rope moves over sheaves. Moreover for some rope constructions deterioration starts internally, and rope which looks good from outside may be dangerous due to high level of deterioration of internal wires. Corrosion and abrasion cause missing some amount of metal from wires. This is called as loss of metallic cross-section area (LMA), and is normally measured as relative amount in percentage to the cross section area of a new rope. According to relevant norms, the rope should be discarded when LMA value reaches limit, established for particular rope construction and application.

## Ropes discard policy

The following policies can be considered for discarding wire ropes.

- Discard on timely basis (automatic discard), i.e. after a set period, e.g. 12 months.
- Discard for reason, i.e. when technical condition of rope is bad, and continuing its operation is dangerous.

Using “automatic discard” policy one may be in risk to continue operating rope, which is much deteriorated, and is dangerous. On the other hand discarded rope may have good condition and could be extended in operation. Premature replacement makes unreasonable costs.

Discard for reason means that the rope may be in service until discard criteria not reached. Discard criteria are referred in relevant standards and norms. This approach requires knowledge about rope condition, which can be obtained resulting proper rope inspection.

Wire ropes can be inspected destructively or nondestructively. Destructive inspection can be carried with relatively short section of rope and gives direct reading of rope breaking strength. Results of destructive testing represent rope section which was destroyed, but the question is how to refer these results to the rest length of rope.

## How ropes can be inspected nondestructively

### Visual testing

Visual testing (VT) enables to reveal outer defects such as corrosion, broken and missing wires if rope surface is accessible for visual examination. VT may be accompanied with haptic testing, use of mirror, magnifying glass, and is carried at low speed. For these reasons VT is tiresome, and requires sufficient time being very subjective. Most wires in the rope may not be visually inspected [1]. Only outer wires are available for examination, but these wires disappear inside the rope on half of their length, and may be covered with heavy grease, that reduces effectiveness of such inspection (Fig. 1). Ropes with protecting coating may not be inspected visually.

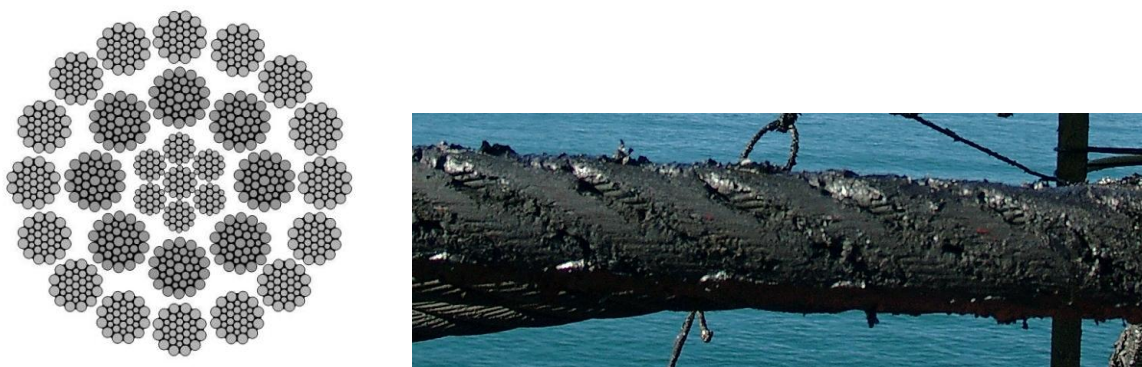


Figure 1. Cross section of multilayer rope (left) and heavy greased crane rope (right).

Note, that low rotation multilayer rope, widely used for lifting operations, start deterioration from inside, however inner broken wires may not be revealed visually. Nevertheless visual inspection in combination with use of magnetic instruments considerably increase reliability of information obtained from tested rope.



## MFL rope inspection

Nowadays MFL principle is common for nondestructive testing of wire ropes. MFL instruments can precisely and fast measure LMA to assess level of abrasion and corrosion, and detect outer and inner LFs even under the grease or protecting coating. To obtain high LMA accuracy and LF sensitivity MFL equipment should contain strong magnets to magnetically saturate the rope under test, and inspect the rope at applied magnetic field, i.e. while the rope is magnetically saturated. The operating principle is described at Fig. 2.

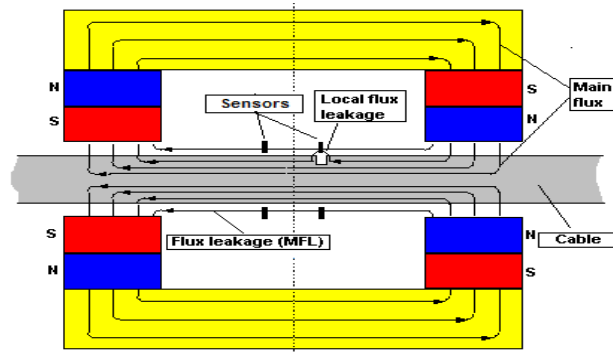


Figure 2. MFL instrument with strong magnetization. Principle of operation.

Magnetic head of the instrument usually comprises magnetizing system with permanent magnets, surrounding the rope under test and producing the magnetic flux along the rope. While rope is passing through the head, the section of rope inside the head is magnetically saturated. Sensors (Hall generators or coils), which are located inside the head close to the rope surface, catch magnetic flux leakage distortion, created by LF or/and LMA. Permanent magnets must be strong enough to magnetically saturate the rope, i.e. to reach working point A at hysteresis curve (Fig. 3). Most of equipment, designed for rope NDT, operate MFL principle, and for this reason inspection of rope with such instruments often called magnetic rope testing (MRT).

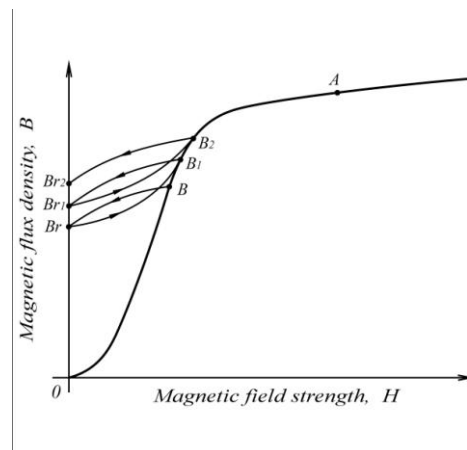


Figure 3. Hysteresis curve. Inspection with applied strong (A) and residual weak magnetization.

The larger is rope diameter the stronger magnets should be used, thus magnetic system becomes heavier and bigger. State-of-the art MFL rope tester INTROS [2] comprises magnetic heads (MH) with strong permanent magnets to inspect ropes of different diameter. Weight and size of magnetic heads are shown in the table 1.

Table 1

<i>Rope Ø, mm/ MH type</i>	<i>6-24/ MH 6-24</i>	<i>20-40/ MH 20-40</i>	<i>40-64/ MH40-64</i>	<i>60-85/ MH 60-85</i>	<i>80-120/ MH 80-120</i>	<i>100-150/ MH 100-150</i>
<i>Weight, kg</i>	<i>3</i>	<i>8</i>	<i>15</i>	<i>60</i>	<i>82</i>	<i>112</i>
<i>Size, mm</i>	<i>264x188 66</i>	<i>330x205x190</i>	<i>330x235x190</i>	<i>690x526X288</i>	<i>895x520x440</i>	<i>950x550x490</i>

Nevertheless there are two important reasons to uphold strong magnetization:

- Magnetic properties of the rope may vary due to operational conditions, mechanical and thermal effect, etc. and variation in magnetic condition may cause reading errors. Strong magnetization makes a magnetic property uniform and so provides higher inspection reliability and increases measuring accuracy;
- Uniform magnetic flux in the rope provides higher sensitivity to both outer and inner broken wires.

Weak magnetization instruments for inspection of rope in residual magnetic field, recently appeared on the market may seem as worthy alternative to MFL instruments mentioned above due to relatively small weight. However weak magnetization may not provide uniform steel magnetic properties and so performance of relevant instruments is worse: they have lower sensitivity, especially to inner defects; readings obtained from consecutive runs vary ( $B_r$ ,  $B_{r1}$ ,  $B_{r2}$  at Fig. 3) i.e. measuring repeatability is poor. Even use of sensors of higher sensitivity and increase of gain factor may not improve their performance. Besides, the testing results from weak magnetization instrument depend on previous magnetic condition of the rope. For instance, “magnetic spots” on the rope, created by heating, mechanical impact, etc. may be interpreted as defects. This was proved experimentally, by comparative test of weak and strong magnetization instruments available on the market [3].

### **Survey of standards and guidance for NDT of wire ropes**

ASTM E1571 [4] is one of the basic documents, which describes relevant terminology, operating principles, application, equipment, procedures, standards for calibration, etc. This standard was recently accepted in Brazil in Portuguese language by change of the cover. The Guidance for magnetic NDT of steel wire ropes was issued by Russian Federal Department of Industrial Safety in 2000, and accepted in Ukraine in 2003. It contains basic knowledge regarding inspection methods, procedures, reports, qualification, and other helpful information.

Standards for inspection of lifting equipment usually refer to nondestructive inspection of ropes as a considerable mean for increase safety. E.g. safety codes for underground mining industry in many countries describe in details requirements for ropes NDT [5], and provide discard criteria. Depending of rope application – hoisting, balance, conductor, etc. rope discard criteria may vary. Usually standards provide maximum LMA value and LF number at certain length of rope as discard criteria. ISO 4309 [6] refers to rope NDT by electromagnetic method as an aid to visual inspection and recommends initial MRT as soon as possible after installation of rope, considering such inspection as reference point for further examinations of rope.

Carrying and hauling ropes of aerial cableways also play important role in providing safe operation. Relevant norms are accepted in USA, Canada [7, 8], Russia, other countries. European norm EN 12927-8 [9] is dedicated to MRT of aerial ropes and is compulsory for use in all countries in European Union.

Ropes of large diameters are widely used at offshore vessel cranes. These ropes are very expensive and they carry important and expensive equipment, e.g. pipelines, drilling installations, etc. Rope failure may stop operation and cause huge losses. For this reason customers are interested to keep offshore ropes in service as long as possible, but avoiding unreasonable risk. Guidance for MRT of offshore crane ropes [10, 11], accepted by IMCA in 2008 and 2009, explain important questions to assist with rope inspection and rope integrity management.

### Practical aspects of MRT

During MRT the rope is passing through testing/magnetic head. Equipment must be ruggedly designed to meet industrial requirements. Holding equipment in hands during inspection as well as high rope speed is hazardous and may injure inspector and damage equipment. Equipment is recommended to reliably fix while rope moves through, and keep speed not exceeding 1,5-2 m/s. In case of inspection of stable ropes (bridge ropes, guy ropes) magnetic head moves along the rope with tugging slings or self-propeller device. Data logger of rope tester INTROS can be fixed on the magnetic head and moved along the rope to record data, thus no long cable is necessary in this case (fig.4).



Figure 4. MRT of bridge rope. Data logger INTROS (circled) is fixed on magnetic head

For better performance it is recommended to magnetize rope prior to inspection run, and make at list two runs for comparison. Lubricant and grease do not affect reading while protruding broken wires may damage the instrument, and it is recommended to cut off protruding wires prior to MRT. Magnetic heads may have wheels or sleeves which align rope in the head, and the latter also protects from protruding wires. Equipment must be equipped with encoder to fix the position of defects. Wire rope tester INTROS measures LMA and reveals LF, and records all data into built-in memory for downloading and further analysis. Test data are arranged in traces format as shown on fig. 5. Following traces are available: LMA, LF, traces from individual sensors, rope speed. On-line registration of traces is also possible (fig. 6) that enables inspector to stop the rope for visual examination in case of suspected defect. Feedback from customers operating INTROS during long time showed that extending rope life based on their NDT, and prompt planning of purchasing new ropes and exchange may provide sufficient benefits [12, 13].

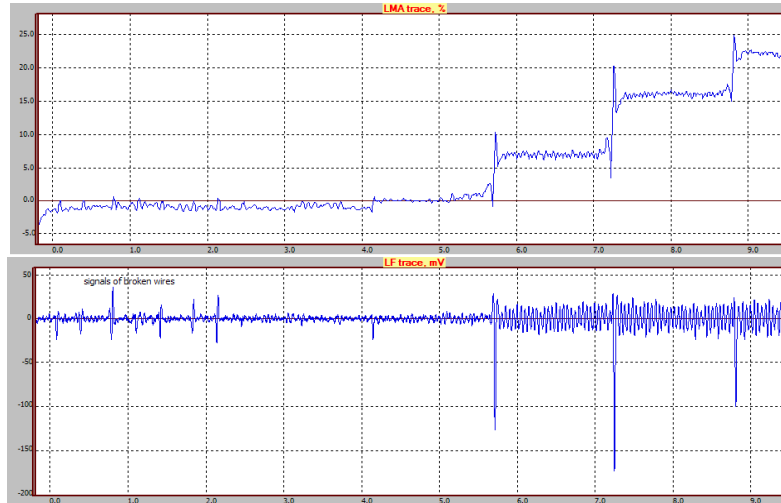


Figure 5. LMA (upper) and LF rope traces obtained from INTROS.

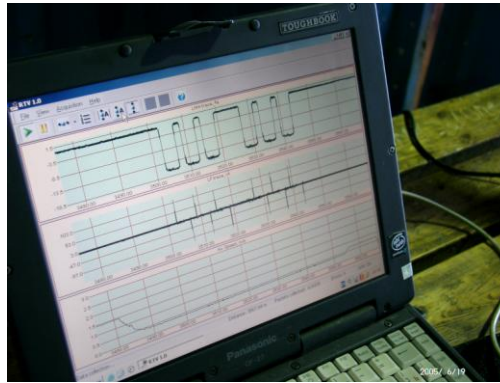


Figure 6. Real time LMA and LF traces shown on laptop screen.

### Assessment of rope residual strength

Providing examination of rope, the pursued target is assessment of residual strength of the rope in order to know residual life with consideration of its operational condition. Assessment result enables inspector to appoint the next inspection in reasonable manner. Intron Plus has created a mathematical model of rope deterioration that allows calculating rope safety factor, which, in turn, is used for assessment of rope residual strength [14]. Experiments with ropes carried in rope laboratories in France, Finland, and Ukraine, and following comparison of experimental results with assessed residual strength showed their good agreement. This makes possible to assess rope residual strength based on the LMA and LF traces. As a result distribution of safety factor (SF) along the rope length can be obtained. Fig.8 shows distribution of SF for the bridge stay rope construction 1+7+7/7+14+24+33z+34z+41z, diameter 72 mm containing defects at the distance of 225, 235, 270 (out-of-lock wires) and 315 m (2 outer broken wires). The minimum SF value is noted at the distance 315 m, and it is equal to 2.4. Considering relevant norms minimum permissible SF value is as much as 2, and it can be concluded, that the rope may still remain in service. Assessment of rope residual life time requires accessible data from several consecutive inspections obtained from the same rope.

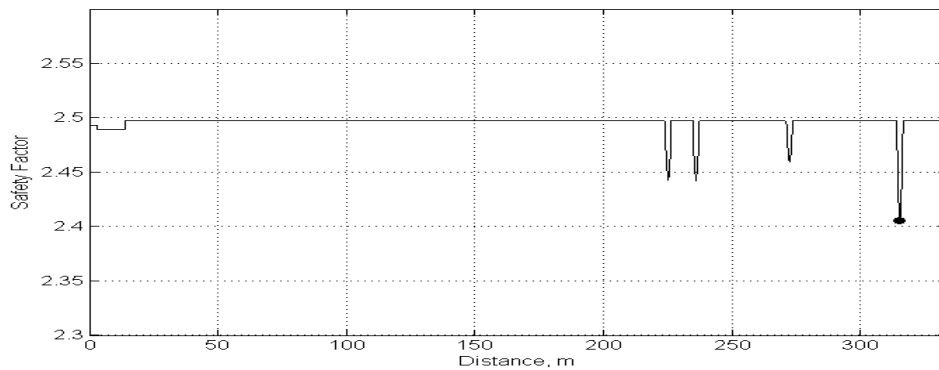


Figure 8. Distribution of rope safety factor of 72 mm bridge rope.

### Conclusion

Nondestructive inspection of wire ropes with strong magnetization MFL instruments enables accurate assessment of technical condition of ropes, providing reliable basis for either timely discard of rope or extension its life. In-time discard increase safety of rope installation, while justified extension provides economical benefits.

### References

1. R.Verreet. A new method for detecting wire rope defects. OIPEEC Conference Proceedings. Athens, Greece. 2006, p.p. 55-61.
2. A.Mironenko. Nondestructive inspection of steel wire ropes. Proceedings of MICNDT 2011.
3. V.Sukhorukov. Magnetic Flux Leakage Method: Strong or Weak Magnetization? Materials Evaluation, vol. 5, 2013.
4. ASTM E1571-11. Standard practice for electromagnetic examination of ferromagnetic steel wire rope.
5. South African Standard SABS 0293. Condition assessment of steel wire ropes on mine winders. 1996.
6. ISO 4309-2010. Cranes – Wire ropes – Care and maintenance, inspection and discard.
7. ANSI B77.1-2006. American National Standard for passenger ropeways.
8. Z98-07. Canadian Standard for passenger ropeways and passenger conveyors.
9. EN 12927-8. Safety requirements for cableway installation designed to carry persons – Ropes – Part 8: Magnetic rope testing.
10. IMCA SEL 022, M194. Guidance on wire rope integrity management for vessels in the offshore industry. October 2008.
11. IMCA SEL 023, M197. Guidance on non-destructive examination by means of magnetic rope testing. August 2009.
12. A.Mironenko and V.Sukhorukov. Non-destructive testing of mining ropes: technical and economical aspects. OIPEEC Conference Proceedings. Athens, Greece. 2006, p.p. 81-86.
13. A.Mironenko and V.Sukhorukov. Non-destructive testing of steel wire ropes in Russia. Insight, vol.6 June 1998. P.p. 395-397.
14. A.Vorontsov, V.Volokhovskiy, D.Slesarev. Combined approach to damaged wire ropes life-time assessment based on NDT results and rope mechanics – 9th International Conference on Damage Assessment of Structures (DAMAS 2011) 11–13 July 2011, St Anne's College, University of Oxford (Journal of Physics: Conference series, Vol. 305, 2011).

## **Sizing of Cracks of Mild Steel Material using Alternating Current Field Measurement (ACFM) Technique**

<sup>a</sup>Jeffrey Jamil, <sup>b</sup>Dr. Syed Yusainee Syed Yahya, Dr. Khazali Hj. Mohd Zin

<sup>a</sup>Non-Destructive Testing Unit, SIRIM Berhad, 40700, Shah Alam, Selangor, Malaysia

<sup>b</sup>Faculty of Applied Sciences, Universiti Teknologi MARA, 40450, Shah Alam, Selangor, Malaysia

<sup>a</sup>jeffry@sirim.my; <sup>b</sup>syedy237@salam.uitm.edu.my; khazalika@gmail.com

**Keywords:** Alternating Current Field Measurement, ACFM, Crack Sizing, Non-Destructive Testing

### **Abstract**

This paper describes an investigation and sizing of surface cracks using Alternating Current Field Measurement (ACFM) technique when it interacts with surface defects in metal component. The ACFM Standard Weld probe 256/5 kHz was used in this study. The test was performed on surface cracks at different depths, lengths, orientations and inclined at various angles. The characteristic signals generated by the surface cracks obtained from  $B_x$ ,  $B_z$  and 'Butterfly plot'. The signals were evaluated using ACFM analysis software. The study also revealed that the ACFM technique can measure a surface cracks with depth 0.5 mm was clearly observed in  $B_x$ ,  $B_z$  and 'butterfly plot' signal. The correlation observed between the experimental results of sizing and actual depth and length of simulated surface cracks is found to be excellent.

### **Introduction**

Non-destructive testing (NDT) is known to be very effective in the detection of cracks in steel component [1]. However, limitations of detecting and sizing of cracks are also always a concern for other NDT methods such as, liquid penetrant inspection (LPI) and magnetic particle inspection (MPI). To overcome this problem, ACFM is an electromagnetic technique that capable of detecting and sizing of length and depth such as fatigue crack in metallic component [1]. The ACFM technique also has been widely used in oil and gas industry, road bridge welds testing, petrochemical plant vessel, high temperature welds chemical tanker to detect and size surface breaking cracks in a wide range of structural materials. In this study, ACFM technique is used to inspect four mild steel plates of thickness 19 mm with various depths, angles and orientations. In this paper, the principle of the ACFM technique will be introduced. Next, the sample preparation and methodology of ACFM instrument setup and testing procedure is described. Finally, experimental data of  $B_x$  and  $B_z$  components are also presented.



## The Principle of ACFM

ACFM method is an electromagnetic inspection method that does not require electrical contact with the surface under inspection. Many studies utilize the ACFM technique to provide an accurate and reliable crack sizing in fracture mechanics such as surface cracks. The technique involves the use of a handheld probe containing two magnetic field sensors and an electric current induction system. An ACFM probe connected directly to an ACFM system electronically, with all control the storage and data by a Personal Computer (PC). Then the probe is placed on the surface to be inspected and an alternating current is induced into the surface. When no defects are present the alternating current produces a uniform magnetic field above the surface. Any defect present will perturb the current forcing it to flow around and underneath the defect, this cause the magnetic field to become non-uniform and sensors in an ACFM probe measure these field variations [1].

## Characteristics of $B_x$ , $B_z$ , and Butterfly Plot

The ACFM technique consists of two component parts of the magnetic field above the surface,  $B_x$  and  $B_z$  as shown in Figure 1.0 [2].  $B_x$  is the magnetic field strength parallel to the crack edge, with the  $B_z$  component is the magnetic field strength perpendicular to the material surface. With no defect present, a uniform current flowing in the  $Y$ -direction, as a result the magnetic field in the  $X$ -direction,  $B_x$  is uniform. The presence of surface crack is noted by decreased in  $B_x$  component and strong peak produced in the  $B_z$  signal, both components are recorded as a function of time [3]. By plotting  $B_x$  against  $B_z$ , a butterfly plot can be drawn. A complete loop indication of butterfly plot has confirmed the presence of crack. Figure 2.0 shows a typical ACFM defect indication.

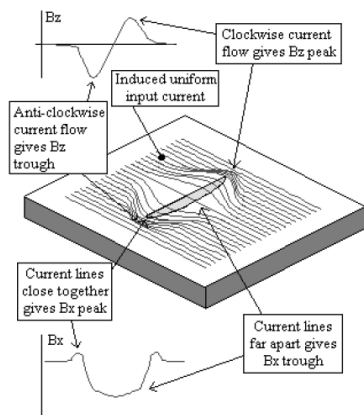


**FIGURE 1.0:** Field Directions and Coordinate System used in ACFM

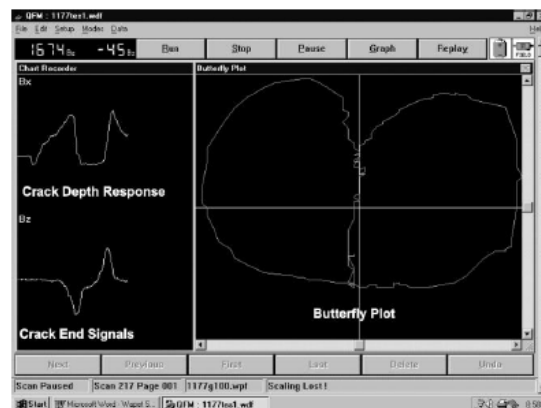


**FIGURE 2.0:** ACFM Indication as shown on Computer Screen Generated by Software Analysis

## Experiment and Methodology

The ACFM equipment was used and connected with a personal computer (PC) that has sufficient system capabilities to support the ACFM software. The ACFM Standard Weld probe 256/5 kHz (see Figure 3.0) was carried out on a 19 mm thickness of mild steel plate. The technique will form a uniform current which will be induced to flow in to the component being tested. The test was performed on surface cracks at different depths, lengths, orientations and inclined at various angles. The characteristic signals generated by the surface cracks obtained from Bx, Bz and 'butterfly plot' displays were evaluated using ASISTant software as shown in Figure 4.0.

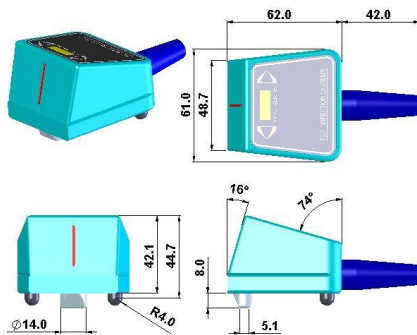


FIGURE 3.0: ACFM Standard Weld Probe

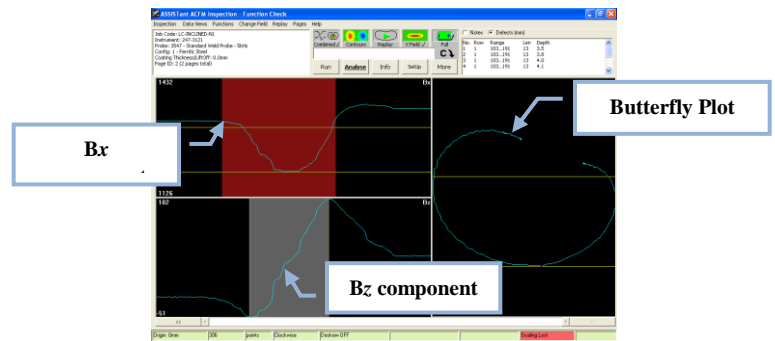
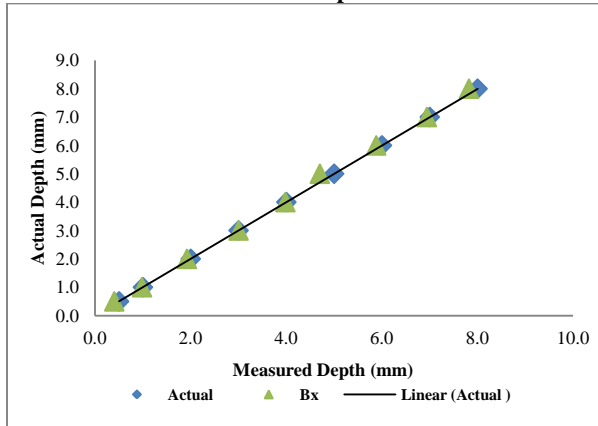


FIGURE 4.0: Bx and Bz Indications and X-Y plot (Butterfly Plot)

## Result and Discussion

The experiments were carried out on mild steel plate containing various types of surface cracks. Five trials were conducted for each sample. Figures 5.0, 6.0, 7.0 and 8.0 shows a comparison of the predicted depth of the Bx component compared with actual depth. While Figures 9.0, 10.0, 11.0 and 12.0 shows a comparison of the predicted length of the Bz component compared with actual length. The correlation observed between the experimental results and actual depth and length of simulated surface cracks for ACFM techniques is found to be excellent.

**FIGURE 5.0**  
Evaluation of Longitudinal Surface Cracks Depth using  
ACFM (Bx component) with Comparison to  
Actual Depth



**FIGURE 6.0**  
Evaluation of Transverse Surface Cracks Depth using  
ACFM (Bx component) with Comparison to  
Actual Depth

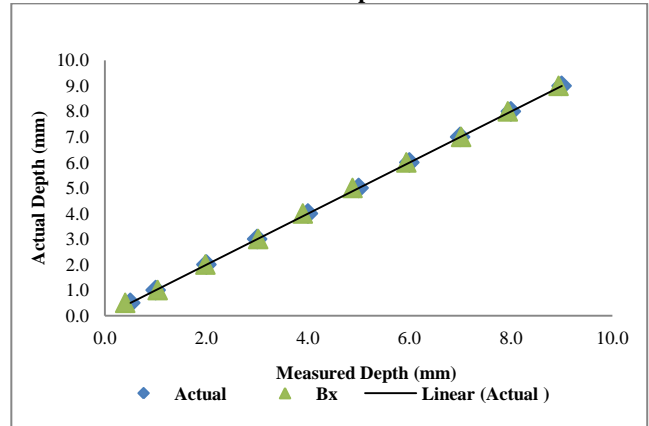


**FIGURE 7.0**  
Evaluation of Inclined Longitudinal Surface Cracks  
Depth using ACFM (Bx component)  
with Comparison to Actual Depth

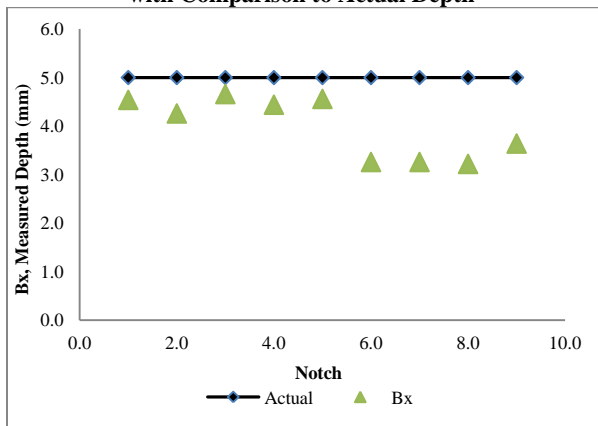


**FIGURE 8.0**  
Evaluation of Inclined Transverse Surface Cracks Depth  
using ACFM (Bx component)  
with Comparison to Actual Depth

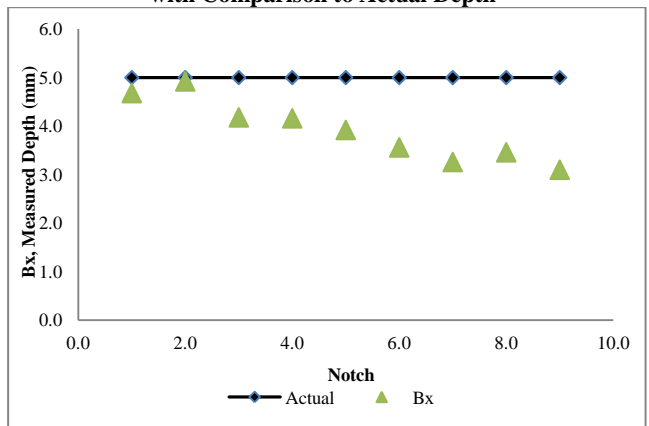


**FIGURE 9.0**  
Evaluation of Longitudinal Surface Cracks Length  
using ACFM (Bz component)  
with Comparison to Actual Length

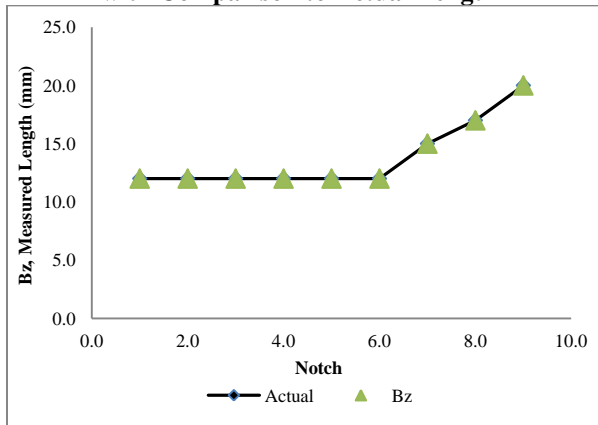


**FIGURE 10.0**  
Evaluation of Transverse Surface Cracks Length using  
ACFM (Bz component)  
with Comparison to Actual Length

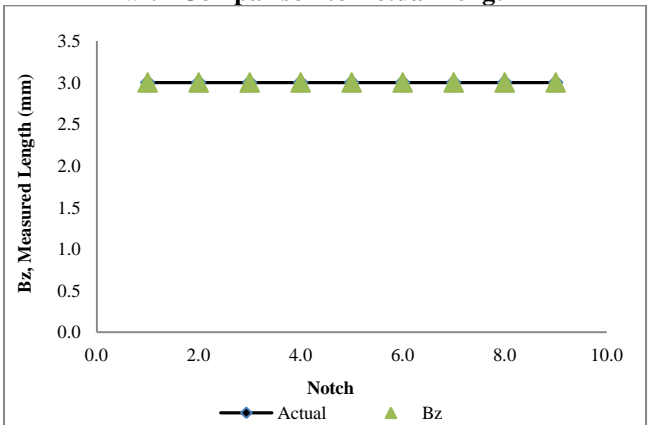


**FIGURE 11.0**  
Evaluation of Inclined Longitudinal Surface Cracks  
Length using ACFM (Bz component)  
with Comparison to Actual Length

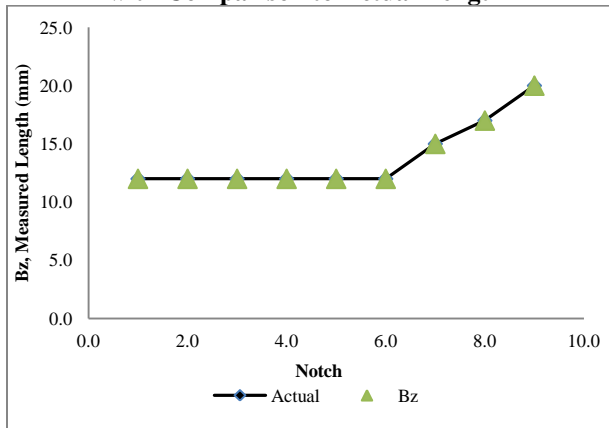
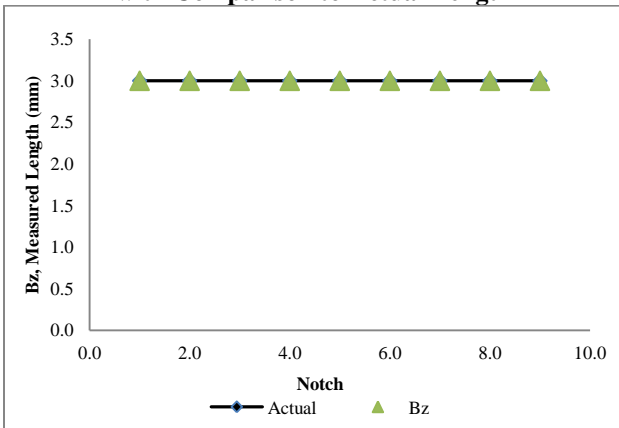


**FIGURE 12.0**  
Evaluation of Inclined Transverse Surface Cracks  
Length using ACFM (Bz component)  
with Comparison to Actual Length



### Depth and Length Measurement of Surface Cracks using ACFM Techniques

It can be seen that accurate result can be obtained from the length measurement obtained for ACFM techniques as shown in Tables 4.1 and 4.2 . For longitudinal surface cracks, the mean error for depth measurement using the ACFM technique is  $-0.1 \pm 0.15$  mm and the standard deviation is  $0.1 \pm 3.7$  mm, while, for transverse surface cracks is  $0.06 \pm 0.05$  mm and  $0.05 \pm 3.7$  mm respectively. In the case of inclined longitudinal surface cracks, the mean error for depth measurement using the ACFM technique is  $-1.06 \pm 0.75$  mm and standard deviation is  $0.62 \pm 0.75$  mm, while, mean sizing error and standard deviation for length are  $-1.01 \pm 0.9$  mm  $0.62 \pm 0.9$  mm. Small mean errors and standard deviation of depth and length sizing of surface cracks using the ACFM technique makes this technique accurate. However, the geometry, material properties such as changes magnet permeability of the material are important to reduce the measurement error [4].

**TABLE 4.1**  
Consolidate Results of Depth and Length Measurement of Longitudinal and Transverse Surface Cracks  
using ACFM Techniques

Surface Cracks	Parameter	ACFM Measurement		No of Notch
		Mean Error (mm)	Standard Deviation (mm)	
Longitudinal	Depth	$-0.1 \pm 0.15$	$0.1 \pm 3.7$	9
	Length	$0.0 \pm 0.0$	$0.0 \pm 0.0$	
Transverse	Depth	$0.06 \pm 0.05$	$0.05 \pm 3.7$	9
	Length	$0.0 \pm 0.0$	$0.0 \pm 0.0$	

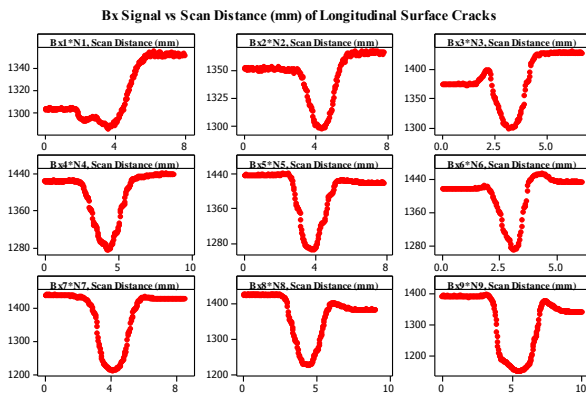
**TABLE 4.2**  
Consolidate Results of Depth and Length Measurement of Inclined Longitudinal and Transverse Surface Cracks using ACFM Techniques

Surface Cracks	Parameter	ACFM Measurement		No of Notch
		Mean Error (mm)	Standard Deviation (mm)	
Longitudinal	Depth	$-1.06 \pm 0.75$	$0.62 \pm 0.75$	9
	Length	$0.0 \pm 0.0$	$0.0 \pm 0.0$	
Transverse	Depth	$-1.01 \pm 0.9$	$0.62 \pm 0.9$	9
	Length	$0.0 \pm 0.0$	$0.0 \pm 0.0$	

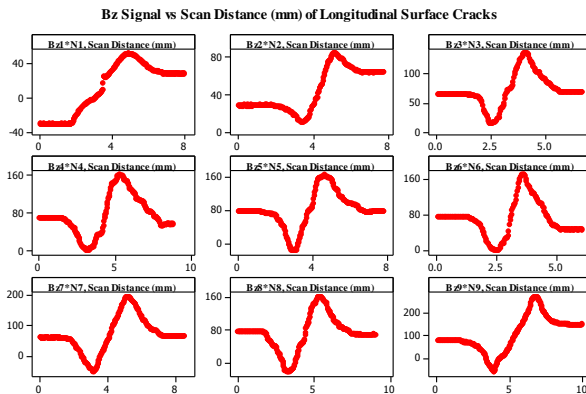
## Characteristic of Bx, Bz and ‘Butterfly Plot’ of Surface Cracks

When the probe scanned along the sample consist of surface cracks, some of the current diverted away from its centre and concentrates near to the cracks ends. As a result perturbation in Bx and Bz component. The Bx along the length of the defect is increased (i.e. change in current density) gives an indication of depth related to amplitude. Bz gives a negative and positive response at either end of the defect caused by current generated poles. Notch 1 with orientation longitudinal and transverse with 0.5 mm depth was clearly observed in Bx, Bz and ‘Butterfly plot’ as shown in Figures 13.0 and 14.0. Bz signal exhibits a sharp peak near one crack end, and equally large dip near the other. Meanwhile Bx signal shows a long dip that reaches a minimum at the crack centre. ‘Butterfly plot’ also known as Bx and Bz graph, the perturbation of the signal cause the loop which start from the top and return to the the same represent the existence of surface crack.

**FIGURE 13.0**  
**ACFM Displays of Longitudinal Surface Cracks**

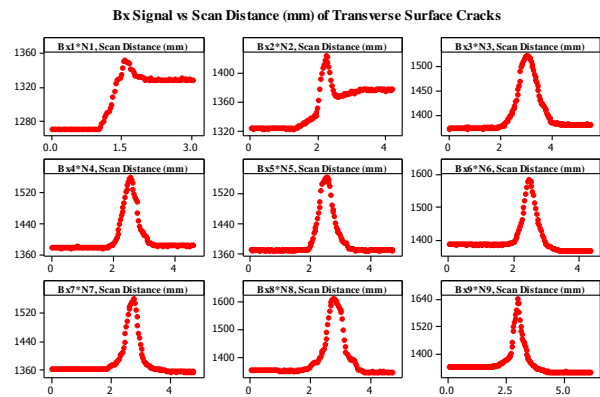


**a) Bx Signals of Longitudinal Surface Cracks**

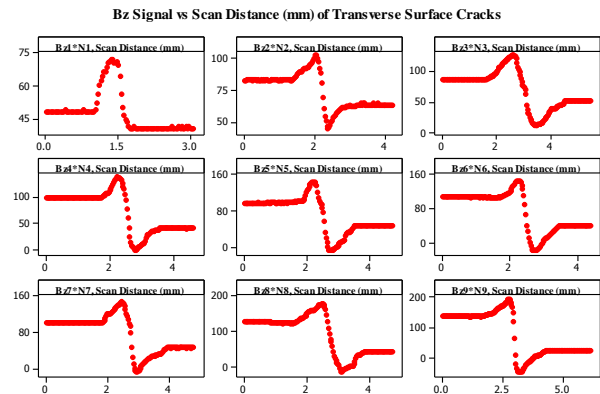


**b) Bz Signals of Longitudinal Surface Cracks**

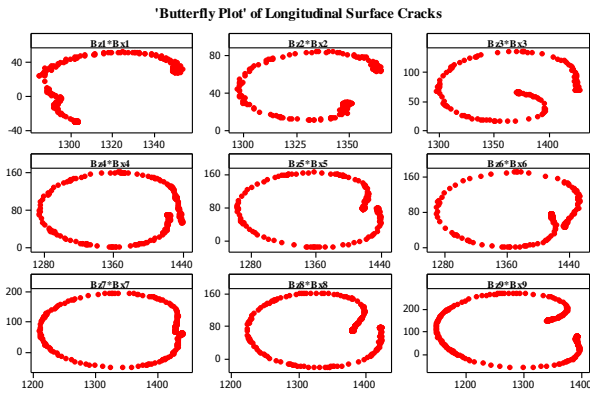
**FIGURE 14.0**  
**ACFM Displays of Transverse Surface Cracks**



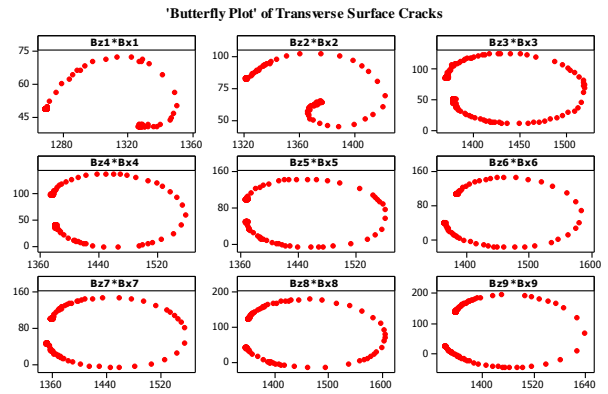
**a) Bx Signals of Transverse Surface Cracks**



**b) Bz Signals of Transverse Surface Cracks**



c) 'Butterfly Plot' of Longitudinal Surface Cracks



c) 'Butterfly Plot' of Transverse Surface Cracks

## Conclusion

As a conclusion, small mean errors and standard deviation of depth and length sizing using the ACFM technique makes this technique more close to the actual value. The correlation observed between the experimental results of sizing and actual depth and length of simulated surface cracks is found to be excellent. Surface cracks with depth 0.5 mm were clearly observed in Bx, Bz and 'Butterfly plot' signal. The presence of surface cracks diverts some of the current away from it centre of the crack and concentrates it near the cracks ends, as a result giving rise to perturbations in Bx, Bz component and 'butterfly plot'.

## References

- [1] Knight, M. J., Brennan, F. P., Dover, W. D. (2002). Effect of Residual Stress on ACFM Crack Measurements in Drill Collar Threaded Connections. *NDT&E International*, 37, 337-343.
- [2] Masserey, B. and Mazza, E. (2007). Ultrasonic Sizing of Short Surface Cracks. *Ultrasonics*, 46, 195-204.
- [3] Gaynor, T. M., Roberts, D.L., Homan, E. (1997). Reduction in fatigue through crack detection by alternating current field measurement, *SPE Drilling and Completion*, 12, 37-42.
- [4] Lugg, M.C. (2005). Crack Detection – Applications of the Alternating Current Field Measurement Technique for Weld Testing, *Materials Evaluation*, 68, No. 11, 1216-1221.



## MODELLING AND ANALYSIS OF THE RUST IN OIL CONDUITS

Naouar LAAIDI, Sougrati BELATTAR\*

Laboratory of Electronics, Instrumentation and Processing of the Signal

Faculty of Sciences, B.P 20.24000 El Jadida, Morocco

[\\*belattars@hotmail.com](mailto:belattars@hotmail.com)

### Abstract

Maintenance of pipes and pipelines used in transporting gases or liquids is a challenge for the industry in general and oil in particular seen the expensive consequences that can occur due to several reasons, such as: development of defects of cracks types, rust ... etc. which can cause leakage of the transported substance or rupture of these conduits with all that behaving like economic loss in addition to the pollution of the environment.

In this paper, a nondestructive testing study of these conduits, based on the principle of infrared thermography and numerical modeling in three dimensions is presented.

The purpose of this article is to show, the thermal behavior of pipelines in the presence of defects of corrosion type. For this, a defect of rust type of different sizes and positions in the studied structure is considered and simulated.

For different simulated configurations, the thermographical images and spatial variation of the temperature on the input surface of the studied structure are presented and analyzed. The numerical solution of this problem was performed using numerical software based on the finite element method.

Keywords: corrosion, rust, conduits, infra-red thermography, finite elements.

### 1. Introduction

The problem of corrosion is a concern for many industries such as nuclear, chemical and petroleum. These defects can cause a serious economic and environmental damage, that is why it is important to monitor regularly these structures to detect the earliest possible potential anomalies that may exist [1, 2]. The goal of this study is to show, by calculating the surface temperature and the analysis of the obtained thermographical images, the effect of the eventual presence of a rusted region in the conduits on the temperature distribution.

For this study, we modelled a conduit by a steel cylinder as used in transporting oil or gas and the defect by a circular layer of rust. The dimensions of the rust layer are taken as parameters.

### 2. Principle of the method

When a material is thermally requested, the heat diffuses in uniform way in material. The presence of an eventual defect within the material acts like a heat concentrator or heat insulator and changes the process of heat diffusion. It follows from there the appearance of a cooler or a hotter region on the surface compared to the close one without anomaly [3].

### 3. Structure of the model

The studied device is represented by a cylindrical structure, fig.1, having the following geometrical parameters: external diameter  $d=254\text{mm}$ , the cylinder thickness  $e_p = 19\text{mm}$  and the conduit length  $l=1000\text{ mm}$ .

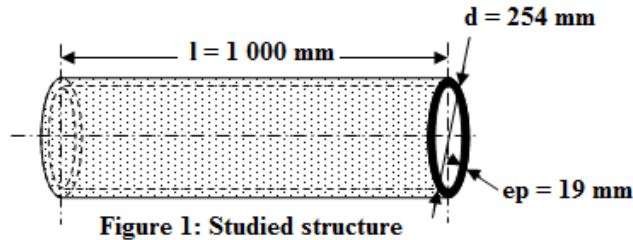


Figure 1: Studied structure

### 4. Mathematical model

The problem is to solve following thermal equation:  $a \nabla^2 T = dT/dt$  (1)

Where  $a = \lambda / \rho c$  : is called thermal diffusivity.

The numerical method of the finite elements is used[4, 5]. Indeed, the analytical resolution is impossible being given the problem geometry. The method consists in using an approximation by finite elements of the unknown functions  $T$  to discretize the variational form of the equation (1) and to transform it into system of algebraic equations of the form:  $[A] T = F$ . (2)

With  $A$ : square matrix of dimension  $[Nh, Nh]$ ,  $F$ : a vector of  $Nh$  components.

$T$ : the vector of the temperatures to be calculated.

We start by building the variation form of the equation (1). We carry out a spatial discretization which consists in calculating the elementary integrals by using the finite element and a temporal discretization.

There are many specialized software which make it possible to implement the method of resolution of problems by finite elements in a more or less simple and convivial way. They take care in particular of the grid of the studied object, the automatic numbering of the elements and the nodes, the calculation of a solution then of the chart of the results.

In this study, we used commercial software "Comsol" based on the finite element method and which makes it possible to calculate the evolution of temperature at any moment and in any point of material. The material is considered isotropic. The calculation of the thermal answer is made in the case of a portion of oil pipe, subjected to a step of flow on the outer face, continuous and is extended at  $Q=50\text{W/m}^2$  density. the Inner surface of the pipe were subjected to convectional heat transfer with heat transfer coefficient,  $h=10\text{ W/m}^2\cdot\text{K}$ . The initial temperature is of  $T_0=25\text{ }^\circ\text{C}$ .

### 5. Results of simulation

#### 5.1 Considered model

In order to detect the rust thermal effect on the thermal state of the steel pipe, many situations are considered. The study concerns the effect of the diameter of a circular rust stain, the effect of the depth of the rust in the steel layer and finally the effect of the pipe thickness on the surface temperature on the given structure for a given defect.

Generally, from a thermal point of view the rust element is compared to water, since both have very close thermal characteristics [6]. When the rust attacks a cylindrical structure, the steel section decreases with the increase of corrosion layer [7], which involves a no homogeneous reduction of

steel section accompanied by its embrittlement and a modification of the interface physical properties (increase then reduction in adherence) [8]

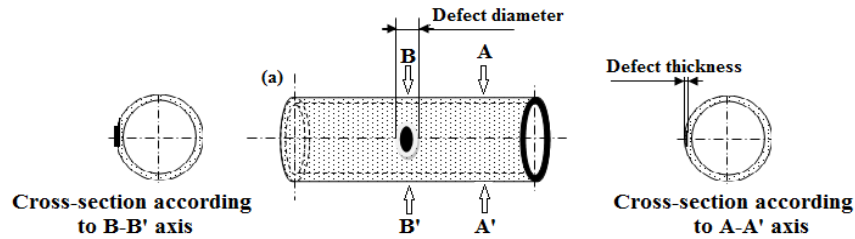


Fig.2: Considered model

The physical and geometrical characteristics of the pipe and the rust are recapitulated in the table below (table 1)

Pipe	
External diameter	254mm
Cylinder thickness	19mm
length	1000m
thermal conductivity	44.5 w/m.K
Rust	
Thermal conductivity	0.6 w/m.K

Table 1: physical and geometrical characteristics of pipe and rust.

## 5.2 Effect of the rust layer diameter

In order to illustrate the effect of the diameter of the rusted layer on control, three layers of rust in the shape of circular stain of a constant thickness (6mm) and with variable diameters: 60mm, 80mm and 100mm, are considered Fig.3.

The calculated thermographical images (figures 4 and 5) and the spatial evolutions of the surface temperature fig.6 show that the more the diameter of rust increases, the more the surface temperature of the entry face increases and consequently the detectability of the defect becomes easier, but the excess of temperature brought by the presence of defect remains weak and the difference between the healthy state of control and the state with defect is about  $0,10^{\circ}\text{C}$  for  $d = 60\text{mm}$ ,  $0,214^{\circ}\text{C}$  for  $d = 80\text{mm}$  And  $0,26^{\circ}\text{C}$  for  $d = 100\text{mm}$  this shows that the use of such results on the experimental level requires a very accurate infra-red cameras of a sensitivity about 0,01

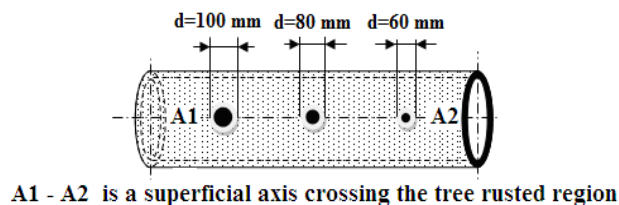


Figure 3: structure of the model

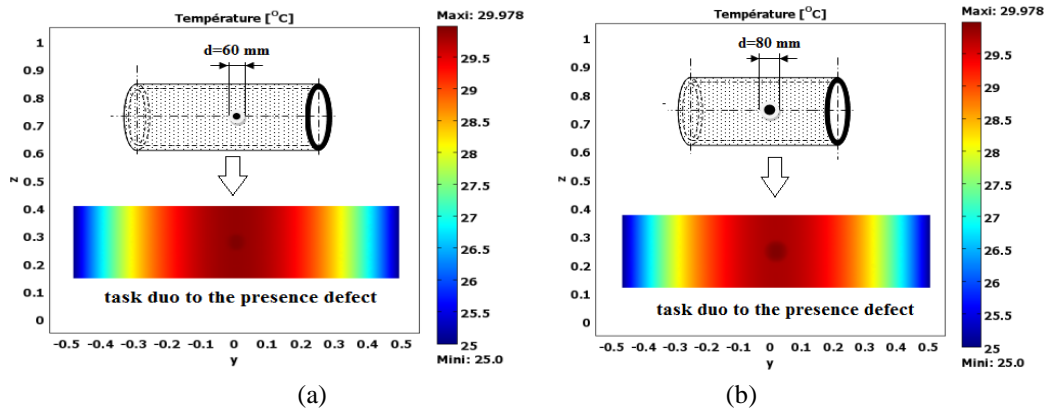


Figure 4: Thermographical image of the conduit input face (a)  $d=60$  mm, (b)  $d=80$  mm

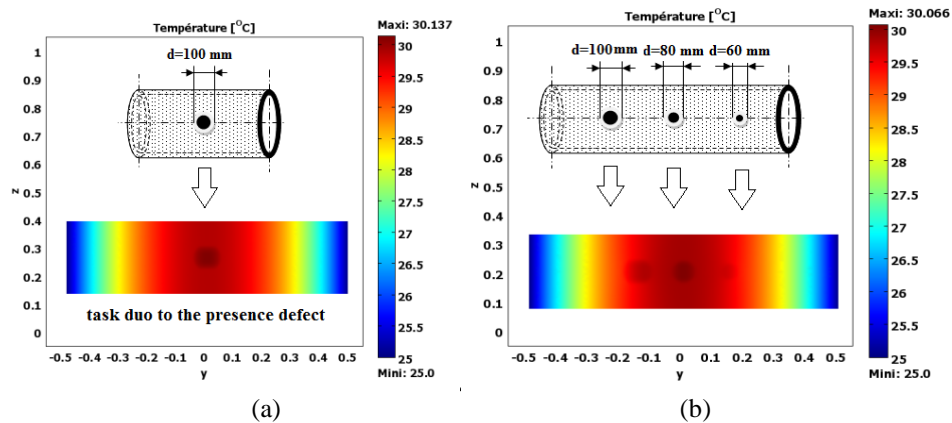


Figure 5: Thermographical image of the conduit input face (a)  $d=100$  mm, (b) Thermographical image of the conduit input face for the three cases together  $d=60, 80$  and  $100$  mm

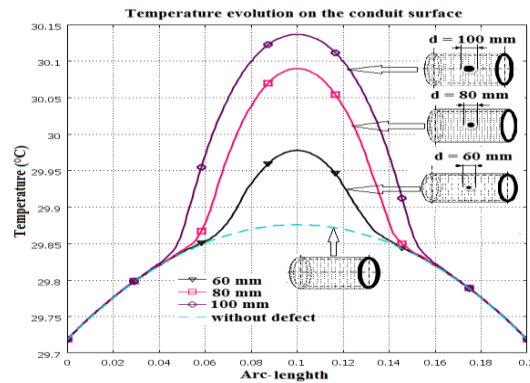


Figure 6: spatial evolution of the temperature on the entry face

### 5.3 The effect of rust layer thickness

We consider the same conduit as before, but this time we are interested in the defect thickness as a parameter taking the following values: 4 mm, 6 mm and 9 mm. The diameter of the rust task is constant and equal to 80 mm. The thermographical images of the three cases (Figures 8, 9, 10 and 11) and the evolution of the spatial surface temperature (Fig. 12) obtained show that the more the rust layer thickness increases, the more the surface temperature of the entry face also increases and consequently the detectability of these defects becomes easier.

Similarly, one can show that the temperature changes due to the presence of the defect remain weak compared to the healthy state of control. Indeed the difference in temperature of the healthy structure and that containing the defect is of  $0.15^{\circ}\text{C}$  for  $e_d = 4\text{ mm}$ , of  $0.24^{\circ}\text{C}$  for  $e_d = 6\text{ mm}$  and of  $0.30^{\circ}\text{C}$  for  $e_d = 9\text{ mm}$ . On the experimental level, accurate measurements are essential for such detections.

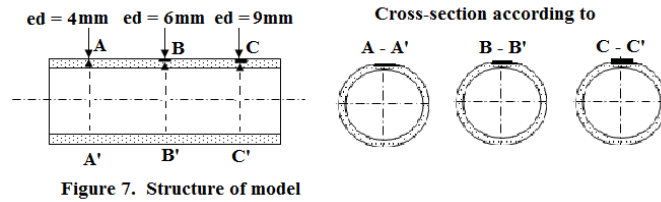


Figure 7. Structure of model

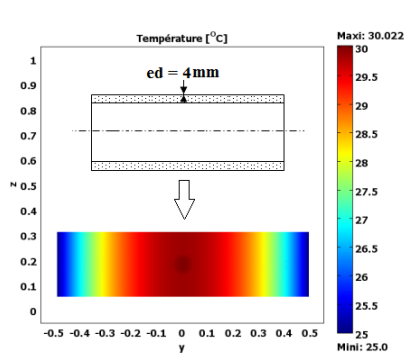


Figure 8: Thermographical image of the entry face ( $e_d=4\text{ mm}$ )

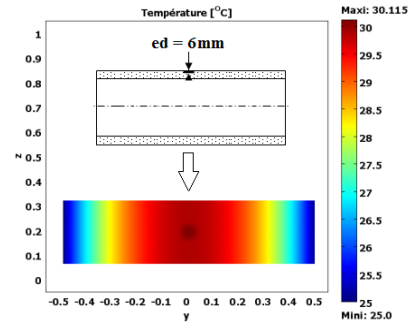


Figure 9: Thermographical image of the entry face ( $e_d=6\text{ mm}$ )

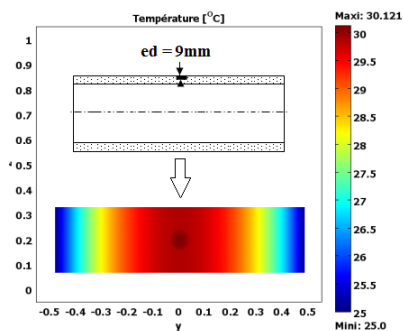


Figure 10: Thermographical image of the entry face ( $e_d=9\text{ mm}$ )

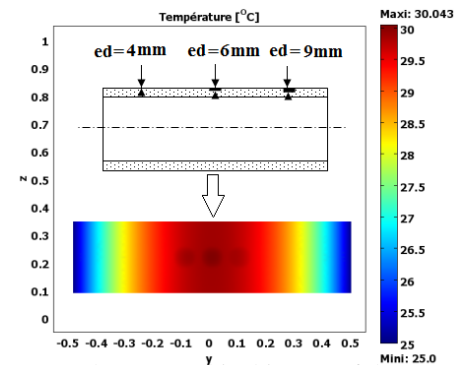


Figure 11: Thermographical image of the entry face for the three cases together

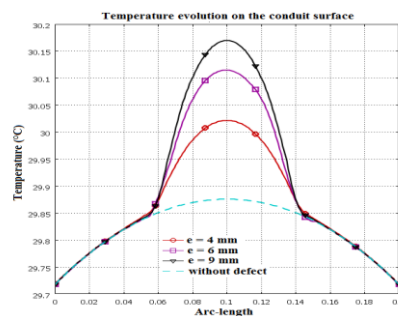


Fig.12: change of the temperature on the entry face

## 6. Conclusion

In this paper, we presented the effect of several parameters of the circular rust layer on its detectability in steel conduits, namely the effect of its diameter and its thickness.. In general, one can draw the following conclusions:

- The detectability of corrosion is easier for a larger rust diameter.
- The detectability is easier for a larger thickness.

## 7. References

- [1] A. Vageswar et al: NDT&E International 42 (2009) 275–282
- [2] J.-H. Lee, S.-J. Lee: NDT&E International 42 (2009) 222–227.
- [3] J. Rhazi, S. Naar.(2005), Aptitude de la thermography infrarouge à détecter les fissures et nids d'abeille dans le béton. 12ème colloque sur la progression de la recherche québécoise sur les ouvrages d'art, Quebec, Canada, 13p(10-11 mai 2005).
- [4] A. Elballouti, S. Belattar. : PCN 35 (May 2007) 43-47.
- [5] Elballouti, A., Belattar, S., *IJMPT*, Manuscript Reference No.: IJMPT-4NDT-02, (to be published).
- [6] Molina F.J., Alonso C., Andrade C.Numerical model. Materials and Structures, 26(1993)., 532-548.
- [7] .Mickael Dekoster, Olivier Blanpain, François Buyle-Bodin, Olivier Maurel, (2004). Etude de l'évolution des coefficients de sécurité des ouvrages en béton armé dégradé selon différents scénarios de corrosion. XXIIIèmesRencontresUniversitaires de Génie Civil 2004 - VILLE & GENIE CIVIL.
- [8] Quang Thanh Nguyen, Sabine Caré, Yves Berthaud, A. Millard : L'objet (2005) 8 – n°2/.



## DISTRIBUTION OF RADIATION AROUND LABYRINTH TYPE EXPOSURE ROOM

Mohamad Pauzi Ismail, Mohd Yusnisyam Yusuf, Shaharudin Sayuti, Noor Azreen Masenwat, Siti Madiha Muhammad Amir and Azhar Azmi

NDT group, Industrial Technology Division,  
Malaysia Nuclear Agency, Bangi, 43000 Kajang.

[pauzi@nuclearmalaysia.gov.my](mailto:pauzi@nuclearmalaysia.gov.my)

**Abstract:** The design of X-ray or gamma ray radiographic exposure room requires some calculations on shielding to provide safe operation of the facility and minimum exposure to radiation workers. Careful design can lead to economical installations with minimal barriers. The design depends on such factors as: maximum energy, maximum intensity, permitted full-body dosage, workload, use factor, occupancy factor, maximum dose output and shielding materials. Choice of shielding materials depends on convenience and cost. The radiographic exposure room is usually made of normal concrete with density of about 2.3 – 2.4 g/cc. Normal concrete is often used for construction of exposure room because of cheap and ease of construction.

Labyrinth or maze type of design is the most popular especially for high energy radiation since it can reduce the radiation to a level that make the door design economic and practicable.

This paper explained and discussed the distribution of radiation dose around the labyrinth type of exposure room.

### Introduction

All works with radiation sources involved a risk of exposure to radiation, which is known as occupational exposure. However, as a general rule, all workers must take efforts to ensure that the exposure he received is kept to a minimum possible. This is known as 'As Low as Reasonably Achievable' (ALARA) concept. For industrial radiography, only external radiation exposure is to be considered. If a radioactive material gets inside the human body it gives rise to an internal radiation exposure, which required quite different method of control. The external radiation exposure is controlled by applying the three radiation safety principles namely: Working time, Distance and Shielding

Radiation exposure received by a radiation worker in radiation area is directly proportional to length of time that the individual spends in that area. Limiting the time spent in a radiation area is one of the main methods to reduce the amount of radiation exposure received by a radiographer. In reality, this can be achieved by proper planning of the job to be carried out and at the same time distributing the work evenly among radiographers involved.

Maximizing distance from a radiation source is a very effective means of protecting radiographer. This is because radiation exposure decreases drastically with increasing working distance from the source. The third method of controlling external radiation exposure is by placing a shielding between the source and the radiographer. Shielding could be made of any suitable materials and is placed as a

barrier between the radiation source and workers. In practice, lead and concrete are used as common shielding materials for x- and gamma rays. Shielding effectiveness for each material depends on its atomic number, density and thickness. It is also dependent on the energy of radiations. The labyrinth design is very practical in reducing lead door thickness (Fig. 1). It reduces the door weight and makes it easy to handle either by manual or motorized.

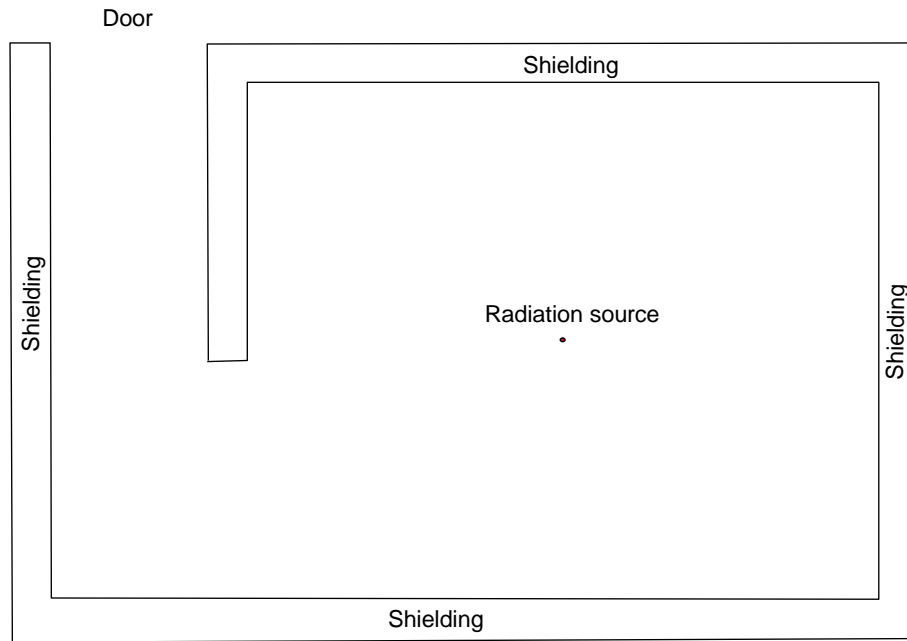


**Fig. 1:** Typical Labyrinth design

## Radiation absorption and scattering

In passing through matter, x- and gamma rays lose their energy to atoms by three ionization processes which are known as photoelectric absorption, Compton scattering and pair production. Photoelectric absorption is an interaction with orbital electrons in which a photon of electromagnetic radiation is consumed in breaking the bond and imparts kinetic energy to the electron. This mode of interaction is most likely to occur when x- or gamma rays of low energy ( $< 0.5\text{MeV}$ ) penetrate matter of high atomic number. The probability of occurrence roughly varies as  $1/E^2$  and  $Z^2$ , where  $E$  is the energy of the incoming photon and  $Z$  is the atomic number of the target material.

Compton scattering is a form of direct interaction between an incident photon and a loosely held orbital electron in which the electron is ejected from the atom and only a part of its kinetic energy is consumed. The photon is scattered incoherently, emerging in a direction that is deviated from that of incident radiation and with a reduced energy. This process, which progressively weakens the photon, is repeated until photoelectric effect completely absorbs the photon. Compton effect occurs when electromagnetic radiations consisting of photons of about  $0.1$  to  $3.0\text{MeV}$  pass through matter. The probability of its occurrence varies directly with the atomic number of scattering element, and approximately inversely with photon energy.

Pair production is photon interaction with electric field surrounding the nucleus of an absorbing atom. The electromagnetic energy of incident photon is completely absorbed in the creation of a positron-electron pair (i.e. 'ion pair') of appropriate kinetic energies. This reaction does not occur for incident radiation energies of less than 1.02MeV. If the original photon has energy greater than 1.02MeV, it is completely used up (absorbed) in the pair production process. The residual energy now appears as the kinetic energy of the newly created positron electron particles. The positron created by pair production may combine with an electron and disappear with the emission of two gamma photons of 0.51MeV each. These will act as other low energy gamma photons and may cause ionization by the photoelectric effect or by Compton scattering. The probability of occurrence of this process increases rapidly with photon energies above 1.02MeV and also increases with  $Z^2$  of the target material.

## Attenuation of X-and Gamma Radiation

When x-rays or gamma rays of a given uniform energy pass through matter, their intensity decreases exponentially to an extent that is a definite function of thickness of the absorbing material. That is, the number of photons will decrease by a constant percentage of the whole for a given thickness of absorber material. The degree to which the radiations are absorbed or scattered gives considerable amount of information about the materials through which they pass. For a beam of radiation having an intensity  $I_0$  incident on a slab of thickness  $x$ , the intensity of the transmitted radiation  $I$  can be calculated using the attenuation formula:

$$I = I_0 \exp(-\mu x) \quad (1)$$

Where  $\mu$  is the attenuation coefficient (usually expressed in  $\text{cm}^{-1}$ ) whose value depends on the type of materials and radiation. It indicates the ability of a shielding material for reducing the intensity of radiation. Value of  $\mu$  is made up from contributions by photoelectric effect ( $\mu_{pe}$ ), Compton effect ( $\mu_c$ ), and pair production ( $\mu_{pp}$ ). The formula (1) can also be written in term of Half Value Layer (HVL) as follow;

$$I = I_0 \exp (-0.693x/\text{HVL}) \quad (2)$$

HVL is dependent upon the type or energy of radiation and the absorbed material and the value can be obtained from various references [1, 4, 5] and the value normally take into consideration the build-up factor.

## Experimental Methodology

A mini exposure room has been constructed using interlocked concrete blocks as shown in Fig. 2. The concrete blocks were made using the Public Work Department (JKR) mix design. The design is 1:2:4 by weight and the water to cement ratio is 0.5. This mix design produces a concrete with density around 2300-2400  $\text{kg/m}^3$ .

A 3.43Ci Selenium-75 was positioned at the centre of the exposure room and radiation survey was made using Radiation monitor controller by Radcal Corporation model 2026C. Radiation dose readings were taken by altering the source to film distance and position of the survey meter from the wall (Fig. 3).



**Fig. 2:** Mini experimental exposure room

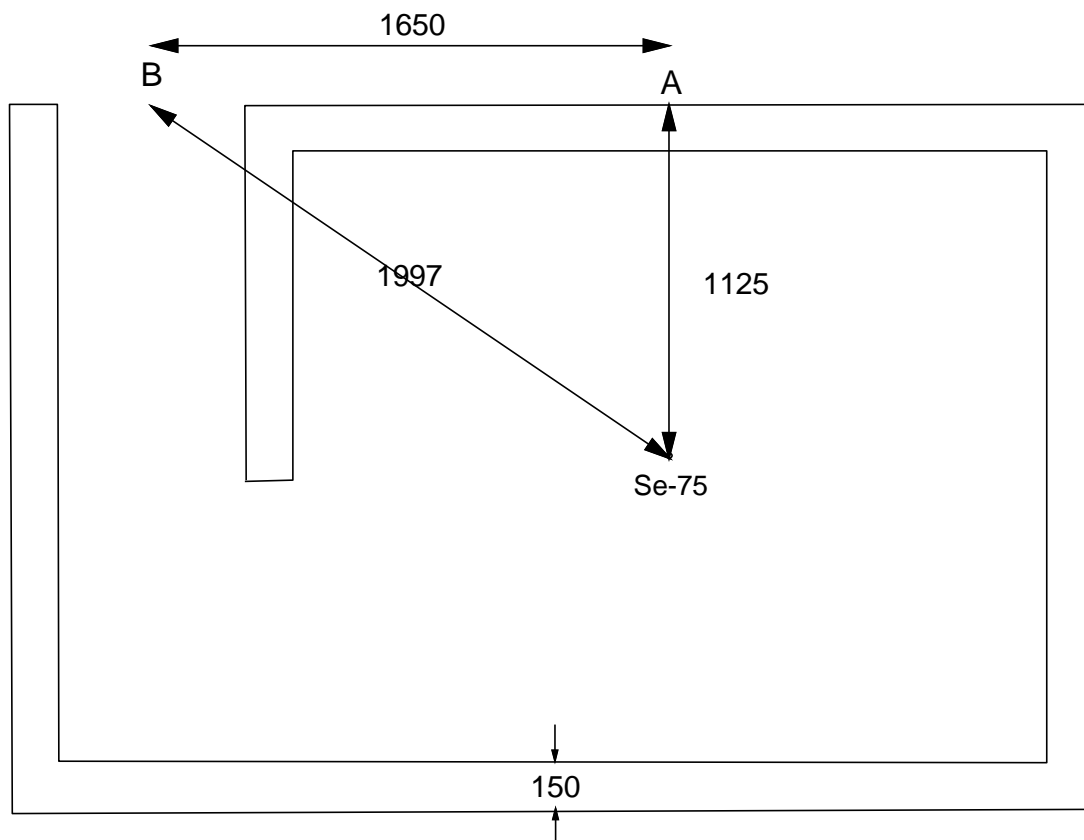


**Fig. 3:** Measurement locations (A, B)

## Results and Discussions

Results of the dose measurement are tabulated in Table 1 and 2. Table 1 shows the calculated values based on the block thickness of 150mm while Table 2 for the effective thickness of 100mm.

Figure 4 and 5 show the dose comparison between calculated and experimental values at location A and B respectively. All calculations are based on primary radiation. It shows that the experimental values are lower than the calculated values at the outside wall (zero distance) and becoming equal when measured at far distance from the wall (1, 2 and 3m from the wall).

Table 1: Dose distribution when considering wall thickness is 150mm

Source: Se-75 <b>3.43</b> Ci on 20 Jul 2012      k = <b>0.203</b> R/h.Ci at 1m      x = 150 mm HVL =      30    mm I1 =      0.69629    R/h d1 =      1    m      Detector height =      860    mm OA =      1125    mm      Wall height =      1500    mm OB =      1997.029    mm									
Detector from outside wall (m)	SFD (cm)	Dose rate (mR/hr)		Calculated for A			Calculated for B		
		A	B	d2 (m)	I2 (mr/h)	Ix (mr/h)	d2 (m)	I2 (mr/h)	Ix (mr/h)
0	30	29.5	4.5	1.26	440.91	13.79	2.07	161.87	2.45
0	60	40.5	6.5	1.15	522.26	16.33	2.01	171.69	2.59
0	90	50.5	9.5	1.13	549.46	17.18	1.99	175.58	2.65
1	30	12	4.5	2.20	144.18	4.51	2.75	92.23	1.15
1	60	14.5	4.5	2.14	151.92	4.75	2.75	92.23	1.15
1	90	16.5	5.5	2.13	154.14	4.82	2.75	92.23	1.15
2	30	5.5	3.5	3.17	69.08	2.16	3.58	54.42	1.08
2	60	7.5	3.5	3.14	70.81	2.21	3.58	54.42	1.08
2	90	7.5	4.5	3.13	71.29	2.23	3.58	54.42	1.08
3	30	3.5	2.5	4.16	40.18	1.26	4.48	34.74	0.83
3	60	3.5	3.5	4.13	40.76	1.27	4.48	34.74	0.83
3	90	4.5	3.5	4.13	40.92	1.28	4.48	34.74	0.83

Table 2: Dose distribution when considering effective wall thickness is 100mm

Source: Se-75 <b>3.43</b> Ci on 20 Jul 2012      k = <b>0.203</b> R/h.Ci at 1m      x = 100 mm HVL = 30 mm I1 = 0.69629 R/h d1 = 1 m      Detector height = 860 mm OA = 1125 mm      Wall height = 1500 mm OB = 1997.029 mm									
Detector from outside wall (m)	SFD (cm)	Dose rate (mR/hr)      Calculated for A					Calculated for B		
		A	B	d2 (m)	I2 (mr/h)	Ix (mr/h)	d2 (m)	I2 (mr/h)	Ix (mr/h)
0	30	29.5	4.5	1.26	440.91	43.76	2.07	161.87	9.89
0	60	40.5	6.5	1.15	522.26	51.84	2.01	171.69	10.49
0	90	50.5	9.5	1.13	549.46	54.54	1.99	175.58	10.73
1	30	12	4.5	2.20	144.18	14.31	2.75	92.23	5.02
1	60	14.5	4.5	2.14	151.92	15.08	2.75	92.23	5.02
1	90	16.5	5.5	2.13	154.14	15.30	2.75	92.23	5.02
2	30	5.5	3.5	3.17	69.08	6.86	3.58	54.42	4.00
2	60	7.5	3.5	3.14	70.81	7.03	3.58	54.42	4.00
2	90	7.5	4.5	3.13	71.29	7.08	3.58	54.42	4.00
3	30	3.5	2.5	4.16	40.18	3.99	4.48	34.74	2.93
3	60	3.5	3.5	4.13	40.76	4.05	4.48	34.74	2.93
3	90	4.5	3.5	4.13	40.92	4.06	4.48	34.74	2.93



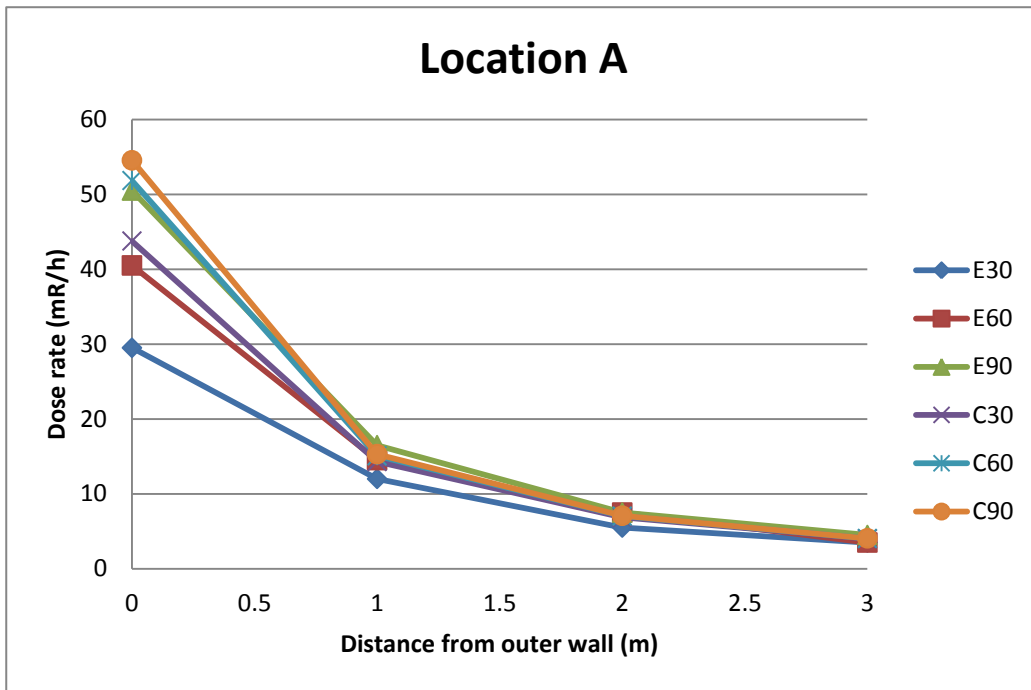


**Fig. 4:** Dose rate vs distance from the wall at location A (100mm effective thickness)

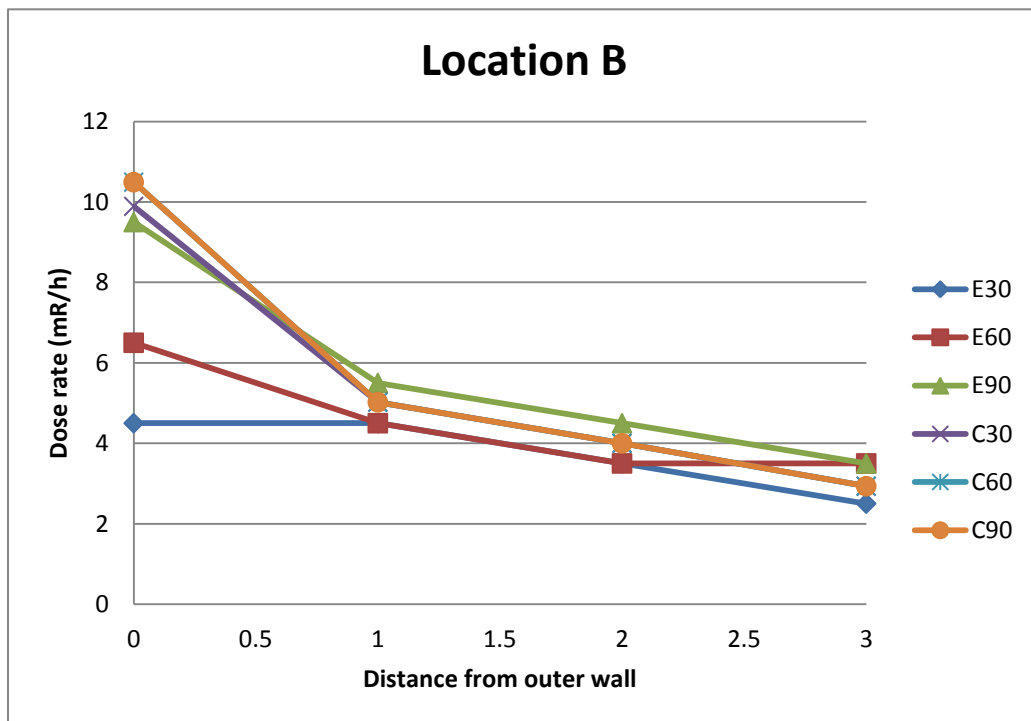


**Fig. 5:** Dose rate vs distance from the wall at location B (100mm effective thickness)

## Conclusion

For open source, no leakage radiation is to be considered. The experimental value is lower and equal to the calculated value based on primary radiation. Therefore calculation based on primary radiation is adequate and calculation for secondary radiation i.e. scattered and leakage radiation may not be required.

## Recommendation

This experiment is using low energy source Se-75 where the scatter radiation effect may not significant. It is recommended that Ir-192 or higher energy source being use to confirm for the effect of scattered radiation.

## Acknowledgment

The first author would like to thank to Research and Innovation Management Centre for providing fund to this project (NM-R&D-11-16). The author also would like to express his appreciation to all NDT staffs - especially to Abdul Bakhri, Rahmad, Suhairy and Mohd Kamal Shah for their assistance in preparing and testing of concrete samples.

## References

1. ANSI/HPS N43.3-2008, American National Standard For General Radiation Safety – Installations Using Non-Medical X-Ray and Sealed Gamma-Ray Sources, Energies Up to 10 MeV
2. [http://www.ndt-ed.org/EducationResources/CommunityCollege/RadiationSafety/safe\\_use/shielding.htm](http://www.ndt-ed.org/EducationResources/CommunityCollege/RadiationSafety/safe_use/shielding.htm)
3. [http://www.concreteconstruction.net/Images/Normal%20Concrete%20for%20Radiation%20Shielding\\_tcm45-344093.pdf](http://www.concreteconstruction.net/Images/Normal%20Concrete%20for%20Radiation%20Shielding_tcm45-344093.pdf)
4. LEM/TEK/33 Rev. 1, 02 December 2008, Code of Practice on Radiation Protection in Industrial Radiography.
5. Radiation Safety for Industrial Radiography, Malaysian Nuclear Agency, 2004.

## SEE THE INVISIBLE–INNOVATIVE TECHNOLOGY AS TOOL for SAFETY and QUALITY

Isaac EINAV

STAR.IK Ltd (STAR. International Consultant)

Richmond Hill, Ontario, Canada, L4C 3Z6,

Phone +1-905-237-5520, e-mail: starik18@gmail.com

### Abstract

Today technology requires better quality and safety of operation, more reliable information on the current status, prognosis for usability and object's life expectation.

Mechanical stresses are not visible to most of conventional NDT methods and they are usually the main and the first indicator of problems and to deal with this we are introducing Indicator of Mechanical Stresses (IMS). Not the search for defects but for condition of deterioration to estimate the possible failure based on measuring concentration and the gradient of mechanical stress on Ferro-Magnetic parts. Therefore, innovative approach for early detection of condition to assure quality and safety is required.

**Key words:** Indicator Mechanical Stresses (IMS), Mechanical Stress Concentration, Stress Detection and Classification.

## 1. INTRODUCTION

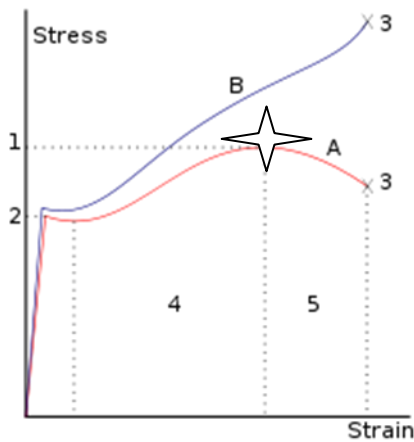
To assure quality and safety of industrial performances, to more reliable of results in-service inspection (ISI) or early diagnostics (Preventive Maintenance or remain life prediction), to measure conditions which cannot be determined by conventional NDT methods required another approach. Engineers can design structures for certain strength, to estimate the greatest possible stress, to define "fitness for service". But in most case it is an estimate. Measurements of mechanical stresses can assist to define the condition. The new approach is not the search for defects but for the causes of failure by measuring mechanical stresses for their critical level. The new device, Indicator of Mechanical Stresses, IMS could be a good tool in providing the requested information.

Talking about measurement of mechanical stresses, it is important to remember the definition of NDT (detection or measurement of the properties, integrity of materials, parts, assemblies or structures without impairing their ability to assure safety of operation) as well as advantages and limitation of each method or technique and the measurement mechanical stress as complimentary technique to basic NDT methods.

## 2. BASIC PRINCIPLE of STRESS-STRAIN DIAGRAM

Before discussing principles of residual mechanical stresses and application of Indicator Mechanical Stresses (IMS) lets refresh basic principle of Stress-Strain diagram including Ultimate Tensile Strength (UTS) which is the maximum stress that a material can withstand before necking (fracture or breaking). Generally, linear stress-strain relationship up to point 2 (Fig. 1) is the elastic region when the slope return to Zero after removal of stress. After point 2 (yield point), the curve typically decreases but the deformation continues.

The stress increases on account of strain hardening (area 4) until it reaches the ultimate strength, (point 1). Up to this point, the stress in cross-sectional area behaves uniformly (Poisson contraction). The actual rupture point is in the same vertical line as the visual rupture point. However, beyond point 1 a neck forms (area 5) where the local cross-sectional area decreases more quickly than the



rest of the sample resulting in an increase in the true stress. In a sufficiently ductile material, when necking becomes substantial, it causes a reversal of the engineering stress-strain curve (curve A); this is because the engineering stress is calculated assuming the original cross-sectional area before necking. The reversal point is the maximum stress on the engineering stress-strain curve, seen as a decrease in the stress (area 5) until failure. The neck becomes unstable and the specimen ruptures (fractures, point 3).

1. Ultimate strength
2. Yield strength
3. Fracture
4. Strain hardening region
5. Necking region

**A: Engineering stress**

**B: True stress!!!!**

Fig 1. A stress-strain typical curve:

### 3. PRINCIPLE OF MECHANICAL STRESS MEASUREMENT AND IMS

The principle of mechanical (residual) stress measurement used for design devices based on magneto-elastic effect that ferromagnetic materials change magnetic properties under the influence of mechanical stress. This principle use to build magneto-elastic and magneto-anisotropic indicators, including Indicator of Mechanical Stress, IMS.

High uncertainty due to standard approach to solving challenges and ignoring certain physical phenomena has been long time obstacles for implementation of electromagnetic techniques in practice. It is known that the upper layer (0.2 mm) of metal has not typical, designed stress condition due to various stress influences like oxidation, mechanical micro-scratches etc. and some difficulties accrues in application, for example devices based on effect of Barkenhausen. Another reason for low confidence of measurement mechanical stresses using electromagnetic fields indicators are magneto-mechanical hysteresis and attempts to get the result by one of the parameters of hysteresis loops (for example, based only on coercive force  $\sigma$  or only on residual induction B).

Any relationship between B and  $\sigma$  has a point inverse relationship after which the connection between B and  $\sigma$  become reverse, i.e. the same level of output signal can be received for two different mechanical stresses. The phenomenon of mechanical hysteresis is observed for example, near and the zone of plastic flow (points 2-3, Fig 1).

When constructions made from steel and which had suffered numerous mechanical changes including local plastic deformation in the process of preparing and mounting, conventional “stress-meters” often provide false results.

This connection between mechanical stresses and magnetic properties called magneto-elastic sensitivity ( $\Lambda$ ): where **B** is the magnetic induction and  $\sigma$  is mechanical stress (load)

$$\Lambda = \partial B / \partial \sigma \quad (1)$$

Principle of operation magneto-anisotropic converter based on effect of rotating magnetic induction vector B in the primary measurement coil. The voltage U at the output of the measuring coil  $\omega$  is described by the formula

$$U = K B_c S_0 f_{\Pi} \sin \beta \omega \quad (2)$$

where  $B_c$  - average value of induction;  $S_0$  - area covered by windings;  
 K- coefficient proportionality;  $f_{\Pi}$  - voltage frequency.  
 $\beta$  - angle between the vector measuring winding  $\omega_2$  and magnetic induction B;

The formula obtained for similar direction vectors  $\vec{\sigma}$  and  $\vec{B}$ . By rotating vector  $\vec{B}$  it is possible to characterize changes of its orthogonal components.

A more detailed analysis shows that the output of "cross" magneto-anisotropic converter at once (i.e., before any processing) produces a signal proportional to the difference of Principal (Mechanical) Stresses (DPMS):

$$\tau = \frac{\sigma_1 - \sigma_2}{2} \quad (3)$$

Achieved result is important, because according to the stress-strength criteria (Yield) deformation of material occurs when  $\tau$  tension strength

$$\tau_{\max} = \frac{\sigma_1 - \sigma_2}{2} \geq \sigma_T \quad (4)$$

Location of stress concentration appearance there is anomalous change of magnetic properties of metal.

A detailed consideration of this physical nature and the fact that all useful information is contained in several parameters of hysteresis loop was resulted in development of the Indicator of Mechanical Stress (IMS) model "StressVision" and an algorithm to process information. Information processing algorithm used in Indicator of Mechanical Stresses ("StressVision") equipment, in particular, makes it possible to resolve the problem of magneto-mechanical hysteresis and provide accurate results.

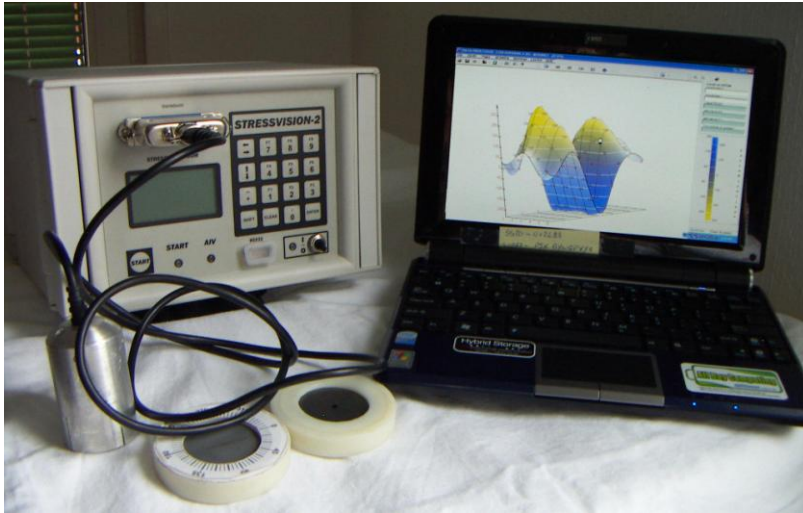
Magneto-anisotropic ("cross") transducers used in IMS are two mutually-perpendicular U-shaped coils one is an activation coil and the other coil is a measuring coil. Transducers measure anisotropy of magnetic properties in ferromagnetic metals under external load using Magneto-elastic converters within the limitations of equipment. IMS measures Electromotive Force (EMF) by inducing magnetic field which generated by excitation coil and picked up by receiving coil, 2 perpendicular magnetic circuits in the probe (transducer). If material has isotropic magnetic properties, EMF induced in measuring coils mutually compensated and the output signal is Zero (well balanced magnetic field). If there is anisotropy of magnetic properties, unbalance of EMF occurs which results in appearance of output signal with values depends on the value and orientation of main mechanical stresses upon the surface of metal being tested by detecting Mechanical Stress Concentration (MSC) and the difference of Principal Mechanical Stresses (DPMS).

IMS results as dimensionless, i.e. qualitative comparison (less-than-equal).

To assess the conditions and operational risk, it is not-so-important to find stresses but their concentration and rate of change of stress (gradients). Normally, in the centers (peaks) mechanical stress concentration (MSC) defects are formed. They are dislocation-generators. With sufficiently high gradients, these locations begin to move. Eventually, cracks are developed. If in the area under inspection there are no stress concentrations or gradients, there will be no metal destruction.

IMS allows identification of MSC and gradients to show the exact coordinates and quantify their development without any additional measurements. This allows, on the one hand, making conclusions about the current condition of the surveyed site and helping assessing the remaining life. On the other hand, to make conclusive decisions about location of the gradients and concentration in precisely location on the maps and how to deal with concentrators and gradients, i.e. to prevent these sources from occurrence and formation of defects

## Indicator of Mechanical Stresses, IMS



For ferritic metals

To evaluate the criticality of the concentrations of the stresses and the gradient are more important parameters than the stresses themselves

The equipment is suitable for testing all Fe steels and can be used on painted and/or coated surfaces with a maximum gap of 4 mm.

Scanning programme requires to collect of minimum 25 readings (grid of 5x5 readings minimum) and recommended thickness up to 1/2 inch.

Fig 2. Indicator of Mechanical Stresses (IMS) consist of data collector, probe (transducer) and Laptop for results processing and storage

### Some of the benefits applications of IMS are:

- - simplicity of the data collection (1-2 sec);
- -; high sensitivity of measurements;
- - rapid analysis of the results;
- - visual presentation of results (2D or 3D diagrams);
- - surface cleaning not required (paint/mud/rust gap up to 4 mm)
- - low cost of inspection;
- - portable (2.5 kg);
- - no need for qualified NDT level 2 or 1 personnel

## 4. SOME OF STUDY CASES DONE BY IMS

Selected cases provided below are to clarify applications and to identify benefits using IMS as a tool to confirm the quality of process (welding, stress relief etc.) or safe serviceability of item as part of ISI or Preventive Maintenance or for the aging construction. IMS could be also be used with great level of success for research and more in depth investigation of stress level inside the part

***General acceptable criteria for the stress gradient as recommended by manufacturer*** (for 9 mm thickness, non-nuclear applications and strongly depends on metal's conditions, without external/internal stresses)

- 1- Stress gradient up to 350 units (difference between top and bottom highest points) is conceder as acceptable working condition
- 2- Stress gradient from 350 to 400 is considered as high working stress level but still can be accepted but it is recommended that the equipment be monitored for increase of gradient.
- 3- Stress gradient from 400 to 450 is considered as critical (defects could have developed already) and can be recommended for replacement as soon as possible (Stress gradient 400-420 could be accepted but with frequent monitoring)
- 4- Any stress gradient 450 to 500 and above should be recommended for immediate care (even if there are no detectable defects)

#### 4.1 Bended plate

Development of the stress level (popular explanation).

The randomly selected plate 200 x 250 mm and 10 mm thicknesses was measured for residual the stress level, bended, flatten and measured again after been bended (bending along the central line, 4)

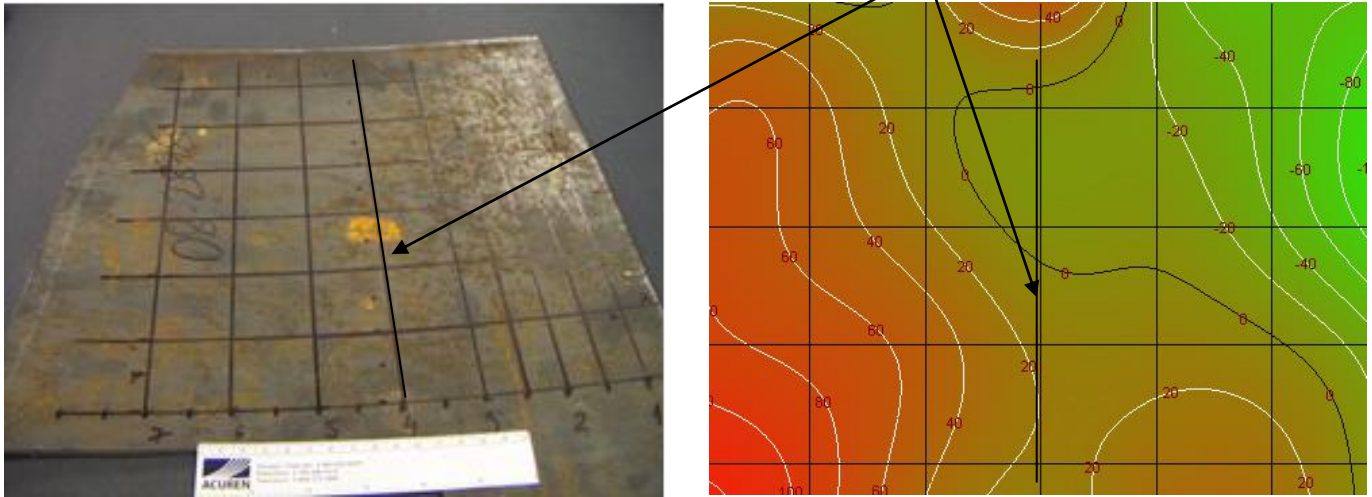


Fig. 3 Plate (general view) and the stress conditions (residual stress) before the bend  
The gradient of stress level is about 200 and concentrations are normal results

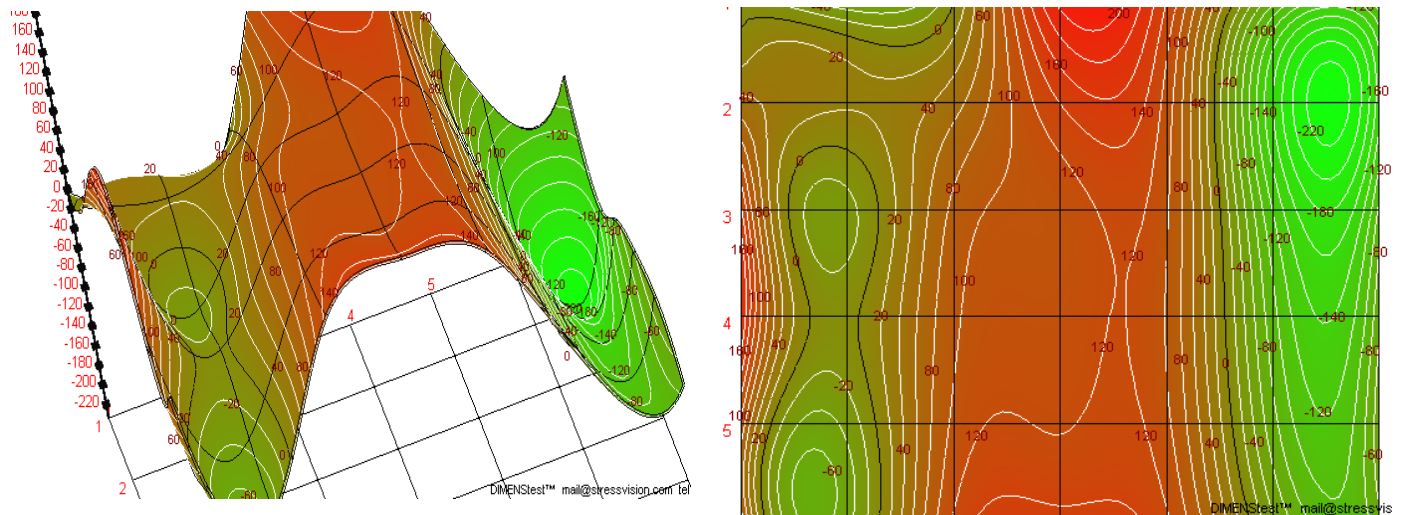


Fig. 4 3D image and 2D after bending

Results are self-explanatory.

The maximum gradient after the bending was 360 the area around the bending line (not critical but clearly detected by IMS).

Same regarding the concentration, high but not critically high (no high picks).



#### 4.2 Welded pipe 6" diameter, 6 mm thick, standard test piece with known defect

(by RT and/or UT)

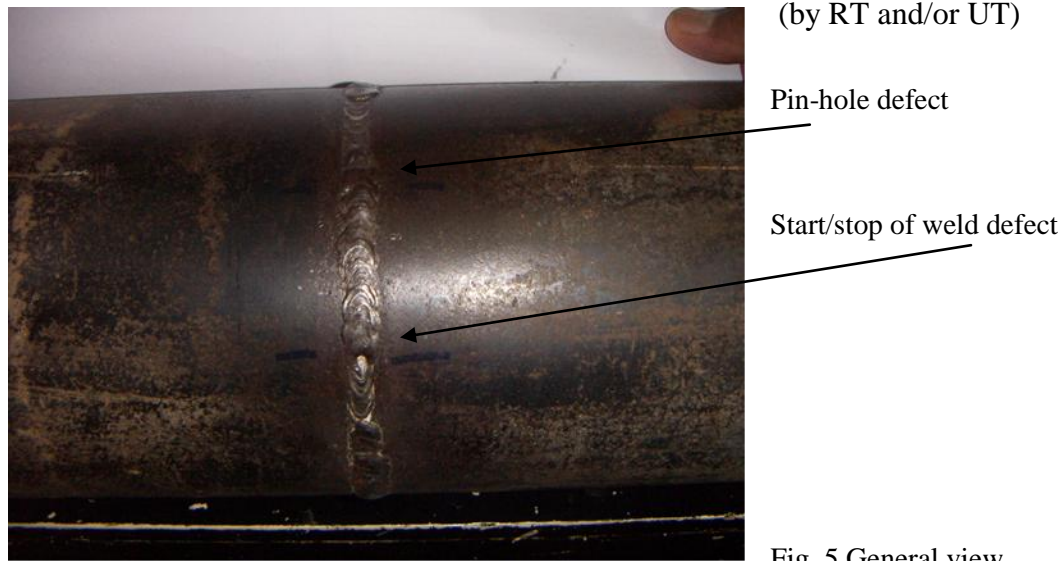


Fig. 5 General view

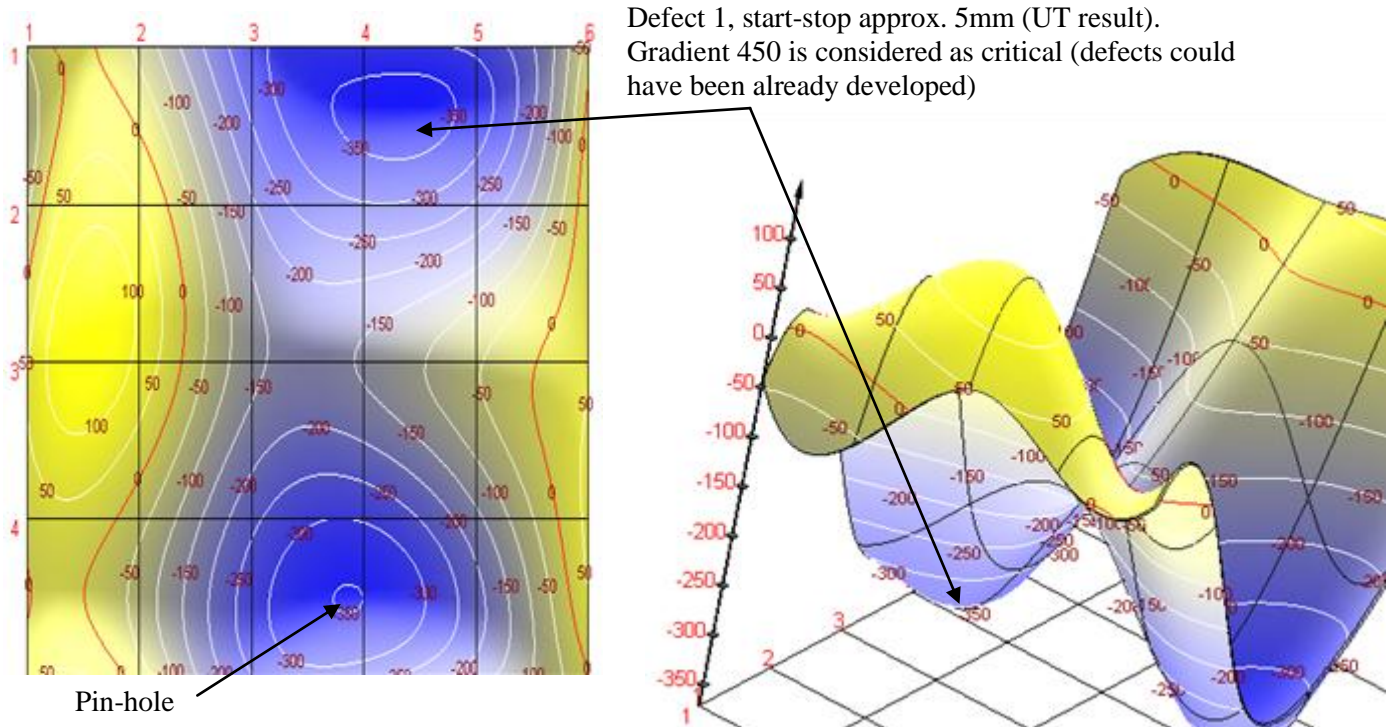


Fig. 6 2D result of Stress mapping and Gradient and 3D result of Stress mapping and Gradient

Defect No.2: pin hole with 1mm diameter (UT result) and as 2-3 mm IMS results at X=3.8 and Y=4.5. Gradient of 450 is considered as critical

IMS results confirmed exact location of high stress areas and with much better accuracy of size of stressed area (pin-hole). 1 mm defect by UT/RT versus 2 mm high stress area detected by IMS

#### 4.2 Conformity of the quality stress relief, Heat Treatment (HT) process.

Two steel plates 10 mm thicknesses were welded with low quality of welds. The tested are was marked and tested for stress concentration and gradient before and after of the Heat Treatment 520°C for 8.5 hours. After the Heat Treatment process, the plate was measured again using same mapping grid.

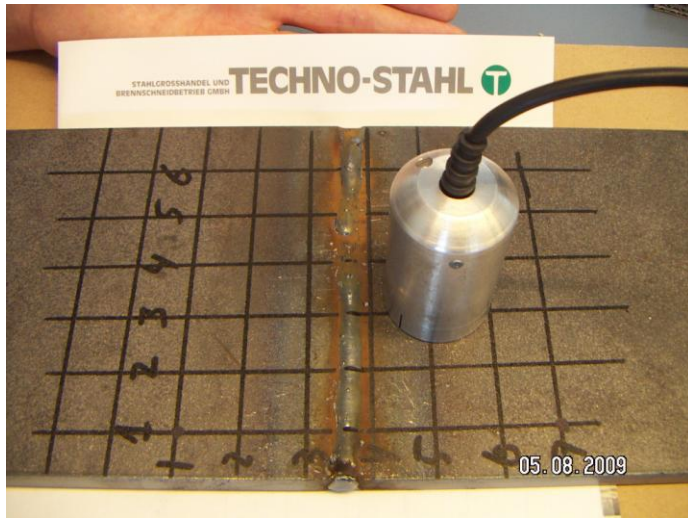


Fig. 7 Welded plate to qualify HT process

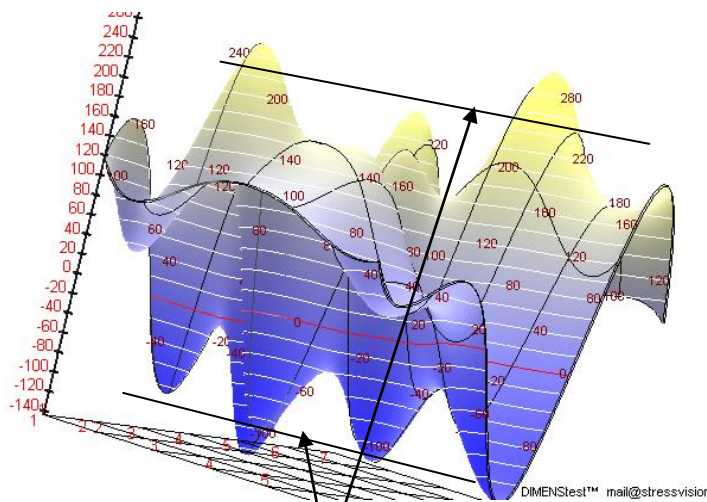
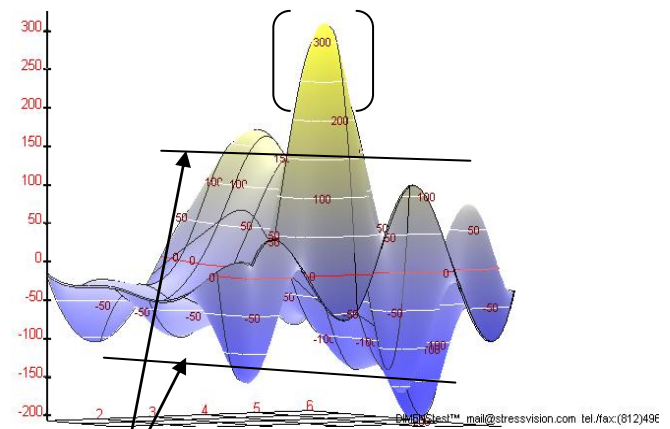


Fig. 8 3D image of welded plate before HT with high stress gradient



after HT and considerable stress relief

The high gradient of Mechanical Stresses before HT has clearly shown that the reduction of the stress level after HT, meaning the good quality HT process was done properly!).

However, after HT, the new concern was a strong pick (in brackets) which was generated by the sharp edge of one of supporting polls holding the plate during the heat treatment process. After repair of sharp edge, the problem was gone, not only confirming the quality of stress relief process by HT process but also improving the quality of the process.

### 4.3 Case of the low quality Heat Treatment (HT), incomplete process

Similar to the previous case, plates were welded and measured for stress concentration and gradient before and after designed incomplete process ( 520°C for 3.5 hours instead of 8 hours).

After the Heat Treatment process the plate was measured again using same mapping grid. Results of the gradient of Mechanical Stresses before HT was about 450 and after was only 400.

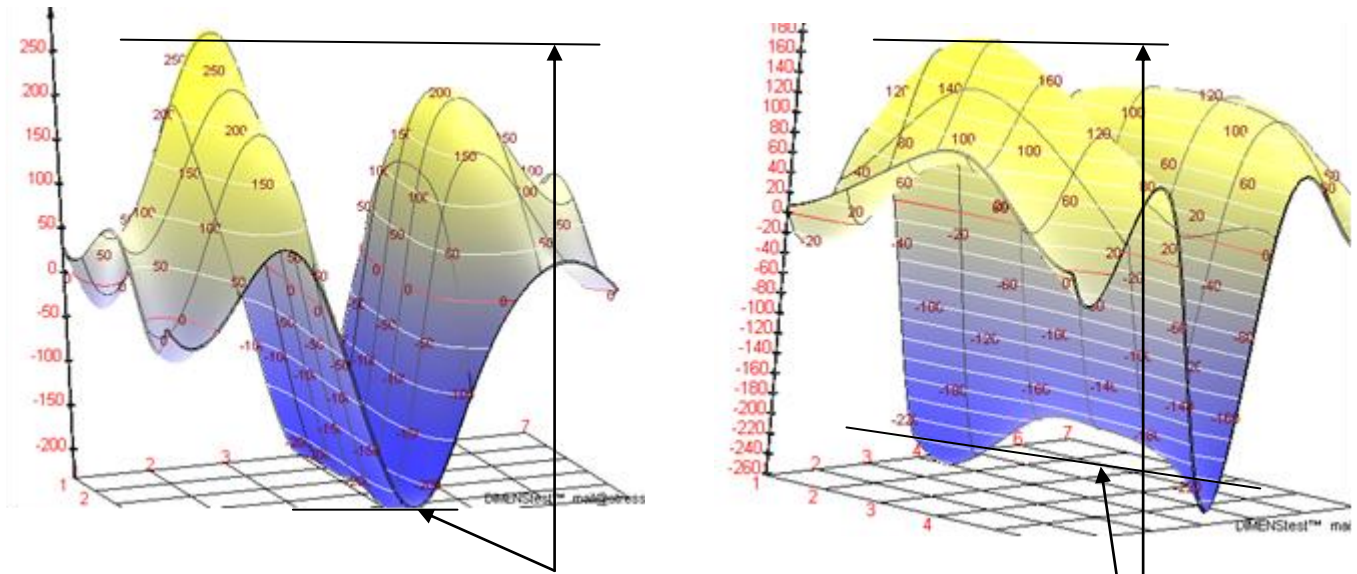


Fig 9 Results 3-D before the HT (gradient 450)

and after partial HT (gradient 400)

Low quality of HT was measured with only minor improvement of stress relief, surface and subsurface only.

Hardness was not measured but very likely would show hardness improvement (surface testing).



#### 4.5 In-Service Inspection, LPG Storage tank ( pressure of 15 atm)



Stress measurements of LPG tank under internal pressure (15 atm.)  
The randomly zone selected for inspection was joining of circumferential (vertical) and horizontal welds.

Fig. 10 General view of T-weld joint, LPG tank under pressure

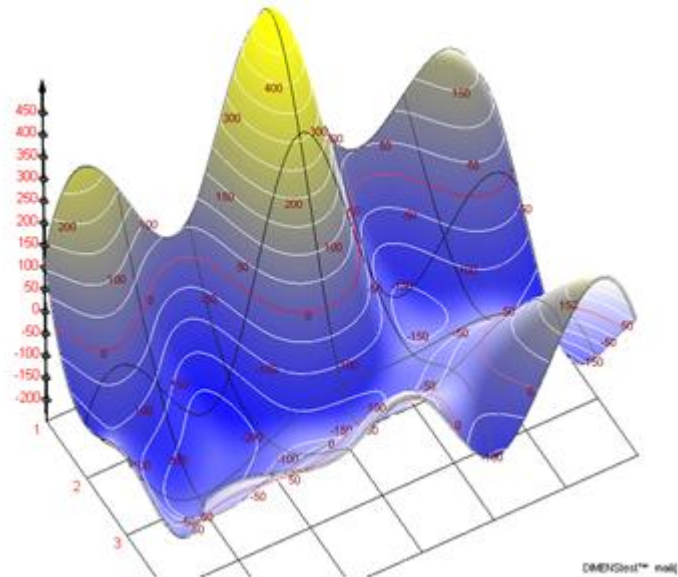
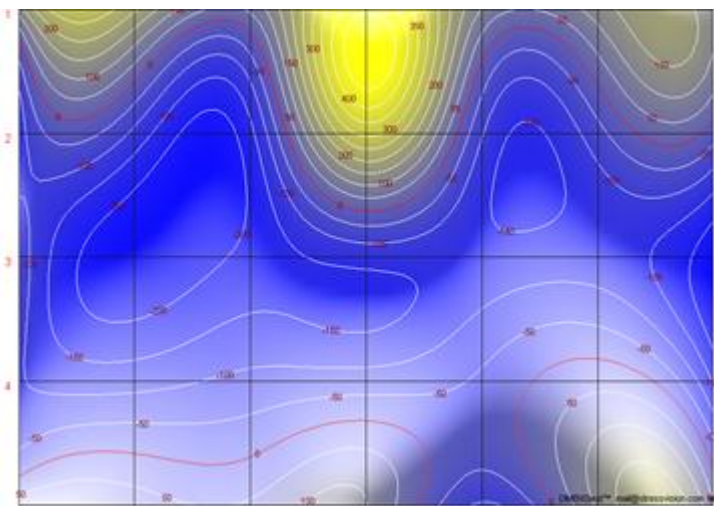


Fig. 11 images of 2D and

3D with peak in the area of welds junction

By monitoring after 9-12 months we could receive an information on stability (or increase) of stress in critical areas and to make a proper assessments.

#### 4.6 Bridge Crane, 20 tons (serviceability of aging item)

Technical information: Lift max 20 tons, length 22m, age over 20 years  
Purpose: For safety of operation of old crane. To investigate the condition of mechanical stresses and to evaluate crane's life extension (ISI) prior to de-commission.

Cost of a new crane is about 3 Million USD.

Selected areas (one area near the driving wheel and another area at the center of the crane frame) were measured before the load test then under load of 10t, 20t and immediately after removal the max load and the next day

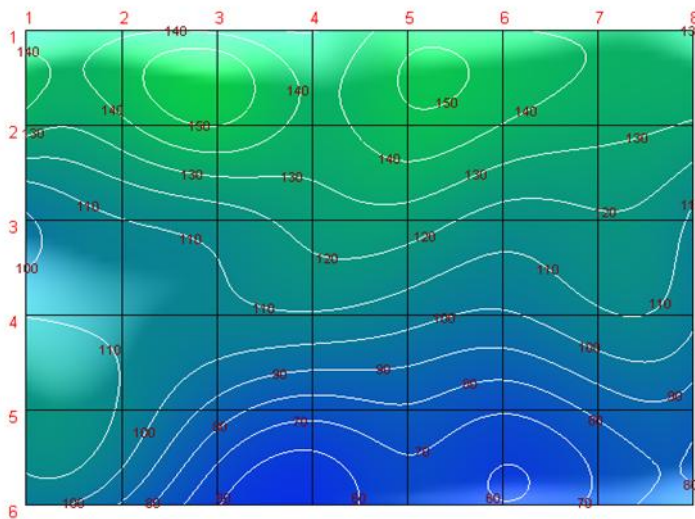
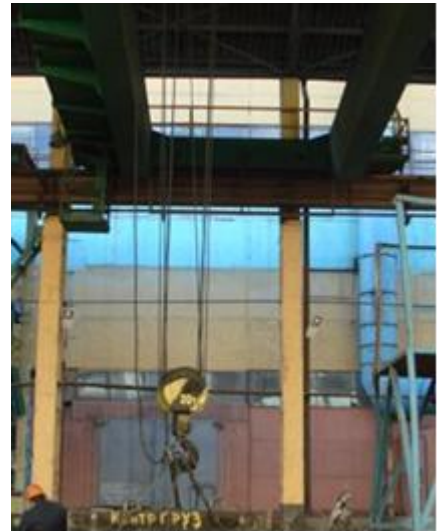


Fig 16 Crane center beam– before load (no stress)

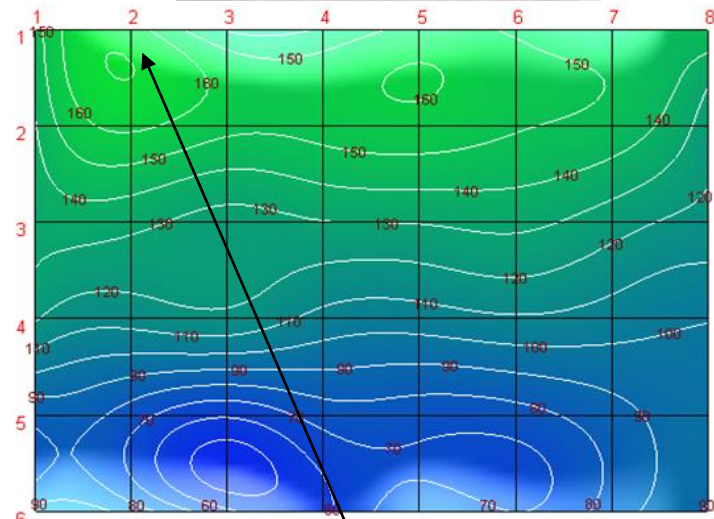


Fig 17 under 10 tons load, stress increase at top left corner

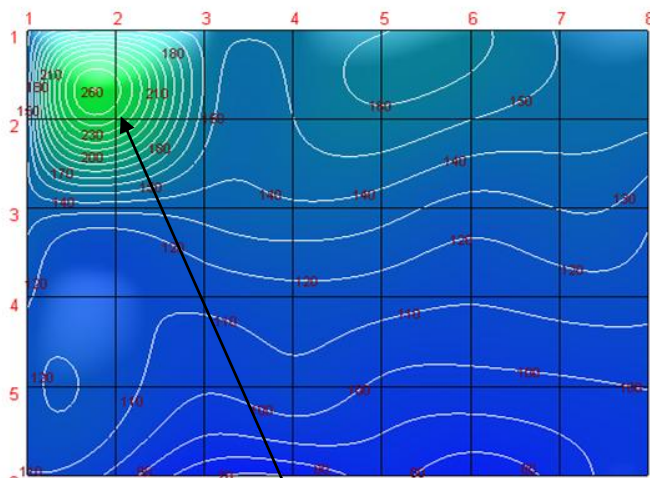
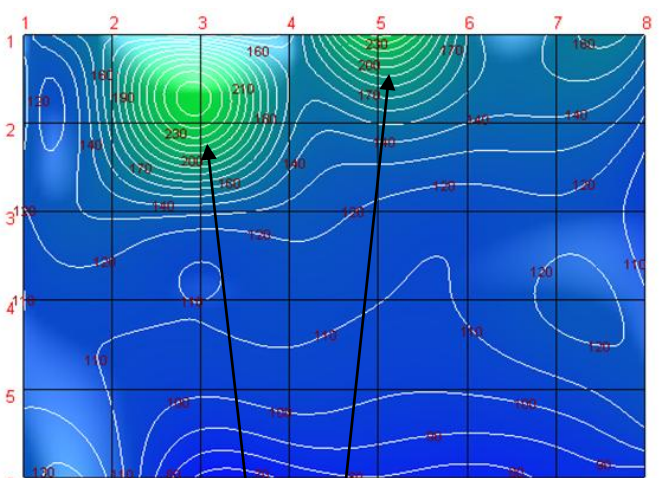


Fig 18 Center beam under 20 tons load (strong increase) and after removal of load with still very high stress gradient and concentration, shifting 20 mm right



Recommendations were to extend Crane's operation life for another 9 months with limiting the working load to 10 tons and to monitor stress conditions again after 9 months (at same areas).

Saving the cost of new crane, 2.8 Mil USD

## 5 CONCLUSIONS

5.1 The Indicator of Mechanical Stresses, IMS could be an useful tool in providing reliable information on status of the item (object) based on stresses to assure operational safety, to evaluate and to monitor conditions and life prognosis, for quality and for assessment of predicted life and preventive care. This technique can be used for immediate and advanced information and to be used as complimentary with conventional NDT, to confirm the critical findings.

5.2. The IMS is originally designed for ferrite metals with thickness up to 12 mm. It is better to use as method of comparison "before and after" for more reliable results. Any changes in applications, of metallurgical composition (to paramagnetic metals) or thickness above 10-12 mm needs to be further investigated to determine acceptable stress levels.

5.3 Study of Stress Relief (Heat Treatment or other methods) and the quality and efficiency of relief for the whole thickness of metal is required a special attention and investigation.

5.5 Additional studies are recommended for each specific application to assure better results evaluation, for learn on applications or limitations of the Stress Indicator.

5.6 The Indicator of Mechanical Stresses is now commercially available. As a relatively new technique, is not covered yet by International standards but it is in the process for accreditation.

## REFERENCES

1. Prof. Zhukov S.V., Mr. Zhukov V.S "Technical description of Indicator of Mechanical stresses". Ferrologica LLC, Russia, 2008
2. ASNT NDT Handbook, Volume 10, Section 7 and 8, USA, 2004
3. Dr. Bida, etc. "NDT methods for testing Stress-Strain properties of Oil Pipes", Russian journal of NDT, Number 10, October 2002
4. Жуков В.С. и др./ журнал "Трубопроводный транспорт: теория и практика", №1, стр. 84, 2004, Дефект - условие разрушения?
5. Жуков С.В.,- по заказу ЗАО «Коксохиммонтаж»,- СПб: ДИМЕНСтест, 1997. Исследование напряженно-деформированного состояния сварных металлических резервуаров РВС-10000 в процессе монтажа// Отчет о НИР, н.р

## ACCREDITATION OF THE MALAYSIAN CERTIFICATION BODY FOR NDT IN ACCORDANCE TO MS ISO 17024

<sup>1a</sup>Salbiah Hussein, <sup>2b</sup>Abd. Nassir Ibrahim

<sup>1</sup>Department of Skills Development  
Ministry of Human Resource

<sup>2</sup>Malaysian Nuclear Agency

<sup>a</sup>salbiah.h@mohr.gov.my; <sup>b</sup>nassir@nuclearmalaysia.gov.my

**Abstract:** Malaysian Qualification and Certification Scheme for NDT personnel began to operate in 1986 with the Department of Skills Development acts as the National Certification Body. The scheme was developed based on an internationally accepted standard for certification of NDT personnel ISO 9712. Since the implementation of the scheme more than 300 NDT personnel has been certified in radiography, ultrasonic, eddy current, magnetic particles and liquid penetrant method level 1, 2 and 3. One of the most basic requirement for a certification body as stipulated in ISO 9712 version 2005 is that certification body operating based on this standard shall be accredited to ISO 17024. Acquiring accreditation to ISO 17024 for the National Certification Body is a long process. It began since 2006 and accreditation was only granted in October 2012. This paper discusses the role of the Department of Skills Development in developing NDT personnel to fulfil the national requirement. Problems and obstacle encountered during the process of gaining accreditation to ISO 17024 will also be discussed.

**Keywords:** Non-destructive Testing, Certification Body, Certification Scheme

### Introduction

Up to 1980's, Malaysia was well known as one of the developing countries whose economy depends on the agricultural sectors. Malaysia was well known as the biggest exporter of rubber, palm oil, coconut and pineapple. In addition prime commodity such as tin was also considered as the biggest contributor to the economy. This situation remained till early 80's when the government finally decided to transform the economic dependence from agricultural to industrial sector. At about the same time PETRONAS intensified its oil and gas activities that include the installation of Petronas Gas Utilization Pipeline Phase 1 (better known as PGU1). These developments together with developments in other industrial sectors helps to make non-destructive testing (NDT) technology as one of the most important and critical technology required by the country. The ability of this technology to detect and characterize serious and dangerous defects in critical engineering components allowed various engineering plants to operate at a high degree of safety and reliability. In addition, it also helps industries to improve their productivity by minimising the possibility of unexpected shut down due to component failure.

Although the ability of NDT technology to contribute toward better plant safety, reliability and productivity is well proven, the usefulness of data generated still depend on many factors. Of all these factors, the competency of NDT operator is considered as one of the most crucial factor that determine whether or not the data generated really represent the integrity of the component they inspect. In addition to these, factors such as the reliability of equipment and the application of appropriate quality management system by the organization also play equally important role in determining the validity of the inspection results. In view of the importance of competency of manpower involved in NDT works, all standards related to the application of NDT methods in the world require NDT operators to be trained, qualified and certified by the appropriate Certification Body. Many countries throughout the world have developed their own respective Qualification and Certification Scheme for NDT Personnel to cater the requirement of standards related to the



application of this technology. In some other countries, where local qualification and certification scheme is not yet exist, NDT operators are required to be qualified and certified by some schemes that are widely accepted by industries in their respective countries.

### **Application of Internationally Accepted Standard for NDT Certification in Malaysia**

All standards worldwide that are related to the application of NDT specify that all NDT works shall be executed by certified personnel. As an example, American Society for Mechanical Engineering Code ASME Section VIII, Division 1 (2007), UW51 for Radiographic Examination of Welded Joint (2) specifies:

“The Manufacturer shall certify that personnel performing and evaluating radiographic examinations required by this Division have been qualified and certified in accordance with their employer’s written practice. SNT-TC- 1A11 shall be used as a guideline for employers to establish their written practice for qualification and certification of their personnel. Alternatively, the ASNT Central Certification Program (ACCP) 11 or CP-18911 may be used to fulfil the examination and demonstration requirements of SNTTC-1A and the employer’s written practice”

Similar practiced has also been adopted in Malaysia. Generally heavy engineering components that require NDT produced by Malaysian manufacturers are either for domestic usage or for export. Components produced for domestic usage are normally produced based on standards accepted worldwide. In this case the requirement of certification of NDT personnel is specified in the applicable standards. Components for export on the other hand are produced based on standard applied by the importing countries. In this case importing countries insist that personnel performing NDT inspection must be certified in accordance to the standard applied in these countries. Certification schemes applied by Malaysian industries in accordance to their popularity are as follows:

1. SNT-TC-1A: American Certification Scheme adopted by the American Society for NDT (ASNT). It is also known as “an employer based certification scheme”
2. PCN: Scheme adopted in United Kingdom (Central Based Certification Scheme)
3. CSWIP: Scheme adopted for the Certification of Welding Inspector in the United Kingdom (also central certification scheme)
4. EN 473: Scheme adopted by the members of European Union (Central Based Certification Scheme)
5. ISO 9712: Scheme developed by the ISO which is meant to harmonize certification practice all over the world. Currently ISO 9712 and EN473 have reached an agreement to have a single harmonize certification scheme

Malaysian manufacturers are producing products that are exported to various part of the world. Thus it has become a common practice in the past that a single NDT operator needs to have multiple certificates to allow him to perform inspections on all types of products. Thus in this way, the cost of certifying personnel becomes very expensive. As a result, only few local NDT operators have an opportunity to receive proper training and certifications. Many operators claim to have been trained and certify in accordance to SNT-TC-1A. However, judging from their performance, most of these claims are doubtful.

### **Establishment of Malaysian Qualification and Certification Scheme for NDT Personnel**

Although NDT has been practiced in Malaysia since early 60’s, its demand increased tremendously in around 80’s. Mega projects related to oil and gas such as PETRONAS Gas Utilization Phase 1 and Phase 2 (known PGU 1 and PGU2) that involved installation of 32km and 685km gas pipelines

respectively, have become the prime factor that led to significant increase of demand for this technique. Such unexpected demand for NDT cannot be fulfilled completely by local NDT personnel. It was realized even before the execution of these projects that the existing number of NDT operators was far more than adequate. This situation resulted the following:

1. Employment of incompetent personnel; and
2. Importing personnel and services from abroad that affect the cost effectiveness of projects.

This scenario led to the establishment of a National Qualification and Certification Scheme for NDT Personnel back in 1986 with the Department of Skills Development (DSD) formerly known as the National Industrial Training and Trade Certification Board (NITTCB) acted as the National Certification Body (NCB) to administer the scheme. The scheme was based on ISO 9712. At the national level, such a scheme was established as a result of close collaboration between Malaysian Nuclear Agency, DSD, the Atomic Energy Licensing Board (AELB), SIRIM, PETRONAS and few other government agencies and private sectors. At the International level, this effort gained strong support from the International Atomic Energy Agency (IAEA) that saw NDT as one of the most critical technology needed by member states that intend to exploit nuclear power as one alternative for energy resources.

When the scheme was first established, it has no intention whatsoever to replace international qualification and certification schemes that were already in used in this country such SNT-TC-1A, PCN and CSWIP. Instead, its main objective was to provide a good opportunity to local NDT operators to be trained, qualified and certified by a scheme that adopt an international standard, locally and at a much lower cost. The move is proven successful when up to December 2012, a total amount of 3517 personnel has been qualified and certified through the scheme. Majority of the certified personnel are local and few are non-local that came from countries such as Myanmar, Philippines, Yemen, Uzbekistan, etc. Total number certified by the scheme for various NDT techniques is given in Table 1.

**Table 1: Number of Personnel Certified in Various NDT Techniques up to 2012**

Method	RT	UT	MT	PT	ET	RI
No. of Certified NDT Personnel (all levels)	2683	510	114	118	66	26

#### **The Need for Accreditation of NDT Certification Body by the National Accreditation Body**

Acceptance by industries is it local or international, has been considered as one of the major issue for certification of NDT personnel by local scheme in almost all developing countries. In many cases, NDT certificates issued by local Certification Bodies are either totally or partially rejected by local industries. NCBs have to make multiple efforts to convince industries that the quality of their scheme is comparable if not better than commonly applied international schemes. Degree and speed of success varies from one country to another. In Malaysia, such a scheme (for radiography) is full recognized by the AELB and PETRONAS. With recognition from these 2 important main players, local industrial radiography certificates are accepted by almost all ranges of industry. However, the situation is rather difficult for other NDT methods where recognition is still very limited. Thus, the NCB has taken a drastic step to get them accredited to ISO 17024 with the hope that such a move will help to elevate the status of local certification scheme to be at par with other international schemes

Accreditation of NCB to ISO 17024 in IAEA member states is considered as one of the most important activities supported by this Agency. This is a part of the IAEA contribution toward harmonization of NDT certification practice where a single standard ISO 9712 has been used as the basis for the establishment of NCB in member states all over the world. It is clearly indicated by ISO 9712: 2005 and ISO 9712: 2012 that the all certification bodies for NDT that claim to comply with ISO 9712 shall conform to the requirement of ISO 17024.

As a National Certification Body, the DSD sees accreditation to ISO 17024 as a very important and significant step in its effort to ensure that NDT certificates issued will get a good recognition both at home and abroad. In theory at least, accreditation to ISO 17024 qualifies NCB of this country to sign a mutual recognition agreement (MRA) with other accredited Certification Bodies. As an example, in the case of Chinese Certification Body that was accredited in 2012, the immediate follow up action upon accreditation was for them to negotiate the MRA with the European Federation of NDT (EFNDT). It is the wish of DSD to follow this similar step when the time is appropriate. If this can be achieved, personnel certified by the local NCB will be recognized to perform inspection on products to be exported to any European Union member states.

### **National Certification Body**

Department of Skills Standard (DSD) is an agency under the Ministry of Human Resource who responsible to manage, coordinate and promote skills training program and career development based on skills competencies. DSD was regulated under National Skills Development Act 2006 (ACT 652) which was established in September 1<sup>st</sup> 2006.

As national certification body, DSD's functions mainly are:

- i. to develop National Occupational Skills Standard (NOSS) and training curriculums;
- ii. responsible in skills accreditation and certification through accreditation of training organizations and certification of personnel;
- iii. responsible in personnel skills upgrading, instructor development, capacity building, industrial experts engagement and organizing skills competition through the Centre of Instructor and Advanced Skill Training (CIAST); and
- iv. to engage industry driven training system through National Dual Training Systems (NDTS)

DSD was first established in 1971 under the name of National Industrial Training and Trade Certification Board (NITTCB). During that time, economics was shifted from agricultural-based to an industrialised-based. Massive economic development had caused lack of skilled workers and semi-skilled workers in every sector of occupations. A lot of training programmes were offered and expanded in public training institutes through Ministry of Youth and Sport, Indigenous People's Trust Council (MARA) and other agencies. However, there is no standardise of training programmes and this had caused the competency of output from various training agencies were at different levels. This is where NITTCB which was represented by government, industry and worker, responsible to develop standardise training programmes and also responsible in assessing and accredit skills level that was achieved by any individual to ensure it has meet the standard that has been developed. Initially, NITTCB has developed 23 programmes occupational industrial with three (3) levels of competencies (Basic, Intermediate and Advance Level).

In 1989, NITTCB was replaced by National Vocational Training Council (NVTC) to formulate, promote and coordinating vocational and industrial skills training in line with national economic development. In 1991, government has established *Jawatankuasa Kabinet Mengenai Latihan (JKML)* to advise the

government on direction of skills training structure and also to encourage involvement of private sectors in developing skills training programmes. During that time, after almost 18 years of NITTCB was developed, only 35 occupational industrial programmes were established (compared to 23 programmes at initial stage) due to lack participation from private industrial sectors. With the advice from industrial experts on skills programme, *Piawaian Ketukangan Kebangsaan (PKK)* was replaced with National Occupational Skills Standard (NOSS) in order to make national skills certification more flexible, effective & user-friendly.

## Skills Training Evolution & Transformation

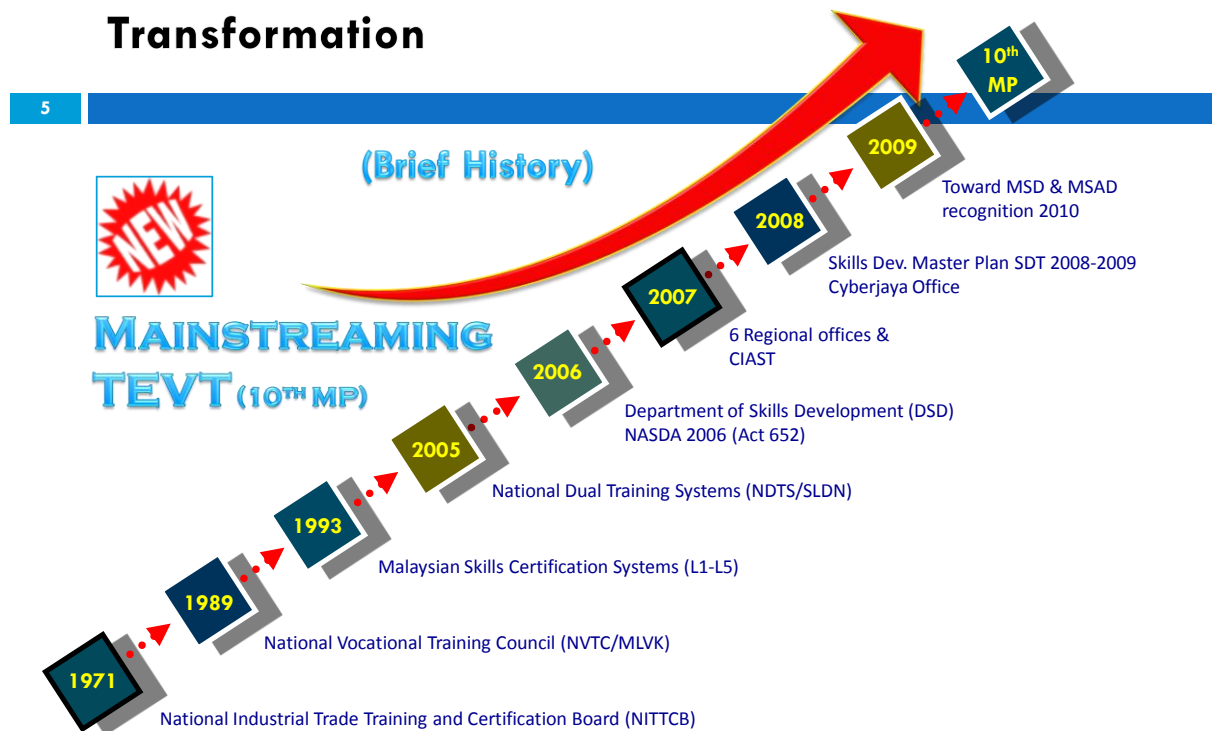


Chart 1: Brief History on Skills Training Evolution & Transformation

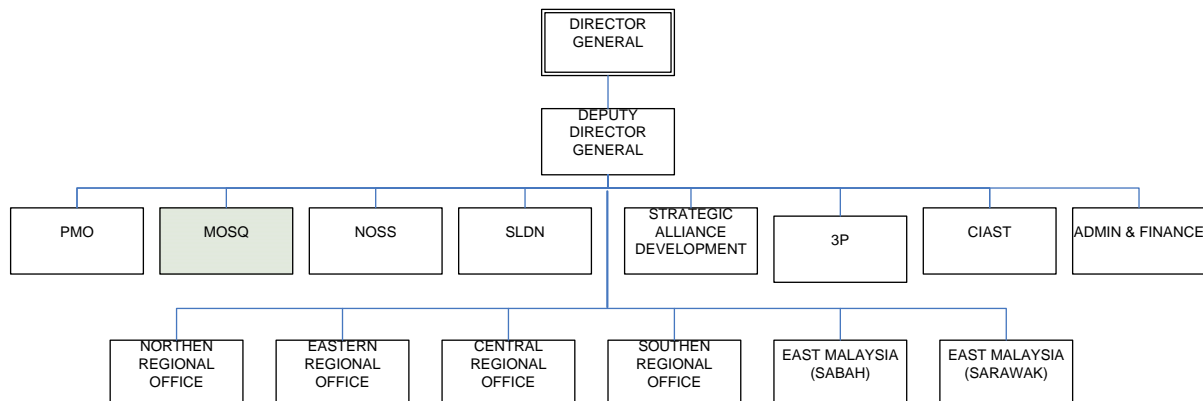
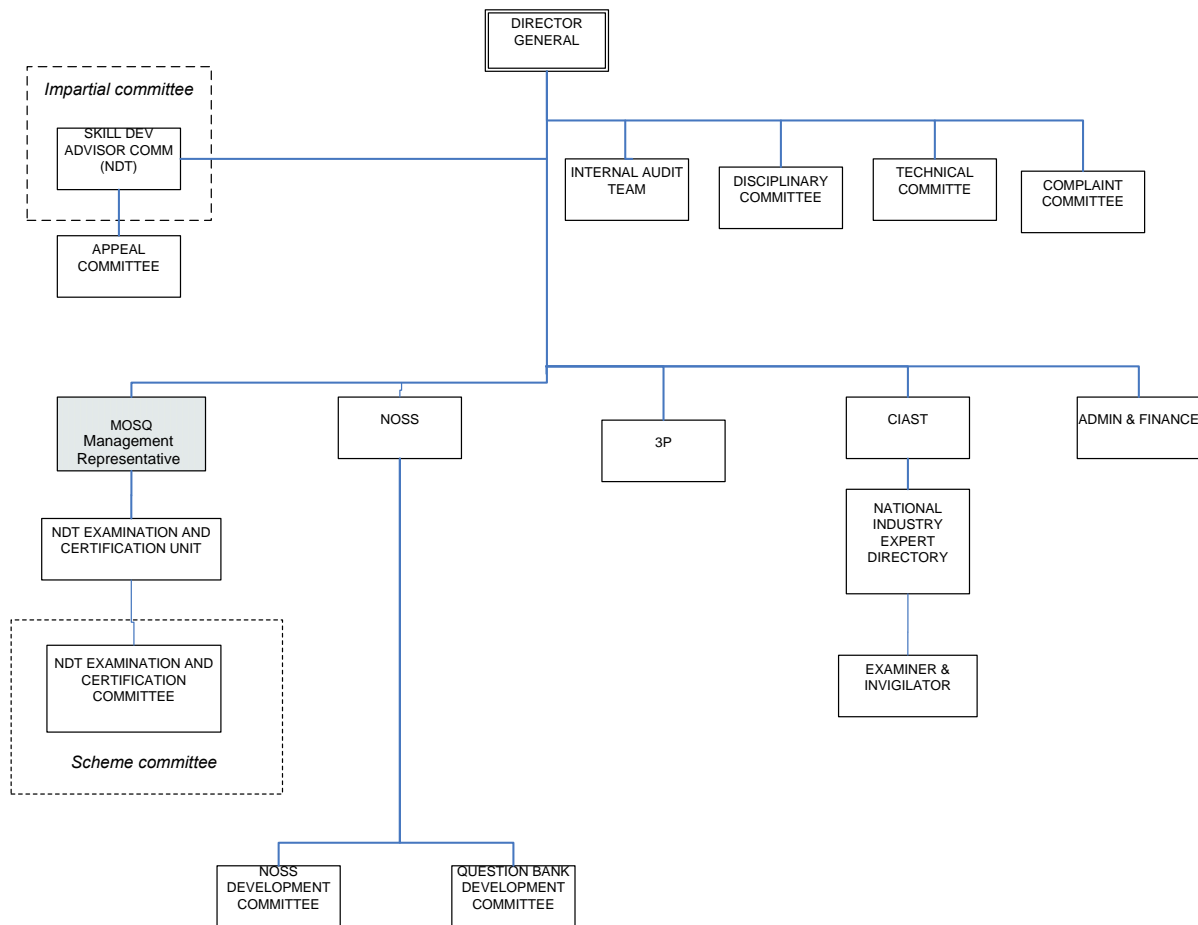


Chart 2: Organization Chart of DSD

Chart 2 shows the organization of DSD. However, not all the sections related to activities of certifying NDT personnel. In certifying NDT personnel, the most responsible section is Malaysian Occupational Skills Qualification (MOSQ). In order to comply with requirement of MS ISO 17024,

DSD has to set up two (2) important committees, which are impartial committee and scheme committee. Chart 3 shows the position of impartial and scheme committee related to certifying NDT personnel.



**Chart 3: Organization Chart of DSD as Certification Body (CB) for NDT Personnel**

The CB is headed by a Director General (DG). There are four committees directly under DG's responsible and order; Internal Audit Team, Disciplinary Committee, Technical Committee and Complaint Committee. The impartial committee is the advisor committee to the CB which is named Skills Development Advisor Committee (JPPK) for NDT. JPPK will advise the DG on direction of NDT industry including the demand and supply needs and other related issues. An appeal committee is under responsible of the impartial committee which will be set up on-demand.

The NDT Examination and Certification Unit (in MOSQ Section) is the administrating unit of examination and certification of NDT personnel. All application on examination and certification are submitted to this unit and will be processed according to procedures and work instruction related. All examination results and certificate applications will be reviewed, discussed and endorsed in a monthly scheme committee meeting. This scheme committee is called the NDT Examination Result Committee and the NDT Certification Committee. These two committees were represented by industry experts from various NDT methods, stakeholders, training centres and regulatory bodies. The chairman of both committees is the Management Representative (MR) who is the director of MOSQ section to prevent any conflict of interest that may occurred during the process of decision making on examination results and certification granting.

Other than that, the development of NOSS and examination questions bank are under responsible of NOSS section. Meanwhile, the 3P section is responsible for the planning of training direction of

training, research on occupational and industry-needs and tracer study. List of examiners and NDT experts are pooled and updated in the National Industry Expert Directory under responsible of CIAST.

### Milestone and challenges

The decision in getting accreditation was made back in 2006. But, only after 2008, massive numbers of workshop were set up in order to develop, compile and arrange all the policy, procedures and guidelines related to certification of NDT personnel. A scientific visit sponsored by IAEA with a purpose of benchmarking on implementation of certification process done by Australia Institute of NDT, was taken place on August 2008.

In 2010, an application of accreditation was submitted to national accreditation body, Department of Standard Malaysia (DSM) and on July 2010, the adequacy of the documents was reviewed. 40 concerns were raised up by DSM during that time, in order to improve the system document. A year later, in October 2011, the improved version of system document was resubmitted to DSM. An adequacy audit was conducted on January 2012, where JPK received 13 minor of NCRs and 8 observations. DSM also conducted a witness audit on February and Mac 2012, in order to witness the effectiveness of system implementation. DSM had a visit during examination held, monitored the process of granting certification in scheme committee meeting and also did a site visit to one of NDT training centre. During that time, another 6 observations were raised up. After submitted all the intended actions, a verification audit was carried out by DSM in September 2012. Finally, on 3 October 2012, DSD was successfully granted with MS ISO 17024 accreditation.

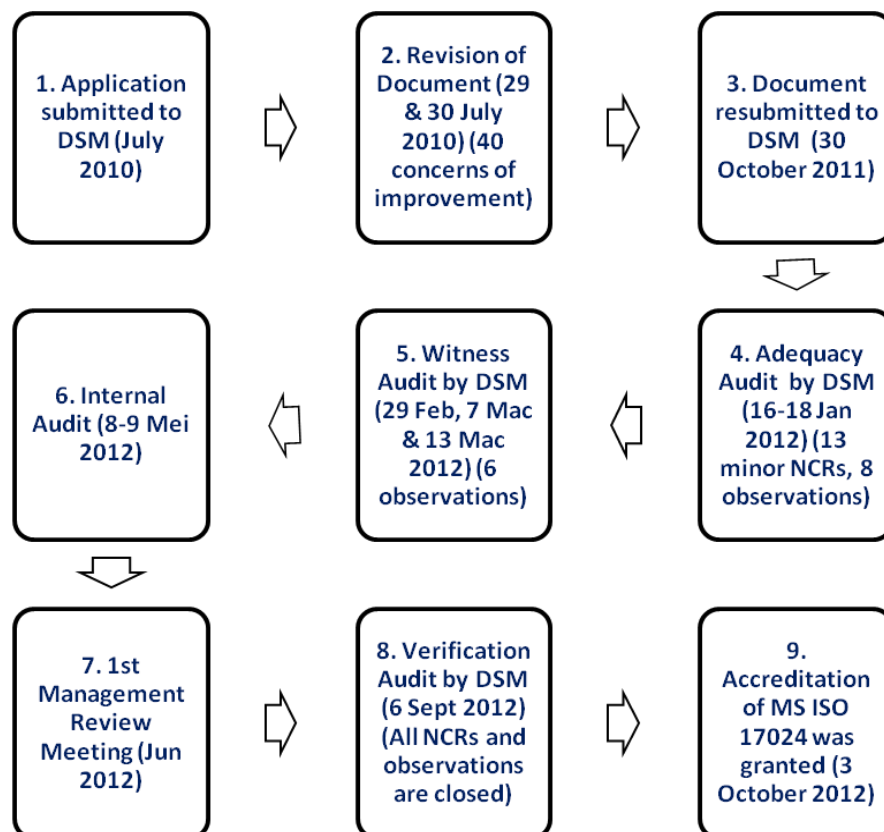


Chart 3: Accreditation Milestone

### The Way Forward



Accreditation of NCB is a long process and requires tremendous effort, time and cost. It was achieved through consistent and persistent efforts. Another more gigantic challenge lies ahead is the maintenance of the system. For this purpose DSD has formed its own internal audit team to periodically monitor the performance of the Department and compliance to the standard. Involvement of local NDT experts as a part of the internal audit team will help to ensure that the internal auditing can be performed in the most effective manner prior to external auditing from the National Accreditation Body.

Few months after accreditation, the NCB begins to appreciate the advantage of getting accredited. A lot of lesson has been learned and a lot of continuous improvements to the certification system have been introduced to ensure that the system is perfect. Currently, the NCB has started to examine the possibility of having MRA with other Certification Bodies, following the example of China. The DSD has set a realistic target of 2015 as a year where the NCB will start to approach EFNDT for possible MRA. It is a difficult but not impossible task that has to be faced by the NCB.

## **Conclusion**

Accreditation of local NCB to ISO 17024 by the National Accreditation Body is considered as recognition to the NCB ability to implement NDT Certification process in accordance to standards that has been established and accepted internationally. It is a good starting point toward recognition of NDT certificates issued by local NCB by members of international NDT community. Through continuous effort and improvement to the system it is expected that local NCB will be able to part of MRA with other well known International Certification Body.

## TECDOC 628 2013, NEW REVISION

Isaac Einav<sup>(1)</sup>, Elena Azizova<sup>(2)</sup>, Nassir Ibn Ibrahim<sup>(3)</sup>, Patrick D. Brisset<sup>(4)</sup>

<sup>(1)</sup> STAR.IK Ltd (STAR. International Consultant), Richmond Hill, Ontario, Canada, L4C 3Z6,

Phone +1-905-237-5520, e-mail: [starik18@gmail.com](mailto:starik18@gmail.com)

<sup>(2)</sup> Navoi Mining and Metallurgy Combinat, Navoi Street 27, Navoi 706800, Uzbekistan,  
phone:+998-79-2276044, email: [nmzndt@ya.ru](mailto:nmzndt@ya.ru)

<sup>(3)</sup> Nuclear Malaysia, Bangi Komplex, 43000 Kajang, Selangor, Malaysia,  
phone: 0060 3 89282908, email: [nassir@nuclearmalaysia.gov.my](mailto:nassir@nuclearmalaysia.gov.my)

<sup>(4)</sup> International Atomic Energy Agency (IAEA), Vienna, Phone +43 1 2600 2 174 ,  
email: [p.brisset@iaea.org](mailto:p.brisset@iaea.org)

### Abstract

Today technology requires better quality and safety of operation, more reliable detection and better trained NDT personnel.

IAEA had been working for more than decade to support training NDT personnel among Member States and to promote harmonization of certification, all in compliance and working with ISO standards. TECDOC628, Training guidelines in Non-destructive Testing techniques was the leading document on the syllabus for NDT training.

The latest revision of ISO9712-2012 had required of updating Tecdoc 628 Rev 2 (2008)

**Key words:** TECDOC628, Training of NDT personnel, Member States (MS).

### 1. INTRODUCTION

The International Atomic Energy Agency (IAEA) promotes industrial applications of radiation technology including non-destructive testing (NDT) through its various activities such as technical co-operation (TC) projects (national and regional projects) and coordinated research projects (CRPs). National programmes have been established in Member States for training and certification of NDT personnel. National Certifying Bodies have also been established based on International Organization for Standardization (ISO) Standard.

As a part of these efforts, the IAEA has been actively involved in developing training materials.

Since the issuance of IAEA-TECDOC-628 in 1991, NDT technology has experienced significant changes. In addition, over the last ten years, as a result of research and development activities worldwide, new NDT techniques and equipment have been introduced

To accommodate the latest developments of ISO9712-2012, training materials need to be updated. Accordingly, revision of the existing version of IAEA-TECDOC-628 was considered essential to meet the demands of end-user industries in the Member States.

The content of the IAEA-TECDOC-628 has been revised based on new changes of ISO9712-2012, on the experience of the experts, as well as comments of the end-user industries. The details of the topics on each subject have been expanded to include the latest developments in the respective method

## **2. NDT Objectives in IAEA**

Promotion of NDT technologies to Member States (MS)

Developing new nuclear technology for NDT (through CRP)

Supporting ISO 9712

Promotion of international harmonization for training and certification of NDT personnel

Assistance in establishing national accreditation and certification bodies

## **3. TECDOC628**

This document contains a body of knowledge for non-destructive testing. It was developed to provide guidelines for trainers, training organizations, and certification bodies, detailing the subject matter and the content for each level of certification. It is general in nature but the contents of the training should be adapted to the needs, procedures, materials and products of the customer. The recommended training hours are consistent with the edition of the standard ISO 9712 in effect at the time of preparation.

Training should end up with an examination and could lead to a certification. Examination requirements are partially covered by this TECDOC, but detailed information about this and certification can be found in ISO 9712.

## **4. SOME OF MODIFICATIONS TECDOC 628 REV 2013**

**4.1** Each level for each method was modified, improved by content and misprinting based on new ISO9712:2012. Total 7 methods, Radiography Testing (RT), Ultrasonic Testing (UT), Magnetic Particle Testing, (MT), Liquid Penetrant testing (PT), Eddy-Current Testing (ET), Leak Testing (LT) and Visual Testing (VT)

**4.2** Regrouping of training syllabus, separate chapter for General Engineering, Materials and Processes and Defects. This topics repeats for each method and level. Most of Member States are applying for NDT training and certifications usually in 2-3-4 methods. Once, the student had passed this chapter, no needs to spend training time to repeat this again, each time.

**4.3** Introducing Syllabus for Digital RT level 2.

**4.4** Developing Code of Ethics

**4.5** Distance training. Principles of Distance Training, advantages and limitations are introduced in this TECDOC and subject of further development and modifications

**4.6** Awareness of development syllabus for advanced and innovative techniques

**4.7** Appendixes like CODE OF ETHICS, PRACTICAL WORKSHOPS, WEIGHING OF LEVEL 3 PROCEDURE WRITING, SAMPLES OF NDT REPORTS (FOR UT, RT, MT and PT), ADVANCED METHODS, DISTANCE TRAINING etc.

## **5 NDT FUTURE in IAEA**

Continue transferring the NDT technology to MS.

Introducing new and advance technological standards and practices based on the latest innovations using computer support Digital techniques like Digital Radiography DIR, Time-of-Flight-Diffraction TOFD, Arrow inspection, Remote Controlled Eddy Current and others techniques of NDT for Preventive Maintenance (PrM), In-Service-Inspection (ISI) of Nuclear, Pipelines and others fields.

Introducing Member States to develop national standards on training and certification of NDT personnel conforming to ISO 9712.

Assisting MSs with International harmonization of NDT standards, practices and certifications to ISO9712.

Advising National Certifying Bodies (NCBs) and Professional NDT Societies in Member States.

Strengthening cooperation with ICNDT

Development of NDT books and other training materials

## **6 CONCLUSIONS**

**6.1.** The content of the IAEA-TECDOC-628 has been revised based on new changes of ISO9712-2012, on the experience of the experts, as well as comments of the end-user industries. The details of the topics on each subject have been expanded to include the latest developments in the respective method.

**6.2.** The incorporated changes will help the end-user industries to update their NDT qualification and certification schemes, and course materials.

**6.3.** This publication, like the previous version, will continue to play an important role towards international harmonization in the field of NDT.

**6.4.** Future effort to be made by IAEA in developing and promoting Innovative techniques of NDT and Distance NDT training

## **REFERENCES**

1. ISO 9712:2012, Non-destructive testing -- Qualification and certification of NDT personnel
2. SO/TR 25107:2006, Non-destructive Testing-Guidelines for NDT training syllabus
3. EN473-2008, NDT -- Qualification and certification of NDT personnel-General principles
4. ACCP-CP-12012 revision ASNT Central Certification Program
5. BS-en-473:2000- NDT — Qualification and certification of NDT personnel —General principle

## **Verification/Calibration and Assessment of Non-Destructive Testing (NDT) Equipment/Instrument**

**Ang Chee Kheong**

**Joining Inspection & Technology Services**

**SIRIM Berhad**

### **Abstract**

*Non-destructive testing (NDT) is used in wide range of industrial areas. The mainstream application are in oil & gas, petrochemical, power generation, aerospace, automotive, railway and pipeline industries. NDT techniques rely heavily on human skill and knowledge for the correct assessment and interpretation of test results. Thus the personnel qualification and certification of NDT personnel is a must to ensure that the capabilities of the techniques being exploited. However, besides the personnel qualification, it is indeed to ensure that the accuracy repeatability and reproducibility of the NDT test. Thus the NDT equipment needs to be calibrated, verified or assessed for its performance. This is also comply to the accreditation requirements of **MS ISO/IEC 17020** : "General criteria for the operation of various types of bodies performing inspection under Department of Standards Malaysia. Under these schemes, verification/calibration or assessment of the equipment need to be performed at an interval (normally at an interval of 12 months) to ensure the accuracy, repeatability and reproducibility of the test. In this paper, it will discuss the verification/calibration or assessment of ultrasonic equipment in accordance to **BS EN 12668-1:2010**: "Characterization and verification of ultrasonic examination equipment" and **BS EN 15317:2007** " Characterization and verification of ultrasonic thickness measuring equipment."*

### **Introduction**

It is well known that Non-destructive testing (NDT) being widely used in oil & gas, petrochemical, power generation, aerospace, automotive, railway and pipeline industries. Besides, the NDT techniques rely on qualification and certification of the personnel and its skill fullness. The NDT equipment needs to ensure that the accuracy, repeatability and reproducibility of the NDT test. This not only comply the requirement of the MS ISO/IEC 17025: "General requirements for the competence of testing and calibration laboratories" and MS ISO/IEC 17020: "General criteria for the operation of various types of bodies performing inspection" under Department of Standards Malaysia. If NDT companies seeking accreditation

for MS ISO/IEC 17020 under Malaysia Inspection Bodies Accreditation Scheme (MIBAS), Department of Standards Malaysia then the verification/calibration or assessment of the equipment need to be performed at an interval (normally at an interval of 12 months) to ensure the accuracy, repeatability and reproducibility of the test. In this paper, it will discuss the verification/calibration or assessment of ultrasonic equipment in accordance to **BS EN 12668-1:2010**: "Characterization and verification of ultrasonic examination equipment" and **BS EN 15317:2007** "Characterization and verification of ultrasonic thickness measuring equipment". The equivalent ASTM standard is ASTM E1324: "Standard Guide for Measuring Some Electronic Characteristics of Ultrasonic Examination Instruments".

### **Why these Standards?**

The BS EN standards were discussed in this paper because most of ultrasonic manufacturers made reference to these standards for issuing the certificate of conformity on their ultrasonic equipment. The user or owner of the equipment usually refer to BS EN 12668-3 Clauses 3.2.1 & 3.2.2 or Appendix 1 of ASME Article 4 to verify the performances of the ultrasonic instrument for linearity of the time-base and linearity of equipment gain. However, it should be noted that the above mentioned standards only apply to that ultrasonic equipment itself only. It only uses the transducer and the calibration block (usually refer as combined equipment) to confirm the instrument's linearity. So the traceability is doubtful at this stage. The traceability we can only said that is the calibration block and the personnel who perform the verification. There is no any external device which can be traceable to national laboratory to verify the characteristics and performance of the instrument. This means that the electrical performances and characteristics of the ultrasonic instrument need to verify by the traceable external devices for the purpose of traceability. These issues are addressed in the BS EN 12668-1:2010 and BS EN 15317:2007 standards.

### **Accredited Laboratory or Manufacturer Certified to ISO 9001?**

The question now is that calibration/verification carried by the manufacturer which is ISO 9000 certification acceptable? It shall be noted that the MS ISO/IEC 17020 or MS ISO/IEC 17025 require that it shall be performed by competent laboratory. A competent laboratory under any accreditation scheme is an accredited laboratory. Therefore the verification/calibration by the non-accredited manufacturer is not acceptable.



The manufacturer can be audited and certified to an international management systems standard called ISO 9001. This standard is widely used in manufacturing and service organisations to evaluate their system for managing the quality of their product or service. Whilst effective as a management evaluation tool, ISO 9001 does not evaluate the technical competence of a supplier. This means that the evaluation of a supplier against ISO 9001 does not assure you or your customers that the test, inspection or calibration data are accurate and reliable.

Throughout the world, many countries now rely on a process called Laboratory Accreditation (in Malaysia called SAMM) as a means of independently evaluating laboratory competence. Unlike ISO 9001 certification, laboratory accreditation uses criteria and procedures specifically developed to determine technical competence. Specialist technical assessors conduct a thorough evaluation of all factors in a facility that affect the production of technical data. The criteria are based on an international standard called ISO/IEC 17025 (MS ISO/IEC 17025 in Malaysia), which is used for evaluating laboratories throughout the world. This standard specifically addresses factors relevant to a laboratory's ability to produce precise, accurate test and calibration data, including:

- technical competency of staff;
- validity and appropriateness of the methods;
- traceability of measurements and calibrations to national standards;
- appropriate application of measurement uncertainty;
- suitability, calibration and maintenance of test equipment;
- the testing environment;
- sampling, handling and transportation of test items;
- quality assurance of test, inspection or calibration data.

Therefore, the NDT companies seek accreditation under the MIBAS scheme need to send their equipment to the manufacturer accredited to ISO/IEC 17025 and not certified to ISO 9001.

## BS EN 12668-1:2010 and BS EN 15317:2007

The performance requirements of ultrasonic instrument in BS EN 12668-1:2000 are listed in Table 1. The performance tests are divided into 3 groups:-

- (i) Group1: Tests to be performed at manufacture on a representative sample of the ultrasonic instruments produced.
- (ii) Group 2: Test to be performed on every ultrasonic instrument:
  - a) by the manufacturer, or his agent, prior to the supply of the ultrasonic instrument (zero point test);
  - b) by the manufacturer, the owner, or a laboratory, at twelve months intervals to verify the performance of the ultrasonic instrument during its lifetime;
  - c) following the repair of the ultrasonic instrument.
- (iii) Group 3: Tests for the complete system (ultrasonic instrument and probe combined) are given in BS EN 12668-3 and these are performed at regular intervals on site during their lifetime.

It also recommended by the standards that the instrument after repair shall be checked or verify using appropriate group1 or group 2 tests. It is due to the fact that the parameters of instrument may have been influences by the repair.

Table 1

	<b>BS EN12668-1</b>		<b>BS EN 12668-3</b>
	<b>Group 1</b>	<b>Group 2</b>	<b>Group 3</b>
	<b>Subclause</b>	<b>Subclause</b>	<b>Subclause</b>
Physical state and external aspects	9.2	9.2	3.4.2
<b>Stability</b>			
Stability against temperature	8.2		
Stability after warm up time	9.3.2	9.3.2	

Display jitter	9.3.3	9.3.3	
Stability against voltage variation	8.3	9.3.4	
<b>Transmitter pulse</b>			
Pulse repetition frequency	8.4.2		
Effective output impedance	8.4.3		
Transmitter pulse frequency spectrum	8.4.4		
Transmitter voltage, rise time, reverberation and duration	9.4.2	9.4.2	
<b>Receiver</b>			
Cross talk damping from transmitter to receiver during transmission	8.5.2		
Dead time after transmitter pulse	8.5.3		
Dynamic range	8.5.4		
Receiver input impedance	8.5.5		
Time-dependant gain	8.5.6		
Temporal resolution	8.5.7		
Amplifier frequency response	9.5.2	9.5.2	
Equivalent input noise	9.5.3	9.5.3	
Sensitivity and signal-to-noise ratio			3.4.3
Accuracy of calibrated attenuator	9.5.4	9.5.4	3.2.2

Linearity of vertical display	9.5.5	9.5.5	3.2.2
Linearity of equipment gain			3.2.2
Linearity of time-base	9.6	9.6	3.2.1
<b>Monitor gate</b>			
Response threshold and switching hysteresis with a fixed monitor threshold	8.6.2		
Hold time of switched output	8.6.3		
<b>Proportional output</b>			
Impedance of proportional output	8.7.1		
Linearity of proportional output	8.7.2		
Frequency response of proportional gate output	8.7.3		
Noise on proportional gate output	8.7.4		
Influence of the measurement signal:: position within the gate	8.7.5		
Effect of pulse shape on the proportional gate output	8.7.6		
Rise, fall and hold time of proportional gate output	8.7.7		
<b>Additional tests for digital ultrasonic instruments</b>			
Linearity of time-base for digital ultrasonic instruments	8.8.2	8.8.2	3.2.1
Digitisation sampling error	8.8.3		
Response time of digital instruments	8.8.4		

The performance requirements of ultrasonic measuring equipment in BS EN 15317:2007 are listed in Table 2. The performance tests are also divided into 3 groups:-

- (i) Group 1: Tests to be performed by the manufacturer (or the manufacturer's agent) on a representative sample of the ultrasonic thickness measuring equipment produced. These tests allow the manufacturer to verify and support the technical specification for the equipment.
- (ii) Group 2: Test to be performed on all ultrasonic thickness measuring equipment:
  - a) by the manufacturer, or his agent, prior to the supply of the equipment (pre-commissioning test);
  - b) by the manufacturer, the owner, or a laboratory, at annual interval to verify the performance of the equipment during its lifetime;
  - c) following any equipment repairs.
- (iii) Group 3: Tests to be completed by the operator on site prior to and at the completion of any series of measurements.

Table 2

Title of test	Group 1	Group 2	Group 3
<b>Physical</b>			
General mechanical state and external aspects		10.4	10.4 and 11.2
<b>General characteristics</b>			
Stability against temperature	9.3		
Low battery warning	9.4	9.4	
Battery operational time	9.5		
Operational voltage range	9.6	9.6	
Operational current range	9.7	9.7	
Operational temperature	9.8		

<b>Transmitter</b>			
For each pulse width and energy setting			
PRF	9.9	9.9	
Transmitter pulse shape, rise-time and peak voltage	9.10	9.10	
<b>Receiver</b>			
Frequency range of operation	9.11		
<b>Performance</b>			
Minimum and maximum measurable thicknesses	9.12	9.12	
Accuracy and resolution	9.13	9.13	
Range of velocity setting	9.14		
Calibration mechanisms	9.15		11.3
Calibration setting storage	9.16	9.16	11.4
<b>Display/Data</b>			
Data storage	9.17		11.5
Printing	9.18		
Display and recall	9.19	9.19	
Display response time	9.20		

The clauses mention in both standard are used to verify the ultrasonic equipment to ensure that the equipment is qualified or fit to be used for testing and inspection. Therefore , the owner or user of the equipment to verify the performed of the ultrasonic instrument and the ultrasonic thickness measuring equipment in according to the Group 2 test of BS EN12668-1 and BS EN 15317:2007 standards.



The items of equipment essential to assess ultrasonic instruments in accordance with the tests in group 2 of the BS EN 12668-1 are as follows:

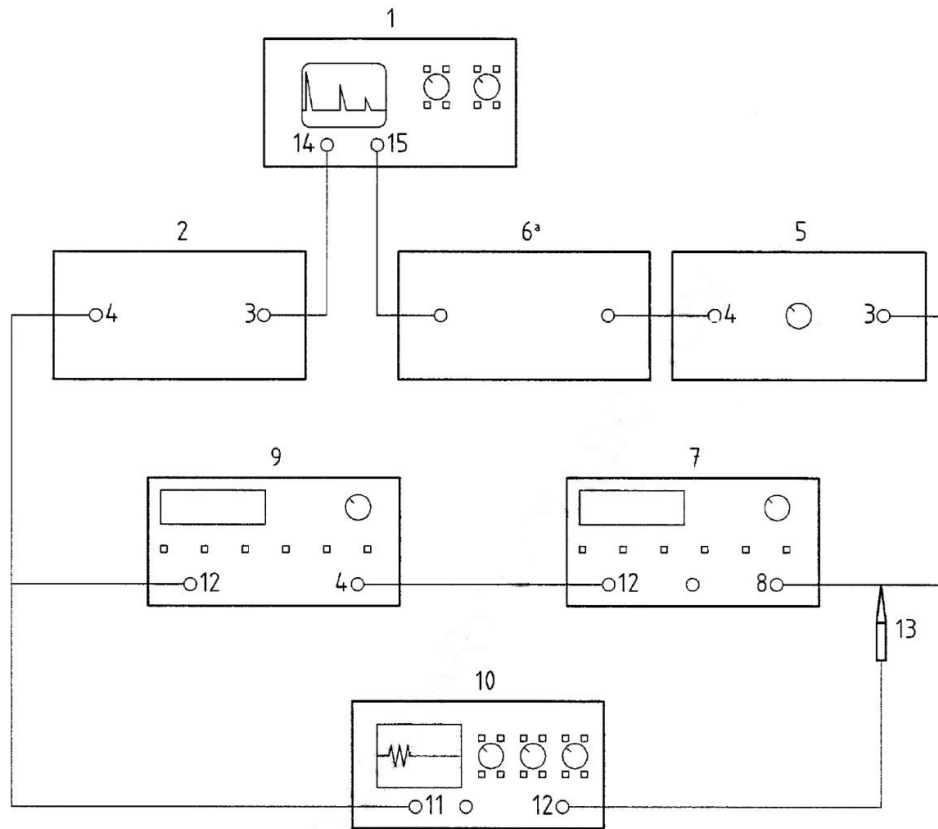
- a) oscilloscope with a minimum bandwidth of 100 MHz;
- b) 50 Ohm  $\pm 1$  % non-reactive resistor;
- c) standard 50 Ohm attenuator with 1 dB steps and a total range of 100 dB. The attenuator shall have a cumulative error of less than 0.3 dB in any 10 dB span for signals with a frequency up to 15 MHz;
- d) two signal generators with an external trigger or gate capable of producing a gated burst of sinusoidal radio frequency signals of variable amplitude in the range suitable for the equipment being tested;
- e) variable DC power supply suitable to replace any battery used in the ultrasonic instrument;
- f) variable transformer to control mains voltage.

While the items of equipment essential to perform Group 2 tests of BS EN 15317:2007 on ultrasonic thickness measuring equipment are as follows:

- a) digital or analogue oscilloscope with a minimum bandwidth of 100 MHz with attenuating or high voltage probes;
- b) 1 x 50 Ohm  $\pm 1$  % or 1 x 75 Ohm  $\pm 1$  % non-reactive resistor depending on the oscilloscope to be used;
- c) variable dc power supply;
- d) digital or analogue voltmeter;
- e) analogue ammeter.

All the tests in both standards, except for those of stability, use electronic means of generating the required signals. The characteristics of the equipment employed and its stability shall be adequate for the purpose of the tests.

Those items mentioned above to perform the verification of ultrasonic instrument shall have not broken in traceability that means it shall traceable to national laboratory. Figure 1 shows the general purpose set-up for equipment for ultrasonic instrument



# Key

1	ultrasonic instrument	9	pulse generator/counter
2	fixed attenuator	10	100 MHz oscilloscope
3	input	11	input channel A
4	output	12	external trigger output
5	variable RF attenuator	13	X10 scope probe (100 MHz)
6	termination pad*	14	transmitter output
7	gated RF signal generator	15	receiver input
8	RF-output		

\*Termination pad only required to match impedance of flaw detector to test instruments

Figure 1 General purpose set-up for equipment for ultrasonic instrument

From Figure 1, it should be noted that the external devices are used to check the performances of the ultrasonic instruments and these devices are traceable to national laboratory if only performed by accredited laboratory. If the verification of ultrasonic equipment meets the acceptance criteria as specified by these standards, the equipment is said to be fit to be used for carrying the inspection and testing. Let us take an example in clause 9.5.5 of BS EN 12668-1:2010, it specifies the requirement for linearity of vertical display. Table 2 shows the acceptance level for vertical display linearity.

Table 2 Acceptance levels for vertical display linearity

External attenuator setting dB	Target % screen height	Acceptable amplitude % screen height
1	90	88 to 92
2	80	(Reference line)
4	64	62 to 66
6	50	48 to 52
8	40	38 to 42
12	25	23 to 27
14	20	18 to 22
20	10	8 to 12
26	5	3 to 7

This is different from clause 3.2.2 of BS EN 12338-3 that in this clause the external attenuator to verify the gain setting of the instrument. In clause 3.2.2 of BS EN 12338-3 only verify the gain setting within the instrument its self and therefore traceability is at doubt.

While in BS EN 12668-1:2010, an external device that is calibrated attenuators is used to checked the gain setting of the instrument. In addition, the ultrasonic instrument shall also meet the requirement of other clauses mention in the standards(See Table 1).

## Acceptance criteria

The Table 3 shows the acceptance criterion of group 2 test of BS EN 12668-1:2010.

Table 3

<b>Group 2 Test of BS EN12668-1</b>		
<b>Title of test</b>		<b>Acceptance criteria</b>
	<b>Subclause</b>	
Physical state and external aspects	9.2	Visual inspect for physical damage which may influence its current operation.
<b>Stability</b>		
Stability after warm up time	9.3.2	not vary $> \pm 2\%$ of full screen height (signal amplitude) less than $\pm 1\%$ of full screen width(time base)
Display jitter	9.3.3	not vary $> \pm 2\%$ of full screen height
Stability against voltage variation	9.3.4	-amplitude & position shall be stable -automatic cut off before $\pm 2\%$ of full screen height change or $\pm 1\%$ of full screen width from initial setting
<b>Transmitter pulse</b>		
Transmitter voltage, rise time, reverberation and duration	9.4.2	a) transmitted pulse voltage within $\pm 10\%$ of the manufacturer's specification. b) pulse rise time less maximum value quoted by manufacturer's specification c) pulse duration within $\pm 10\%$ of the manufacturer's specification d) any pulse reverberation $< 4\%$ of peak-peak transmitter pulse voltage.
<b>Receiver</b>		
Amplifier frequency response	9.5.2	within $\pm 10\%$ of the bandwidth specification in technical specification.
Equivalent input noise	9.5.3	9.5.3
Accuracy of calibrated attenuator	9.5.4	a) not exceed $\pm 1$ dB in any successive 20 dB span or the full range, whichever is smaller. b) not exceed $\pm 2$ dB in any 60 dB span or the full range whichever is smaller

Linearity of vertical display	9.5.5	refer to Table 2 in this paper or Table 4 in the standard
Linearity of time-base	9.6	deviation not > $\pm 1\%$ of the full screen width
<b>Additional tests for digital ultrasonic instruments</b>		
Linearity of time-base for digital ultrasonic instruments	8.8.2	time base non-linearity not exceed $\pm 0.5\%$ of the screen width

Figure 2 shows another example of transmitter pulse parameters to be measured for an ultrasonic equipment, the acceptance criteria is specified in BS EN 12668-1:2010 Clause 9.4.2

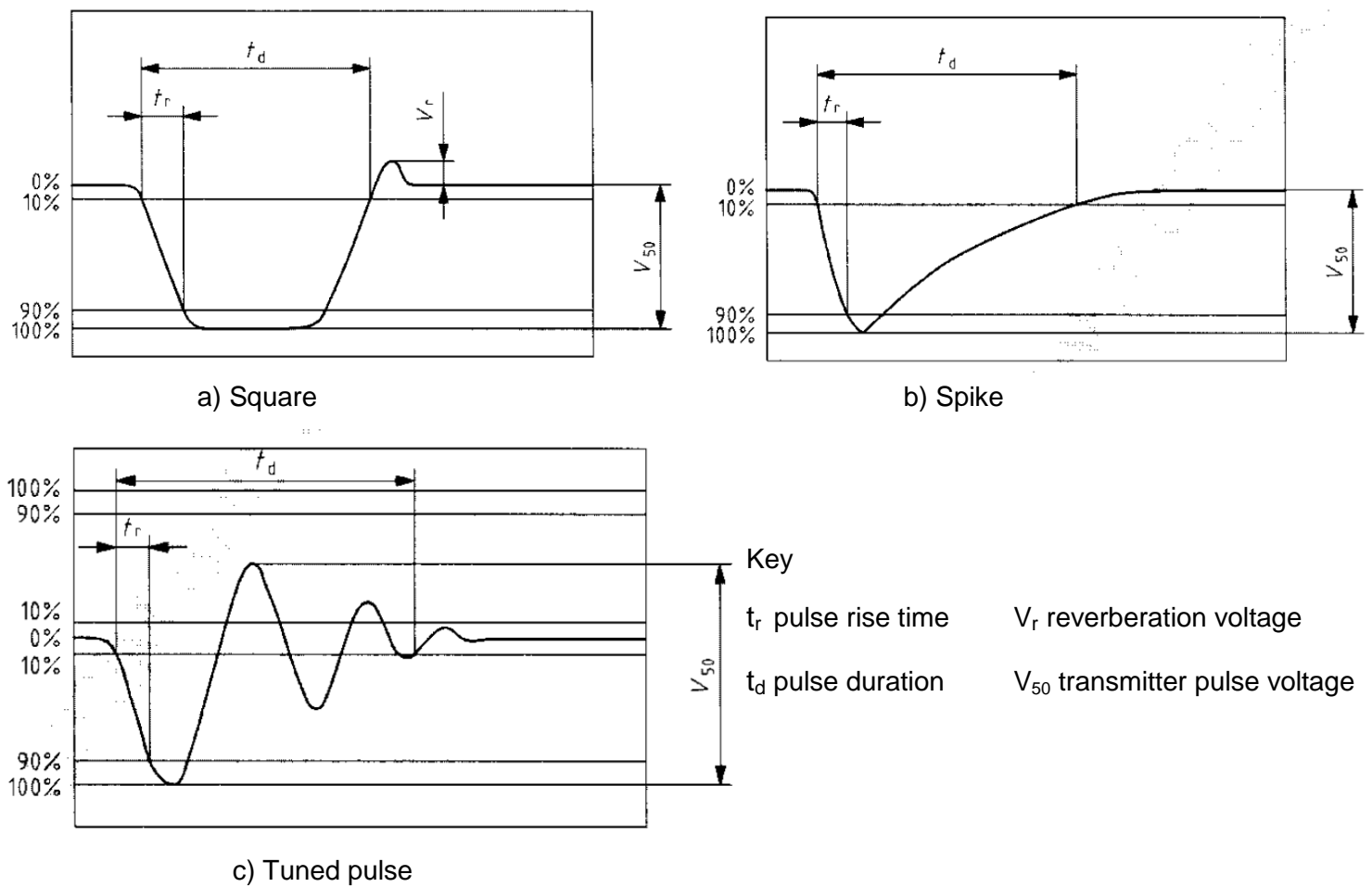


Figure 2 Transmitter pulse parameters to be measured

Similarly, the acceptance criteria for the ultrasonic measuring equipment shall fulfill the requirements of the BS EN 15317:2007. The Table 4 shows the acceptance criterion of group 2 test of BS EN 15317:2007.

Table 4

Title of test	Group 2	Acceptance criteria
<b>Physical</b>		
General mechanical state and external aspects	10.4	Visual inspect for physical damage which may influence its current operation
<b>General characteristics</b>		
Low battery warning	9.4	The indicated reading shall remain within the specified accuracy and resolution at that range. The low voltage warning shall be displayed within $\pm 5\%$ of the specified voltage.
Operational voltage range	9.6	The indicated reading shall remain within the specified accuracy and resolution at that range.
Operational current range	9.7	The indicated reading shall be within $\pm 10\%$ of that specified at the minimum & maximum specified voltage.
<b>Transmitter</b>		
For each pulse width and energy setting		
PRF	9.9	within $\pm 20\%$ of that given in the manufacturer's technical specification.
Transmitter pulse shape, rise-time and peak voltage	9.10	a) transmitted pulse voltage within $\pm 10\%$ of the manufacturer's specification. b) pulse rise time less than maximum value quoted by manufacturer's specification c) pulse duration within $\pm 10\%$ of the manufacturer's specification d) any pulse reverberation $< 4\%$ of peak-peak transmitter pulse voltage
<b>Performance</b>		
Minimum and maximum measurable thicknesses	9.12	shall be within the manufacturer's specified accuracy and resolution.

Accuracy and resolution	9.13	shall be within the manufacturer's stated accuracy & resolution.
Calibration setting storage	9.16	shall be within the manufacturer's stated accuracy & resolution.
<b>Display/Data</b>		
Display and recall	9.19	Data shall conform to the manufacturer's specifications.

The acceptance criteria for the verification of the ultrasonic instruments mentioned in Table 3 and Table 4 in accordance to BS EN 12668-1:2010 or BS EN 15317:2007 is to ensure that the equipment is fit to be used for inspection or thickness measurement. This is also to ensure the accuracy, repeatability and reproducibility of the non-destructive testing or inspection. In addition, there is no broken linkage in traceable if the verification of the equipment is carried out by third party accredited laboratory.

## Conclusion

Therefore the non-destructive testing companies seeking accreditation under the MIBAS scheme should verify the ultrasonic instruments in accordance to the requirements of BS EN 12668-1:2010 and BS EN 15317:2007 to ensure that the accuracy, repeatability and reproducibility of the non-destructive testing and inspection.

## References

1. ILAC Publications
2. SAMM, MIBAS publications, Department of Standards Malaysia
2. BS EN 12668-1:2010 "Characterization and verification of ultrasonic examination equipment"
3. BS EN 15317:2007 "Characterization and verification of ultrasonic thickness measuring equipment."



## **Early Experience on the Implementation of MS ISO 17020:1998 at NDT Group, Malaysian Nuclear Agency**

Siti Madiha Muhammad Amir<sup>1</sup>, Dr. Abd Nassir Ibrahim<sup>1</sup>, Azhar Azmi<sup>1</sup>,  
Dr. Mohamad Pauzi Ismail<sup>1</sup>, Dr Noriah Mod Ali<sup>2</sup> and Sapizah Rahim<sup>1</sup>

NDT Group<sup>1</sup>,  
Industrial Technology Division,  
Radiation Health and Safety Division<sup>2</sup>  
Malaysian Nuclear Agency

### **Abstract**

MS ISO/IEC 17020:1998 is an internationally recognized standard for competence of inspection bodies. This international standard specifies general criteria for the operation of various types of bodies performing inspection regardless of the sector involved. This standard is intended for the use of inspection bodies concerning with recognizing the competence of the workers belong to the inspection bodies. The NDT Group at Nuclear Malaysia was earlier accredited to MS ISO 9001:2008. However, realizing the importance and benefits of MS ISO/IEC 17020:1998, the group has decided to go for accreditation of MS ISO/IEC 17020:1998. This article shares the early experiences including the challenges on the implementation of the MS ISO/IEC 17020:1998 at NDT Group, Malaysian Nuclear Agency.

**Keywords : MS ISO/IEC 17020, competence, inspection bodies**

### **Introduction**

ISO 17020:1998 is an internationally standard for the competence of inspection bodies. It contains the general criteria for the operation of various types of bodies executing inspection. This standard requires both aspects involving the quality management system as well as the evaluation of the technical competence of the inspection body.

The objectives of ISO 17020 are to promote confidence in inspection body; hence this gives assurance that the services provided by the inspection body are accepted by clients and authorities. Having accredited with the standard, it promotes confidence in information about the conformity of inspected items with regulation, standards, specifications, inspection schemes, contracts, including general requirements.

In Malaysia, the organization responsible for national standardisation and accreditation is known as the Department of Standards Malaysia (DSM). Its main role is to foster and promote various standards, standardisation and accreditation as a means of advancing the national economy, promoting industrial efficiency and development, benefiting the health and safety of the public, protecting the consumers, facilitating domestic and international trade and furthering international cooperation in relation to standards standardization [1]. In relation with ISO/IEC 17020:1998, DSM has published the MS ISO/IEC 17020:1998. It is a Malaysian Standard which is identical with the ISO/IEC 17020:1998 and this standard is being used as one of the references in the system.

The NDT Group of Malaysian Nuclear Agency (NDT Group) has been involved in the Non-Destructive Testing (NDT) inspection services for the past 25 years. The NDT Group has vast experiences in inspecting engineering components such as plant piping, pipelines, heat exchanger tubes, pressure vessels and many others. In the initial stage of obtaining the accreditation for providing quality services to the clients, the NDT Group was earlier certified with ISO 9001:2008 in 2005. However, after realizing the importance and benefits of MS ISO/IEC 17020:1998, the group decided to go for accreditation of MS ISO/IEC 17020:1998. Since the MS ISO/IEC 17020:1998 is intended for recognizing the competence of inspection bodies, hence the accreditation award is an important achievement for our NDT Group in Nuclear Malaysia.

### **Milestone and Challenges towards implementing MS ISO/IEC 17020:1998 in Nuclear Malaysia**

The system in Nuclear Malaysia started with the Adequacy Audit which was done twice started with Nuclear Malaysia audit team then followed with the Department of Standards Malaysia. There was no non-compliance (NCR) issued during the audits. The Adequacy Audit with Nuclear Malaysia auditors was executed on the 23<sup>rd</sup> March 2010 and followed by Adequacy Audit with Standards Malaysia on 30<sup>th</sup> June 2010. Next, was the Pre-Assessment and it was done twice with Nuclear Malaysia audit team as well as assessors nominated by the Standards Malaysia. During the Pre-Assessment that was conducted on 10<sup>th</sup> August 2010 by Standards Malaysia, the lead and technical assessors were present and technical witnessing executed during this audit was on liquid penetrant method. Three (3) NCR and two (2) observations were issued during the Pre-Assessment on the technical and also on the management aspect. The next step was to go for the compliance audit. The compliance audit was conducted on the 3<sup>rd</sup> October 2011 with the presence of lead assessor and technical assessor for technical witnessing for radiography and ultrasonic methods. Two (2) NCR and six (6) observations were issued during the compliance audit. Before the granting of the certificate, the reports of all the audits went through the Inspection Accreditation Evaluation Panel for evaluation. The Diagram 1 shows the flow of the audits towards the certification.

### Milestone towards the certification

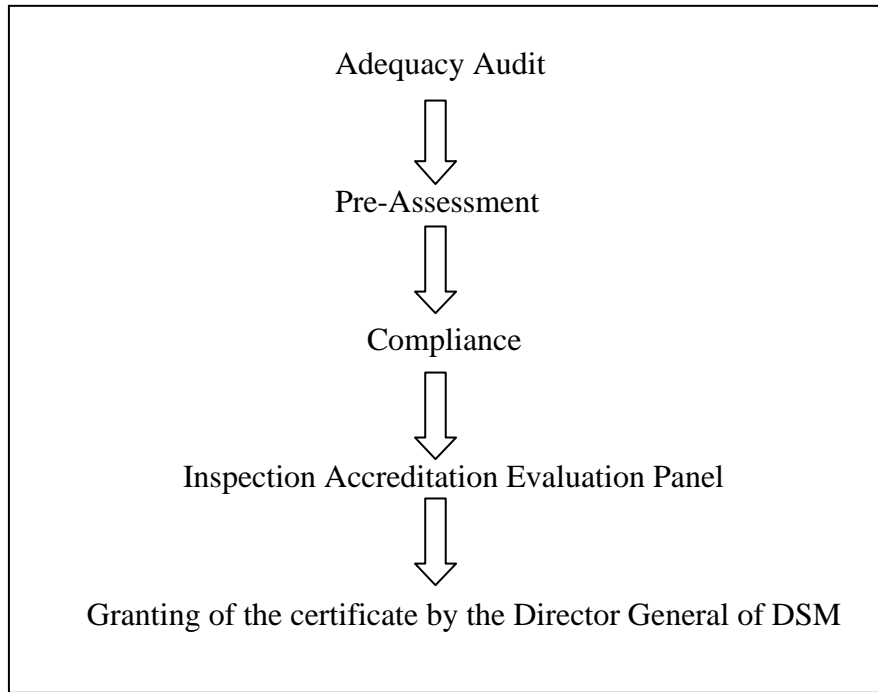


**Diagram 1**

NDT Group at Nuclear Malaysia was finally awarded for MS ISO 17020:1998, type A from the Department of Standards Malaysia on the 25<sup>th</sup> April 2012 for radiography, ultrasonic and liquid penetrant methods. The methods and scope of the accreditation is shown on Table 1 with the team involved in the system is shown in Diagram 2.

### Scope of Accreditation

Items, Materials or Products Inspected	Type and Range of Inspection
Metallic Weldments and Base Metals	Radiographic Testing -Pre and In-service Inspection
Metallic Weldments and Base Metals	Ultrasonic Testing -Pre and In-service Inspection
Metallic Weldments and Base Metals	Dye Penetrant Inspection -Pre and In-service Inspection

**Table 1**

## NDT Group Nuclear Malaysia Organisation Chart [2]

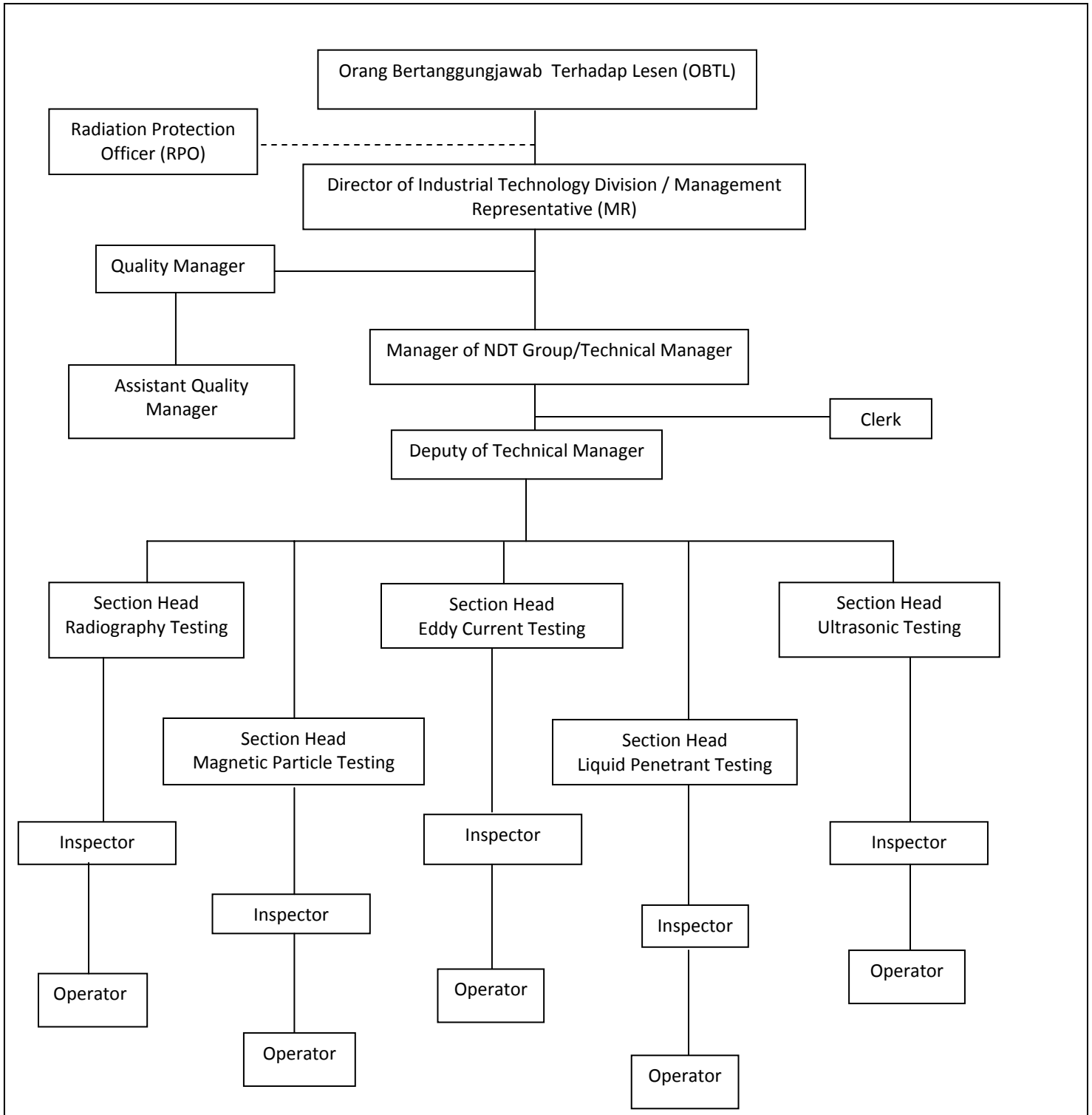


**Diagram 2**

In realizing the aspirations for obtaining the certification, there were challenges faced during the process. The most challenging is on the technical witnessing. As MS ISO/IEC 17020:1998 encompasses a requirement on witnessing the inspection lively, which made MS ISO/IEC 17020:1998 is distinctive as compared to ISO 9000, some issues on the subject should be addressed in proper and timely. The first is issue on coordinating on time schedule between different independent parties. The timeframe of work schedule of inspection body most of the time do not match with the work schedule that the witnessing party is available. Frequently, the work schedule of inspection body is clients dependent. The inspection body, their clients and witnessing party have their own deadlines and constraints, hence, time management, coordination and cooperation in this case is crucial. Sometimes this situations end up with delaying the time for witnessing to another anticipated date that both parties (inspection body and witnessing party) are available.

The MS ISO/IEC 17020 is different with the ISO 9000 in terms of the participation of the personnel. For ISO 9000, only relevant personnel were involved in the system. However, with the MS ISO/IEC 17020:1998 everybody in the NDT Group is involved. The top-down participation is very important and is the key factor that contributes to the successful certification of MS ISO/IEC 17020:1998. The commitment of participation from all levels; top management to technician level is very much required. Thus, explanation and strong motivation is needed to motivate the staff and understanding their role and participation in the system.

## **Conclusion**

Accreditation of NDT Group, Nuclear Malaysia to MS ISO/IEC 17020:1998 by Standards Malaysia demonstrates the competence, impartiality and performance capability of the Nuclear Malaysia NDT inspection body. However, the biggest challenge is to maintain the system in the organization. This situation can only be achieved with strong effort, continuous improvement and high motivations from all personnel in the system. In short, the commitment and participation from all levels is the main factor in ensuring the system is maintained.

## **References**

- [1] MS ISO/IEC 17020:1998, General Criteria for the Operation of Various Types of Bodies Performing Inspection, Department of Standards Malaysia
- [2] Quality Manual ISO 17020:1998, NDT Group, Malaysian Nuclear Agency

## Determination of optimal exposure for Computed Radiography systems using exposure chart

Sapizah Rahim<sup>1\*</sup>, Harianto Saleh<sup>2</sup>, Ilham Mukriz Zainal Abidin<sup>1</sup> and Arshad Yassin<sup>1</sup>

<sup>1</sup>: NDT Group, Industrial Technology Division, Malaysian Nuclear Agency, 43000 Bangi Kajang, Selangor, Malaysia

<sup>2</sup>: Faculty of Science & Technology, National University of Malaysia, 43600 Bangi, Selangor, Malaysia  
\*sapizah@nuclearmalaysia.gov.my

Digital Industrial Radiography (DIR) is a technique in Non Destructive Testing (NDT) which combines radiographic technique with digital detectors or readers. Several studies have concluded that DIR technique can reduced the radiation dose up to 20% of exposure time. However, currently there is still no guideline or reference in obtaining optimal exposure for computed radiography system. In this work, we have established an exposure chart for computed radiography system for aluminum samples. The normalized signal-to-noise ratio (SNR<sub>n</sub>) values and sensitivity level have been considered in achieving optimal exposure prior to any manipulation of the digital images by image processing softwares. The results have provided insight for future guidance in DIR for a comprehensive inspection and reliable defect assessment.

*Keywords: Computed Radiography System; optimal exposure; exposure chart*

## INTRODUCTION

Digital Industrial Radiography (DIR) is a powerful technique that widely used in Non-Destructive Testing to detect subsurface and internal defects of welding and discontinuities of processes. This technique can be use to examine an object or material with technologies that does not affect the object's future usefulness. Basically DIR technology used radiography technique with combination of digital detector or reader gives benefits to NDT practitioners especially for radiographers such as no film processing needed, automatic defect recognition, fast examination and only short exposure time required [1]. The demand on DIR technologies always increase with the advancement of computer technology to incorporate computers in assisting the process of detecting, acquiring and recording images of DIR.

There are several systems have been developed in DIR technologies for examples digital detector array, flat panel system (a-Se or a-Si) and Computed Radiography [2]. Computed Radiography (CR) uses similar equipment to conventional radiography but the film to create the image is replaced by imaging plate (IP). The imaging plate basically consists of a flexible polymer carrier foil covered with a layer sensitive to X-rays consisting of a BaFBr mixture doped with Eu<sup>2+</sup>. X-ray and gamma ray quanta result in an avalanche of charge carriers i.e. electrons and holes in the BaFBr crystal lattice. These charge carriers may be trapped at impurities sites (electrons at a halogen vacancy) or holes at an interstitial Br<sup>2+</sup> molecule. Red laser light excites electrons trapped in a Br- vacancy to a higher state from which they may tunnel and recombine with a nearby trapped hole. Transfer of the recombination energy excites a nearby located Eu<sup>2+</sup> ion and upon return to its ground state this Eu<sup>2+</sup> ion emits a blue photon. This process called photo stimulated luminescence. The

imaging plates can be reused up to a thousand times without any significant loss in quality if no mechanical damages appear [1].

Computed Radiography gives some advantages such as high linearity, high dynamic range ( $> 10^5$ ) and high sensitivity. However, there are still having limitations on CR imaging for example, loss on spatial resolution from scattering of the laser light beam during image plate readout. Laser light scatter results in the deexcitation of locations in the phosphor that are somewhat larger than the size of the laser beam and potentially larger than the separation between laser positions. Furthermore, CR system has limited maximum signal-to-noise ratio SNR because of structure noise from the imaging plate production process, which cannot be reduced by system calibration.

Nowadays, many manufactures have developed their CR system to enhance the performance and quality of the CR system as well as for digital images. There are several factors affecting the quality of a CR image including geometrical un-sharpness, signal/noise ratio, scatter and contrast sensitivity. There is also having several additional factor such as scanning parameter which affect the accurate reading of images on exposed imaging plates using optical scanner [3]. To ensure that the CR systems enabling to produce satisfactory and repeatable results, the CR systems should be calibrate according to EN 14784 which is also describes the classification of these systems in combination with specified metal screen for industrial radiography.

In film radiography, all film based standards require minimum optical density e.g. more than 2.0 and maximum unsharpness which is more than 0.1 mm for both welding and casting inspection. The exposed films are accepted only if they have this minimum optical density. A similar procedure can also be applied in CR imaging. Each CR system provides intensity values or grey values of each picture element (pixel). All pixel in the region of interest (ROI), which is to be evaluated, should exceed a minimum intensity (or grey value), in similar way as minimum density in film radiography should be exceeded. The minimum intensity for each CR system is dependence on class system which is characterized by a signal-to-noise ratio (SNR) range and by a certain basic spatial resolution value in a specified exposure range. In this work, we have established an exposure chart for an optimal exposure of CR system using blue imaging plate at aluminum material.

## METHOD

The experimental setup for aluminum step wedge exposure is shown in Figure 1 . It consists of an x-ray tube (GEIT, Germany) as the radiation source, phosphorus IP (Blue and White type, Dürr NDT, Germany) and a CR reader (HDCR, Dürr NDT, Germany) that read and digitizes the images from the IP. For our CR system, the generated images are analysed using commercially available dedicated image processing software for radiography images called Isee! [5]. The distance between focal spot in the X-ray tube to the imaging plate was 100cm with the sensitive layer (white and blue type) of the imaging plates were facing the X-ray source. Table 1 provides the basic characters of our CR system that have been quantitatively evaluated in our previous work [6]. After made an exposure, the IP was scanned using reader with the background and anti-shading correction has been corrected before the IP was used to be exposed according to EN14784. The reading direction of the IP was always in horizontal position to the reader or scanner.



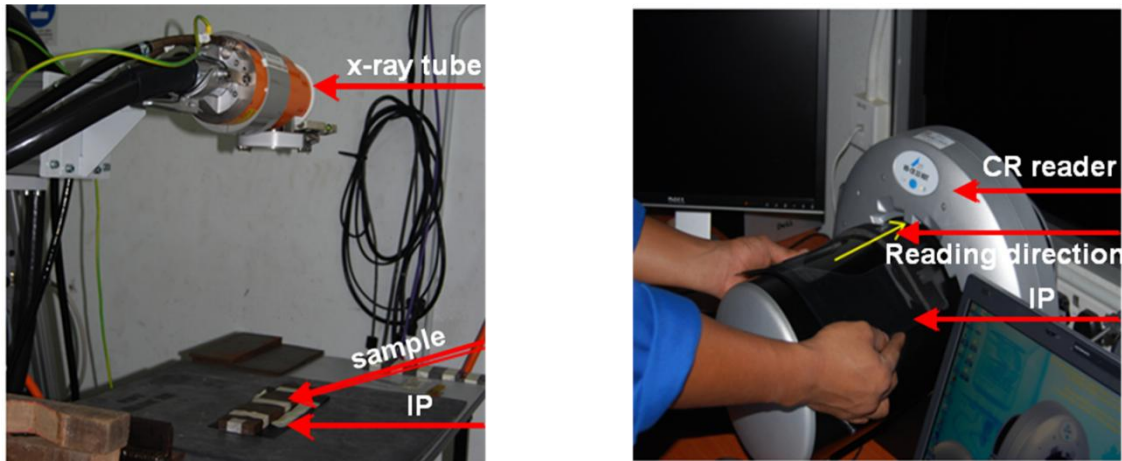


Fig. 1: CR system setup

**Table 1: Basic physical character of the CR system used for this work**

Feature	Computed radiography
Pixel Size ( $\mu m$ )	25
Field size (pixels)	9487 X 3930
Analogue Digital Converter (ADC, bit)	12

## DISCUSSION

In practical, CR system class for HD-Durr required the minimum normalized signal-to-noise ratio ( $SNR_n$ ) of the IP images should be higher than 130 [7] for acceptable image density and sensitivity to permit successful image manipulation. The  $SNR_n$  values are measured on pre-defined region of interest (ROI) and based on fixed basic spatial resolution. In our work, the target  $SNR_n$  is set at 130 and the exposure time in the experiment is varied to achieve this targeted  $SNR_n$ . The basic spatial resolution and  $SNR_n$  from the IP images were measured and obtained by analysis using the Isee! software. The aluminum step wedge was exposed to four different penetrating energies,  $kV = 100, 120, 140$  and  $160$  for both blue and white type of IP with a constant current,  $I = 3$  mA, as summarised in Table 2.

**Table 2: Experimental radiographic parameters for the exposure chart establishment**

Penetrating energies (kV)	Current, I (mA)	Focus film distance, FDD (cm)	Thickness (mm)
100, 120, 140 and 160	3	100	1.5
			2.5
			5
			7
			10

The consecutive radiographic exposure chart for the aluminum step wedge is shown in Fig. 3. As can be observed in both blue and white type IP's exposure charts, the exposure is decreased with the increased of the x-ray tube energy which is similar to film radiography's exposure chart. However, blue IP needed slightly high exposure compare with white IP exposure. The resolution and grain size of each type of IP play main role in this establishment of exposure chart where the white IP needed less exposure while blue IP needed high

exposure. The exposure chart established, will provide a reference to select appropriate exposure settings with different experimental condition i.e. thickness, in obtaining acceptable image quality for analysis manipulation.

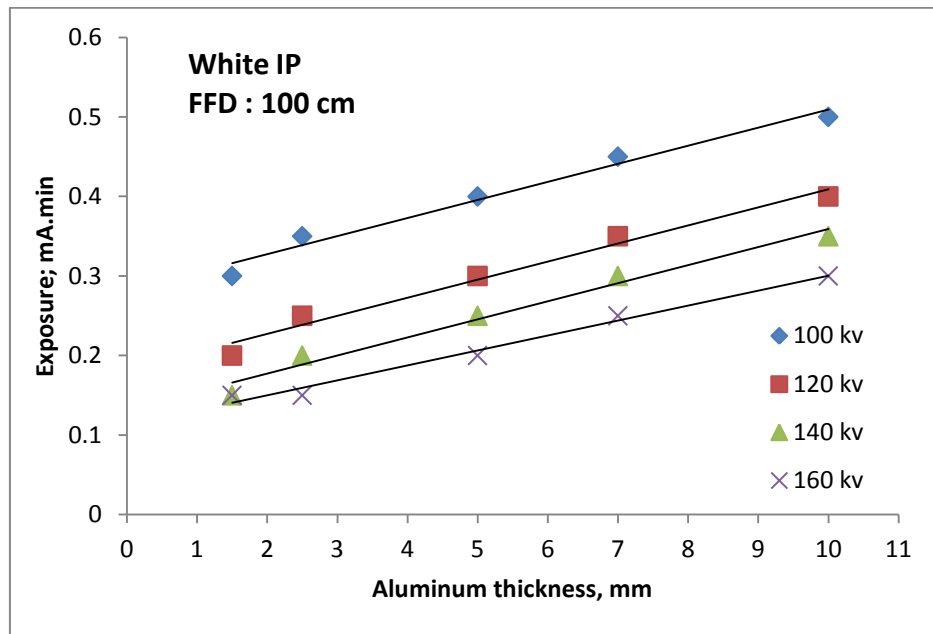


Fig 3(a) : Exposure chart for white type imaging plate

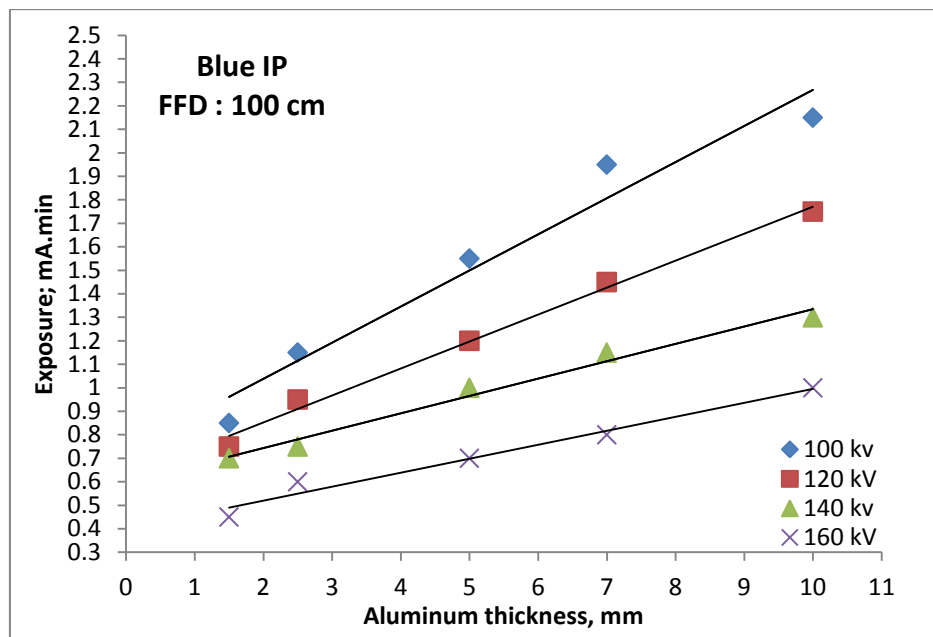


Fig 3 (b) : Exposure chart for blue type imaging plate

#### 4. Conclusion

This paper has reported the establishment of an x-ray exposure chart for aluminum step wedge using CR system. Experimental measurements has been carried out with target  $SNR_n$  for the images from the IP for acceptable image density and sensitivity to permit successful image manipulation. With the exposure chart established, it will reduce the trial and error in

CR for obtaining quality radiographic images and maintain repeatable and reliable radiographic results.

### **Acknowledgements**

The authors would like to thank the Malaysian Nuclear Agency and National University of Malaysia (UKM) for the support.

### **References**

- [1] J.A. Rowlands, 'The physics of computed radiography', *Physics in Medicine and Biology*, Vol. 47, pp. R123-R166, 2002.
- [2] U. Ewert, U. Zscherpel, M. Horkey, J. Kennedy and M. Hutchinson, 'A new computer based concept for digital radiographic reference images', *Journal of Nondestructive Testing*, Vol. 7, No. 12, pp. 1-13, 2002.
- [3] E. Deprins, 'Computed radiography in NDT applications', *Insight – Non-Destructive Testing and Condition Monitoring*, Vol. 46, No. 10, pp. 590-593, 2004.
- [4] R. Honea, M.E. Blado and Y. Ma, 'Is reject analysis necessary after converting to computed radiography', *Journal of Digital Imaging*, Vol. 15, Suppl. 1, pp. 41-52, 2002.
- [5] O. Alekseychuk, 'Isee! The BAM radiographic image analysis software, BAM.
- [6] K.A.M. Salleh, A.R. Hamzah and W.M.S.W. Hassan, 'Modulation transfer function (MTF) and noise power spectrum (NPS) studies on three industrial digital radiography systems (IDR)', *Insight – Non-destructive Testing and Condition Monitoring*, Vol. 51, No. 6, pp. 321-326, 2009.
- [7] EN 584-1, Non-destructive testing – Industrial radiographic film – Part 1: Classification of film systems for industrial radiography.

## **A LOW COST GAMMA-RAY FLUOROSCOPIC SYSTEM FOR Se-75 AND Ir-192 INDUSTRIAL RADIOGRAPHY SOURCES**

K. Iamsamang and N. Chankow

Department of Nuclear Engineering, Faculty of Engineering, Chulalongkorn University  
Phyatai Road, Patumwan District, Bangkok 10330, Thailand  
E-mail : nares.c@chula.ac.th

### **ABSTRACT**

Fluoroscopy has been widely used only for low energy x-ray and gamma-ray below 100 keV due to insufficient photon-to-light conversion efficiency of commercially available fluorescent screens. The new Kyokko fluorescent screen, namely PI200, has been claimed by the manufacturer for MeV radiography. However, there is no report on using with high energy gamma-ray except for 300 keV x-ray. A gamma-ray fluoroscopic system using the PI200 fluorescent screen was therefore designed and constructed to be tested with gamma-rays emitted from Selenium-75 ( $^{75}\text{Se}$ ) and Iridium-192 ( $^{192}\text{Ir}$ ) industrial radiography sources. The image on the fluorescent screen was viewed by a cannon 500D digital camera connected to a laptop computer via USB port allowing the user to remotely control the camera, to view the image and to transfer the image data to the computer. The test results indicated that the image quality was inferior to those obtained from x-ray film and imaging plate but it was successfully used to inspect foreign materials in steel pipe, paper parcel and concrete column. The exposure time required for a 50 Ci Se-75 or Ir-192 gamma-ray source was less than 60 seconds. Moreover, the two images of a specimen taken at different source positions parallel to the specimen plane could be combined to make Anaglyph or multiple Object (MPO) image for viewing in 3D.

### **INTRODUCTION**

In industrial radiography, film has been used extensively as recording medium. During the past decade, film is gradually replaced by imaging plate (IP) and digital detectors like linear detector and flat panel digital plate. The IP gives excellent image quality with great reduction in the exposure time [1- 3]. However, the imaging plate and the image reader are still costly even though the plate can be reused for up to 1,000 times as claimed by the manufacturer. The linear detector and the digital plate are also costly particularly the digital plate. All the mentioned recording media can give sufficient image quality for inspection of industrial specimens with sensitivity of 2 - 3 % of the specimen thickness or better.

X-ray fluoroscopy has been commonly used in medical diagnosis using x-ray energy below 100 keV. Image on the fluorescent screen can be viewed real-time directly via lead glass to avoid exposure to x-rays or indirectly using reflecting mirror and/or CCTV (closed circuit television) system. Fluoroscopy is simple and low cost but has limited use due to insufficient photon-to-light conversion efficiency. The new Kyokko PI200 fluorescent screen has been claimed by the manufacturer that it can be used for MeV radiography [4]. However, there is no report on using it with high energy gamma-rays except for 300 keV x-ray. Our preliminary experiment found that the PI200 screen was fluoresced when exposed to high energy gamma-rays from Ir-192 and Cs-137 sources.

This main objective of this research is to design and construct an image viewing system using a Kyokko PI200 fluorescent screen to convert transmitted gamma-rays to light and a digital camera to view image on the fluorescent screen.

## EXPERIMENTAL AND RESULTS

The developed system was mainly consisted of a Kyokko PI200 fluorescent screen and a Cannon 500D digital camera. The screen must be contained in a light tight box so that the image formed on the screen by transmitted gamma-rays could be seen by the digital camera. To avoid noisy signals caused by exposure of the image sensitive device, so called “complementary metal-oxide-semiconductor (CMOS)” chip, of the camera to gamma-rays, the camera must be placed off beam. As illustrated in figure 1, the camera body was placed behind a lead block while an angle mirror lens reflected the image on the fluorescent screen to the camera. By using an 18-55 mm lens and 30 cm x 30 cm fluorescent screen, the camera must be fixed at approximately 50 cm to view the whole screen. A 35 cm x 35 cm x 60 cm light tight box was thus constructed to accommodate the 30 cm x 30 cm PI200 fluorescent screen and the camera. The inner walls of the light-tight box, except the front side where the fluorescent screen was, were also lined with 3 mm thick lead sheets to prevent scattered x-rays within the box from reaching the camera. In practice, the front side of the box would be placed facing the source while the specimen was placed right in front of the box. The selected digital camera connected to a microcomputer allowing the user to remotely perform camera settings as well as to display and store the image via USB cable.

The system was first tested for its sensitivity to gamma-rays from 9 Ci Ir-192 at 20 cm distance using different camera settings and exposure times. As expected, the brightness of the image increased linearly with increasing of ISO and the exposure time up about 100 then level off. The aperture setting (f) had little effect on the image brightness. The noisy signals on the image increased with increasing of the exposure time and the ISO setting.

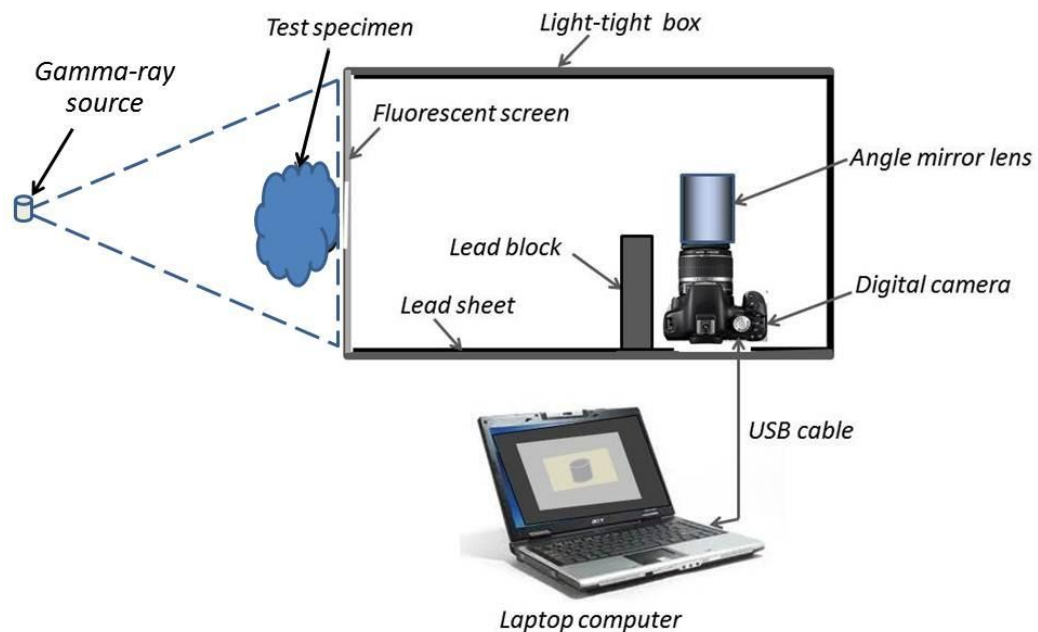


Figure 1 Schematic diagram of the light-tight box to accommodate a 30 cm x 30 cm PI200 fluorescent screen and a Cannon 500D digital camera



Figure 2 Canon 500D digital camera with 18-55 mm and angle mirror lenses

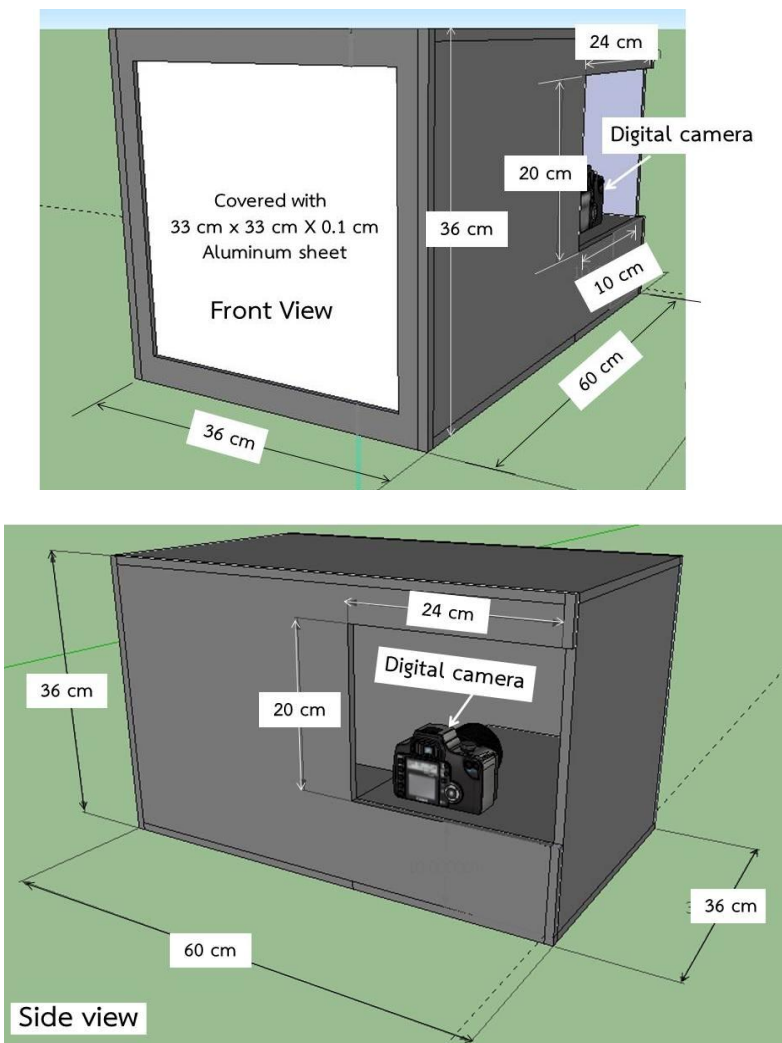


Figure 3 Perspective front and side views of the light-tight box

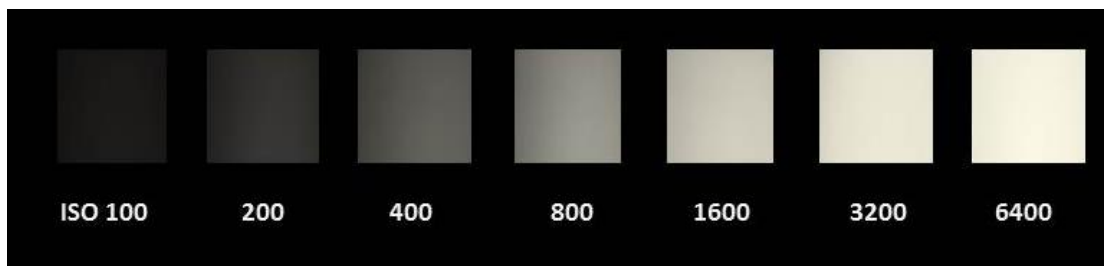


Figure 3 Grey levels of the image at different ISO settings for 20 s exposure time obtained from exposure to gamma-rays from 9 Ci Ir-192 at 20 cm

Table 1 Average grey levels at at different ISO settings and exposure times obtained from exposure to gamma-rays from 9 Ci Ir-192 at 20 cm

ISO setting	Exposure time (seconds)				
	10	20	30	40	50
100	8.27	15.39	28.29	37.6	46.25
200	17.49	36.24	54.04	72.71	86.10
400	36.52	68.6	95.37	119.02	136.09
800	71.47	116.01	150.91	173.58	189.29
1600	121.04	171.54	200.45	213.08	220.48
3200	171.98	209.69	226.45	243.79	252.42
6400	212.72	244.92	254.7	254.97	254.99

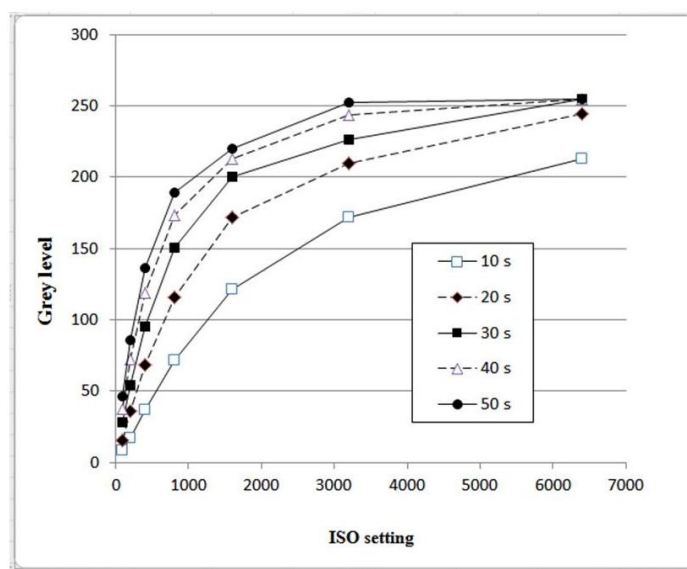


Figure 4 Grey levels of the image at different ISO settings and exposure times obtained from exposure to gamma-rays from 9 Ci Ir-192 at 20 cm

After that it was tested with gamma-rays from a 70 Ci Se-75 source at 40 cm distance with ISO setting at 200 and the exposure times between 5 – 50 seconds. The average grey levels increased linearly with increasing of the exposure time as shown in figure 5. This was because the average grey levels were not exceed 100.



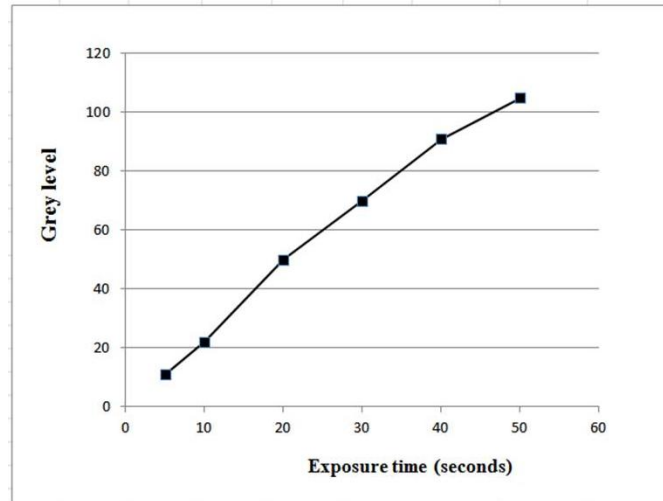


Figure 5 Grey levels of the image at ISO 200 with different exposure times obtained from exposure to gamma-rays from 70 Ci Se-75 at 40 cm

The system was finally tested with 2 specimens containing defects including 2 cm thick steel plate and 5 mm thick steel plate with a welding joint. The defects on the two images could not be seen for both Se-75 and Ir-192 sources as illustrated in figure 6 and 7. However, the images showed different grey level for parts of the specimens having different thicknesses. The system was therefore tested for inspection of specimens containing objects and foreign materials inside including parcel containing various objects, steel pipe containing stones and soil and concrete block with a steel bar at its center. The objects and foreign materials inside the three specimens could be clearly observed for both gamma-ray sources as illustrated in figure 8 - 10. Figure 11 shows an anaglyph image obtained from combination of two images of the paper parcel taken at different positions 6 cm apart. The three dimensional effect can be viewed with red-cyan eye glasses.

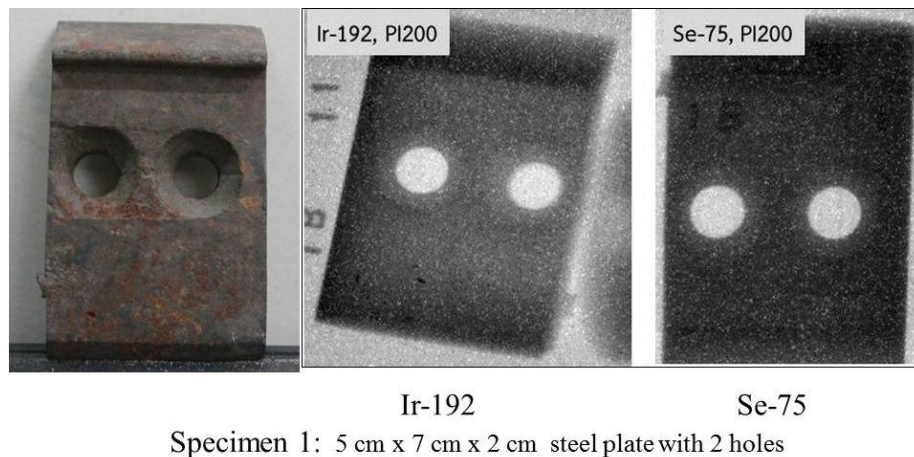
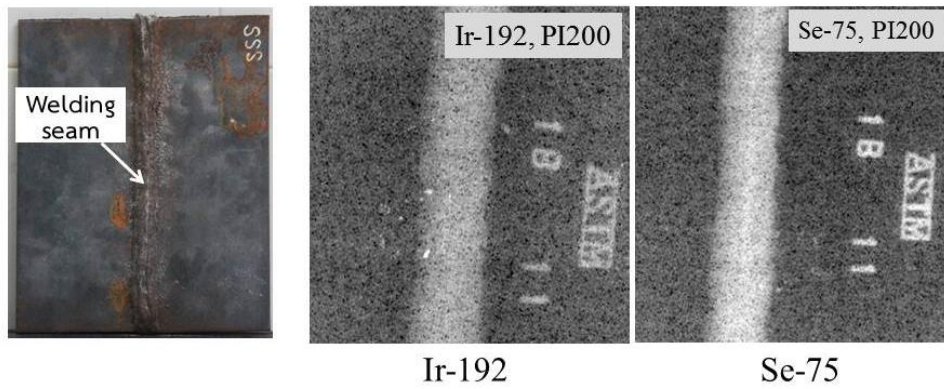
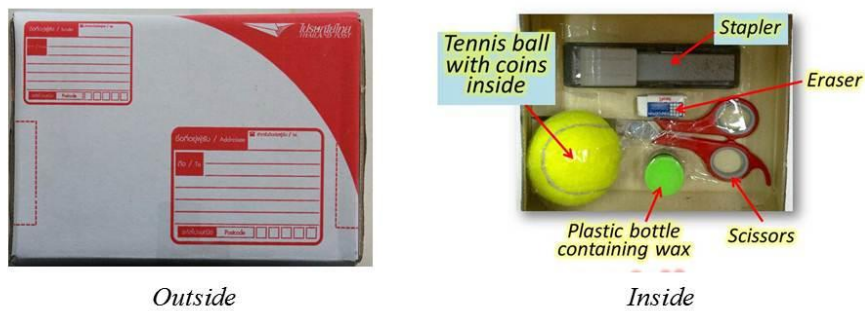


Figure 6 Defective steel plate having 2 holes and images obtained from Se-75 and Ir-192 sources



Specimen 2: 20 cm x 24 cm x 0.5 cm steel plate with welded joint

Figure 7 Steel plate having defective welded seam and images obtained from Se-75 and Ir-192 sources



Specimen 3: 14 cm x 20 cm x 8 cm paper parcel

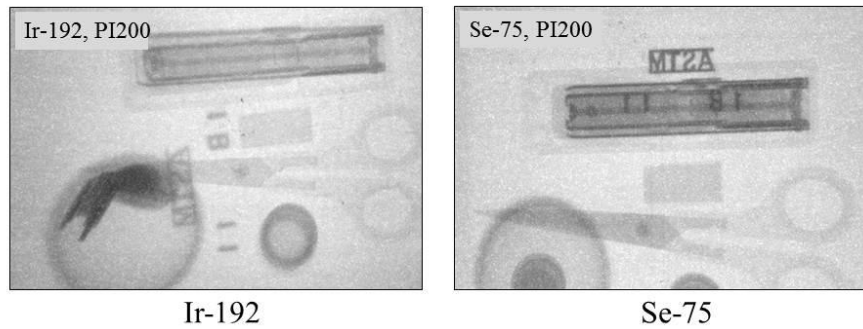


Figure 8 Paper parcel containing various objects and images obtained from Se-75 and Ir-192 sources

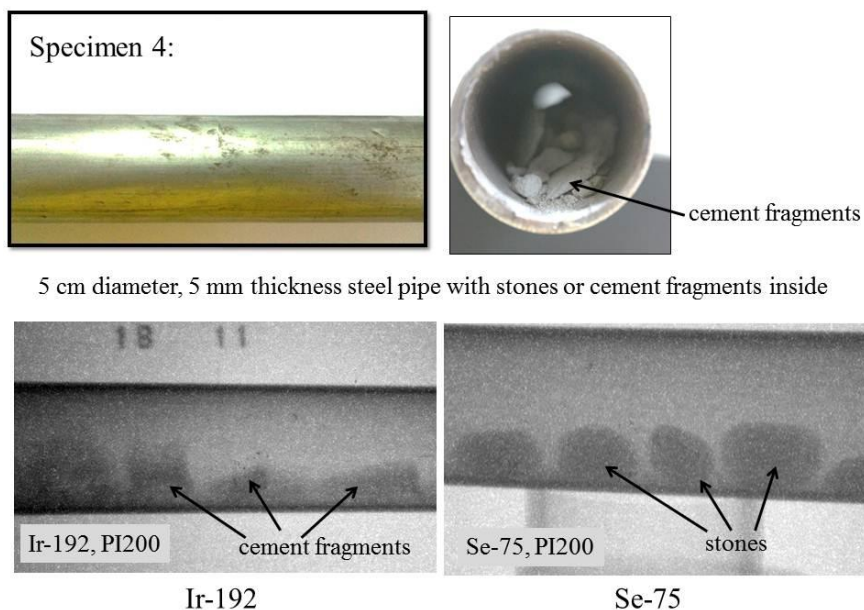
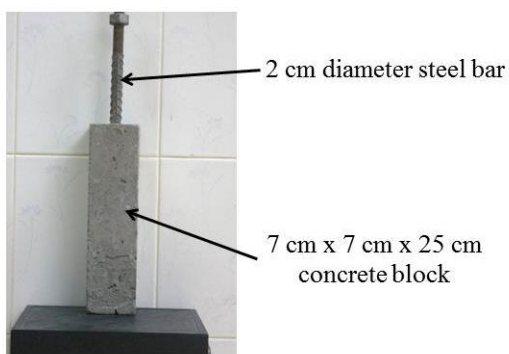


Figure 9 Steel pipe containing stones or cement fragments and images obtained from Se-75 and Ir-192 sources



Specimen 5: Concrete block with a steel bar at its center

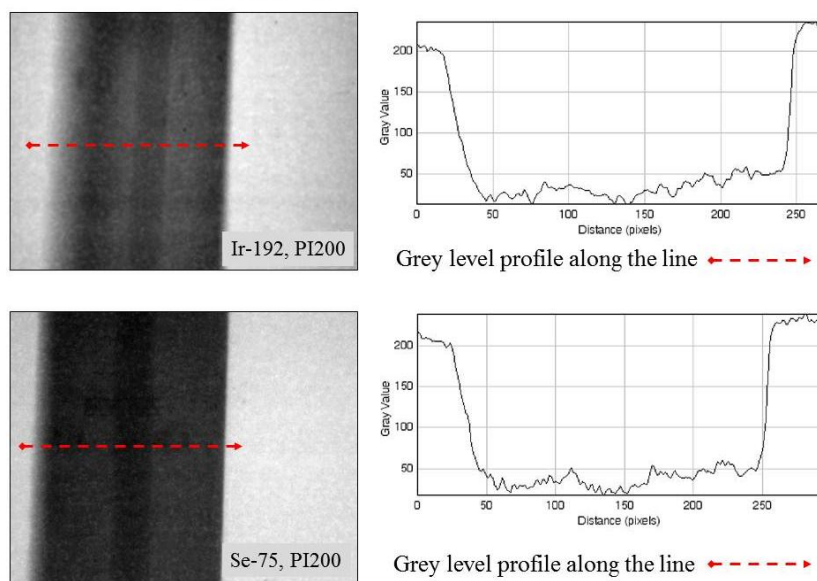


Figure 10 Concrete block with steel bar at its center and images obtained from Se-75 and Ir-192 sources

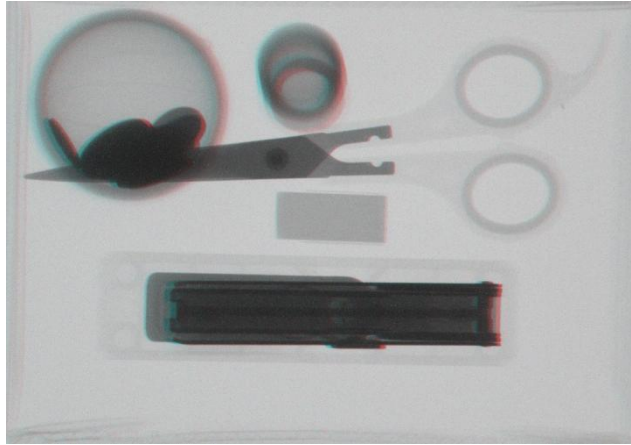


Figure 11 Red-cyan anaglyph image of the paper parcel containing various objects

## CONCLUSIONS AND DISCUSSIONS

This research showed that the Kyokko PI200 fluorescent screen could be used for high energy gamma-ray fluoroscopy particularly with the most common industrial radiography sources i.e. Se-75 and Ir-192. The method employed for viewing the image on the fluorescent screen is also appropriate. The modern digital cameras are extremely light sensitive. They allow users to control as well as to set parameters from a microcomputer via USB port. The obtained image can be displayed on microcomputer screen within seconds with no need for chemicals as in film processing. The developed system is simple, economical and applicable for inspection of specimen but the image quality is still not good enough to reveal small defects. However, the developed system can still be improved and redesigned for using on site. Size and weight of the light-tight box can be reduced significantly if required by using lens with shorter focal length and/or smaller fluorescent screen depending on size of the specimen. The anaglyph image makes 3D viewing effect easy and convenient for routine inspection of specimens but still needs further improvement.

## REFERENCES

1. ASTM. *Radiography and Radiation Testing*. Vol 3, 2nd ed. (Nondestructive Testing Handbook), American Society for Nondestructive Testing, 1985.
2. R. Funklin. *Application of Neutron Radiography Using Neutron Imaging Plate for inspection of Ancient Objects*. Master Thesis, Department of Nuclear Technology, Graduate School, Chulalongkorn University, 2009.
3. T. Yantapla. *Development of Microfocus Radiographic Technique Using Imaging Plate*. Master Thesis, Department of Nuclear Technology, Graduate School, Chulalongkorn University, 2009.
4. <http://www.mcc-phosphor.com/english/products/x-ray/fluorescent/>. (accessed on January, 2013).

## Damage Classification in CFRP Laminates Using the NDT/E Approach

<sup>a1</sup>M.T.H.Sultan, <sup>b</sup>A.S.M.Rafie, <sup>c</sup>N.Yidris,  
<sup>d</sup>F.Mustapha and <sup>e</sup>R.Zahari

<sup>a</sup>Department of Aerospace Engineering, Faculty of Engineering  
Universiti Putra Malaysia, 43400 UPM Serdang  
Selangor Darul Ehsan

<sup>a1</sup>thariq@eng.upm.edu.my, <sup>b</sup>shakrine@eng.upm.edu.my,  
<sup>c</sup>nyidris@eng.upm.edu.my, <sup>d</sup>faizal@eng.upm.edu.my,  
<sup>e</sup>rizal@eng.upm.edu.my

Keywords: Nondestructive, Destructive, X-Ray Radiography, SEM Fractography, Low Velocity Impact (LVI)

**Abstract.** There are two main factors that need to be considered as important parameters that affect the response of a structure: kinetic energy ( $E = \frac{1}{2}mv^2$ ) and potential energy ( $E = mgh$ ). For instance, if one has a large mass but with lower height, the amount of damage produced on the structure may not be the same as if one has a smaller mass with a higher dropping height although the potential energies will be the same. Therefore, before performing tests on the structures, the selection for the appropriate test apparatus and test procedures must be made carefully to ensure that the test conditions are similar to the actual impact conditions. In this current work, a study was conducted to fully understand the damage progression and growth, not only should the impacted surface be evaluated, but also the cross sectional defects on the impacted area must be accurately identified and examined. In this current work, the impacted test specimens will be observed at different magnifications to distinguish the types of failure mechanisms using Scanning Electron Microscopy (SEM). To perform this, the impacted specimens will be examined by two different approaches: surface defects and cross-sectional defects. This allows the failure mechanism to be observed more precisely.

### Introduction

Currently, researchers are working on two different types of tests to imitate the actual situations under controlled conditions. To stimulate in-service conditions (debris flying and hitting the aircraft during take-off and landing) in the aircraft, an instrumented high-speed gas gun can be used. This gas gun uses compressed gasses (usually nitrogen) as its driving propulsion power. Fundamentally the gun applies Newton's law of motion to describe the projectile motion in a barrel [1]. The gas gun consists of five major parts: the pressure reservoir unit, the firing mechanism unit, the launching unit, the catch chamber and the velocity measurement. The overall schematic view of the instrumented gas gun is shown in Figure 1.

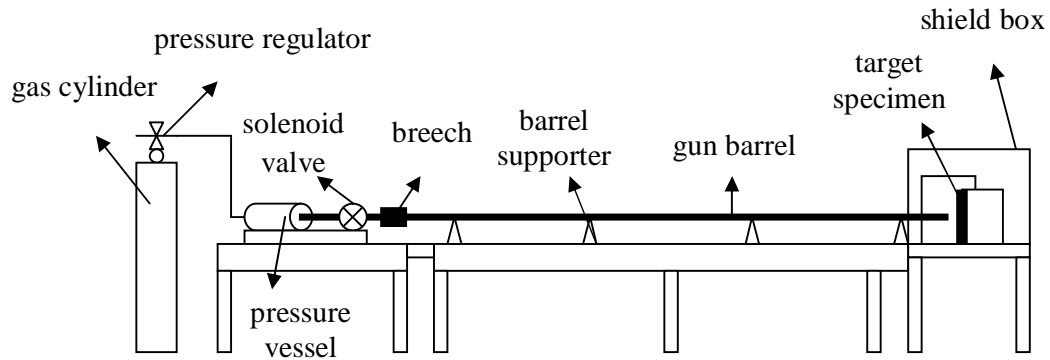


Fig. 1: Schematic view of the instrumented gas gun.

For situations such as the dropping of hand tools during maintenance work, the best apparatus that can be used to stimulate this situation is the instrumented drop test rig. These drop weight testers have been used quite widely and can be of various designs for a variety of applications [2-3]. For applications where heavy impactors are used, the impactors are usually guided by a rail during their free fall from a given height. The impactor consists of three main components: a dropping crosshead, an impactor rod, and an impactor nose. The impactor nose can take on different shapes (hemispherical, conical and blunt) depending on their applications. The schematic view of the free fall drop test rig is shown in Figure 2.

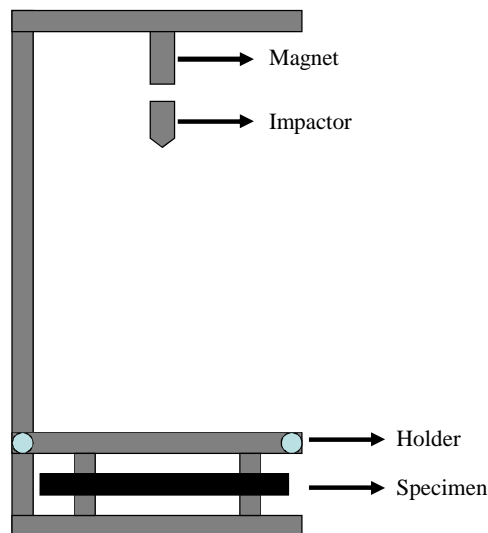


Fig. 2: Schematic view of the free fall instrumented drop test rig.



Instrumented drop towers can be divided into two categories: small towers (which perform up to 250 J) and large towers (which have the capacity of delivering impacts up to 2000 J). Choosing a suitable combination of cross-head mass and drop height plays an important role in determining the impact energy to perform the impact test for both small and large towers [4]. To date, there is still no American Society for Testing and Materials (ASTM) standard for impact test methods with composite materials, which has resulted in arguments and debates amongst the composites community [5].

This current work discusses experimental results for low velocity impacts in structures made from woven carbon fiber reinforced polymer (CFRP) prepreg plates of different layer thicknesses, under varying impact energy levels. The main objective of this study was to perform a series of low energy impacts in CFRP composites, and then to carry out a sequence of SEM investigations to evaluate the failure modes. To perform this SEM investigation, the impacted specimens will be examined by two different approaches: surface defects and cross-sectional defects. This allows the failure mechanism to be observed more precisely.

### **Methodology and Experimental Set Up**

The composite material chosen for the research reported here is a woven Carbon Fibre Reinforced Polymer (CFRP) prepreg manufactured by ACG (Advanced Composite Group). The type of material used was MTM resin systems (42%RW) with CF2900 fabric (280 g/m<sup>2</sup>, 12K and 2 × 2 twill fabric). The composite plate was fabricated by a hand lay-up method and the curing processes used a standard vacuum-bagging procedure with the application of elevated temperature and pressure in an autoclave (cured for 30 minutes at 120°C at 5.8 bar). Nominal size of the test specimens was 250 mm long and 150 mm wide. PZT sensors of type Sonox P5 were placed at three different positions of the test specimens in order to record the responses from the impact event. A total of 32 plates were used to perform the damaging tests at 22 different energy levels for the 12-layers specimen. The impact energies for the 12-layers specimens were set to range from 0.37 J to 41.72 J. The remaining 10 plates were used to check the repeatability of the test by carrying out further tests at four selected energies (three tests each at 41.72 J and 20.86 J and two tests each at 31.29 J and 10.43 J). For 11-layers and 13-layers, 4 plates were used to perform the impact test at four different energy levels (41.72 J, 31.29 J, 20.86 J and 10.43 J).

A standard drop-weight impact-testing rig was used to induce low-velocity impact damage in CFRP laminates. The overall features of the testing apparatus are as shown in Figure 3. This testing apparatus consists of a large platform equipped with an instrumented impactor that is movable in both the x and y directions that allows for varying locations of impacts to be carried out. This instrumented impactor was allowed to fall from a determined height guided by a rail to strike onto the test specimen clamped horizontally on both sides. The impactor was a hemispherical steel cylinder of Young's modulus equal to 210 GPa.



This impactor was controlled electro-magnetically during the test whilst a simple mechanical catching system was designed to prevent multiple impacts on the test specimen. The required impact energy was attained by selecting an appropriate combination of impactor mass and drop height. For example, an impactor of total mass  $m = 2.25$  kg was raised to a height,  $h = 1.89$  m to perform an impact of 41.72 J. A series of impact tests (energies ranging from 0.37 J to 41.72 J) were performed in order to introduce damage into the specimen. Similar tests were performed on different sample thicknesses to achieve different contact force histories and responses.

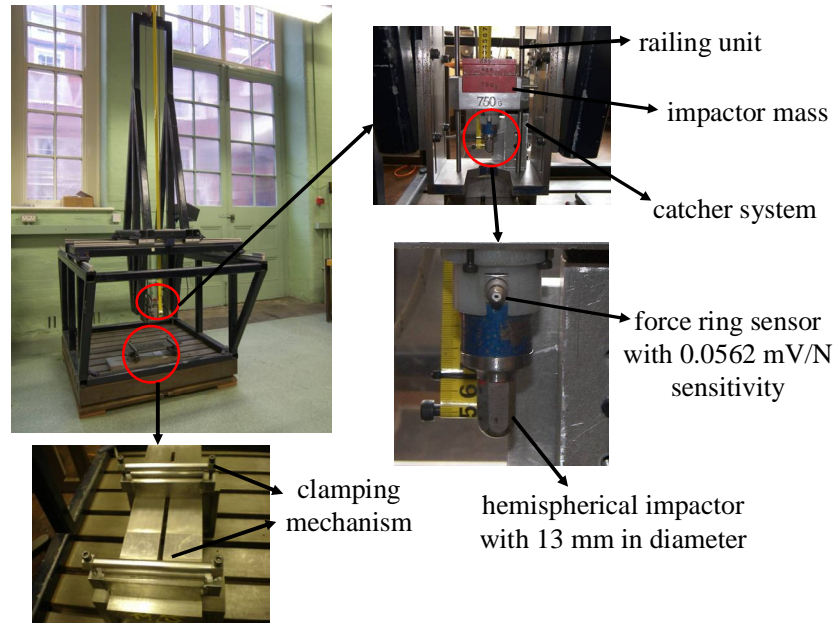


Fig. 3: Drop test machine.

The impacted plate specimens were then examined using two different types of NDT approaches, namely X-ray radiography and SEM fractography. From the SEM fractography, two different types of damages were observed. The first observation was on the surface defects of the impacted samples whilst the second type, usually categorised as destructive testing, visualised the cross-sectional defects to look at the internal damages. Cross-sectional fractography involves the process of sectioning the defected zone in a sufficient number of small sections at different impacted locations to look at the failure modes as shown in Figure 4. The SEM was used to capture a series of microscopical images in the thin sections. These images were then used to visualise the progression and growth of the damages.

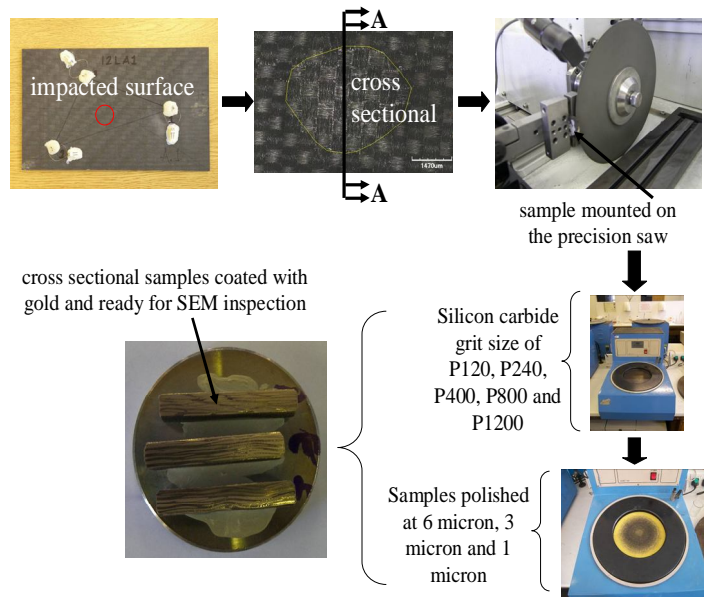


Fig. 4: Entire process of sectioning the defected zone.

## Test Results

Results obtained from the PZT sensors will not be discussed here since they have been previously published elsewhere; readers can consult [6] for details. In addition, results from a wavelet-based approach for feature extraction and the statistical approach for damage detections have been completed [7-9]. Discussed in this current paper are results obtained from SEM fractographs using varying impact energies. The damage observed in this study can be categorised according to three different energy levels. Matrix cracking or breakage was identified at impact energies below 20.86 J, interlaminar delamination was seen at impact energies between 20.86 J and 31.29 J, whilst fibre cracking and breakage was identified at impact energies above 31.29 J.

Results from the SEM micrograph images allow the identification of three critical impact energy thresholds. The first threshold is for the onset of matrix cracking and breakage and was identified at the impact energy of 20.86 J. For fibre cracking the threshold was identified as between 20.86 J and 31.29 J. Finally, the third threshold for most of the damages was distinguished above 31.29 J. The overall failure modes observed from all the specimens are collected and presented in Table 1. A simple nomenclature was defined to identify the types of failure mode. The labels MC, MB, FC and FB were associated accordingly with matrix cracking, matrix breakage, fibre cracking and fibre breakage, whilst the labels 1 and 0 indicate that the failure mode was 'observed' or 'not observed' respectively.

Table 1: Progression of failure modes for all the specimens.

Impact Energy (J)	Specimen Classifier											
	11 Layers				12 Layers				12 Layers			
	MC	MB	FC	FB	MC	MB	FC	FB	MC	MB	FC	FB
41.72	1	1	1	1	1	1	1	1	1	1	1	1
39.11					1	1	1	1				
36.50					1	1	1	1				
33.89					1	1	1	1				
31.29	1	1	1	1	1	1	1	1	1	1	1	1
28.68					1	1	1	0				
26.07					1	1	1	0				
23.47					1	1	1	0				
20.86	1	1	1	0	1	1	0	0	1	1	0	0
18.25					1	1	0	0				
15.64					1	1	0	0				
13.04					1	1	0	0				
10.43	1	1	0	0	1	1	0	0	1	1	0	0
7.82					1	1	0	0				
5.21					1	1	0	0				
2.60					1	1	0	0				

Table 2 shows the crack length measured along the crack line for the specimens. It was observed that as the amount of impact energy increased, the length of crack measured also increased. It was also found that as the number of layers increased, the length of crack decreased. This supports the hypothesis that the more layers the sample has, the more energy it can absorb with less resulting damage. As a result, the crack length measured for 13 layers has a lower value compared to 11 and 12 layers.

Table 2: Measured crack length for all the specimens.

Impact Energy (J)	Crack Length (mm)		
	11 Layers	12 Layers	13 Layers
41.72	0.5	0.4	0.25
31.29	0.34	0.2	0.15
20.86	0.21	0.13	0.1
10.43	-	-	-

By simply inspecting the cross-sectional defects in the damaged area, more information about the damage caused to this material can be retrieved. Three types of damage were observed in the cross-sectional defect images, they were: interfacial micro-cracking, parallel cracks and a single catastrophic crack. Figure 5 shows the overall results of the tests conducted. The results from the bubble chart reveal that a lower number of layers moves one toward the higher damage area, and that these are shifted in an almost parallel fashion. This is due to the fact that, as the number of layers decreased, the size of damage area increased.

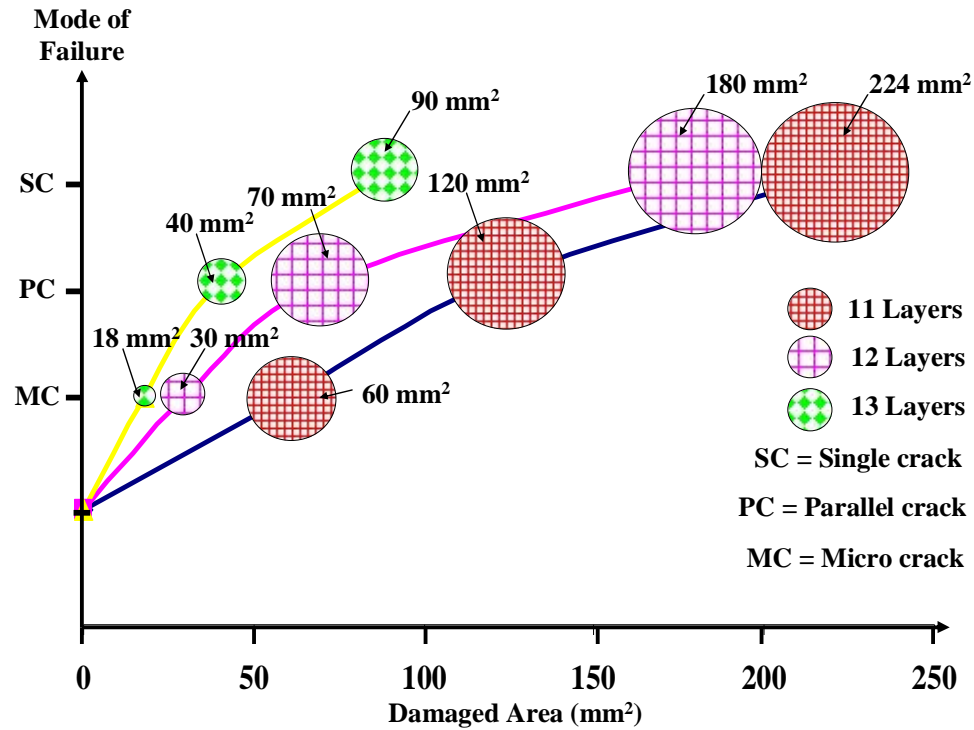


Fig. 5: Overall results of the test in term of damaged area.

## Conclusion

The failure analysis using SEM images produce a better understanding of the damage mechanisms. For this work, micrograph images were captured at different magnifications, which allow one to look at the failure modes more precisely. To understand the damage initiation and growth, it is very important to know the correlation between the failure modes and the contact force recorded. In the work conducted here, it could be concluded that damage will first initiate in the form of interfacial micro-cracking; this was observed at impact energies of less than 20.86 J. Parallel cracks (in the perpendicular direction) will follow in the next stage; this can be detected at impact energies between 20.86 J and 31.29 J. Due to the effect of impact parameters, such as large contact force, these parallel cracks can join and produce a single catastrophic crack. This was found at impact energies above 31.29 J.

## Acknowledgement

This work is supported by University Putra Malaysia under RUGS Grant (Initiative 5), No. 9313100.

## References

1. A.J. Stilp, and V. Hohler. *Experimental methods for terminal ballistics and impact physics. High Velocity Impact Dynamics*. John Wiley & Sons Inc., 1990.
2. D. Ambur, C. Prasad, and W. Waters. A dropped-weight apparatus for low-speed impact testing of composite structures. *Experimental Mechanics*, 1995, 35(1), 77-82.
3. W.J. Cantwell, and J. Morton. Impact perforation of carbon fibre reinforced plastic. *Composites Science and Technology*, 1990, 38(2), 119-141.
4. R.W. Rydin, M.B. Bushman, and V.M. Karbhari. The influence of velocity in low-velocity impact testing of composites using the drop weight impact tower. *Journal of Reinforced Plastics and Composites*, 1995, 14(2), 113-127.
5. M.C. Cheres, and S. McMichael. Instrumented impact test data interpretation. *ASTM STP 936*, 1987, 9-23.
6. M.T.H. Sultan, K. Worden, W.J. Staszewski, S.G. Pierce, J.M. Dulieu-Barton and A. Hodzic. 2009. Impact damage detection and quantification in CFRP laminates; a precursor to machine learning. Proceedings of 7<sup>th</sup> International Workshop on Structural Health Monitoring, Palo Alto, CA.
7. M.T.H. Sultan, W.J. Staszewski and K. Worden. 2010. Wavelet Feature Extraction for Impact Damage Analysis for CFRP Laminates. Proceedings of 10<sup>th</sup> International Conference on Recent Advances in Structural Dynamics, Southampton, UK.
8. M.T.H. Sultan, K. Worden, J.M. Dulieu-Barton, W.J. Staszewski, A. Hodzic and S.G. Pierce. 2009. Identification of impact damage in CFRP laminates using the NDT approach. Proceedings of AEROTECH III, Kuala Lumpur, Malaysia.
9. M.T.H. Sultan, A. Hodzic, W.J. Staszewski and K. Worden. 2010. A SEM-Based Study of Structural Impact Damage. Proceedings of 7<sup>th</sup> BSSM International Conference on Advances in Experimental Mechanics, Liverpool, UK.

## Improved Direct Assessment Technique for External Corrosion on Pipelines using a 3D Laser System

Pierre-Hugues ALLARD, Jean-Simon FRASER, Carl MERCIER, Patrice PARENT

CREAFORM

5825 rue St-Georges, Lévis (QC), Canada, G6V 4L2; Phone: (418) 833-4446

e-mail: [pierre-hugues.allard@creaform3d.com](mailto:pierre-hugues.allard@creaform3d.com), [jean-simon.fraser@creaform3d.com](mailto:jean-simon.fraser@creaform3d.com),  
[carl.mercier@creaform3d.com](mailto:carl.mercier@creaform3d.com), [patrice.parent@creaform3d.com](mailto:patrice.parent@creaform3d.com)

### ABSTRACT

This paper presents a new 3D laser inspection technique for pipeline external corrosion assessment. Pipeline operators worldwide are increasing their inspection standards for pipeline integrity as they are getting pressure from regulatory authorities to ensure safe operation of their pipeline networks. The industry is constantly looking out for more efficient inspection methods to replace traditional NDT techniques such as pit gage and ultrasonic thickness gages. The proposed inspection solution is comprised of a 3D laser scanner, code compliant fully integrated software, and a rugged field-pack to optimize deployment in the field. We will illustrate how the latest 3D optical innovations support the need for improved data quality, inspection speed, repeatability and on-site report generation for this application. A dynamic referencing system by scanner design compensates for any pipeline movement or vibrations to obtain repeatable metal loss measurements. Typical encoders requiring mechanical attachments to the scanned object are replaced by a contactless 3D positioning system using triangulation. Demonstration of the system capacities applied to pipeline integrity will be discussed.

**Key Words:** 3D, laser, scanner, optical, NDT, metrology, pipeline integrity, corrosion, mechanical damage, burst pressure, ASME B31G

### 1. Introduction

Pipeline operators have to inspect their pipeline network directly or through NDT inspection service companies. In-line inspection (ILI) tools allow the identification of zones with critical external corrosion by magnetic flux leakage (MFL) or ultrasonic (UT) methods. The code specifies that a prove-up from the outside of the pipeline is required for critical zones, often requiring excavation. Various techniques can be used for external corrosion assessment to identify appropriate remediation. Each technique presents certain limitations which can be minimized or avoided with the latest 3D optical innovations coming from dimensional metrology and now applied to NDT applications.

A manual measurement method using pit gauges makes the inspection operator dependant, brings variable results, a lengthy inspection process considering the high number of data points required, and limited report quality.

UT methods require constant water coupling which becomes difficult on rough surfaces due to water loss. The thickness reading is also greatly affected by any probe misalignment to the surface. Precision is limited by the front wall echo interface. UT probes must be positioned with a mechanical scanner complying with different pipe diameters, adding complexity while reducing portability. Furthermore,

the small size of a UT probe for a full coverage C-Scan requires high speed displacement for reasonable inspection time. This method is more suited for internal corrosion considering a smooth external surface.

Conventional one-line laser systems eliminate the need for water coupling and offer a much larger coverage. Unfortunately, they also bring other limitations in portability caused by the mechanical fixture to hold the system as it rotates around the pipe. We also need to consider the system sensitivity to laser lift-off and its incapacity to compensate for vibrations which quickly impact measurement accuracy.

The latest innovations in 3D optical keep the advantages of the conventional laser method while solving most of its disadvantages. The EXAscan (1) shown on figure 1, patented and manufactured by Creaform (2), uses a dynamic referencing system which allows a light scanner design with small dimensions and a non-contact process. The 3D scan is perfectly scaled to be representative of the real geometry and allows easy external defect visualisation. The analysis software must be able to manage a large quantity of data to generate a report in minutes with comprehensive results to facilitate assessment.

This document presents how these issues can be addressed using a portable 3D laser scanner and appropriate analysis software. The scanning procedure will be described, followed by the demonstration of enhanced results through data quality, scanning speed and finally, reproducible results.

## 2. Scanning Procedure with a 3D Laser Scanner

### 2.1 Equipment

It is fairly simple to use a 3D laser scanner. Required material includes the 1 kg 3D scanner, a laptop computer with Pipecheck (3) software installed and a battery pack, all carried on-site with a special vest the inspector wears to perform the inspection. The equipment is shown in figure 2.



Figure 1: Portable 3D laser scanner

- (1) EXAscan: Product trademark property of Creaform
- (2) Creaform: Registered company under Creaform inc. in Canada
- (3) Pipecheck: Software trademark property of Creaform

### 2.2 Setup

The first step is to prepare the pipeline surface for the scan and calibrate the unit. As with all other inspection techniques, a sandblasted surface clean of dust and dirt will yield better results. The 3D scanner requires the use of reflective targets that are typically 6 mm diameter stickers or magnets applied randomly on the pipeline. The spacing between targets will be approximately 10 cm but varies depending on the pipe diameter.



## 2.3 Data Collection

The second step is to acquire the corroded area of interest on the pipeline outside diameter. Once the acquisition parameters are set, the inspector holds the scanner at approximately 25 cm from the pipe surface and pulls the trigger to start the acquisition. The scanner is manually moved along the pipe to paintbrush the area of interest. The inspector will look at the laptop screen to validate the scan coverage. The 3D file is saved in STL format.



Figure 2: On-site inspection with the 3D laser scanner solution

## 2.4 Analysis

The third step is the data analysis. The inspector enters the pipeline parameters and analysis criteria before calculation are launched based on the pipeline 3D scan file. These parameters are useful for burst pressure calculation and to apply interaction rules. A report is auto-generated in Excel format, ready for assessment to determine pipe remediation.

# 3. Improved Data Quality

## 3.1 Dynamic Referencing System

Dynamic referencing represents one of the most important innovations for pipeline external corrosion inspection with laser. Ensuring in-situ laser acquisitions with constant accuracy within specifications is a challenge that can be easily overcome by positioning the scanner spatial referential directly on the pipe, as shown in figure 2 and 6. Since the pipe and the spatial referential are linked together, they both move in a synchronised manner which compensates the pipe and scanner movements. On the other hand, a static measurement system will only achieve comparable results in a controlled lab environment.

### 3.2 Virtual Pit Gauge Method

The manual pit gauge inspection technique is the point of comparison for all other techniques developed for external corrosion analysis since the ASME B31G and equivalent code were written based on single point measurements in a grid pattern. The numerical method must therefore reproduce the manual method to obtain comparable depth measurements. The proposed analysis software uses a virtual pit gauge to simulate the physical contact between the pit gauge and the pipeline.

Depth measurement with laser requires a virtual reference surface to find the distance between the actual pipe topography and the nominal external surface. The construction of this pipe reference surface is essential to obtain meaningful results. One method consists in regressing a perfect cylinder feature aligned with the scanned pipe. However, this method does not compensate for any flatness, ovality or deformations affecting the real pipe geometry, as demonstrated by the light blue line across the scan on the left side of figure 3. The proposed method using a virtual pit gauge compensate for the pipe geometrical deviations with a best-fitted surface made from the unaffected areas around the corrosion, as shown on the right side of figure 3.

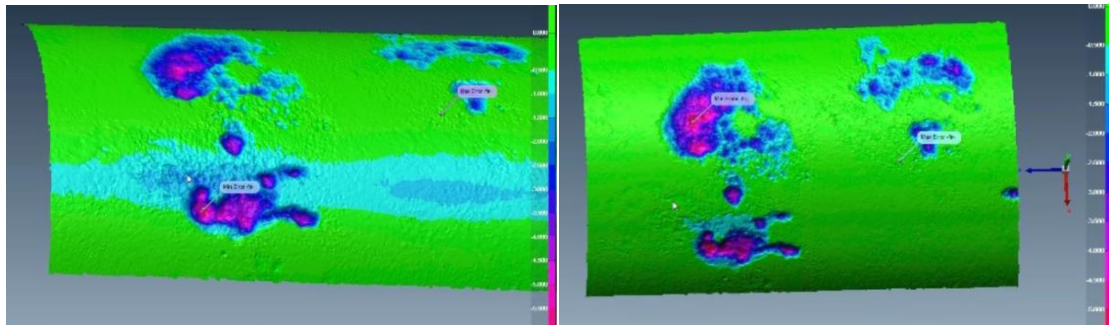


Figure 3: Cylindrical reference vs Virtual pit gauge reference surface

### 3.3 Repeatable Results

Corrosion depth measurements on a 8mm wall thickness pipe were taken using a virtual pit gauge analysis method. The data collection and the analysis were performed 3 times by 3 different inspectors. The variations between the scans were kept within +/-50 microns, regardless of the inspector who performed the scan and analysis.

**Table 1: 3D Scanner Repeatability**

		Position	1	2	3	4	5	6	7	8	9	10
Inspector 1	Scan 1	Depth (in)	0.032	0.032	0.036	0.036	0.034	0.040	0.039	0.053	0.049	0.056
	Scan 2	Depth (in)	0.032	0.032	0.037	0.035	0.035	0.040	0.039	0.054	0.048	0.056
	Scan 3	Depth (in)	0.032	0.033	0.035	0.035	0.033	0.039	0.038	0.055	0.049	0.055
		Δ Depth	0.000	0.001	0.002	0.001	0.002	0.001	0.001	0.002	0.001	0.001
Inspector 2	Scan 1	Depth (in)	0.032	0.032	0.038	0.035	0.033	0.038	0.039	0.051	0.046	0.053
	Scan 2	Depth (in)	0.031	0.033	0.037	0.036	0.032	0.038	0.038	0.053	0.045	0.054
	Scan 3	Depth (in)	0.031	0.032	0.036	0.035	0.033	0.039	0.040	0.051	0.047	0.054
		Δ Depth	0.001	0.001	0.002	0.001	0.001	0.001	0.002	0.002	0.002	0.001
Inspector 3	Scan 1	Depth (in)	0.033	0.035	0.038	0.036	0.033	0.038	0.037	0.052	0.045	0.053
	Scan 2	Depth (in)	0.034	0.034	0.037	0.038	0.035	0.038	0.037	0.052	0.045	0.055
	Scan 3	Depth (in)	0.033	0.034	0.038	0.037	0.035	0.039	0.039	0.054	0.047	0.055
		Δ Depth	0.001	0.001	0.001	0.002	0.002	0.001	0.002	0.002	0.002	0.002
Inspector 1		Max Depth	0.032	0.033	0.037	0.036	0.035	0.040	0.039	0.055	0.049	0.056
Inspector 2		Max Depth	0.032	0.033	0.038	0.036	0.033	0.039	0.040	0.053	0.047	0.054
Inspector 3		Max Depth	0.034	0.035	0.038	0.038	0.035	0.039	0.039	0.054	0.047	0.055
		Δ Max Depth	0.002	0.002	0.001	0.002	0.002	0.001	0.001	0.002	0.002	0.002

### 3.4 Auto-Generated Reports

Inspection results are available immediately after the analysis is done as shown in figure 4, and through an auto-generated report in Excel format shown in figure 5. Having both 2D and 3D representations of the corroded pipe ensures a clear visualization and understanding of the surface condition for the entire scan. A color scale helps to quantify the variations in corrosion deeper than a specified percentage of the nominal wall thickness. The analysis software will automatically find the deepest points to retrieve the most probable path of failure on the corrosion zone and apply an overlay on the 3D view. Each corrosion zone is analysed separately, according to the selected interaction rules, to obtain its position, maximum depth and burst pressure.

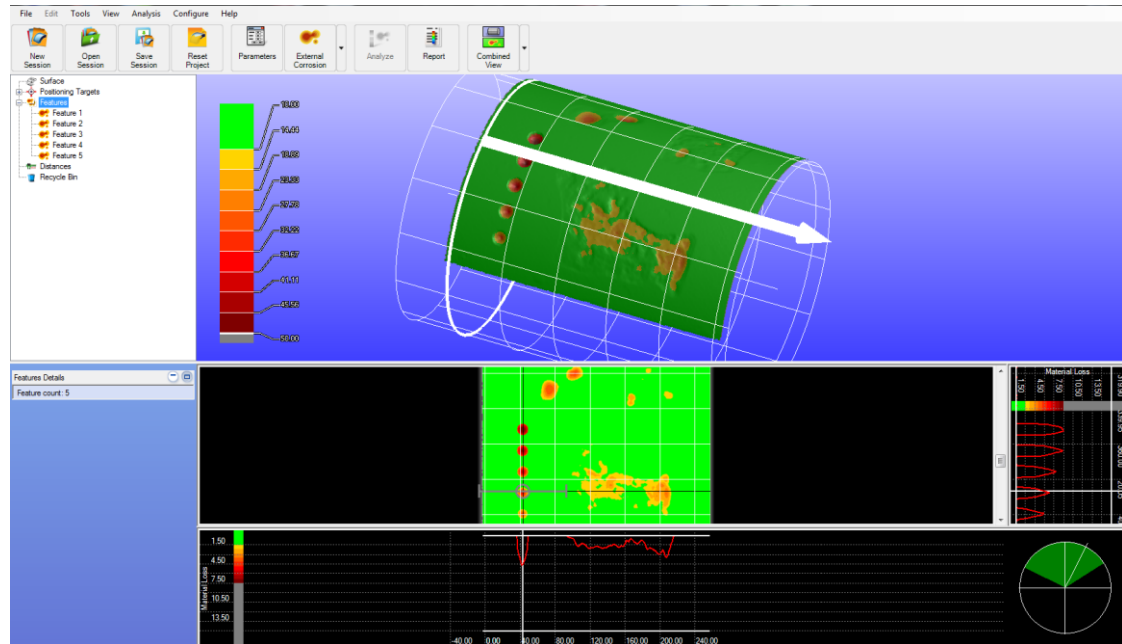


Figure 4: Analysis results in 2D and 3D after calculation

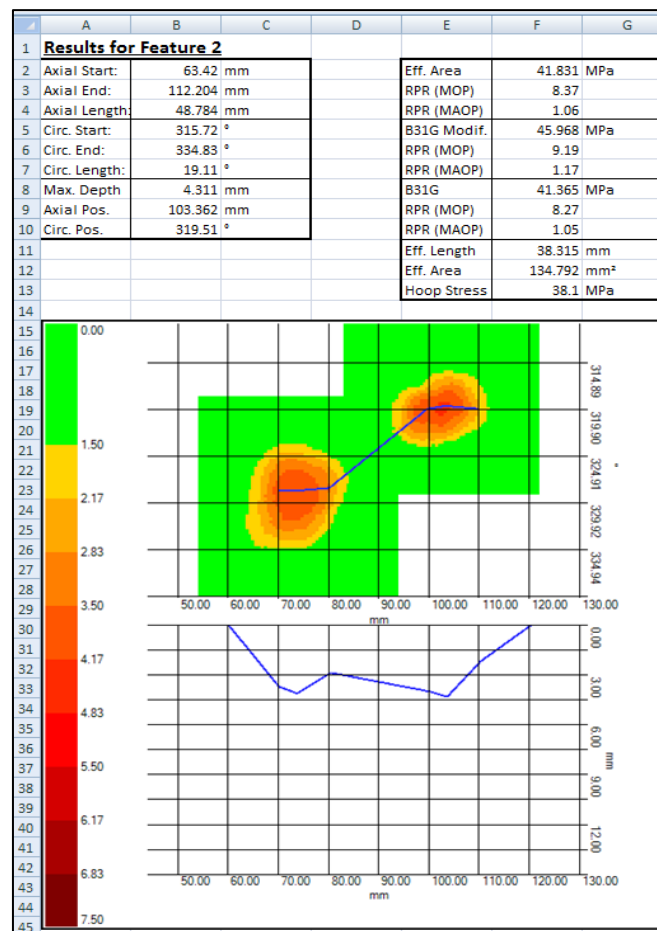


Figure 5: Auto-generated external corrosion report in Excel

#### 4. Inspection Speed

With an acquisition rate of 25 000 points per second, the scanned surface is reconstructed in real-time to form a 3D mesh file (.stl). The inspector can validate the data collection by looking at the laptop computer screen as shown in figure 6. It takes less than 10 minutes to scan 1m<sup>2</sup> at a 1.5 mm resolution. Running a complete analysis will take less than 30 seconds. One person alone is able to carry the system on-site and perform both the scan and the analysis.

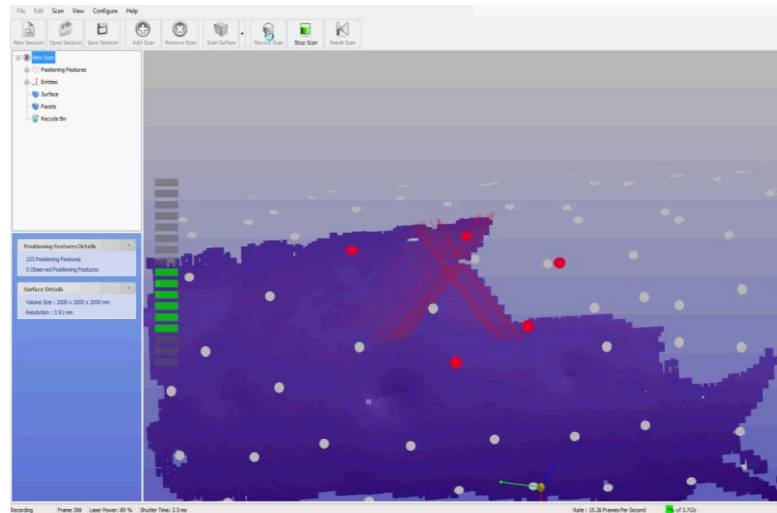
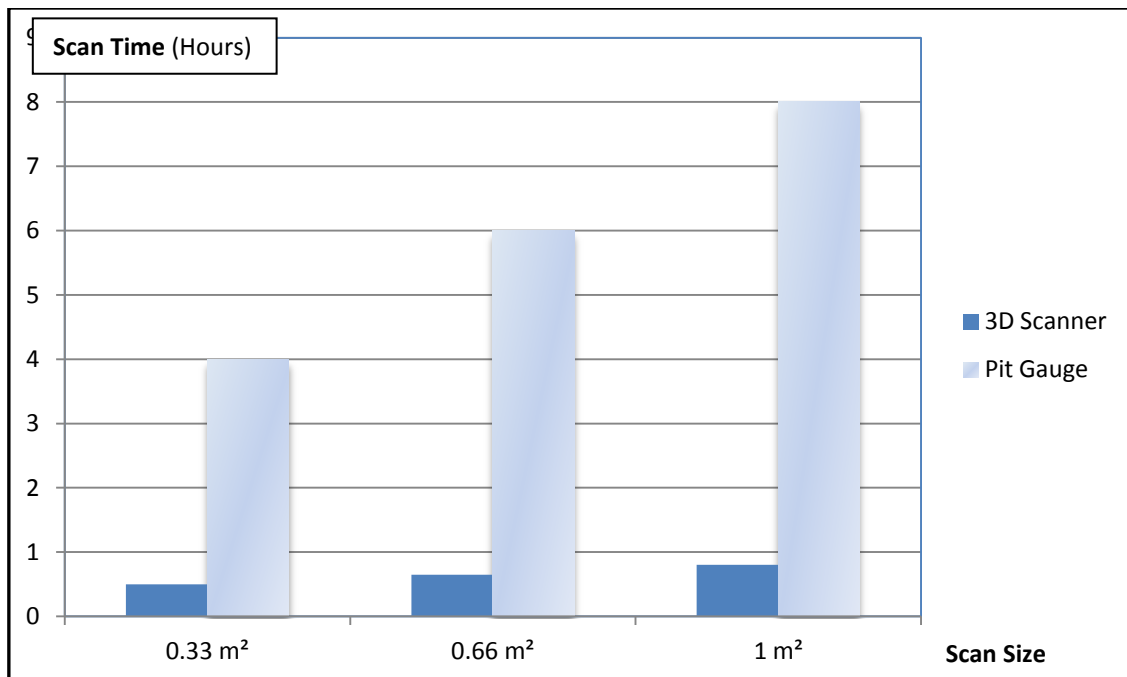


Figure 6: Data collection mode in Pipecheck

Graph 1 shows a scanning speed comparison between the pit gauge technique and the 3D laser scanner solution using a 10mm grid pattern. This trial takes into consideration setup, scan and analysis time. The larger the scan, the more advantageous it becomes to use the 3D laser solution. Therefore, using the 3D laser method for a large corrosion zone can reduce the inspection time by a factor of 10 and more.



Graph 1: Scan speed comparison

## 5. Repeatable Data Collection

This section explains the importance of various scanner and software features to ensure repeatable results, regardless of the environment and operator.

### 5.1 Positioning System

Reflective targets must be positioned on the pipe so the scanner can reference itself by triangulation with its binocular vision. The reflective targets are randomly positioned on the pipeline to create a unique pattern and also facilitate the setup, as shown on figure 7. If the same pipe surface is scanned twice with different target positioning, both scans will be the same, again to eliminate the operator skill factor.

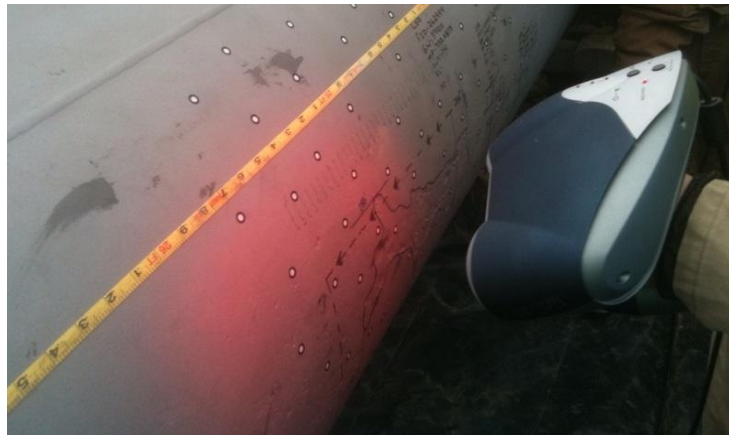


Figure 7: Reflective targets randomly positioned

Since data is not distorted from a scanner misalignment with the pipe, using 3D surface representation increases depth measurement accuracy. The 3D scanner allows scan angles up to 45 degrees in any direction and scanner orientation.

### 5.2 Focal Distance

Another important scanner feature to consider is the focal distance, considering optimal inspection can only be achieved within a certain distance range between the scanner and the pipe. Using a proximity indicator on both the software scanning window and scanner using LED, the inspector is kept informed at all time during acquisition. However, the system will automatically stop the data acquisition if the scanner is out of focus.

### 5.3 Surface Reconstruction

During the acquisition with the 3D laser scanner, a mesh surface file is updated in real-time to avoid computing point clouds. When data points are not linked together, it leaves the possibility of overlapping multiple points on the same location creating noise in the scan. Furthermore, merging point clouds generate deviations that can be avoided with a mesh file.

### 5.4 Automated Analysis

Data analysis follows the same approach to ensure repeatability with pre-programmed calculation and software operations. The inspector only needs to input the known pipeline parameters required for

burst pressure calculation and interaction rules in the table shown in figure 8. The analysis is based on ASME B31G code to comply with code and ensure best practices.

**Pipecheck - Parameters**

Analysis | SFlow | Pit Gauge | Color Map | Report - Overview | Report - Features

**Interaction Parameters**

Critical Factor: 10.00 % Method: Connecting Box

Threshold for Corroded Area: ☒ Use Critical Factor Value ☐ Other Value 0.00 %

Axial Criteria: 20.0 mm Circumferential Criteria: 20.0 mm

**Filter Features**

Filter Small Features: ☒ None ☐ Minimum Depth To Keep 20.00 %

Minimum Length To Keep: 10.00 mm

**Pressure**

MOP: 5.00 MPa MAOP: 39.37 MPa

**Worst Case Profile**

Resolution: 10.0 mm

Configuration: Official Demo Part \* Save Load OK Apply Cancel

Figure 8: Pipe parameters input table for data analysis

## 6. Conclusions

1. The portable 3D laser scanner solution discussed in this document is the logical evolution over traditional NDT techniques for pipeline external corrosion inspection.
2. The latest innovations in 3D laser scanning provide improved data quality using a unique dynamic referencing system and appropriate reference surface.
3. The inspection speed can be reduced by a factor of more than 10 times the pit gauge technique considering the time to setup, perform the inspection, and run the analysis to generate a report.
4. Repeatable results are ensured by the scanner design and auto-generated report within a +/- 50 microns accuracy.
5. This inspection procedure proves to reproduce the manual pit gage technique and follows code regulation.

## References

- 1) ASME B31G, Manual for Determining the Remaining Strength of Corroded Pipelines, American Society of Mechanical Engineer, 2009



# Application of a 3D Laser Inspection Method for Surface Corrosion on a Spherical Pressure Vessel

Pierre-Hugues ALLARD, Jean-Simon FRASER, Carl MERCIER, Patrice PARENT

CREAFORM

5825 rue St-Georges, Lévis (QC), Canada, G6V 4L2; Phone: (418) 833-4446

e-mail: [pierre-hugues.allard@creaform3d.com](mailto:pierre-hugues.allard@creaform3d.com), [jean-simon.fraser@creaform3d.com](mailto:jean-simon.fraser@creaform3d.com),  
[carl.mercier@creaform3d.com](mailto:carl.mercier@creaform3d.com), [patrice.parent@creaform3d.com](mailto:patrice.parent@creaform3d.com)

## ABSTRACT

Oil & Gas pressure components found on power plants and refineries must be inspected on a regular basis to ensure fitness-for-service. Corrosion is one of the most critical and recurrent degradation that must be inspected under API-579 code. Various non-destructive methods have been used to measure corrosion. A contact method is always problematic due to the deteriorated external surface. Encoding a scan is also a challenge, requiring mechanical scanners or fixture to fit the specific component geometry for referencing the defect position. 3D laser scanning is emerging as an efficient alternative for accurate surface degradation and offers the versatility needed to inspect various geometries with a same system. The analysis is performed using post-treatment software to generate all required measurements for assessment. This paper describes how metal loss can be measured from a 3D laser mesh file compared to a reference surface. Case study of a corroded spherical pressure vessel will be discussed.

**Key Words:** 3D laser scanner, NDT, fitness-for-service, pressure vessel, corrosion, API 579, depth measurement.

## 1. 3D laser system for surface inspection

The EXAscan, manufactured by Creaform, is a portable 3D laser scanner used to accurately map the surface of a free form object as seen in figure 1 and 2. A laser cross is projected on the surface while two cameras read the laser cross

profile to build a 3D scan file (mesh) in real time. The scanner is self-positioned by triangulation of randomly positioned reflective targets. This non-contact inspection technique eliminates the need to mechanically fix the scanner to the part being scanned for encoding.



Figure 1: EXAscan in the field with wireless tablet to visualise data



Figure 2: EXAscan 3D laser scanner

The concept of scanner accuracy and resolution must be clarified. The total accuracy of the system is the punctual accuracy in addition to the volumetric accuracy per meter of scan. The accuracy for a 3D laser scanner is defined as the maximum deviation in a spherical radius around the real point value. The volumetric accuracy is the stacking error per meter of linear scan induced by the positioning system or maximum cumulative errors of measurements over a distance. The term accuracy is intrinsic to the scanner design and is not related to the scan resolution for a 3D scanner. The data points in a mesh file are linked together to form an organized pattern of triangles of equal size. Each vertex has the specified accuracy. Resolution is a parameter input specified by the inspector to define the size of the triangles used to build a 3D mesh file. A typical mesh file of a corrosion scan is shown in figure 3.

The 3D laser scanner comes in replacement to the pit gage and ultrasonic probe techniques mainly because of the acquisition speed, the independence from inspector skills, and its 100% coverage of the corroded area instead of single point measurements in a grid pattern.

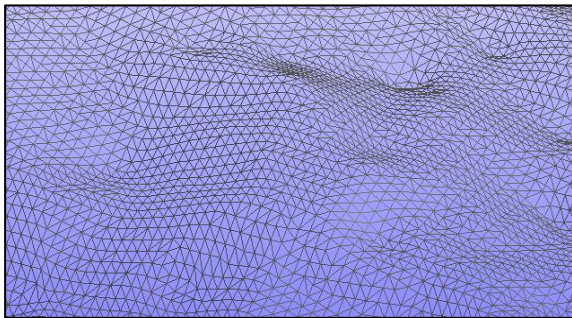


Figure 3: 3D mesh file in STL format

## 2. Analysis of 3D mesh files

The laser offers a complete coverage of the damaged area in 3D allowing any measurement to be taken from the outside surface. The raw data is a mesh file saved in STL file format in VxElements data collection software and is available for future assessments and audits.

In order to measure depth based corrosion from a mesh, a reference surface must be created to recreate a localized nominal surface

without corrosion. There are three ways to generate a nominal reference surface. The first one consists in comparing the scan to the original CAD model. However, the CAD model for components under maintenance is rarely available and can present deviations from the actual geometry. A second method is to create in post-treatment software a theoretical geometry approximating the object initial geometry. The third and most accurate method is to reconstruct a surface based on a free-form model best-fitted to the real component geometry.

The same technique can be used on various structure geometries such as cylindrical, conical or spherical pressure vessels, pipelines, and structural beams with flat surfaces. Pipecheck software should be used to improve efficiency on pipeline inspection.

## 3. External corrosion assessment on a spherical pressure vessel

### 3.1 Introduction

In order to evaluate fitness-for-service of a pressurized component, level-2 assessment is based on a series of depth measurements. Gathering a maximum number of data points with a 3D laser scanning will yield the best estimate of the real component condition, providing the analysis is performed properly.

This case study of external corrosion assessment on a 12.4m diameter spherical pressure vessel describes the different aspects to consider when analysing the data.



Figure 4: Spherical pressure vessel

### 3.2 Scan Procedure

The corroded area must be cleaned to obtain optimal results since the scanner will scan what it sees regardless of the material. Then, positioning targets are randomly placed around the corrosion pattern to allow 3D encoding of the scanner. Typical spacing between targets is approximately 10cm. The area of interest is scanned at 1mm resolution with the Handyscan3D to acquire 100% of the area of interest. A mesh file is created in VxElements and saved as STL file format. This file is imported in Polyworks post-treatment software to create the reference surface, take measurements and generate a report.



Figure 5: Corrosion at the bottom of pressure vessel

### 3.3 Creation of a reference surface using a perfect geometrical feature

The local scan area is used to fit a perfect sphere geometrical feature to serve as a reference surface. We need to choose the best geometry to represent the object. Figure 6 shows the fitted sphere is represented in grey.

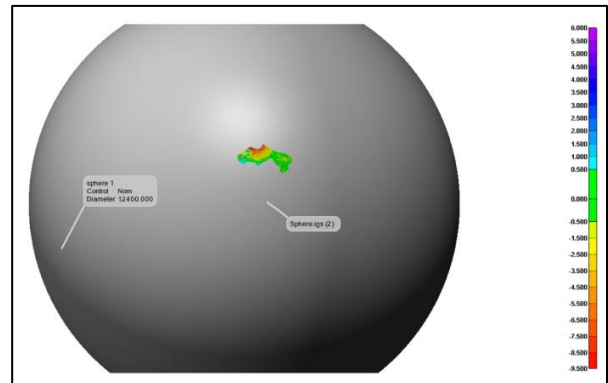


Figure 6: Spherical fit reference

The color map in figure 7 shows a change in curvature at the bottom of the vessel. The deviation from the perfect sphere is shown in red and orange color; green represents a good fit. It means using a perfect sphere is a good solution for most of the vessel but certain areas should be analysed separately for optimal results.

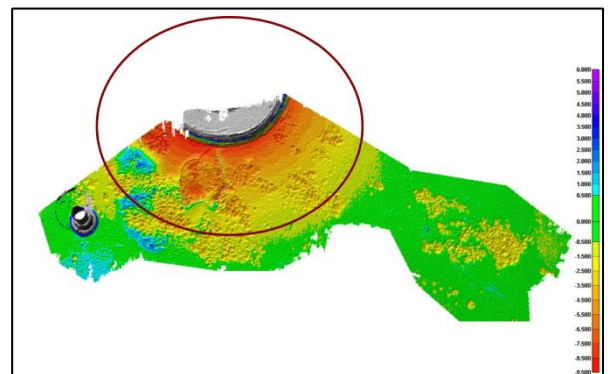


Figure 7: Comparison of 3D scan with spherical fit reference

### 3.4 Localized fit of a perfect geometrical feature

By fitting a spherical entity to a very small area manually selected around the corrosion, we are able to improve the fit locally to obtain more accurate results. With this method, we



need to reject all surfaces outside of the selection as shown in figure 8 and 9. This is an extreme case of an area less spherical than most of the vessel. Therefore, it is possible to quickly analyse corrosion with a perfect localized sphere even if the overall real shape is subject to slight mechanical deformations.

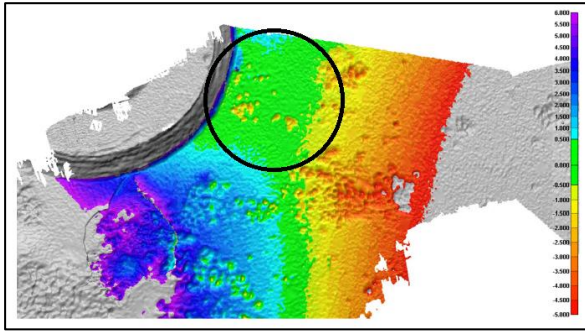


Figure 8: Localized spherical fit

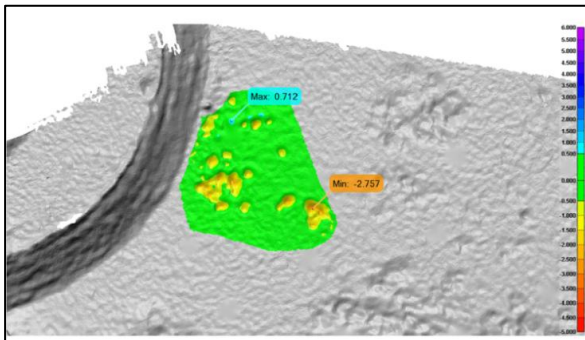


Figure 9: Corrosion analysis with localized fit method

### 3.5 Creation of a free-form model from the scanned geometry

A model following the scanned surface geometry can be created by applying NURBS patches to the surface. The model shown in figure 10 becomes a realistic CAD model representation in IGES file format which can be compared to the initial STL for depth measurements.

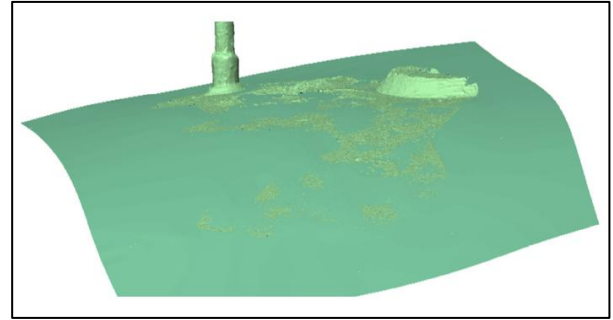


Figure 10: Spherical fit based on localized selection

A free-form model will compensate for geometric deviations such as out-of-roundness, flatness, bends, or any deviation from a theoretical geometry. A better fitted model means more accurate results due to compensation for surface deviations. A good fit is represented in green in figure 11. The warm colored indications represent corrosion based on the color scale which can be adapted according to a specific threshold or critical factor. The cold color indications help to identify positive material deviations on the surface such as paint bubbles and flaking. Paint should be removed from these areas before inspection for improved results.

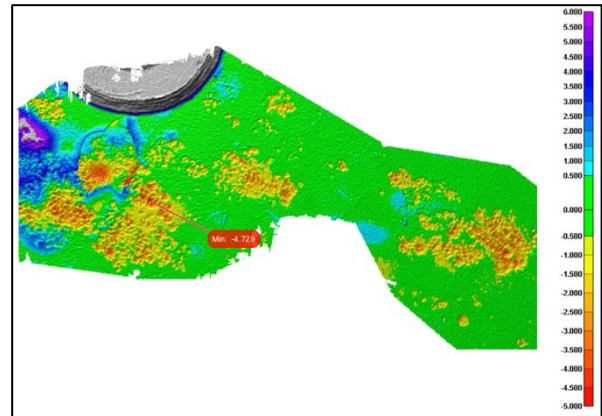


Figure 11: Reference surface using a free-form model

## 4. Measurements comparison

### 4.1 Comparison of a 3D color map maximum depth measurement with a pit gauge

A curved surface inspected with a real mechanical pit gauge will measure depth values smaller than 3D color map comparison generated from a spherical reference. The pit

gauge creates a straight edge from both side of the corrosion. Therefore, the larger the corrosion pit, the smallest the depth value will be if measured with a pit gauge sitting on un-corroded surface.

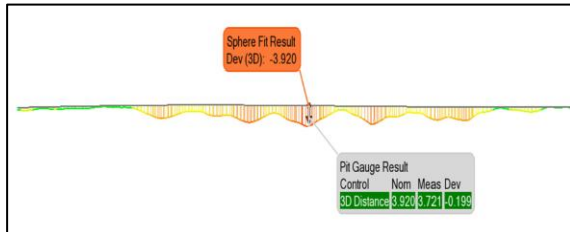


Figure 12: Maximum depth measurement with spherical fit

The maximum depth is automatically found for each corrosion feature. In this case, figure 12 shows the maximum depth is measured at 3.920mm using a spherical fit reference. A straight edge pit gauge measured 3.721mm for the same point, which represents 0.2mm (5%) less than a spherical fit. Hence, a spherical fit measurement will be more conservative than pit gauge. The pit gauge offset value is not predictable. It depends on the size of the damage area and the location of contact points.

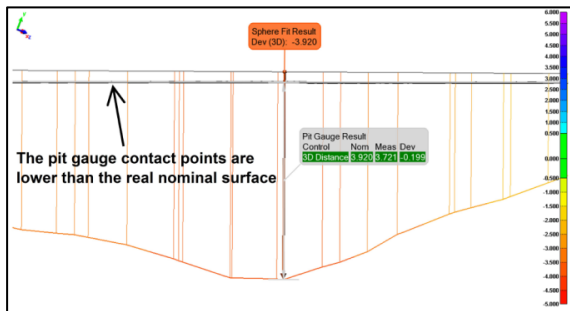


Figure 13: Maximum depth measurement with pit gauge

#### 4.2 Depth grid measurement

A grid pattern of a size determined by the inspector can overlay the 3D scan. In this case, a 10mm x 10mm grid is used for the analysis.

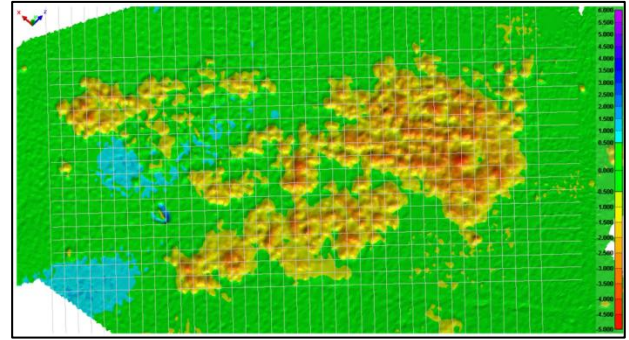


Figure 14: Grid overlay

The deepest point for each square grid is automatically found and can be exported in an Excel table. Estimated burst pressures can be calculated from this depth measurement table. A square grid contains a certain number of data points based on the resolution chosen for the scan as seen in figure 15. The software will calculate the depth of each point within the square grid boundaries and find the maximum value.

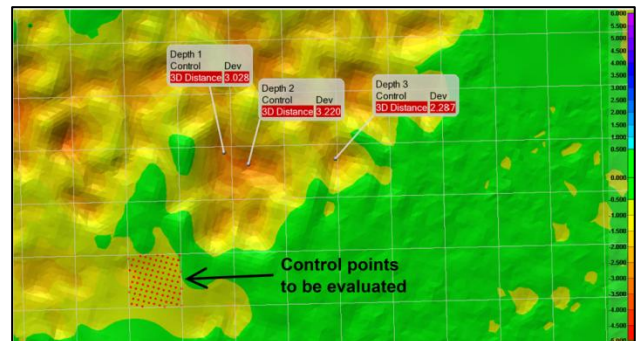


Figure 15: Square grid data points

#### 5. Conclusion

3D laser scanner technique proves to be a very efficient method for external corrosion assessment on pressurised components with the use of a reference surface compared to the 3D scan file.

Three methods exist to create a reference surface depending on the level of precision required: comparing to a CAD file, to a theoretical geometric feature, and a free-form best-fitted model. The level of precision is higher with a reference surface based on a free-form model because it compensates for surface variations to the ideal geometry.

Corrosion on a spherical pressure vessel was inspected based on API-579 level-2 procedure using the 3D laser technique. The pit gage was shown to be less conservative on a curved surface by 5%. A depth grid can be automatically created and exported in Excel to estimate burst pressures.

Many oil & gas components with various geometries such as pressure vessels and pipelines can be inspected with the same equipment because of the scanner design being non-contact and the software versatility.

## References

1. Martin Fingerhut, "Application of Laser Profilometry for Fitness-for-Service Assessment on Pressure Vessel External Corrosion", IPC 2012, September 24-28, Calgary, Canada.
2. Pierre-Hugues Allard, "Pipeline External Corrosion Analysis using a 3D Laser Scanner", 18<sup>th</sup> WCNDT, April 16-20 2012, Durban, South Africa.
3. American Petroleum Institute and the American Society of Mechanical Engineers, "Fitness-for-Service API 579/ASME FFS-1 (API 579 Second Edition)", API Publishing Services, 2007

## Video Endoscopic Metrology for Pipeline Welding

Alfred Ng

GE Measurement & Control, Inspection Technologies, [a.ng@ge.com](mailto:a.ng@ge.com)

### 1. Abstract

This paper addresses the upcoming requirement of welding inspection on the internal weld profiles of pipeline and manifold structures in oil and gas equipment industry. Pipeline and manifold structures are subject to high pressure subsea/deep sea environment. Inspecting critical welded joints are essential to ensure safety. However, the limited access and complex internal geometry are making it difficult to carry out inspection with existing metrological tools.

3D Phase Shifted Measurement (3DPM), the latest developments in industrial video endoscopy technology have enabled three-dimensional surface scanning of equipment internal spaces. The optical metrology technique has been adapted to the size restrictions of a six millimeter diameter videoprobe, to allow the 3D visualisation and measurement to be transferred to Remote Visual Inspection (RVI). With this capability, videoprobe can be used as a metrological tool for internal welding profile measurement.

### 2. Introduction

Welding is an essential manufacturing process particular for oil and gas equipment such as pipeline, drill pipe, well head and other manifold structures. With oil and gas exploration moving to subsea and even deep sea, the quality and reliability of weld are critical for the operation, safety and environment.

Non Destructive Testing (NDT) methods like Ultrasonic Testing (UT), Radiography Testing (RT), Eddy Current Testing (ET), and Penetrant Testing (PT) have been used extensively for welding inspection to identify cracking, porosity, incomplete penetration, misalignment, inclusions, lack of fusion and other welding defects. However, most of the testing are performed on the external surface of the weld. With UT and RT, indirectly, we could interpret the UT signals or RT images to have a limited understanding of the internal surface condition of weld such as penetration, undercut or concavity. Below is a List of weld features and specification typically required to be evaluated and measured:

- Root penetration shall not exceed 3 mm.
- Root concavity shall not exceed 1 mm smoothly merging.
- Misalignment shall not exceed 1 mm.
- Undercut shall not exceed 0.5 mm.
- Lack of penetration / fusion shall not be permitted.
- Cracks shall not be permitted.
- Burn through shall not be permitted.
- Surface breaking porosity within the root pass shall not be permitted.



Remote Visual Inspection equipment such as videoprobe is a solution that allows visual inspection of inaccessible area of equipment. Conventionally, videoprobe provides visual of internal welding defect and allows evaluation qualitatively (including decolourization). With the latest development, videoprobe is featured with three-dimensional surfacing scanning capability, it is now possible to view a full 3D map or point cloud of the inspected weld surface. It allows measurement of the weld such as root profile, undercut, mis-alignment and provides more precise information of the weld. With this capability, videoprobe can be used as a metrological tool for welding inspection.

### 3. Videoprobe Measurement Technology Development

For years, RVI Videoprobe development are focused on accessibility with smaller in probe diameter, longer in length, articulation and image quality with brighter illumination and CCD camera pixel resolution. Over time, the needs of inspection are getting more demanding. The interpretation of what was “seen” often depended on the inspector and experience. There is no objective way to quantify the defect observed. In fact, the measurement of flaws and discrepancies is as important as their detection and identification.

To have measurement capability, with only few millimeters in probe diameter, it was a challenge but several solutions nevertheless developed. In 1992, Welch-Allyn launched the first measurement technology “Shadow Measurement” on its VP2000 “Shadowprobe”. Shadow measurement (Fig. 1) relies on a shadow triangulation of tip-to-target distance. A shadow measurement tip projects a shadow line across an inspection image. The position of the shadow in the image is related to the distance from the tip to the object. With this information, the shadow measurement software can accurately calculate the size of defects. Shadow measurement accuracy depends on the distance from the videoprobe distal end to the object. Image sharpness and contrast is less important. The object plane must be perpendicular for some types of measurement and may be skewed for other types of measurements.

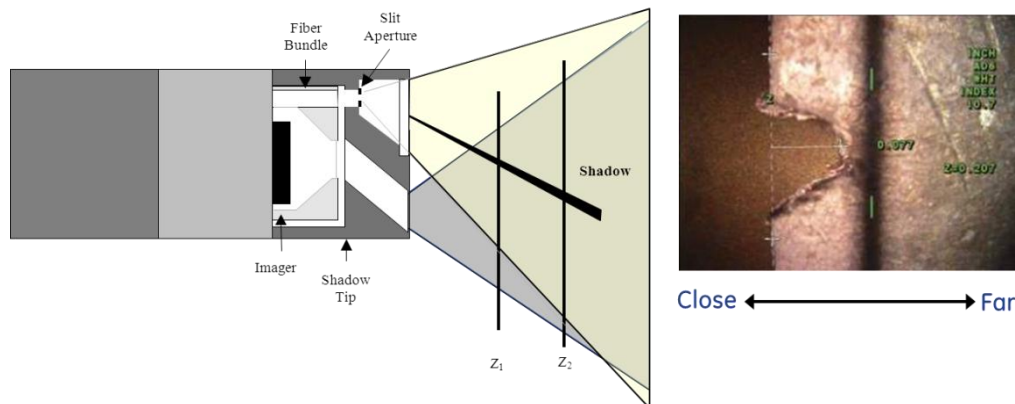


Figure 1: Diagram of a shadow measurement and corresponding image

In 2000, RVI equipment manufacturers came out a different method called Stereo Measurement (Fig. 2) based on the principle of Stereo vision. Using two prisms oriented in angles, the image captured by videoprobe camera is divided into left and right views. By knowing the angle separation and using

specific algorithms, the videoprobe system performs triangulation geometry to obtain accurate measurements. The accuracy of stereo measurement systems depends on the separation distance between the prism, the sharpness and contrast of the image, and the distance from the videoprobe distal end and the object being measured. Stereo measurement does not depend on perpendicularity between the object plane and the videoprobe distal end.

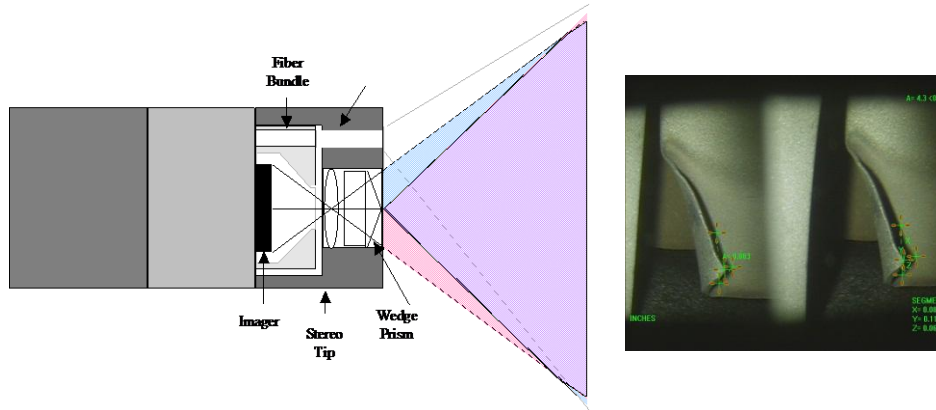


Figure 2: Typical videoprobe stereo measurement.

Both measurement techniques are performed on a two-dimensional image. There are certain measurements such as the perpendicular distance of two points on two planes cannot be obtained. The volumetric information, for example, the concave or convex of a surface profile cannot be easily identified.

Aware of the limitations of Shadow and Stereo measurement methods, in 2010, GE Inspection Technologies launched the first 3D Videoprobe measurement system. It gives a new dimension of endoscopy measurement and more important, provides the needy demand from oil & gas Industry a solution for welding inspection to meet the high quality standard of oil & gas equipment for subsea/deep sea environment.

#### 4. Three Dimensional Phase Measurement Technology

3D Phase Measurement is based on an existing optical metrology technique known as optical phase shifting. This generally involves sequentially projecting three or more structured light patterns onto a surface, capturing an image of each pattern on the surface and then processing the pattern images to produce a 3D map of the surface.

In the body of 3D PM videoprobe tip adaptor, there are two lighting system, glass fibers for white light transmission for illuminating the area of interest and two miniature LED fringe projectors placed on both side of the CCD camera (Fig. 3). When the operator has identified the area where he want to make the measurement, he switches on the LED fringe projectors to project three phase shifted gray gradient patterns on the surface. The system captures the 3D data of the image and generates a point cloud of the surface profile. With these data, the operator can perform various type of measurement of length, multiple length, depth to plane, point to line and area.

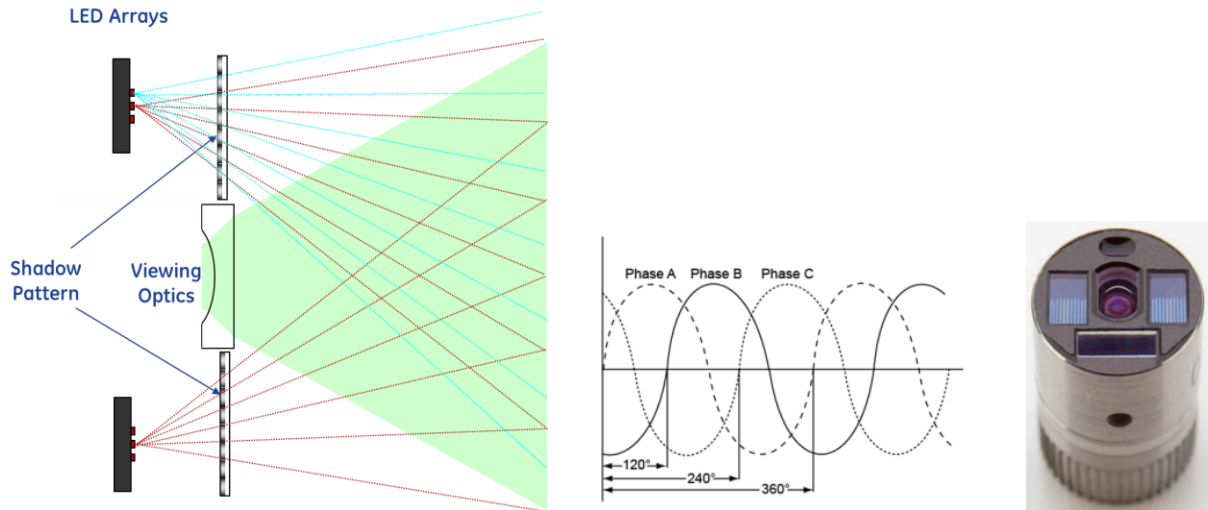


Figure 3: Diagram of phase measurement in the videoprobe, and image of a 6mm-diameter 3D phase measurement tip.

Accuracy depends on the distance from the distal end of the videoprobe to the object plane. The object plane may be skewed without affecting accuracy. 3D Phase Measurement provides measurement accuracy of the order of  $\pm 3\%$  much greater than that of other 2D measurement methods.

More important, it is the first time that the internal surface condition can be viewed in a 3D Point Cloud which can be rotated, zoomed and viewed to provide further information on the shape of a defect and the location of the measurement cursors. With this 3D visualization, more design/process error, defect development and failure can be revealed.

## 5. Videoprobe as a metrological tool for Pipeline welding inspection

An important application of the new technology is the measurement of Pipeline welding. 3D Phase Measurement can quantify the weld features such as root penetration, undercut, mis-alignment (Hi-Lo) and provide a manipulation of weld root profile (Fig 4, Fig 5 and Fig 6).

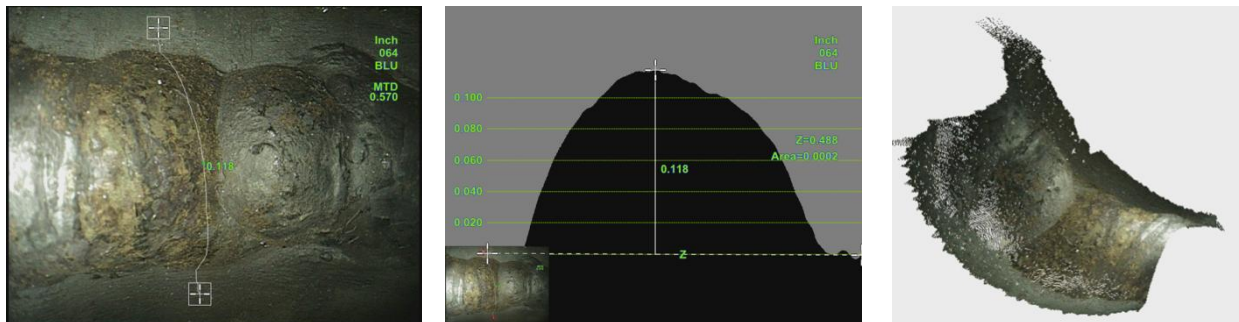


Figure 4: 3D scan and profile measurement of a weld bead (left)

Figure 5: Cross-section profile view of the same weld bead; note the curvature (center)

Figure 6: Point cloud view of the weld bead and the surrounding part (right)

3D Phase Measurement is available for videoprobe with 6.1mm in diameter and 2m to 30m in length. It would be suitable for most of the pipeline inspection. Mechanical or air articulation of probe could help the positioning for optimized image scanning. Figure 7 shows a Videoprobe setup (with centering and indexing device) in operation for welding inspection in a riser fabrication shop.



Figure 7: 3D PM Videoprobe in operation

Of course, there are some limitations of 3D Phase measurement. It is difficult to capture a 3D Phase measurement image if the surface is too shiny or reflective. The scanning distance from probe tip to surface cannot be more than 50mm to capture a large area. Positioning accessories such as centering and indexing devices might be required to facilitate the image scanning.

## 6. New Applications and Developments

Video endoscopy with 3D image capture and measurement capability allows a resurgence of interests in many industries. For aircraft engine and power turbine inspection, 3D Phase measurement provide a precise measurement of tip clearance (tip to shroud), a critical parameter that the industry has been looking for years for a better monitoring solution.

Video endoscopy metrology would be an analytical tool for corrosion measurement. 3D PM provides the depth of corrosion and its profile (Fig. 8 and Fig. 9) that allows analysis of the formation and development. With a reliable measurement data, corrosion monitoring or control and prevention are feasible.

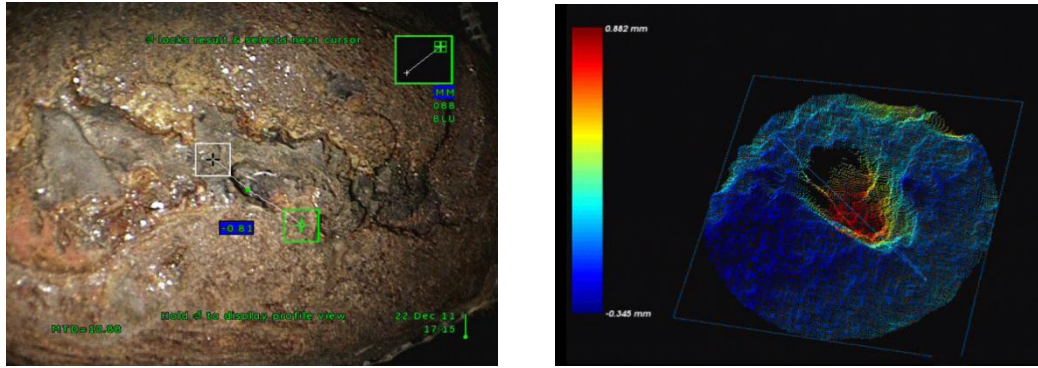


Figure 8: Depth measurement of a corroded surface (left)  
Figure 9: 3D Point Cloud of the area of interest with color mapping (right)

With its portability and easy operation, videoprobe with 3D PM can be an “in-situ” metrology tool for parts that could not be easily disassembled for measurement in laboratory. In some cases, the area of interest cannot be positioned for measurement with existing metrological devices. Bringing the videoprobe to the area of interest is a convenient and speedy solution.

In future, it should be possible to compare the 3D images obtained with the CAD model of the parts. It would be a feedback to the part design or manufacturing process for improvement or for repair of the defective part. From here, many new applications would be feasible.

## 7. Conclusion

3D Phase Measurement is a fundamentally different approach to defect measurement characterization and a significant breakthrough for video endoscopy technology. Never before has 3D surface scanning of small internal spaces been possible. The videoprobe system offers increased accuracy, increased productivity, measurement technique validation for the operator, and considerably more information about a welding profile and process.

## Determining the authenticity of gold jewelries by ultrasonic testing

Amry Amin Abas<sup>1</sup>, Dr. Mohamad Pauzi Ismail<sup>1</sup>, Dr. Mohd Harun<sup>2</sup>, Noorhazleena Azaman<sup>1</sup>, Suhairy Sani<sup>1</sup>

Non-destructive Testing Group<sup>1</sup>,  
Material Technology Group<sup>2</sup>,  
Industrial Technology Division, Malaysian Nuclear Agency

### Abstract

Authenticity of gold jewelries has long been an issue especially to pawn traders. There are cases where jewelries which are overlaid, usually silver and other alloys are coated with a thin layer of gold being declared as pure gold. When this happens, losses will concur to the pawn traders. There are destructive methods of determining gold authenticity and the karat value by using nitric acid and aqua regia where a certain part of the jewelry needs to be scraped. This method should be avoided as certain parts will have marks on them and this will lower the value of the jewelry and the pawn traders might face legal action from the owners. This paper will discuss a non destructive method of determining the authenticity of gold and its limitations by using ultrasonic inspection. This method can also be applied for archaeological artifacts.

### Introduction

Gold leasing or used gold trading is a large business as gold is highly sought after precious metal known for its high value. Processed gold comes in many forms such as coins, bullions, bars, jewelry and others. A total of 171,300 [tonnes](#) of gold have been mined in human history, according to [GFMS](#) as of 2011(1). The world consumption of new gold produced is about 50% in jewelry, 40% in investments, and 10% in industry. Therefore, the jewelry industry consumes most of the gold production in the world.

In Malaysia, gold in the form of jewelry are accepted to be leased at government approved pawn centers. Micro credits will be given to the gold owners whereby the amount will be determined on the gold value. This programme has assisted the community to obtain quick funding for their perusal. The gold jewelry can be obtained by the owner after 6 months by paying the agreed lease value.

The gold trading and leasing has been plagued by a problem of determining gold jewelry authenticity. There are numerous cases where the pawnbrokers were cheated by lessors who claims that their gold jewelry are authentic gold. Usually the pawnbrokers will perform several destructive or non-destructive test to determine the karat and the authenticity of gold. The destructive test are scraping test, aqua regia (nitric acid) test and bite test. But these destructive test are non-favourable because they lower the value of the jewelry. Non-destructive tests are visual test, density test, discoloration test , magnetic test and x-ray fluorescence test. It is important to note that there is no single test that can be absolute, it will take a few test to determine the authenticity of gold.

There are a few cases where jewelry owners claiming their jewelry are gold as of certain karats. The price of lease depends on the karat number where lesser karat number will reduce the value of gold.



There are also cases where the jewelry are gold plated and the base of the jewelry being other metals such as steel, silver or even tungsten. Some of these fake gold jewelry are detected by the tests conducted and some are not. Therefore another method using ultrasonic testing is being studied to complement the existing methods and improve detection capability of fake jewelry.

### Ultrasonic method

This paper will discuss the possibility to use ultrasonic testing as a non-destructive method to determine the authenticity of gold. The principle of test is by determining the velocity of sound wave in the jewelry. Velocity of gold is around 3240m/s which is low compared to other metals that are usually used in fake jewelries such as tungsten which is around 6600m/s. The velocity,  $v$  is determined from the following formula which is

$$V = s/t \quad (1)$$

Where  $s$  is distance of wave travel and  $t$  is the time of flight. Therefore, the thickness of part where the measurement of time of flight of ultrasonic waves will have to be measured. Since jewelries are commonly small and has odd shapes, the measurement of thickness using mechanical devices would render to be inaccurate. In this experiment, measurement of thickness is done employing Digital Radiography technique.

### Methodology

Ultrasonic measurement is performed using ultrasonic flaw detector with probes of 2mm diameter and 5 MHz frequency. The method applied is pulse echo contact technique. The jewelries samples are as in Figure 1.



Figure 1 : Jewelry samples

The thickness of the jewelries is measured using Digital Radiography technique. The source of radiation used is x-ray with energy of 70-100kV and intensity of 5mA. The exposure time is set to 60s. The setup is shown as in Figure 2. The imaging of x-ray penetration is done using blue IP imaging plate. The reference for measurement was based on the wire diameter of standard duplex wire IQI.





Figure 2 : Setup of Digital Radiography

### Result

Measurements of velocity and thickness were taken for 4 samples. Then sound velocity were calculated. The results are as Table 1.

**Table 1 : Experimental results**

Sample name	Measured thickness (mm)	Calculated Velocity (m/s)	Material Composition at Surface (EDX)	Material Composition of Internal (EDX)	Estimated velocity (m/s)
GLG2-1	3.66	4825	Au 98%, Pt 0.5%, Ag 1.8%	Ag 100%	3650
RL3-1	2.51	4766	Au 94%, Cu 6%	Cu 73%, Zn 27%	~4500
RL1-1	2.75	4269	Cu 94%, Au 6%	Cu 68%, Au 31%	~4000
GLG1-1	2.14	4030	Au 100%	Ag 100%	3650

Table 1 shows the thickness of the samples measured using Digital Radiography, Calculated Velocity of samples, material composition measured using EDX on the surface and internal and also the estimated velocity based on the material composition using known velocity values. From table 1 it is shown that Au is only present at the outer surface only except for RL1-1 which has 31% Au internally. Among the 4 elements present, Au has the lowest velocity at 3240m/s whereas other elements have higher velocity values as in Table 2.

**Table 2: Relative velocity difference of elements**

Element	Velocity (m/s)	Difference relative to Au (%)
Au	3240	N/A
Zn	4210	30
Ag	3650	13
Cu	4760	47

Table 3 gives the percentage of difference between the measured velocity of samples and velocity of Au. This table shows that there is 24%-49% of velocity difference between the samples and Au. This difference shows that the samples which are fake gold jewelries has higher velocity values.

**Table 3 : Difference of velocity between jewelry and Au**

Sample name	Measured Velocity (m/s)	Velocity of Au (m/s)	Velocity difference of sample (%)
GLG2-1	4825	3240	49
RL3-1	4766	3240	47
RL1-1	4269	3240	32
GLG1-1	4030	3240	24

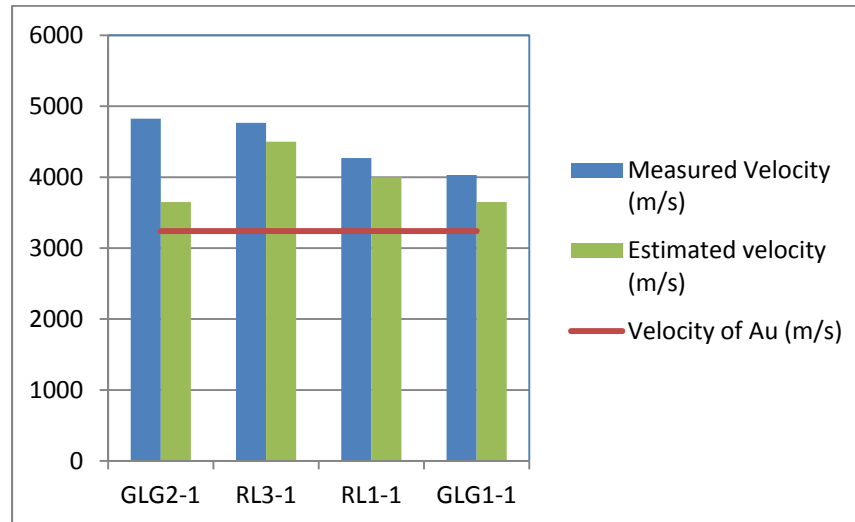


**Figure 3 : Relation between the measured velocity of samples, estimated velocity of samples and velocity of Au**

Although the results shows that the there are difference in velocity of the samples as compared to Au, further work has to perform to verify the measurement comparing to various Karat of gold jewelries. This is important to verify the method is consistent and reliable.

### Conclusion

It is still early to conclude that ultrasonic testing can be used to determine the authenticity of gold jewelries. The measurement itself is difficult due to the shape and size of the jewelries. Certain jewelries with odd shapes will prevent detection of back wall or even through transmission measurement to be performed. Elements with poor contrast in velocity to Au can be measured as Au mistakenly. Therefore to determine the authenticity of gold jewelries, one cannot rely on ultrasonic method only. Other non destructive evaluations should be performed such as density measurement, XRF, XRD, EDX and others.

### Further work

The ultrasonic measurement techniques shall be improved using smaller diameter probes with higher frequency. Measurement will be done on known Karat of gold jewelries as a comparison. Statistical methods will be used to determine the accuracy of measurements.

### Reference

1. World Gold Council , [www.gold.org](http://www.gold.org)
2. Dr. Mohd Bin Harun, Dr. Mohamad Pauzi Bin Ismail dan Amry Amin Abas, *Teknologi ultrasonik dalam pengujian ketulenan fizikal barang kemas berongga*. Gold Traders Conference 2013.
3. Josef Krautkrämer, Herbert Krautkrämer, *Ultrasonic Testing of Materials*, Springer-Verlag 1983.

**DETERMINATION OF WELDED JOINTS METAL'S  
MECHANICAL PROPERTIES BY STRENGTH PARAMETERS  
IN STRESS CONCENTRATION ZONES DETECTED  
BY THE METAL MAGNETIC MEMORY METHOD**

*S.M. Kolokolnikov, Al.A. Dubov (Energodiagnostika Co. Ltd., Moscow),  
A.Yu. Marchenkov (SRU MEI, Moscow)*

**Abstract**

The magnetic memory of metal (MMM) is an after-effect, which occurs in the form of metal residual magnetization in components and welded joints formed in the course of their fabrication and cooling in the weak magnetic field of the earth and in the form of irreversible change of components' magnetization in zones of stress concentration and damage under working loads (ISO 24497–1:2007(E)). Experience with carrying out comprehensive testing of welding specimens by the MMM method with subsequent stress concentration zones (SCZs) detection and determination of the mechanical properties by hardness characteristics is described. It is shown that the microhardness and consequent mechanical properties in the SCZs considerably exceed the average level of above characteristics.

**Keywords:** Hardness; Magnetic memory of metal; Mechanical properties; Non-destructive testing; Residual stresses; Strain.

Physical properties in materials during welding form a specific stressed state conditioned by the inhomogeneity of thermal and strain fields, formation of the high level of residual stresses and various stress concentrators (design, geometrical, structural and due to defects in the form of discontinuity flaws).

One of the important and complicated problems of modern NDT of various-type welded joints' quality is searching for and detection in them of a "weak link" in the integrated complex system of "strain inhomogeneity – structural and mechanical inhomogeneity – welded joint defects – structural and process stress concentrators" factors, i.e. of zones with high inhomogeneity of the stressed state or stress concentration zones (SCZs). This is important both at fabrication of welded joints, i.e. directly after welding for the technological process optimization, and during their operation. Here the case when the welded joint defects, being stress concentrators, coincide with maximum stresses due to working loads, is the most dangerous.

The analysis of the criticality of various process defects of welded joints in paper [1] demonstrated that in some cases stress concentration caused by the butt joint shape can be more dangerous than that caused by the detected internal process defects in the form of pores and inclusions.

For detection of welded joints SCZs based on the 100% examination of steel welded structures it is suggested to use the metal magnetic memory (MMM) method, which is becoming more common in practice.

Formation of a magnetic (domain) structure in welded joints occurs simultaneously with crystallization during the metal cooling in a magnetic field of the earth and passing through the Curie point (approximately 768°C for carbon steel grades). Domain boundaries fixing nodes with access to the weld surface in the form of self-magnetic leakage fields (SMLF) form on the occurring welding defects. In conditions when the thermal strain and stress

energy is by order higher than the energy of a weak external magnetic field, the distribution of the residual magnetization in the weld metal is conditioned by the appropriate RS distribution. Thus, by reading of SMLF that form during welding, we have the opportunity to perform the integral assessment of the weld's actual state.

Papers [3, 4] demonstrate that both macro defects, based on conventional NDT methods, and micro damages and local structure variations can be detected in SCZs of welded joints. However, determination of the metal's mechanical properties in SCZs with small length (from units to several tens of microns) is rather problematic.

For on-line non-destructive testing of the metal's actual mechanical properties the specimen-free method is the most practicable. It allows to determine the parameters of other mechanical properties of the metal by hardness characteristics, for example, the yield strength ( $\sigma_{0.2}$ ), ultimate stress ( $\sigma_r$ ), uniform deformation ( $\delta_{uni}$ ), etc. This specimen-free method is based on correlations of hardness characteristics and strength characteristics [5, 6, 7].

The main objective of this study was to conduct a comprehensive investigation of specimens with residual welding stresses through preliminary detection of SCZs in them by the MMM method and subsequent determination in these zones of the weld metal's and the near-weld zone's mechanical parameters using the above-mentioned specimen-free method.

### The procedure for testing of specimens with residual welding stresses using the MMM method

Three specimens with residual welding stresses were fabricated of steel 20 in accordance with [8]. Table 1 presents the welding technique data for each specimen respectively. Figure 1 shows the specimens' configuration.

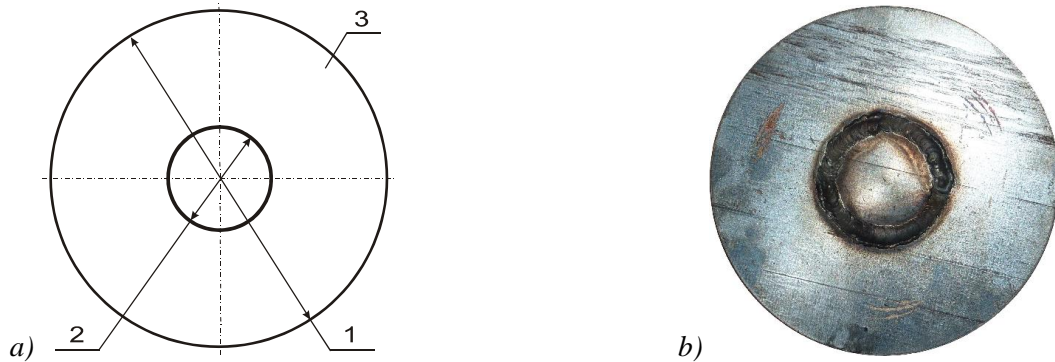


**Figure 1.** Specimen (Steel 20) with residual welding stresses: *a* – specimen sketch; *b* – general view of the specimen; 1 – specimen diameter  $D_o=130$  mm; 2 – weld axis diameter  $D_w=40$  mm; 3 – thickness  $S=4$  mm.

**Table 1** Welding techniques used for specimens fabrication

No. of specimen	Welding technique
Specimen No.1	TAG welding with CB08Г2C wire deposit. $I=50$ A (DC).
Specimen No.2	TAG fusion welding. $I=60-70$ A (DC).
Specimen No.3	TAG fusion welding. $I=60-70$ A (DC).

The intrinsic stressed state in welded units with weld-ins of inserts, nozzles, etc. was simulated by means of deposition and fusion along the closed loop.

Specimens inspection by the MMM method was performed using the TSC-3M-12 instrument and the Type 2M scanning device (figure 2). Figure 3 shows the scheme of the specimen inspection.

The parameter inspected by the MMM method is the intensity  $H_p$  of the self-magnetic leakage field (SMLF) along the line of scanning. The magnetic field measurement unit is A/m. Recording of two SMLF intensity components – normal  $H_p^y$  (perpendicular to the specimen's surface) and tangential  $H_p^x$  (tangential to the specimen's surface along the line of scanning) was performed during the inspection. The SMLF intensity was recorded along the radial lines of scanning by sectors with a step of  $15^\circ$ . Figure 3 shows the scheme of inspection. The direction of scanning with the instrument sensor is shown with arrows in figure 3.



**Figure 2.** Inspection of specimens using the type 2M scanning device of the TSC-3M-12 instrument.

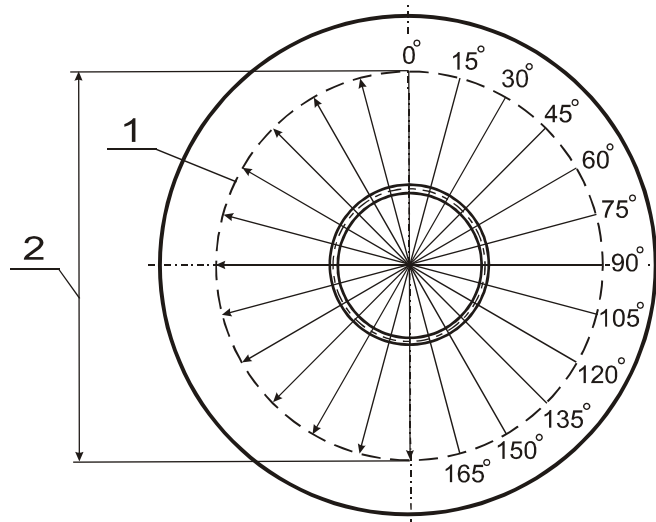


**Figure 3.** Scheme of the specimen inspection. Lines with arrows correspond to the direction of scanning within the specimen inspection area: 1 – specimen inspection area boundary; 2 – diameter of the specimen inspection area  $D_{insp}=100$  mm.

The evaluation criterion of the MMM inspection results is a complex of SMLF gradients for each intensity component ( $dH_p^y/dx, dH_p^x/dx$ ). The field gradient measuring unit is  $A/m^2$ . The objective the inspection by the MMM method is detection of maximum field gradient value corresponding to maximum SCZs.

To assess the inhomogeneity of the welded joints' stressed state by the magnetic parameters a relative magnetic index  $m$  was used [9]:

$$m = \frac{(dH_p/dx)_{max}}{(dH_p/dx)_{ave}},$$



where  $(dH_p/dx)_{max}$  – is the maximum gradient value in a SCZ,  $(dH_p/dx)_{ave}$  – is an average gradient value on the segment of inspection.

Indentation testing by the specimen-free method was carried out in maximum SCSZs and, for the sake of comparison, on SCZ-free weld segments in order to determine the mechanical characteristics of the weld metal and near-weld zone material. However, considering that in SCZs the potential variations of the metal's properties may occur at the microstructural level, the indentation tests were used to determine microhardness with subsequent conversion of mechanical characteristics to the macro level, taking into account the scale factor [10, 11].

Microhardness measurements in specimens weld sections indicated in figure 3 were performed using the automated microhardness tester “Instron Tukon 2500” (figure 4) at the laboratory for mechanical and process testing of structural materials of the Moscow Energy Institute (MEI (TU)).

During testing 2 to 5 microhardness measurements in heat-affected zone (HAZ) on each weld side and directly on the weld were performed in each weld section. Then the arithmetic mean value of microhardness was calculated. This value was used for the analysis and conversion of the mechanical characteristics.

### Results of specimen No.1 inspection

Testing of specimen No.1 revealed three sections at  $0^\circ$  ( $m_{max}=5,3$ ),  $15^\circ$  ( $m_{max}=4,9$ ) and  $30^\circ$  ( $m_{max}=5,3$ ) with maximum SCZs.

Figure 5 shows the results of the specimen inspection in the section at  $0^\circ$ . The detected SCZs within the limits of the surfacing boundaries and HAZ are characterized by the maximum values of the field gradient ( $dH_p^y/dx$ ,  $dH_p^x/dx$ ).

Similar pattern of SMLF intensity and field gradients distribution was recorded in the sections at  $15^\circ$  and  $30^\circ$ .

Two sections at  $105^\circ$  ( $m_{min}=1,5$ ) and  $120^\circ$  ( $m_{min}=0,8$ ) with minimum gradient values being close to the average value across the entire weld perimeter ( $4,5 \times 10^3 \text{ A/m}^2$ ) were specified for the comparative study.



**Figure 4.** Automated microhardness tester “Instron Tukon 2500”.

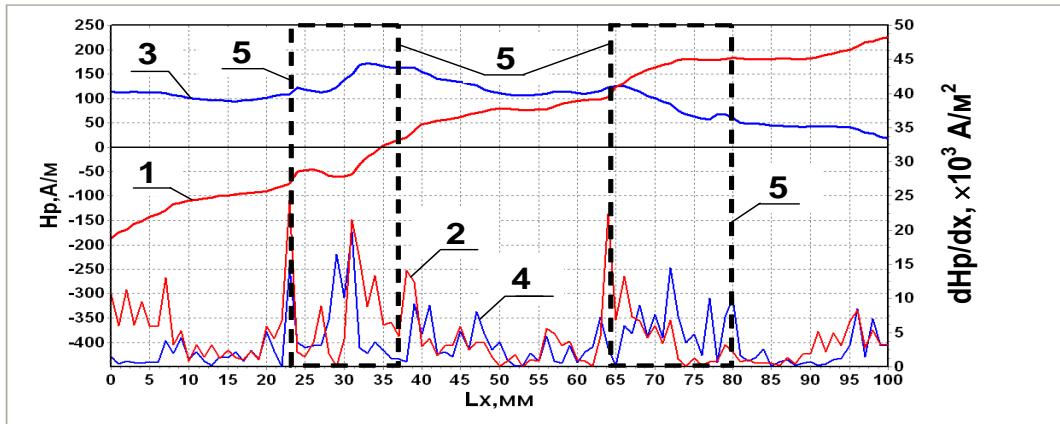


**Figure 5.** Results of specimen No.1 inspection in the section at 0°: 1 – the graph of the normal component distribution of the field intensity  $H_p^y$ ; 2 – the graph of the normal component gradient of the field intensity  $dH_p^y/dx$ ; 3 – the graph of the tangential component gradient of the field intensity  $H_p^x$ ; 4 – the graph of the tangential component gradient of the field intensity  $dH_p^x/dx$ ; 5 – weld boundaries.

Figure 6 shows for comparison the results of the specimen inspection for the section at 120° and identifies the zone with minimum gradient values for the comparative analysis of indentation study results.

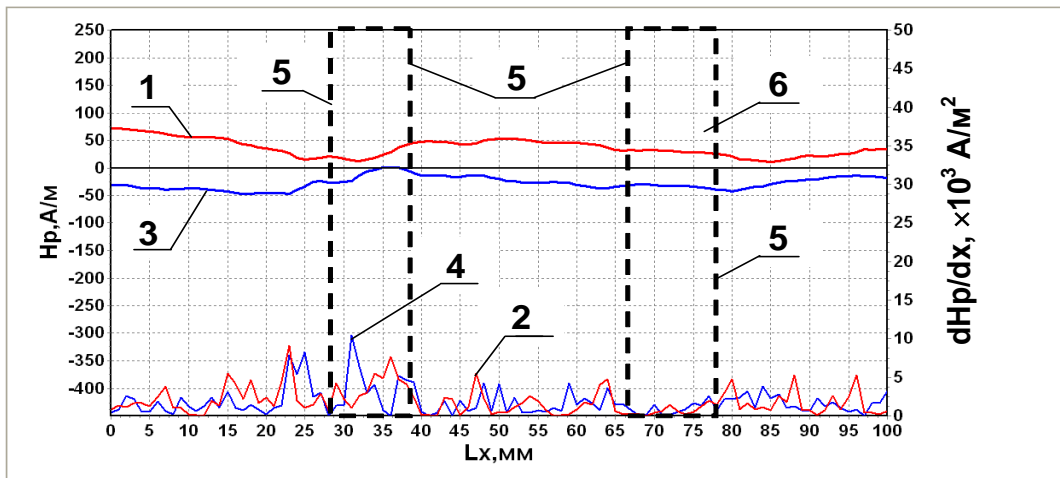


**Figure 6.** Results of specimen No.1 inspection in the section at 120°: 1 – the graph of the normal component distribution of the field intensity  $H_p^y$ ; 2 – the graph of the normal component gradient of the field intensity  $dH_p^y/dx$ ; 3 – the graph of the tangential component gradient of the field intensity  $H_p^x$ ; 4 – the graph of the tangential component gradient of the field intensity  $dH_p^x/dx$ ; 5 – weld boundaries; 6 – weld section for indentation study.

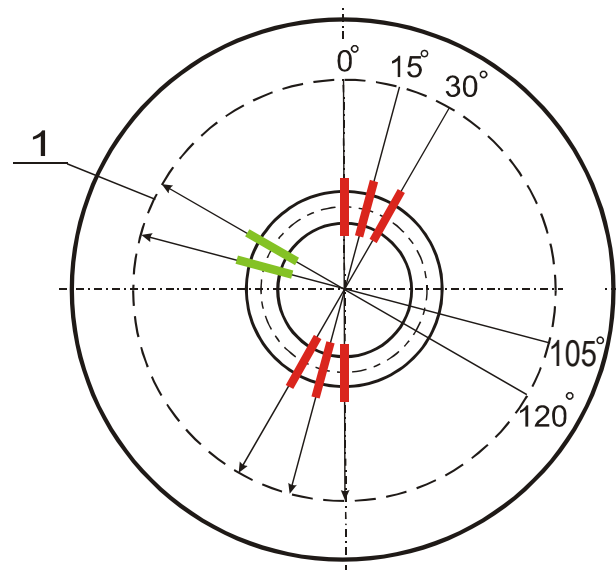


**Figure 7.** Scheme of sections arrangement (marked with thickened stripes) for performance of indentation study on the specimen No.1: 1 – specimen inspection area boundary; --- - sections at 0°, 15° and 30° with maximum SCZs; --- - sections at 105° and 120° without SCZs.

Figure 7 shows the arrangement scheme of sections with SCZs and without them for performance of indentation study on the specimen No.1.

Figure 8 shows the distribution of microhardness  $HV_{0,01}$  (kG/mm<sup>2</sup>) on the weld and HAZ of the specimen No.1 in sections with SCZs and without them specified based on the results of the inspection by the MMM method. Table 2 presents the results of microhardness measurement.

The comparative analysis revealed exceeding of microhardness in SCZs as compared to the section without SCZs:

- in HAZ on the external side of the disk – by 2,5%;
- on weld metal – by 10,5%;
- in HAZ on the internal side of the disk – by 12,4%.

**Table 2** Average values of microhardness  $HV_{0,01}$  (kG/mm<sup>2</sup>) in sections with SCZs and without them on the specimen No.1

Test location	$HV_{0,01}$ (kG/mm <sup>2</sup> ) in sections without SCZs	$HV_{0,01}$ (kG/mm <sup>2</sup> ) in sections with SCZs	Exceeding of microhardness in SCZs as compared to the section without SCZs
External HAZ	285	292	2,5 %
Weld metal (deposit)	335	370	10,5 %
Internal HAZ	283	318	12,4 %

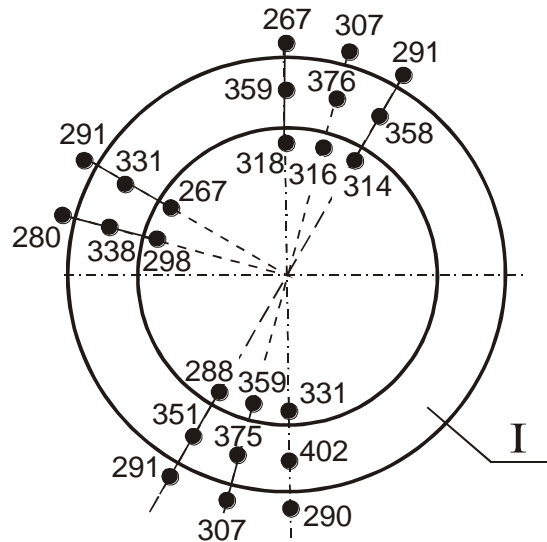


**Figure 8.** Distribution of microhardness  $HV_{0,01}$  (kG/mm<sup>2</sup>) on the weld (I) and HAZ of the specimen No.1 in sections with SCZs and without them specified based on the results of the inspection by the MMM method.

Similar testing was performed on specimens No.2 and No.3. Tables 3 and 4 shows the values of microhardness  $HV_{0,01}$  (kG/mm<sup>2</sup>) measured in sections with SCZs and without them, respectively, on specimens No.2 and No.3. These tables demonstrate that exceeding of microhardness in SCZs as compared to the weld sections without SCZs is greater than 30%.

**Table 3** Average values of microhardness  $HV_{0,01}$  (kG/mm<sup>2</sup>) in sections with SCZs and without them on the specimen No.2

Test location	$HV_{0,01}$ (kG/mm <sup>2</sup> ) in sections without SCZs	$HV_{0,01}$ (kG/mm <sup>2</sup> ) in sections with SCZs	Exceeding of microhardness in SCZs as compared to the section without SCZs
External HAZ	311	415	33,4 %
Weld metal	338	367	8,6 %
Internal HAZ	307	400	30,3 %

**Table 4** Average values of microhardness  $HV_{0,01}$  (kG/mm<sup>2</sup>) in sections with SCZs and without them on the specimen No.3

Test location	$HV_{0,01}$ (kG/mm <sup>2</sup> ) in sections without SCZs	$HV_{0,01}$ (kG/mm <sup>2</sup> ) in sections with SCZs	Exceeding of microhardness in SCZs as compared to the section without SCZs
External HAZ	305	407	33,4 %
Weld metal	339	395	16,5 %
Internal HAZ	309	318	2,8 %

### Determination of mechanical properties in SCZs based on hardness parameters measurement considering the scale factor

Determination of the metal's mechanical properties in SCZs was carried out by means indentation at the micro level with subsequent conversion of mechanical properties values to the macro level by the proposed dependencies presented in papers [11, 12].

The technique is based on determination of the metal's mechanical properties directly by the hardness indentation diagrams (hardness, elastic modulus, etc.) and on calculation of properties by hardness characteristics based on correlations with strength characteristics (yield strength, ultimate strength, etc.) [5, 6]. However, considering that the known correlations of the metal's strength and hardness characteristics were established at the macro level, in this paper strength parameters were converted from the micro level to the macro level, and then the ultimate strength value was determined by the hardness value.

At the first stage the value of the coefficient  $\gamma$  considering the scale factor impact was determined. For this purpose microhardness  $HV_{0,01}$  and Vickers macrohardness  $HV_{10}$  were determined outside a SCZ, and their ratio determined the value of coefficient  $\gamma = HV_{0,01}/HV_{10}$ . Then, considering the obtained coefficient  $\gamma$  for the metal in a SCZ, the macrohardness value was obtained by the ratio  $HV_{10} = HV_{0,01}/\gamma$ .

Taking into account that Vickers and Brinell hardness values at the macro level practically coincide, the ultimate strength was calculated by the known dependence  $\sigma_t = 0,33HB$  (or  $0,33HV$ ).

Let us further consider the example of mechanical properties determination for the specimen No.2 using the described technique.

On the specimen No.2 the average macrohardness in the heat-affected zone (HAZ), but outside the SCZ, was  $HV_{10} = 158 \text{ kG/mm}^2$ . Based on the above results of the study, microhardness outside the SCZ was  $HV_{0,01} = 311 \text{ kG/mm}^2$ .

Thus, the value of the coefficient  $\gamma$  considering the scale factor impact was determined:

$$\gamma = \frac{HV_{0,01}}{HV_{10}} = \frac{311 \text{ kG/mm}^2}{158 \text{ kG/mm}^2} = 1,968$$

The microhardness value in SCZ across HAZ was  $HV_{0,01} = 415 \text{ kG/mm}^2$ .

Further, considering the coefficient  $\gamma$  the metal's hardness in SCZ was converted to the macro level:

$$HV_{macro} = \frac{HV_{micro}}{\gamma} = \frac{415 \text{ kG/mm}^2}{1,968} = 211 \text{ kG/mm}^2.$$

Based on the correlation  $\sigma_t = 0,33 \times HV_{10}$  [12], strength characteristics (ultimate stress) of the metal in a SCZ and outside it were converted to the macro level:

$$\sigma_t = 0,33 \times 158 = 52,1 \text{ kG/mm}^2 - \text{outside a SCZ};$$

$$\sigma_t = 0,33 \times 211 = 69,6 \text{ kG/mm}^2 - \text{in a SCZ}.$$

As a result exceeding of the stress level in a SCZ  $\Delta\sigma_t$  is evaluated compared to the stress level outside a SCZ:

$$\Delta\sigma_t = 69,6 \text{ kG/mm}^2 - 52,1 \text{ kG/mm}^2 = 17,5 \text{ kG/mm}^2.$$

## Conclusions

1. The conducted testing of standard welded specimens by the MMM method detected SCZs, in which the level of the self-magnetic leakage field gradient exceeded the average level by 5,3 times for the specimen No.1 with deposit and by 10,1 times for specimens No.2 and No.3 with fusion.
2. Indentation study revealed exceeding of microhardness in SCZs as compared to section with SCZs:
  - in HAZ from 2,5 to 33,4 %;
  - on deposit weld metal by 10,5%;
  - on weld metal with penetration from 8,6% to 16,5%.
3. Exceeding of the ultimate stress value  $\sigma_t$  in SCZs on specimens No.2 and No.3 as compared to  $\sigma_t$  outside SCZs was approximately 33%.

The obtained exceeding of the  $\sigma_t$  value refers to welds HAZ.

## Bibliography

1. I.I. Makarov. Criteria of process defects evaluation in welded structures // Welding Production, 1975, No. 12. pp.9-11.
2. A.A. Dubov, A.I. Dubov, S.M. Kolokolnikov. Metal magnetic memory method and inspection instruments. Training Handbook. Moscow: ZAO "Tisso", 2008. 363 p.
3. A.A. Dubov, S.M. Kolokolnikov. Quality assurance of welded joints in power engineering by the metal magnetic memory method / Proceeding of the IIW International Conference "Safety and Reliability of Welded Components in Energy and Processing Industry, 10-11 July 2008, Graz, Austria. pp.709-714.
4. A.A. Dubov, S.M. Kolokolnikov. Comprehensive diagnostics of parent metal and welded joints of steam pipeline bends. Doc.IIW-1946 // Welding in the World, 2010, vol. 54, no. 9/10. pp.R241-R248.
5. M.P. Markovets. Determination of metals' mechanical properties by hardness. Moscow: Mashinostroenie, 1979. 192 p.
6. V.M. Matunin. On-line diagnostics of mechanical properties of structural materials. Moscow: MEI Publishing House, 2006. 214 p.
7. V.M. Matunin. Mechanical process testing and properties of structural materials: Training Handbook. Moscow: MEI Publishing House, 2005. 140 p.
8. GOST 26294-84. Welded joints. Corrosion cracking test methods.
9. S.M. Kolokolnikov. Detection and evaluation of welded joints' stressed state inhomogeneity using the magnetic method: Author's abstract, Ph.D. in Engineering Science. Moscow, 2010. 18 p.
10. V.M. Matunin, A.N. Demidov, M.A. Prokhodtsov, B.A. Uzikov. Scale factor influence on the results of Brinell hardness test // Technology of metals, 2008, No.8. pp. 49-52.
11. V.M. Matunin, A.A. Dubov, A.Yu. Marchenkov. General patterns of the scale factor appearance during the metal's strength and hardness determination // Zavodskaya Laboratoria. Diagnostics of materials, 2010, No.8. pp.43-47.

12. A.A. Dubov. Mechanical properties and structure of the metal in local stress concentration zones of engineering products: Author's abstract, Ph.D. in Engineering Science. Moscow, 2012. 20 p.
13. Welding in Engineering: Handbook in 4 volumes/ Editorial Board: G.A. Nikolayev (Chairman) et al. Moscow: Mashinostroenie, 1979. Vol.3 / Edited by V.A. Vinokurov. 1979. 576 p.



## DETECTION OF LOCATION OF PIPELINE INTELLIGENT GAUGE JAMMED IN PIPELINE BY NEUTRON DEVICE

Md Fakarudin Ab Rahman<sup>1,a</sup>, Ismail Mustapha<sup>1,b</sup>, Nor Pa'iza Mohd Hasan<sup>1,c</sup> and Pairu Ibrahim<sup>2,d</sup>

<sup>1</sup>Plant Assessment Technology Group; Industrial Technology Division,

<sup>2</sup>Raymintex, Irradiation Service Division,

Malaysian Nuclear Agency, 43000 Kajang, Selangor, Malaysia

<sup>a</sup>[fakarudin@nuclearmalaysia.gov.my](mailto:fakarudin@nuclearmalaysia.gov.my), <sup>b</sup>[ismail@nuclearmalaysia.gov.my](mailto:ismail@nuclearmalaysia.gov.my), <sup>c</sup>[norpaiza@nuclearmalaysia.gov.my](mailto:norpaiza@nuclearmalaysia.gov.my),

<sup>d</sup>[pairu@nuclearmalaysia.gov.my](mailto:pairu@nuclearmalaysia.gov.my)

**Abstract:** In industrial plants such as electricity generating, petroleum, chemical and petrochemical plants, pipelines are used extensively to transport liquid from one location to another. In radiation vulcanization of natural rubber latex (RVNRL) plants, pipelines are also used to transport latex to storage tank. During one of its maintenance activities, a pipeline intelligent gauge (PIG) that was used to monitor pipe integrity jammed inside the pipe causing interruption to its operation or loading activities. Sealed source technology was utilized to determine the location of jammed PIG in the pipeline. Fast neutrons from a 50 mCi Americium Beryllium (AmBe<sup>241</sup>), with energy range between 0.5 to 11 MeV, were used for the study. Helium 3 (He<sup>3</sup>) detector was used to detect slow neutrons having a range of energy of 30 eV- 0.5 MeV. The investigation was carried out using neutron backscatter technique scanner. By adopting back-scattered technique, the location of jammed PIG in the pipeline has been successfully determined.

**Keywords:** Radiation Vulcanized Natural Rubber Latex (RVNRL); pipeline intelligent gauge (PIG); Neutron backscatter technique; Americium Beryllium (Am-Be<sup>241</sup>); Helium 3 (He<sup>3</sup>) detector

### 1.0 Introduction

Natural Rubber Latex (NRL) is a stable dispersion (emulsion) of polymer microparticles in an aqueous medium (Bowers et. al, 1990). NRL is extracted from *Hevea brasiliensis* tree and is used to produce different kinds of rubber goods like gloves, condoms, balloons and some part of medical and dental equipments, but it is predominantly used in the production of surgical and examination gloves (Sizue O. Roger et. al, 2003). RVNRL is low modulus pre-vulcanized latex based on high ammonia latex concentrate, prepared by irradiation of natural rubber latex with gamma irradiation from cobalt-60 source. It is an organic compound with C-H bond and chemical formulation of (C<sub>5</sub>H<sub>8</sub>)<sub>n</sub>. RVNRL is produced using pipe type continuous gamma irradiator. The formulated latex is transferred by means of a piston pump, acting through the irradiation matrix, which is exposed to the gamma source (Makuuchi, 2003). Piping in the plants is continuously monitored to ensure its integrity. An advance monitoring system known as pipeline intelligent gauge (PIG) was routinely used for this purpose. Typical PIG used for this monitoring purpose is shown in Fig. 1 below. However, during one of its monitoring activities, the PIG was jammed and remained inside the pipe.



Fig. 1 Typical PIG used to verify RVNRL pipe integrity

## 2.0 Neutron Backscattered Technique

A technique that utilizes Neutron Backscattered Instrument has been widely used in industry. The technique has been used extensively for measurement and determination of the extent of emulsion, location of interfaces and liquid levels and level of foam and solids deposition. However, majority of the reports on results of investigation using this technique were not made available due to the confidentiality of the information. A technique that utilized Am–Be neutron source was used to determine the hydrogen content of oil samples from Nigeria by Jonah et al. (1999). They applied the principles of thermal neutron reflection technique in combination with the foil activation method. They found that this method is economical and suitable for the determination of moisture in solid samples.

Fast neutron transmission technique to measure moisture content in sugar and wood samples has been reported by Naqvi (2003). He exploited neutrons having energy of 2.8 MeV that were produced via D (d, n) reaction. These neutrons were transmitted through the wood and sugar samples, and then detected by an NE213 Scintillation detector. Monte Carlo simulation was employed to calculate fast neutron counts. His results demonstrated that neutron device is capable of measuring the moisture in both samples. Later, Hassan et al, (2009) employed neutron backscatter technique for in-situ water measurement in paper-recycling industry. They used similar technique by using Am-Be<sup>241</sup> as a neutron source. They indicated that neutrons have a great potential to be employed by the paper-recycling industry for rapid and non-destructive detection of water in the bulk of used papers.

A fast neutron source emits high energy neutrons that collide with the atomic nuclei of tested material and scatter in all directions with somewhat lower energies. Neutron moisture detection is based on the fact that fast neutrons ( $>0.5$  MeV) from a neutron source (e.g. Am–Be 241) can be greatly attenuated or slowed down to become thermal neutrons ( $<0.5$  MeV) by interaction with hydrogen atoms in water. The back-scattered slowed-down neutrons can be easily detected by a thermal neutron counter. Numbers of backscatter neutrons are directly proportional to the concentration of hydrogen atoms in front of the neutron detector (Charlton, 1985).

This article reports results of investigations on the detection of hydrogen concentration in RVNRL pipeline using spot measurements. It is expected that areas on two side of the jammed PIG will have a significant different in hydrogen concentration. Detection of these differences would provide a good indication of the jammed PIG within the pipe.

## 3.0 Materials and Methods

Neutron Backscatter Technique (NBT) is based on the principle of interaction between neutrons and matter. The technique begins with a radioactive source emitting fast neutrons of high energies that are difficult to detect. These neutrons later interact with matter, losing parts of their energies and finally slowed down to become thermal neutrons. Thermal neutrons most likely will interact with other atoms that have a comparable size with them and it is known that atoms of hydrogen have their sizes and masses close to that of neutron and therefore accounts for the majority of the collisions that reduce the fast neutrons to thermal neutrons. When fast neutrons collide with hydrogen atoms they release energy and some of them become thermal neutrons. These thermal neutrons are scattered in all directions but have a short travel path. Some of them are scattered back towards the scanning head and these are the neutrons counted by the detector.

Fast neutrons are penetrating particles, capable of passing through substantial thickness of material and hence ideal for the stuck PIG scanning. This class of neutrons with energies in the range 0.5-11 MeV, lose their energy by scattering process. In elastic scattering, these neutrons are

slowed down in the collision and at the same time majority of them changed their direction of motion. In the energy range of 30eV-0.5 MeV, elastic scattering is essentially the only process by which neutrons can be slowed down.

When neutrons with energy before collision  $E_1$ , experience head-on collision with nucleus of atom of other material and the energy after collision is  $E_2$ , it is possible to show that the energy transferred to the nucleus is

$$E_2 / E_1 = [(A-1)/(A+1)]^2 \dots\dots\dots(1)$$

where A is the mass number of the nucleus. From equation (1) it can be seen that it is possible for a nucleus to lose all of its kinetic energy in a head-on collision with a hydrogen nucleus. It is for this reason that the presence of hydrogen is considered as a major factor in the slowing down of fast neutrons. It can be seen that the number of collisions required to thermalize a fast neutron is lower for elements of lower atomic number, such as hydrogen. A high proportion of chemical, oil and gas process streams contain hydrogen in one form or another. This is especially true for petrochemical, latex process plant, oil and gas industries where hydrogen is present in practically “every” process material. In general, the concentration of thermal neutrons near the fast-neutron source increases by the presence of hydrogen. The higher concentration of these elements, the shorter are the distances traveled by the thermal neutrons and the higher is their density near the source (Fig. 2).

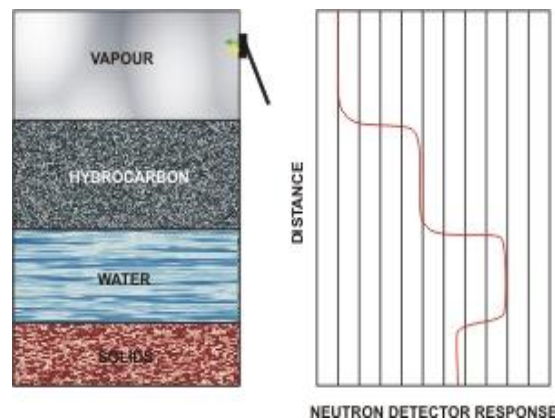


Figure 2: Typical result of neutron backscatter technique investigation

Before the application of NBT, it was a common practice that in the event of PIG jammed in the pipeline, the plant owner has to dismantle the entire of pipe stainless steel. The fact that the pipe is 315 m in length, 7.6 cm in diameter and having 30 corners makes this dismantling and reinstallation of the system very time consuming. It normally takes 3 days to complete the process.

RVNRL piping design is as presented in Fig. 3. It was made of steel and contains straight and bent tubes forming a complex structure. Prior to the application of NBT, it is very important for RVNRL pipeline to be drained off so that only vapour phase remains in the pipe for investigation. It will be easier to distinguish responses from a jammed PIG (somewhat lower hydrogen content) with responses from other area where only vapour with high hydrogen content present. In this investigation, measurement on a standard paraffin block was consistently done from time to time to ensure the stability of equipment before, during and after measurements. The investigation technique was conducted by placing the measurement head on the RVNRL pipeline as shown in

Fig. 3 and the count was recorded. The measurement was recorded for every 5 cm length of RVNRL pipeline.

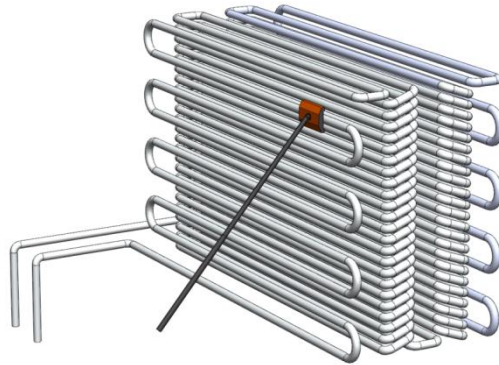


Fig. 3: Typical investigation on pipe in RVNRL plant

#### 4.0 Results and discussion

The reference count on selected areas (known material) and samples for this scanning are shown in Table 1. Data of measurement performed at selected locations on the empty pipe and filled pipe of RVNRL were also recorded and presented in Table 1. High count indicates the presence of material with high hydrogen concentration (eg. Paraffin wax or water), whereas low count indicates the presence of material of low hydrogen concentration (eg. vapour).

Table 1: Hydrogen concentration counts at selected location and samples.

Description	Counts
Standard Block (Paraffin)	25000 - 26000
Vapour at Surrounding	300-700
Water in Hydrant Pipe	13000-14000
Empty Pipe	1000-1500
Pipe Filled with Latex	8000-10000

Prior to the measurement, latex in one side of the pipe was released. By doing so, it is expected that the latex in a portion of pipe from the pipe opening to the location where the PIG was jammed would be drained off whereas the latex on the other side with considerably higher hydrogen concentration will remain in the pipe. The investigation began from the side where the latex was released and proceed inward.

Figure 4 shows the results of thermal neutron counts obtained from measurements of hydrogen inside the pipe. In this figure, sudden increase of the thermal neutron counts indicates increased of the hydrogen concentrations. In other words, it gave indication that there was no latex in the pipe at locations from the initial scanning point to a location 5.8 meters from the initial scanning point. However, beyond 5.8m from the initial scanning point, neutron counts increases that indicate the presence of latex. From this observation, the PIG was detected at 5.8m from the reference point. It is worth to note that the total count from starting point to 5.8m from the initial point is in the area of

800 which is very close to total counts in empty pipe whereas beyond 5.8 m the total count is around 8000 comparable to the count for pipe filled with latex as recorded in Table 1.

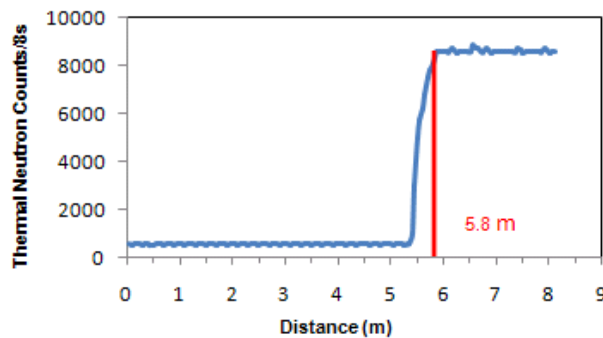


Figure 4: The relationship between the thermal neutron counts and measurements distance

Results of scanning indicated that the actual location of the jammed PIG is at the corner of the RVNRL pipeline as shown in Figure 5. Based on this result, this pipe corner was dismantled and the stuck PIG has been successfully found. Hence, the NBT technique has been proven successful in detecting the location of a jammed PIG within a few hours. Hence, the technique offers minimum cost and time.

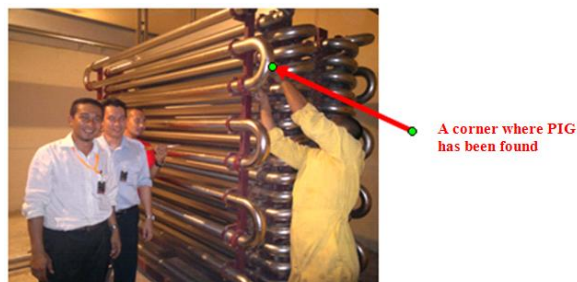


Figure 5: The location of stuck PIG

## 5.0 Conclusion

Results of the neutron backscattered measurement performed on an empty pipe as well as pipe filled with latex as presented in Table 1 provide a good reference data for the detection of PIG in the pipe. It was observed that the value of total counts at scanning location from initial scanning point to 5.8m is comparable to that measured in the empty pipe whereas beyond 5.8m the reading is comparable to those obtain in pipe filled with latex. By dismantling the pipe it was confirmed that the jammed PIG was located at a position of 5.8m from the initial scanning points. Thus it was confirmed that the neutron backscattered technique has been used successfully for detection of the jammed PIG in RVNRL pipe.

## Acknowledgment

The authors would like to extend their appreciations and sincere thanks to all personnel belong to the Plant Assessment Technology Group, Malaysian Nuclear Agency for their support and co-operation especially to Mr. Mior Ahmad Khusaini Adnan and Mr. Airwan Affandi Mahmood. Last but not least thanks also go to Dr. Abdul Nassir Ibrahim (Director, Industrial Technology Division) and Dr. Muhammad Lebai Juri (Director General, Malaysian Nuclear Agency) for their support and encouragement.

## References

J. E Bowers et. al, 1990. Natural Rubber-Producing Plants for the United States. National Agricultural Library.

Charlton, J.S., 1985. Radioisotope Techniques for Problem-Solving in Industrial. Springer, Berlin.  
Sizue O. Roger et. al., 2003. Extractable proteins from irradiated field natural rubber RVNRL Radiation Physics and Chemistry 67, 501–503

Jonah, S.A., Zakari, I.I., Elegba, S.B., 1999. Determination of the hydrogen content of oil sample from Nigeria using an Am–Be neutron source. Applied Radiation and Isotopes 50, 981 - 983.

K. Makuuchi, 2003. An introduction to radiation Vulcanization of Natural Rubber Latex, 168 – 181.  
Naqvi, A .A, 2003. Moisture measurements of wood and sugar samples using neutron transmission technique. Nuclear Instruments and Methods in Physics Research A 497, 569–576.

Norpaiza Mohamad Hasan, Rasif Mohd Zain, Mohd Fitri Abdul Rahman, Ismail Mustapha, (2009). The use of a neutron backscatter technique for in-situ water measurement in paper-recycling industry, Applied Radiation and Isotopes 67 1239–1243.

## **Eddy current thermography: NDT technique fusion for future industrial application**

Ilham Mukriz Zainal Abidin<sup>1</sup>, Masrol Nizam Salleh<sup>1</sup>, Muhammad Hazlam Masri<sup>2</sup>, Mohd Yusnisyafiq Yusof<sup>3</sup>, Mohd Yusnisyam Yusof<sup>1</sup>, Mohd Noorul Ikhsan Ahmad<sup>1</sup>, Mohd Zaki Umar<sup>1</sup> and Maslina Mohd Ibrahim<sup>1</sup>

<sup>1</sup>NDT Group, Industrial Technology Division, Malaysian Nuclear Agency, 43000 Bangi Kajang, Selangor, Malaysia

<sup>2</sup>Chemical Engineering Department, Universiti Teknologi PETRONAS, Bandar Seri Iskandar, 31750 Tronoh, Perak, Malaysia

<sup>3</sup>School of Aerospace, Mechanical & Manufacturing Engineering, Royal Melbourne Institute of Technology University, Bundoora East Campus, Victoria, Australia

[mukriz@nuclearmalaysia.gov.my](mailto:mukriz@nuclearmalaysia.gov.my)

### **Abstract**

Current industry requirements demand advances in non-destructive testing (NDT). Fusion of NDT techniques has proven to increase the capability and reliability of defect detection thus improve inspection results. It can also provide a solution for the limitations posed by a single NDT technique in acquiring the intended information and so achieving the required inspection efficiency. Eddy current thermography is an emerging technology in advanced NDT. The technology combines the well established eddy current testing with thermography inspection to provide a fast and efficient method for defect detection and characterisation over a relatively large area. This paper provides an insight to eddy current thermography system development and its potential for industrial NDT application. Results from 3D FEM simulation and qualitative experimental investigations of eddy current thermography on defect detection in conductive samples are also presented. The work demonstrates the effectiveness of NDT technique fusion in providing comprehensive and reliable defect assessment.

**Keywords:** eddy current thermography, non-destructive testing, fusion, 3D FEM

### **1. Introduction**

The reliability of defect detection within a particular sample can be increased by using several different NDT techniques, especially when the methods are particularly sensitive to different types of defects and material parameters. Complementary information can be provided by the fusion of NDT techniques, which gives better inspection results and more information can thereby be acquired compared to the results from an individual technique. It can also provide a solution for the limitations posed by a single technique in acquiring the intended information and so achieving the required inspection efficiency. Fusion can be achieved via combinations of NDT techniques; association of NDT data for complementary results; or incorporation of different excitation modes to provide a technique for improved inspection capabilities.

Fusion of two NDT techniques has been proposed for the testing of surface defects in rail tracks. A combination of Pulsed Eddy Current (PEC) and Electromagnetic Acoustic Transducer (EMAT) has demonstrated the capacity to accurately characterise surface-breaking defects with depths of up to 20mm. PEC is more sensitive to shallower surface cracks, discriminating defects up to 5mm deep, while the EMAT is more sensitive to surface-breaking defects between 2.5mm and 15mm deep [1]. Both techniques show good accuracy and the integration of the results enable more reliable depth measurement. One example of a system fusion study in NDT is an investigation funded by the US government into the feasibility of using multiple inspection techniques for assessing pipe wall conditions in natural gas pipelines [2]. The techniques considered for fusion in the study are Magnetic



Flux Leakage (MFL), Ultrasonic (UT), thermal imaging and Acoustic Emission (AE). Fusion of MFL with thermal imaging shows the poorest results in the test due to limitations of both techniques in the identification of defect edges. On the other hand, UT and MFL produced the best fusion results because these techniques give the most quantitative NDT information relating to the geometry and location of defects.

Active thermography is another example of NDT technique fusion, which utilises different modes of excitation for thermal stimulation in defect detection by thermographic images. Heating of the material under inspection can be accomplished via the application of sonic or ultrasonic energy using a device such as an ultrasonic welding horn; this is known as vibrothermography, thermosonics or sonic infrared (IR) [3]. The applied excitation vibrates the material under inspection and leads the crack faces to rub against each other, the mechanical energy is converted to heat and the generated heat is detected at the material surface. Disadvantages include the need for contact between the test piece and the ultrasonic welding horn and the unreliability of this contact, which leads to the vibration spectrum produced being highly variable from contact to contact [3]. An alternative to heat lamp or sonic excitation is found in eddy current heating, where the part under inspection is heated by an inductively-generated current flow [4-6]. This technique, also known as induction thermography [7], tone burst eddy current thermography [8], and thermo-inductive [9] inspection, uses induced eddy currents to heat the material being tested [4, 5, 10, 11] and defect detection is based on the changes of the induced eddy current flow revealed by the thermal distribution captured by an infrared (IR) camera. Thermographic data and images can then be immediately assessed to provide an indication of major faults and the data can be further analysed to provide quantitative information of defects inside the inspected sample. This technique is able to detect hidden, subsurface defects even in complex components, in line with other thermographic NDT techniques such as sonic [12] and laser spot thermography [13].

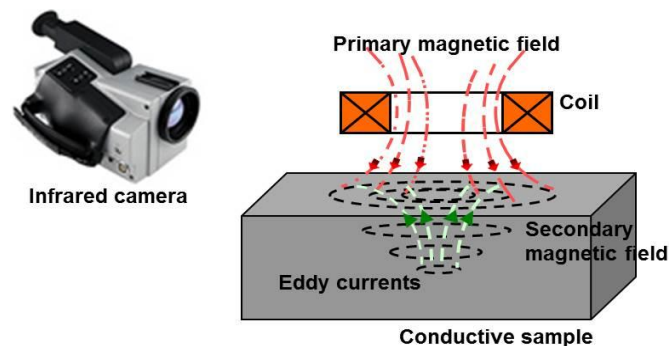


Figure 1: The concept of eddy current thermography

Eddy current thermography involves the application of a high frequency (typically 50–500 kHz) electromagnetic wave to the material under inspection. For pulsed thermography [8, 10] this is simply switched on for a short period (typically 20ms–2s), in contrast to lock-in techniques [14], where the amplitude of the high frequency is modulated by a low frequency lock-in signal. The induced eddy currents are converted to heat through ohmic heating, according to Joule's Law. Both direct heating and diffused heating contribute to defect detection; defects such as cracks, voids or delaminations which are within the range of the eddy current distribution disturb the current flow and thus change the temperature distribution. Defects which do not directly interact with the induced eddy currents may interact with the heat generated at the surface as it propagates through the material (as with traditional heat lamp techniques). Thus, eddy current thermography has many potential advantages over heat lamp and sonic excitation (the change in temperature of the coil itself is very small), there is a little chance of damage to the material under inspection, as heating is limited to a few °C and for near-surface defects, direct interaction with eddy currents can improve detectability [15].

Although NDT technique fusion have shown the capacity for improving defect characterisation and inspection reliability, special attention should be given to the complexity of the integrative system and the possibility of having redundancy of information, which can provide more problems than solutions. Therefore, evaluation and initial investigations are required should integrative NDT techniques be used to overcome the limitations of individual NDT techniques. This is where numerical simulation investigations can be used to their full potential in providing the initial results and evaluating the proposed integrative NDT technique. In this paper, the development of an eddy current thermography system is detailed; including excitation hardware, coil design and camera selection in section 2. Section 3 provides results from 3D FEM simulations and experimental qualitative investigations of eddy current thermography on defect detection. Section 4 concludes the paper with a discussion of the work and the potential of eddy current thermography as a NDT technique fusion system for future industrial application.

## 2. Eddy Current Thermography System

A typical system setup of the eddy current thermography system consists of an induction heating control box which supplies power to the work head. The work head contains a transformer coupled resonant circuit, including two capacitors and the excitation coil itself. The excitation frequency is dictated by the values of the capacitors, the inductance of the coil and the load of the circuit, i.e. the material, volume and proximity of the sample under inspection. A PC which is linked to the IR camera stores the thermal images captured by the camera for subsequent analysis. Figure 2 shows an example of the system setup for an eddy current thermography system.

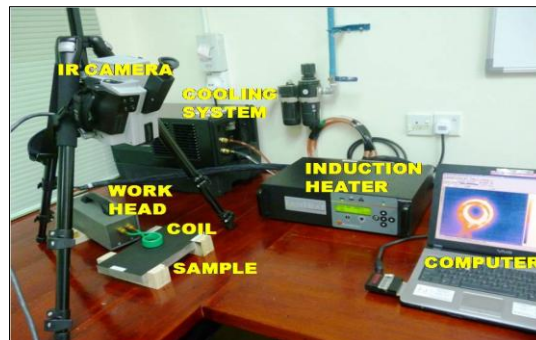


Figure 2: System setup for eddy current thermography system

The excitation subsystem for our system is based around a commercial induction heating system, the Easyheat 224 from Ambrell, shown in Figure 3a. The Easyheat has a maximum excitation power of 2.4 kW, maximum current of 480A and an excitation frequency range of 150 kHz – 400 kHz.



Figure 3: a) The EasyHeat 224 induction heating system; and b) Coils designed according to application

In practice, the inductance of the coil has been found to be roughly proportional to the length of tube to construct the coil; a shorter coil operates at a higher frequency and a longer coil operates at a lower frequency. If the coil inductance is not within a certain range, the circuit will not resonate and the induction heater will not work. In our work, the excitation coils are constructed from 6.35mm hollow high-conductivity copper tube. Water is pumped through the coil during operation to aid in cooling. The coils design depends upon optimum defect detection capability, which is based on the type and geometry of the tested sample. In many cases, new coils need to be designed and fabricated to fulfil the inspection needs. Figure 3b shows some of the coils that have been fabricated for different purposes and applications. One of the major factors influencing coil design is the induction of optimally uniform eddy currents in the object under inspection which will cut across, rather than divert around the expected defects.

### 3. Qualitative Investigation by Eddy Current Thermography Testing

#### 3.1 Simulation on eddy current thermography

Figure 4 shows the 3D FEM simulation results of the interaction between uniform eddy currents with a defect in a conductive sample. The simulations for eddy current thermography for our work were conducted using COMSOL via the multiphysics application. The eddy current flow for the result is visualised by the streamline plot (Figure 4a).

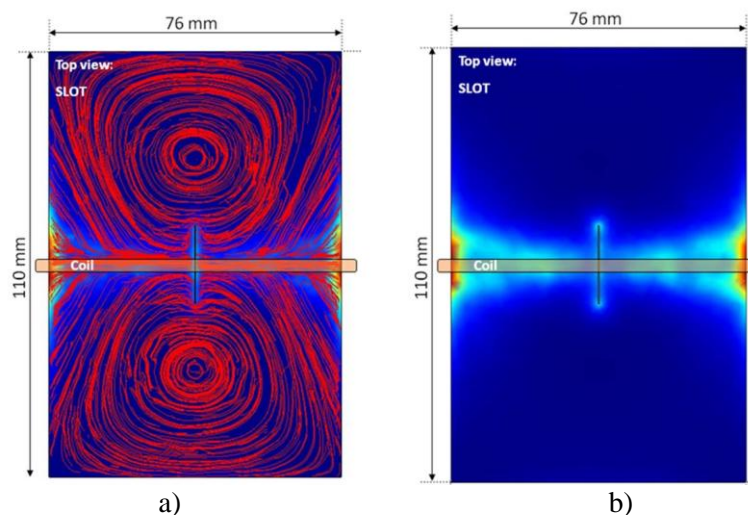


Figure 4: Simulation results for conductive sample after 100ms of heating of a) eddy current, and b) resultant heat distribution

In the presence of the defect, eddy currents will divert to complete their closed loop path, which leaves a unique eddy current distribution based on the defect geometry that can provide useful information about a defect. One notable observation from the streamline plot is that the presence of the defect causes an obvious diversion of the eddy currents around the tip of the defect. The streamline plot also illustrates the large influence that sample geometry has on eddy current distribution; where the eddy current loops encounter a sample edge an area of higher current density is formed, e.g. at the sample edge, under the coil. Thus, defects with the same geometry and orientation, but different position under the sample under inspection can interact with the induced eddy currents in different ways and cause very different heat distributions. Figure 4b shows the resultant heat distribution for the defect, viewed from the top of the sample for surface heating distribution. It can be seen from the top view that for both samples, there are hotter areas directly under the induction coil, plus a build-up of heat at the edges of the sample. In addition to this, the defect exhibits a characteristic heat build-up at the tips of the defect and cooler areas at either side of the defect. Through the graphical results provided by the simulations, the heat distribution due to the presence of a defect was observed, and provides support

for the experimental results. These results provide the visualisation of temperature distribution underlying phenomena due to the presence of a defect inside investigated sample.

### 3.2 Eddy Current thermography experimental investigations

The evaluation of defects in industrial components can be assisted by the use of an artificial crack produced inside a ready-made sample. For example, the use of a Trueflaw sample which has a crack produced by the thermal fatigue cracking mechanism can provide a more realistic test defect. Work on the investigation of a crack inside a Trueflaw sample has been conducted using the eddy current thermography technique. These true parameters of the crack can be used to assess the technique's performance for defect characterisation. Figure 5 shows an example of eddy current thermography results on the Trueflaw sample. From the figure, it can be seen that the crack in the sample can be detected and a good definition of the crack shape can be observed from the thermal image. The Trueflaw sample investigation results can provide the reference for defect quantification applied to other industrial components, e.g. welded sample, turbine blades. Preventive maintenance on welded samples and turbine blades, which are critical components in power generation industries, is an important factor in cost and safety issues within those industries.

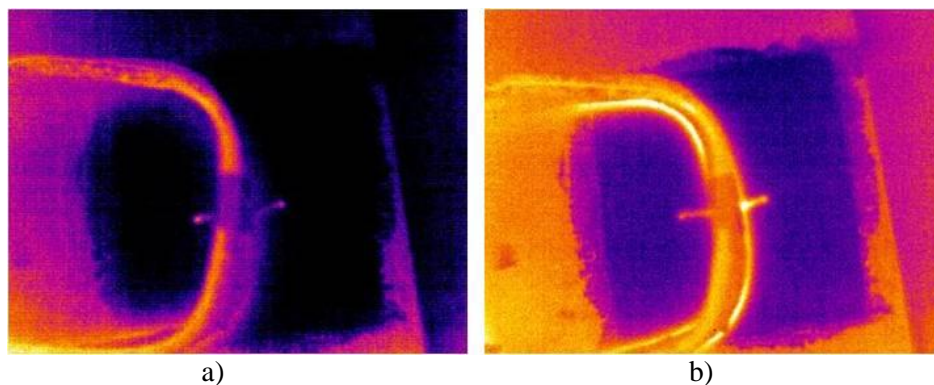


Figure 5: Thermal images showing the crack in the TRUEFLAW sample obtained by eddy current thermography; a) Early stage heating - 100ms, b) Later stage heating - 300ms

From figure 5, in the early stages (100ms), only heat generated at the tip reaches the surface. As the heating period increases to 300ms, heating at the tip of the defect are joined at the surface by a small amount of diffused heat from the bottom of the defect, hence the build up of heat which surrounds the defect. The result shows that a good definition of the defect tip edges can be obtained in the early stage of the heating period, where eddy current heating is dominant and there is less contribution from diffused heat. These observations confirm the results presented by the numerical simulations in section 3.1, where the eddy current follows the path of least resistance which forms the dedicated heating distribution with a particular defect.

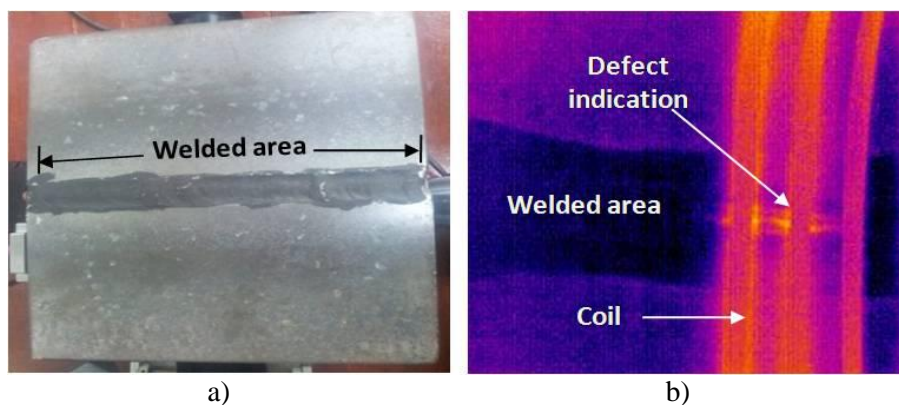


Figure 6: a) Welded sample having surface crack, b) Results by eddy current thermography



Figure 6a shows a welded carbon steel sample having a longitudinal surface crack. The indication of the crack was clearly visible under the eddy current thermography technique (Figure 6b). The investigation on the welded sample provides the means to evaluate the eddy current thermography technique for defect detection, where the pattern of heating is dependent on the eddy current distribution resulting from its interaction with a defect. The employment of the IR camera with the eddy current thermography technique provided the high spatial resolution required to perform the visualisation technique for possible defect characterisation through the mapping of eddy current distribution.

#### 4. Conclusions

The advantages and applications of eddy current thermography testing as NDT technique fusion have been outlined in this paper along with results from 3D FEM numerical simulations and experimental investigation on conductive sample. The simulations have provided an understanding of the fundamental behaviour of eddy current heating and heat diffusion in the presence of a defect. The qualitative investigations on the conductive samples provide the means to evaluate the eddy current thermography technique for defect detection through the mapping and visualisation of eddy current distribution by the use of an IR camera. Good agreement was shown between the results from the simulation and experiment in terms of heating patterns, supported by the graphic visualisation of the heating mechanism provided by the simulations. The work has shown the effectiveness of the eddy current thermography technique, resulted from NDT technique fusion, to be applied on industrial components for an alternative NDT technique in industrial applications. Future work will focus on the characterisation and evaluation of defects for quantitative information.

#### Acknowledgements

The authors would like to acknowledge the support given by Malaysia's Ministry of Science, Technology and Innovation (MOSTI) Sciencefund (03-03-01-SF0086) and the Malaysian Nuclear Agency in the implementation of the work.

#### References

- [1] R.S. Edwards, A. Sophian, S. Dixon, G.Y. Tian and X. Jian, 'Dual EMAT and PEC non-contact probe: applications to defect testing', *NDT & E International*, Vol. 39, pp. 45-52, 2006.
- [2] S. Mandayam, R. Polikar and J.C. Chen, 'A data fusion system for the nondestructive evaluation of non-piggable pipes', retrieved Mac 2013, References 151 National Energy Technology Laboratory website, <http://www.netl.doe.gov/technologies/oil-gas/publications/td/NT41648>.
- [3] M. Morbidini, P. Cawley, M.J.S. Lowe, T. Barden, and D.P. Almond, 'A Investigation of Thermosonics', WCNDT, Montreal, Canada, 2004.
- [4] G. Riegert, T. Zweschper and G. Busse, 'Lock-in thermography with eddy-current excitation', *Quantitative Infra Red Thermography Journal*, Vol. 1, pp. 21-32. 2004.
- [5] B. Oswald-Tranta, 'Thermo-inductive crack detection', *Nondestructive Testing and Evaluation*, Vol. 22, pp. 137-153, 2007.
- [6] S. Pickering and D.P. Almond, 'Matched excitation energy comparison of the pulse and lock-in thermography NDE techniques', *NDT & E International*, Vol. 41, pp. 501-509, 2008.
- [7] J. Vrana, M. Goldammer, J. Baumann, M. Rothenfusser and W. Arnold, 'Mechanisms and models for crack detection with induction thermography', *Review of Quantitative Nondestructive Evaluation*, Vol. 27, pp. 475-482, 2008.
- [8] C.N. Kumar, C.V. Krishnamurthy, B.W. Maxfield and K. Balasubramaniam, 'Tone burst eddy-current thermography (TBET)', *Review of Quantitative Nondestructive Evaluation*, Vol. 27, pp. 544-551, 2008.

- [9] B. Oswald-Tranta, 'Thermo-inductive crack detection', *Nondestructive Testing and Evaluation*, Vol. 22, pp. 137-153, 2007.
- [10] G. Zenzinger, J. Bamberg, M. Dumm, P. Nutz, 'Crack detection using EddyTherm', *Review of Progress in Quantitative Nondestructive Evaluation*, AIP Conference Proceedings, Vol. 760, pp. 1646-1653, 2005.
- [11] J. Bamberg, W. Satzger, and G. Zenzinger, 'Optimized image processing for eddy current thermography', *Review of Progress in QNDE*, Vol. 25A, pp.708-712, 2005.
- [12] M. Morbidini, P. Cawley, M.J.S. Lowe, T. Barden, and D.P. Almond, 'A Investigation of Thermosonics', WCNDT, Montreal, Canada, 2004.
- [13] Burrows SE, Rashed A, Almond DP, Dixon S. Combined laser spot thermo- graphy and ultrasonic measurements for crack detection. *Nondestructive Testing and Evaluation* Vol. 22, pp. 217-27, 2007.
- [14] G. Riegert, Th. Zweschper, and G. Busse, 'Lock-in thermography with eddy-current excitation', *Quantitative Infra Red Thermography Journal*, Vol. 1, pp. 21-32, 2004.
- [15] S. Pickering and D. Almond, 'Matched excitation energy comparison of the pulse and lock-in thermography NDE techniques', *NDT & E International*, Vol. 41, No. 7, pp. 501-509, 2008.



## JOHAN INSPECTION SERVICES SDN BHD

(407107-H)

26, JALAN U1/48, TEMASYA INDUSTRIAL PARK, GLENMARIE

40150 SHAH ALAM, SELANGOR D.E., MALAYSIA

TEL : 603-5569-8822 FAX : 603-5569-8833 EMAIL : office@jis.com.my

www.jis.com.my

### SPECIALIZING IN :-

- ❖ RADIOGRAPHY TESTING
- ❖ RADIOGRAPHY TESTING (SCAR)
- ❖ ULTRASONIC TESTING
- ❖ ULTRASONIC THICKNESS SURVEY
- ❖ MAGNETIC PARTICLE INSPECTION
- ❖ DYE PENETRANT TESTING
- ❖ ULTRA-VIOLET BLACK LIGHT (FLUORESCENT)
- ❖ VACUUM TEST INSPECTION
- ❖ PREHEATING
- ❖ POST WELD HEAT TREATMENT
- ❖ BRINELL HARDNESS TESTING
- ❖ WELDER QUALIFICATION TEST
- ❖ SUPPLY OF WELDING INSPECTORS
- ❖ SUPPLY OF RADIOGRAPHIC FILM INTERPRETERS
- ❖ PIPE COATING INSPECTION (HOLIDAY DETECTION)
- ❖ POSITIVE MATERIAL IDENTIFICATION (PMI)



Electrical Resistance Heat Treatment



Induction Heating



Hardness Testing (UCI/Rebound)



Positive Material Identification



Magnetic Particle Inspection



Ferrite Count



Ultrasonic Testing



Penetrant Testing

ISO 9001:2000



LLOYD'S CERTIFIED

**NON-DESTRUCTIVE TESTING,  
ENGINEERING INSPECTION &  
HEAT TREATMENT SPECIALIST**



## MR Technology Sdn Bhd

MR Technology Sdn. Bhd (MRTSB) was established in Mac 2003. It is a wholly - owned Bumiputra company. MRTSB had been an active in marine engineering , Scada system, scientific instrumentation equipment and Metal Magnetic Memory (advanced NDT) equipment and providing services. In the year of 2012, MRTSB had secured projects and providing specialised engineering services in advanced non-destructive testing to major operating oil and gas company.

### Contact Person

Mohd Noor Baharin  
Technical Project Executive  
[baharin@mrtsb.com.my](mailto:baharin@mrtsb.com.my)

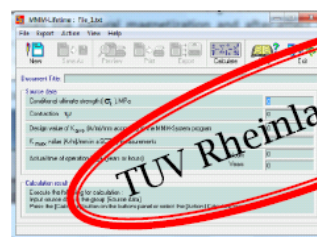
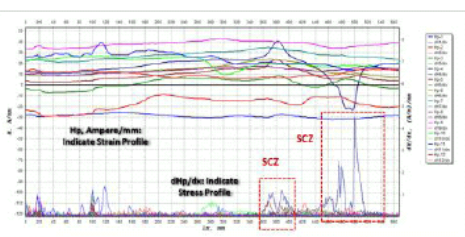
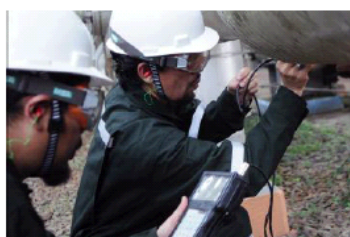


## MMM Technology

MMM technology is an advanced NDT method capable of measuring and displaying the strain & stress profiles of the inspected engineering components, structures & welding under real working load. Specifically, MMM technology is based on the measurement & analysis of the natural self-magnetic energy field generated by the surface of engineering components, structures & welding. The strain & stress profiles are further utilized to determine the stress concentration zones (SCZs), imperfection, and defect. The detection and quantification of the SCZs is very important for early detection of defect formation. Defects such as wear, crack, corrosion, fatigue and creeping will be initially developed and propagate most intensively inside the SCZs area. The MMM technology is recognized by the ISO standard with the code number, ISO 24497-1,2,3:2007 (E). Currently MRTSB is the exclusive agent for MMM Technology in Malaysia.

## MMM Principles

The MMM method uses the natural magnetization and after-effect results as the magnetic memory of metal to actual strains and stress changes in engineering components, structures and welding. The MMM method is the only passive method among the magnetic NDT methods. This technology also capable in predicting the remaining life of the structure by taking into account the stress-strained condition of the pipe.



**TUV Rheinland Certified**



## Types of MMM Technology

- i. Contacting MMM Technology:
- ii. Non-Contacting MMM Technology



## Advantages of MMM Technology

- i. The only passive technique (among all the magnetic NDT technology) in which the MMM technology monitor, detect and measure the natural self-magnetic leakage experienced by the components and structures.
- ii. Fast screening inspection technology for welding, engineering components and structures.
- iii. Capable of monitoring and detecting Stress Concentration Zones (SCZ) or weak areas (SCZ's, high stress-strain area) in engineering components, structures and welding.
- iv. Capable and detect defects such as crack, corrosion, erosion, metal loss and welding defects.
- v. MMM is capable of measuring actual strain and stress profile of engineering components, structures and welding. Stress and stress are the main parameters utilised for engineering failure analysis.
- vi. Capable of inspecting pipe under insulation including the fire proofing material (calcium silicate).
- vii. Capable of inspecting underground piping without any excavation. This is accomplished using the non-contacting MMM technology scanning devices.
- viii. Portable, small-sized and battery operated instruments are used for the MMM technology.

## Application of MMM in Malaysia & Overseas

1. Contacting MMM technology for Sludge Catcher Integrity Assessment Project in MLNG Bintulu, October 2012 to February 2013. Inspection of Sludge Catcher 1 containing 10 Bottles with 42 inches diameter and 360m length.
2. Non-Contacting MMM technology for Sludge Catcher Integrity Assessment Project in MLNG Bintulu, October 2012 to February 2013. Inspection of Sludge Catcher 2 containing 8 Underground Bottles with 48 inches diameter and 320m length. Inspection was conducted without excavation.
3. Mock-up test for Insulated Chiller Pipe (1220mm diameter), Parkview Complex Hong Kong, NTG Pte Ltd Hong Kong, June 2013. Inspection was conducted without removing the insulation.
4. Mock-up test for Insulated Pipe, Petronas Penapisan (Terengganu) Sdn Bhd, May 2013. Inspection was conducted without removing the insulation.
5. Mock-up test for Underground Gas Piping, Gas Malaysia Sdn Bhd, March 2013. Inspection was conducted without any excavation.
6. Mock-up test for Insulated Gas Pipe, Petronas Gas Distribution Centre, Shah Alam, Sdn Bhd, Oct 2012. Inspection was conducted without removing the insulation.
7. Mock-up test for Insulated Gas Pipe, Petronas Gas GPP5 dan 6, Paka, Terengganu. Sept 2013. Inspection was conducted without removing the insulation.



# Malaysian Skills Certificate

*Your career gateway...*



## Department of Skills Development

Ministry of Human Resources  
Level 7 - 8, Block D4,  
Complex D, Federal  
Government Administrative  
Centre, 62530 Putrajaya,  
Malaysia.

Phone: 03-8886 5000  
Fax: 03-8889 2430  
E-mail: [jpk@mohr.gov.my](mailto:jpk@mohr.gov.my)  
Website: [www.dsd.gov.my](http://www.dsd.gov.my)

Department of Skills Development (DSD), Ministry of Human Resources has been accredited with MS ISO 17024 Conformity Assessment — General Requirements For Bodies Operating Certification of Persons in Non-Destructive Testing sector.

As the National Certification Body for personnel skills in Malaysia, DSD strives to pursue recognition of beyond boundaries with **YOU AS OUR AMBASSADOR!**